Development of a New Adhesion Promoter for Metal Adhesion on Polymer Substrates for Printed Circuit Board Production Using Functionalized Silica Nanoparticles

Inaugural-Dissertation

to obtain the academic degree

Doctor rerum naturalium (Dr. rer. nat)

submitted to the Department of Biology, Chemistry and Pharmacy

of Freie Universität Berlin

by

Thomas

From Surabaya, Indonesia

March 31, 2016

This work has been done at Atotech Deutschland GmbH, Berlin, under the supervision of Priv.-Doz. Dr. Constanze Donner, in the period from February 23, 2010 to April 01, 2014.

Date of defense: September 8, 2016

1st Reviewer: Priv. Doz. Dr. Constanze Donner

2nd Reviewer: Prof. Dr. Christina Maria Graf

Abstract

In this work, a novel surface treatment method using functionalized silica nanoparticles to promote the adhesion of electrolessly deposited copper on the surface of dielectric substrates was described. A silylation process based surface modification method has been used to prepare silica nanoparticles of desired size and surface functionality. Two commercially available dielectric materials were used as substrate, ABF-GX 92 (epoxy resin) and polyimide Kapton®200 H (Poly [*N, N'*-(oxydiphenylene)pyromellitimide]). The adhesion strength between copper and dielectric substrates has strong dependence on functional groups at silica surface and particles size. Substrates treated with silica particles containing aminopropyl functional groups (*AP-Monoamine*) exhibit the highest adhesion strength, up to 9.2±0.3 N/cm and 15±0.1 N/cm for copper on *AP-Monoamine* treated epoxy substrate and polyimide film respectively. In particular, the adhesion strength of copper on substrates surface treated with *AP-Monoamine M* (TEM diameter = 18±3 nm) increased with nanoparticles concentration, suspension temperature, and substrate immersion time. From the peeled samples, it was confirmed that the failure resulted in the cohesive failure of dielectric substrates. The strong adhesion was attributed to the strong interaction of the aminopropyl functional groups of the *AP-Monoamine* with palladium and copper species, and the fact that the *AP-Monoamine* was covalently bound to the epoxy substrate or polyimide film surface. Additional, different peel strengths of copper on either epoxy resin or polyimide film treated with three different sizes of *AP-Monoamine* reveal the contribution of the secondary force (mechanical adhesion) on the adhesion strength, which is from the anchoring of copper by filling the nano-roughened structure of epoxy resin or polyimide film surfaces treated with aminopropyl functionalized silica nanoparticles.

Acknowledgements

I would like to thank especially Dr. Hans Jürgen Schreier, for him giving me the opportunity to do this PhD work at Atotech Deutschland GmbH Berlin. Thank you for mentoring, trusting me and providing independence in every stage of my work.

I would like to express my special appreciation and thanks to Priv. Doz. Constanze Donner for encouraging and following my research. Thank you for your brilliant comments and invaluable suggestions. I would also like to thank Prof. Dr. Christina Maria Graf from Freie Universität Berlin for spending her precious time in reviewing my PhD work and valuable discussions.

In particular, I would like to express my gratitude to Dr. Belén Gil-Ibáñez for her guidance during my PhD. Your shared knowledge, encouragement, and critiques were essential to the progress of this work.

Special thanks to Robin Taylor for sharing his invaluable knowledge in electronics industry development. I appreciate the help of Atotech library staff, especially Dr. Anita Depenbrock.

I would like to thank Dr. Stefanie Ackermann, and Lars Kohlmann for collaboration in synthesizing the nanoparticles and teaching me how to work with the Easymax.

I am thankful for the excellent work of Gregoire Dietrich and Hélène Garcin who were always helping me with the AFM measurements. Thank to Dr. Ralf Schulz, Dr. Sascha Dieter, Dr. Nicola Baeulke, Liane Liske, Martina Kußmann for helping me with the FE-SEM and FIB measurements. Thank to Dr. Karl Gerdom, Christian Sebald and Balamurali Heintze for helping me with physical and mechanical tests. I am grateful to Dr. Lars Nothdurft for helping me with EA measurements. I would like to thank Dr. Xiaoting gu and Craig Bishop in Case Western Reserve University (CWRU), Cleveland for their excellent work in helping me with the XPS measurements and data interpretations. I would like also to thank Christian Goroncy in Freie Universität Berlin for his help with the TEM imaging.

I would like to thank Dr. Lutz Brandt, Dr. Meng Hsieh, Ellina Libman, and Dr. Izabela Schmidt from BTT-MIT Atotech USA, and also Dr. Akio Ishikawa and Dr. Joanne Yu

from R&D Atotech Japan for their valuable discussions and helps. Thank you for a very enjoyable phone conference.

I would also like to thank the entire team member of Atotech BTT-PTH, particularly, Dr. Lutz Stamp, Dr. Laurence Gregoriades, Dr. Stefan Kempa, André Beyer, Regina Czeczka for their helps, time, and for sharing the knowledge with me. Special thanks to Dr. Sebastian Zarwell for his invaluable discussions and suggestions. Many thanks to Dr. Dirk Tews and Dr. Fabian Michalik from Atotech BTT-STT for sharing the experiences and technical discussions on the FTIR.

I am grateful to the entire team members of Atotech R&D electronics, who created a relaxed working atmosphere around me. I want to express my special thanks to Dr. Yoshiko Nishihara for her patience in reading my dissertation, Dr. Kay-Oliver Thiel for his invaluable helps, from small until big thing, Dr. Marco Haryono for always taking a good care the lab workplace for us, Dr. Christian Spickermann and Dr. Frank von-Horsten, for numerous productive discussions in theoretical calculation, our secretary Eileen Will for her kindness and generosity. Many thanks to Scheghajegh Kord, Markus Kauer and Deniz Cakir for exchange of knowledge and experiences.

In particular, I would like to express my gratitude to my officemates, Senguel Karasahin and Dr. Taybet Bilkay for being always nice to me and giving me joy. Special thanks to Gerson Krilles and Arnaud Jacquemoud-Collet for their continuous support of my PhD and on top of that thank you for your friendship.

I would like to forward my special thanks to the Langnickel family, especially Volker Langnickel, Marina Yang Langnickel, and Florian Liyau Langnickel for their supports and sharing their happiness with me in Germany.

Last but not the least, special thanks to my family, words cannot express how grateful I am to my beloved parents, for their love, understanding, encouragement and being the greatest support in my life.

Table of Contents

Abstract ..... **i**
Acknowledgements ..... **ii**
Table of Contents ..... **iv**
List of Tables ..... **vii**
List of Schemes ..... **ix**
List of Figures ..... **x**
Chapter 1 - General introduction **1**
1.1. Technology trend of electronics industry 1
1.2. Adhesion challenge in electronics industry 5
1.3. Objectives and outline of the thesis 7
Chapter 2 - Theoretical background **9**
2.1. Polymer/metal adhesion mechanism 9
2.2. Current dielectric/metal adhesion promoter methods 13
2.2.1. Surface roughening with chemical etch 14
2.2.2. Polymer grafting on dielectrics 16
2.2.3. Plasma treatment 18
2.2.4. Silane coupling agents 21
2.2.5. Conclusions 23
2.3. Metallization of polymer surface 23
2.4. Polymer substrates for printed circuit board 25
Chapter 3 - Fundamentals of applied techniques **28**
3.1 Dynamic Light Scattering (DLS) 28
3.2 Zeta Potential 31
3.3. C, H, N, S Elemental Analysis (EA) 34
3.4. Ultraviolet/Visible Spectroscopy (UV-Vis) 34
3.5. Fourier Transform Infra-Red-Attenuated Total Reflectance (FTIR-ATR) 37
3.6. X-ray Photoelectron Spectroscopy (XPS) 39
3.7. Atomic Force Microscope (AFM) 41
3.8. Field Emission Scanning Electron Microscope (FESEM) 43
3.9. Inductively Coupled Plasma- Optical Emission Spectroscopy (ICP-OES) 44

Chapter 4 - Synthesis and characterization of functionalized silica nanoparticles ... 46
4.1. Introduction ... 46
4.2. Experimental ... 49
4.2.1. Materials ... 49
4.2.2. Preparation of functionalized silica nanoparticles ... 49
4.2.3. Purification of the functionalized silica sols by dialysis ... 53
4.2.4. Characterization ... 53
4.3. Experimental results and discussions ... 58
4.3.1. Aminopropyl functionalized silica nanoparticles (*AP-Monoamine*) ... 58
4.3.2. *AP-Diamine* and *AP-Triamine* functionalized silica ... 65
4.3.3. Silica nanoparticles modified with different functional groups ... 70
4.4. Conclusions ... 77
Chapter 5 - Modification of epoxy substrate (ABF-GX92) surface for adhesion enhancement with deposited copper films ... 78
5.1. Introduction ... 78
5.2. Experimental ... 80
5.2.1. Materials ... 80
5.2.2. Sample preparation ... 80
5.2.3. Characterization ... 82
5.2.4. The optimization of process parameters ... 85
5.3. Results and discussions ... 87
5.3.1. Activation of the surface of epoxy substrate ... 87
5.3.2. Epoxy polymer surface modification with aminopropyl functionalized silica nanoparticles (*AP-Monoamine M*) ... 91
5.3.3. Electroless copper deposition on epoxy substrate surface modified with aminopropyl functionalized silica ... 94
5.3.4. Evaluation of adhesion of deposited copper layer on *AP-Monoamine M* modified epoxy substrate ... 96
5.3.5. Failure mode of deposited copper layers on AP-Monoamine modified epoxy substrate ... 109
5.3.6. Adhesion reliability of deposited copper on modified epoxy substrate surfaces after stress test ... 112
5.3.7. The adsorption of palladium species on *AP-Monoamine M* modified epoxy substrate ... 116
5.4. Conclusions ... 119

Chapter 6 - Surface modification of polyimide films with aminopropyl functionalized silica nanoparticles for improvement of adhesion with deposited copper ... 120

6.1 Introduction ... 120

6.2 Experimental ... 122

6.2.1 Materials ... 122

6.2.2 Sample preparation ... 122

6.2.3 Surface characterization ... 124

6.3 Results and discussions ... 127

6.3.1 Permanganate treatment on polyimide Kapton®200 H films ... 127

6.3.2 Polyimide film surface modification with aminopropyl functionalized silica nanoparticles (*AP-Monoamine*) ... 138

6.3.3 Electroless copper deposition on *AP-Monoamine M* modified polyimide films 149

6.3.4 The evaluation of adhesion of deposited electroless copper layers on polyimide films modified by aminopropyl silica nanoparticles (*AP-Monoamine*) ... 157

6.3.5 Failure mode of deposited copper layers on *AP-Monoamine M* modified polyimide film surface ... 163

8. Conclusions ... 164

Chapter 7 - Summary and Outlook ... 165

7.1 Summary ... 165

7.2 Outlook ... 168

Zusammenfassung ... 169

References ... 172

Appendix ... 179

List of publications ... 189

Abbreviations and symbols ... 190

List of Tables

Table 2.1 Typical bonding energies of various bonds type.[48-50] 12
Table 2.2 List of selected literature regarding plasma treatment on polymer surface to enhance adhesion with deposited conductive metal layer 20
Table 2.3 The physical properties of epoxy polymer film ABF-GX92. (Extracted from Ref.[75]) 26
Table 2.4 The physical properties of poly [N, N'-(oxydiphenylene)pyromellitimide] Kapton®HN. (Data extracted from Ref.[77]) 27

Table 4. 1 List of reagents and amounts were used for 100 mL scale synthesis of AP-Hydroxyl in ethanol 50
Table 4. 2 List of reagents and amounts used for the synthesis of AP-Monoamine M 51
Table 4. 3 Measurement parameters for dynamic light scattering (DLS) 54
Table 4. 4 The properties of cantilever with single crystal silicon tips used in AFM measurement 54
Table 4. 5 The MU of different elements on basis of sulfanilic acid measurements 57
Table 4. 6 Particle sizes of aminopropyl functionalized silica nanoparticles (*AP-Monoamine*) measured by DLS, TEM and AFM 58
Table 4. 7 Characteristic bands of bare and aminopropyl silica (*AP-Monoamine*), obtained by FTIR-ATR 63
Table 4. 8 Particle sizes of *AP-Monoamine, AP-Diamine and AP-Triamine* measured by TEM and DLS 65
Table 4. 9 Elemental analysis data of *AP-Monoamine M*, *AP-Diamine*, and *AP-Triamine* 70
Table 4. 10 Particle sizes of *AP-Monoamine M, AP-Ureido, AP-Glycidoxy and AP-Mercapto* measured by TEM and DLS 71
Table 4. 11 The elemental analysis data of silica nanoparticles modified with different functional groups 71
Table 4. 12 Characteristic IR bands of *AP-Monoamine M, Ureido, Glycidoxy, Mercapto* obtained by FTIR-ATR 76

Table 5. 1 Process sequences of electroless copper plating on modified polymer substrates 82
Table 5. 2 The property of cantilever with single crystal silicon tips used in AFM measurement 83
Table 5. 3 Characteristic bands of the epoxy substrate, obtained by FTIR-ATR.[141] 89

Table 6. 1 Process sequences of electroless copper plating on modified polymer substrates 124

Table 6. 2 The property of cantilever with single crystal silicon tips used in AFM measurement 125
Table 6.3 Characteristic bands of polyimide Kapton® 200 H before and after permanganate treatment, obtained by FTIR-ATR. The assignments are made according to reference[168] 130
Table 6. 4 XPS chemical states analysis for C1s, N1s and O1s signals of pristine polyimide Kapton® 200 H 135
Table 6. 5 The component ratio of polyimide surface of pristine and permanganate treated films, and theoretical values 136
Table 6.6 XPS chemical states analysis for C1s, N1s and O1s signals of permanganate and *AP-Monoamine M* treated polyimide films 147
Table 6. 7 The atomic concentration of elements based on the spectra of surface scan in Figure 6. 20 150
Table 6. 8 XPS chemical states analysis for Pd3d and N1s signals of polyimide films treated in alkaline permanganate solution and those treated with alkaline permanganate solution, then subsequently treated with *AP-Monoamine M*. In both cases, the sample were treated in Pd (II) ions solution (Neoganth activator 834), followed by reduction step in DMAB solution 153
Table 6.9 Surface roughness of polyimide films modified with different sizes of *AP-Monoamine* 161

Table A2. 1 The CHNS elemental composition of various functionalized silica nanoparticle measured by elemental analysis 184

List of Schemes

Scheme 4. 1 Base catalyzed hydrolysis and condensation reaction of TEOS 46
Scheme 4. 2 Silica nanoparticles stabilization in ammonia containing ethanolic solution. (Extracted from Ref.[100]) 46
Scheme 4. 3 Reaction of aromatic aldehyde with primary amine to produce imine (bright yellow) and with secondary amine to produce enamine (colorless) 69
Scheme 4. 4 The ring opening reactions of oxirane by acid catalyzed hydrolysis and by nucleophilic ammonium hydroxide addition S_N2 reaction 73

Scheme A1.1 Reaction scheme for the derivitization method.................................... 179

List of Figures

Figure 1.1 Following the technology development, conductor width and space size keeps on reducing gradually in PWB manufacturing. (Adapted from ITRS 2008[12]) ... 1
Figure 1.2 Semiconductor Industry Drivers Showing Compound Average Annual Growth Rates (CAAGR). (Source: Prismark Semiconductor Packaging Report Q1 2013[13]) ... 2
Figure 1.3 Line and space production capabilities dependent on manufacturing technique and copper thickness on the dielectric. (Source: Atotech Customer Survey 2012) HDI - High Density Interconnect, MSAP - Modified Semi Additive Process ... 3
Figure 1.4 Comparison between the AMSAP subtractive process and the SAP process ... 4
Figure 1.5 OEM Roadmap Showing Permitted Copper and Dielectric Roughness for Next Generation IC Substrates. (Extracted from Ref.[16]) ... 5

Figure 2.1 Schematic diagram of Van der waals interaction between polymer and metal ... 9
Figure 2.2 Contact angle of a drop of liquid on solid surface ... 10
Figure 2.3 Schematic diagram of mechanical anchoring between polymer and metal ... 11
Figure 2.4 Schematic diagram of chemical bonding between polymer and metal ... 12
Figure 2.5 Schematic diagram of weak boundary layer in polymer/metal interface ... 13
Figure 2.6 Surface morphology of ABF-GX 92 (epoxy resin/silica blend polymer) before (a) and after (b) subtractive roughening ... 14
Figure 2.7 Illustration of the polymer oxidation mechanism in different process steps. (Extracted from Ref.[21]) ... 15
Figure 2.8 Schematic diagram of “grafting to” (top) and “grafting from” (bottom). (Extracted from Ref.[55]) ... 17
Figure 2.9 Mechanism of “GraftFast” process purposed by Garcia *et al.*,[32] The process involves four main process, (a) photo-assisted reduction of the aryldiazonium compound, (b) the resulting aryl radicals grafted onto the surface and at the same time polynitrophenylene multilayer grows, (c) aryl radicals initiate the polymerization of acrylic acid, (d) polyacrylic acid oligoradicals grafting onto polynitrophenylene layer ... 18
Figure 2.10 Reaction scheme of silane coupling on the surface of dielectrics. (Adapted from Ref.[63]) ... 22
Figure 2.11 Process scheme of electroless copper deposition (a) and Evan’s diagram[73] (b) as a brief way to describe the electroless deposition process of copper ... 24
Figure 2.12 Chemical structure of ABF-GX92 substrate. (Extracted from Ref.[74]) ... 26
Figure 2.13 Reaction between ODA and PMDA to polyamic acid following with dehydration to polyimide. (Adapted from Ref.[76]) ... 27

Figure 3. 1 Schematic of a DLS instrument (adapted from Ref.[79]) 29
Figure 3. 2 The fluctuation of scattered light intensity as a function of time on different particle sizes (adapted from Ref.[80]).. 29
Figure 3. 3 Electrical double layer surrounding the surface of particle. (Reprinted from Ref.[79]) 31
Figure 3. 4 Zeta potential of particles as a function of pH showing the range where the particles should remain stable. (Extracted from Ref.[79]) 32
Figure 3. 5 The change of zeta potential with pH of silica particles carrying different surface chemical group, -OH for bare silica and $–NH_2$ for APTES functionalized silica 33
Figure 3. 6 Typical instrumentation arrangement of CHNS elemental analyzer. (Reprinted from Ref.[84]).. 34
Figure 3. 7 The absorbance spectra of salicylaldehyde reacted with different concentration of 3-APTES 36
Figure 3. 8 A calibration curve showing the absorbance intensity at 404 nm vs. APTES concentration... 37
Figure 3. 9 Representation schematic of a single reflection ATR with *Θ* incidence angle. (Extracted from Ref.[91]) 38
Figure 3. 10 Schematic diagram of photoelectron and auger electron emission process 40
Figure 3. 11 Schematic drawing of XPS using a monochromatic x-ray source.......... 40
Figure 3. 12 Schematic drawing of the AFM set-up 42
Figure 3.13 Three dimensional AFM image of polymer substrate 43
Figure 3. 14 Various signals generated as a result of primary electron interaction with surface or bulk of solid specimen... 44

Figure 4. 1 Stability of colloidal silica sol as a function of pH. (Adapted from Ref.[103]) 48
Figure 4.2 Image of silica nanoparticle obtained by AFM 55
Figure 4. 3 AFM images (a) and TEM images (b) of AP-Monoamine S, M, and L after functionalization with 3-APTES 59
Figure 4. 4 The change of zeta potential of bare and aminopropyl silica nanoparticles with pH. The pH was set to pH3 with 0.1 M HCl and was slowly increased to higher pH with 0.1 M NaOH 61
Figure 4. 5 FTIR-ATR spectra of bare (*AP-Hydroxyl*) and aminopropyl functionalized (*AP-Monoamine*) silica nanoparticle. The spectra were taken with resolution of 4 cm^{-1} 62
Figure 4. 6 The IR spectrum of amino-terminated silica particles may contain NH_3^+ and HCO_3^-. The reaction between surface amino groups atmosphere carbon dioxide can explain the reason for this observation. (Adapted from Ref.[114]) 63
Figure 4. 7 UV-Vis spectra of bare and aminopropyl functionalized silica nanoparticles after chemical derivatization with salicylaldehyde. Bright yellow color was observed after reaction and the sample showed a strong absorption band around 404 nm 64

Figure 4. 8 The change in zeta potential of bare and aminopropyl-functionalized (*AP-Monoamine M, AP-Diamine and AP-Triamine*) silica nanoparticles with pH. The pH was set to pH 3 with 0.1 M HCl and slowly increased to higher pH with 0.1 M NaOH 67
Figure 4. 9 FTIR-ATR spectra of *AP-Monoamine M, AP-Diamine, and AP-Triamine*. The spectra were taken with resolution of 4 cm^{-1} 68
Figure 4. 10 UV-Vis spectra of *AP-Hydoxyl* (bare silica), *AP-Monoamine M, AP-Diamine* and *AP-Triamine* after chemical derivatization with salicylaldehyde. Bright yellow color results after the reaction and has a strong absorption at 404 nm 69
Figure 4. 11 The zeta potential of various functionalized silica nanoparticles as a function of the pH. The pH was set to 3 with 0.1 M HCl and slowly increased by the addition of 0.1 M NaOH 73
Figure 4. 12 FTIR-ATR spectra of silica nanoparticles functionalized with different functional groups (a) and magnified view of the *AP-Mercapto* spectrum for better comparison (b). The spectra were taken with resolution of 4 cm^{-1} 75

Figure 5. 1 Surface preparation of epoxy polymer for copper metallization by (a) Standard industrial PCB production process and (b) Functionalized silica process (this work) 79
Figure 5. 2 Example of quantile plots 86
Figure 5. 3 FE-SEM and AFM surface topography image of epoxy substrate treated with permanganate in different periods of time, (a) 0 min, (b) 1 min, (c) 5 min, and (c) 15 min 87
Figure 5. 4 The scheme of proposed mechanism of the degradation of epoxy polymer chain by permanganate, adapted from the work of Sam et al., 2004[53] 88
Figure 5. 5 FTIR-ATR spectra of the pristine epoxy substrate 89
Figure 5. 6 FTIR-ATR spectra of epoxy polymer surface treated with permanganate at different period of time 90
Figure 5. 7 FE-SEM Surface morphology images of activated epoxy substrate before (a) and after (b) 4 g/L *AP-Monoamine M* treatment 92
Figure 5. 8 FTIR-ATR spectra of epoxy polymer surface treated with (a) 0 g/L, (b) 2 g/L, (c) 4 g/L and (d) 8 g/L of *AP-Monoamine M* 93
Figure 5. 9 The change of intensity ratio of (a) C=O to C=C aromatic stretch and (b) C=N to C=C aromatic stretch 93
Figure 5. 10 The FESEM images of pristine (a) and 4 g/L *AP-Monoamine M* treated (b) ABF-GX92, after 1 min immersion in electroless copper solution. All images were taken with the same magnification 95
Figure 5. 11 Cross-sectional STEM image of electroless deposited copper on (b) only permanganate treated and (c) 4 g/L *AP-Monoamine M* treated epoxy polymer surface. (a) The low magnification STEM image shows the area where the interface was zoomed (blue square) 96
Figure 5. 12 The influence of *AP-Monoamine M* dispersion temperature (a), withdrawing speed (b), and annealing temperature after treatment with *AP-Monoamine M* (c) on the peel strength. *AP-Monoamine M* dispersion with a

concentration of 4 g/L, an immersion time of 5 min, and an annealing time of 10 min were used 97
Figure 5. 13 FE-SEM images of epoxy substrate surfaces treated with a dispersion of *AP-Monoamine M* (c=4 g/L) at (a) 25 and (b) 70 °C. A withdrawing speed of 180 mm/min and immersion time of 5 min were used 99
Figure 5. 14 Peel strength of deposited copper on epoxy substrate modified with 4 g/L of *AP-Monoamine 50 nm* at 60 °C for 5 min. Argon or oxygen plasma was used as surface activation step 100
Figure 5.15 The peel strength of deposited copper on epoxy polymer substrate as a function of the concentration of *AP-Monoamine M.* The treatment was carried out at 60 °C for 5 min 101
Figure 5.16 FESEM surface image of epoxy substrate treated with 0.4 (a), 2 (b), 4 (c), and 8 (d) g/L of *AP-Monoamine M* at 60 °C for 5 min 101
Figure 5.17 The dependence of adhesion strength of deposited copper on modified epoxy substrate on the immersion time in *AP-Monoamine M* dispersion with different concentrations. The dashed lines are guides to the eye 102
Figure 5.18 AFM surface morphology images of epoxy polymer treated with *AP-Monoamine M* dispersion with c= 0.8 g/L at 60 °C for 10 (a), 300 (b), 600 (c) s of immersion time. The measurement window size is 1 x 1 μm^2 103
Figure 5.19 Influence of the *AP-Monoamine* particle size on the adhesion strength. *AP-Monoamine S* (Z-average in DLS= 38±1 nm; diameter TEM= 14±3 nm), *AP-Monoamine M* (Z-average in DLS= 52±1 nm; diameter TEM= 18±3 nm) and *AP-Monoamine L* (Z-average in DLS= 92±2 nm; diameter TEM= 68±7 nm) were used 104
Figure 5.20 FE-SEM image of epoxy substrate surface treated with AP-Monoamine S (a), M (b), and L (c) 105
Figure 5.21 FE-SEM image of epoxy substrate surface covered with (a) *AP-Ureido* (Z-average in DLS= 68±1 nm, (b) *AP-Glycidoxy* (Z-average in DLS= 55±1 nm), (c) *AP-Mercapto* (Z-average in DLS= 38±2 nm), and (d) Native silica nanoparticles (Z-average in DLS= 52±2 nm) 106
Figure 5.22 Effect of different functional groups on functionalized silica nanoparticles on the adhesion strength of the copper layer 107
Figure 5.23 The peel strength of copper on different amine chain functionalized silica modified epoxy substrate 109
Figure 5. 24 FE-SEM images of the surface morphology of peeled off epoxy polymer treated with *AP-Monoamine M* (a) and copper (b) surface after adhesion evaluation. EDX spectra of peeled copper surface (c) 110
Figure 5. 25 FTIR-ATR spectra of peeled copper surface from sample involving copper deposited on *AP-Monoamine M* treated (red line) and only permanganate treated (black line) of epoxy substrate 111
Figure 5. 26 FE-SEM surface morphology image of (a) peeled epoxy polymer treated with *AP-Monoamine L* and (b) the copper surface after adhesion evaluation. Figure (c) is the EDX spectrum of the peeled copper surface 112
Figure 5. 27 Adhesion strength of copper on *AP-Monoamine M* treated epoxy substrate surfaces after HAST and IR reflow tests 113

Figure 5. 28 FE-SEM surface morphology image of copper side after HAST. Some parts of epoxy have been removed and transferred to copper surface after peeling. The sample has peel strength of 4±0.4 N/cm 114
Figure 5. 29 Surface morphology of (a) the peeled epoxy polymer treated with *AP-Monoamine M* and (b) the copper surface after the IR reflow test. Figure (c) is the EDX spectrum of peeled copper surface 115
Figure 5. 30 Surface morphology of peeled off epoxy polymer treated with *AP-monoamine L* (a) and copper (b) surface after IR reflow test 115
Figure 5. 31 Palladium ion concentrations on the epoxy substrate surface as a function of immersion time in AP-Monoamine solution. 0.8 g/L of *AP-Monoamine M* was used 117
Figure 5. 32 Scheme of the reaction mechanism proposed for palladium chemisorption on epoxy substrate surfaces containing aminopropyl functionalized silica 117
Figure 5. 33 Pd concentration on polymer surface (Bar) and adhesion peel strength (Line) as a function of the concentration of the palladium chloride solution. The polymer substrates were modified with a dispersion of *AP-Monoamine M* with concentration of 4 g/L 118

Figure 6.1 Polyimide surface treated with KOH at elevated temperature gives potassium polyamate, which is then converted to polyamic acid with diluted HCl, ligand for deposited metal adhesion.[163] 121
Figure 6.2 Process scheme of electroless copper deposition on *AP-Monoamine* modified polyimide film 121
Figure 6. 3 Chemical structure of (a) Kapton®200 H, (b) Upilex®-S, and (c) Eymyd® L30N 128
Figure 6.4 Normalized FTIR-ATR spectra of untreated (black) and 1 min permanganate treated (red) polyimide film. All peaks are normalized to the peak at 1717 cm^{-1} 129
Figure 6. 5 Reaction scheme of hydrolysis of polyimide to sodium polyamate 131
Figure 6. 6 XPS survey scan of (a) pristine and (b) permanganate treated polyimide films 132
Figure 6. 7 (a) Binding state of the carbon and oxygen atoms in the polyimide repeat unit.[170] XPS C1s spectra for (b) pristine and (c) permanganate treated polyimide films. The dashed line is only shown for a better observation of the peak of the fitted lines 134
Figure 6. 8 The XPS O1s and N1s spectra of (a) and (c) pristine, and (b) and (d) permanganate treated polyimide films. The dashed line is only shown for a better observation of the peak of the fitted lines 134
Figure 6. 9 Chemical structure of (a) imide and (b) isoimide. 136
Figure 6.10 AFM images of the surface morphology of untreated (a) and permanganate treated for 1 min (b) Kapton®200 H polyimide film. A measuring window of 2x2 μm^2 was used. The surface roughness of the polyimide film increases after permanganate treatment from R_{rms} = 1.1±0.1 nm to R_{rms} = 2.6±0.3 nm 137

Figure 6. 11 FE-SEM images of the surface morphology of polyimide film treated with (a) 0.8, (b) 1.6, (c) 4 and (d) 8 g/L of *AP-Monoamine M*. The films were immersed into the suspension for at 60 °C for 5 min. The films were withdrawn from the suspension with a speed of 180 mm/min, and annealed in an oven at 130 °C for 10 min 140
Figure 6. 12 The schematic illustration of particle layer formation in dip-coating driven by the direct adsorption from the solution and by the convective assembly in the meniscus. The figure was adapted from the publication of Jung *et al.,* 2009[144] 141
Figure 6. 13 AFM images of the surface morphology of polyimide film treated with 0.8 g/L of *AP-Monoamine M* for an immersion time of (a) 10, (b) 60, (c) 120, (d) 300 and (e) 600 s 60 °C. A measuring window of 1x1 μm^2 was used. 142
Figure 6. 14 Surface coverage of *AP-Monoamine M* particle on polyimide film surface as a function of immersion time. The film treated with 0.8 g/L *AP-Monoamine M* at 60 °C 143
Figure 6. 15 AFM images of the surface morphology of polyimide film treated with 4 g/L of *AP-Monoamine M* for (a) 10, (b) 60, (c) 120, (d) 300 and (e) 600 s at 60 °C. A measuring window of 1x1 μm^2 was used 144
Figure 6.16 XPS survey scan of polyimide films treated (a) with permanganate and (b) subsequently treated with 4 g/L *AP-Monoamine M* 145
Figure 6.17 XPS C1s and N1s core level spectra of polyimide film treated with permanganate (a) and (c), and subsequently treated with of 4 g/L of *AP monoamine M* (b) and (d) 146
Figure 6.18 XPS O1s core level spectra of polyimide film treated (a) with permanganate and (b) subsequently treated with of 4 g/L of *AP monoamine M* 146
Figure 6.19 Possible reaction mechanism of aminopropyl functionalized silica nanoparticles (*AP-Monoamine M*) with polyimide film surface 148
Figure 6. 20 XPS survey scan of polyimide film treated with *AP-Monoamine M* (4 g/L, 60 °C, 5 min) after the adsorption of Pd (II) ions (i), and after consecutive reduction of palladium from Pd (II) to Pd (0) (ii). Polyimide film treated only with permanganate after the adsorption of Pd (II) ions (iii), and after consecutive reduction of palladium from Pd (II) to Pd (0) (iv) 150
Figure 6. 21 XPS Pd3d and N1s spectra polyimide film treated with permanganate. (a), (c) followed by palladium activation step in Neoganth 834 activator, and (b), (d) after the sample underwent the Pd reduction step in DMAB solution 152
Figure 6. 22 XPS Pd3d and N1s spectra of *AP-Monoamine M* treated polyimide film (a), (c) followed by palladium activation step in Neoganth 834 activator, and (b), (d) after the sample underwent the Pd reduction step in DMAB solution 152
Figure 6. 23 EDX spectrum of an *AP-Monoamine M* treated polyimide film after electroless copper deposition. The sample was measured after 30 s immersion in electroless copper solution at 35 °C 155
Figure 6.24 AFM image of *AP-Monoamine M* treated polyimide films deposited with electroless copper for (a) 0, (b) 10 and (c) 30 s. A measurement window of 1x1 μm was used 155
Figure 6.25 Possible reaction mechanism for the electroless copper deposition on polyimide film surface modified by *AP-Monoamine M*. (a) The strong electronegativity

of the nitrogen atoms from amino group attracts the complexed palladium ions, so that they are adsorbed onto the surface of the particle, and form amino-palladium complexes; (b) complexed palladium ions are reduced by DMAB from Pd(II) to Pd(0). Subsequently, palladium clusters are formed and coordinated by the *AP-Monoamine M* amino groups; (c) Finally, growth of copper on the palladium clusters occurs 156
Figure 6.26 The dependence of the adhesion strength of the deposited copper on the modified polyimide as a function of immersion time. A 0.8 g/L *AP-Monoamine M* dispersion at 60 °C was used. The error bar shows the variation of the peel strength test within a single sample, peeled at three different positions 158
Figure 6.27 Dependence of the peel strength between deposited copper and modified polyimide films on the *AP-Monoamine M* concentration. The polyimide films were immersed in an *AP-Monoamine M* solution for 300 s at 60 °C. The error bar shows the variations of the peel strength within one sample, peeled at three different positions 159
Figure 6.28 Adhesion strength of deposited copper on polyimide film modified with *AP-Monoamine S, M* and *L*. The vertical dash line is the border of the minimum peel strength needed to fulfill the industrial requirement (6 N/cm) 160
Figure 6.29 AFM images show the distribution of (a) *AP-Monoamine S*, (b) *AP-Monoamine M,* and (c) *AP-Monoamine L* on polyimide film surface. The Immersion time was 300 s and the temperature of the dispersion was 60 °C 161
Figure 6.30 FE-SEM image of the surface morphology of peeled-off polyimide films which have been treated with 50 nm AP-Monoamine (a) and (b) a copper surface after adhesion evaluation 163

Figure A1.1 A Calibration curve was created by measuring the absorbance intensity at 404 nm. (Correlation coefficient = 0.99) 182

Figure A3. 1 The TEM images of (a) AP-Hydroxyl S, (b) AP-Hydroxyl M, and (c) AP-Hydroxyl L 184
Figure A3. 2 The TEM images of (a) AP-Monoamine S, (b) AP-Monoamine M, and (c) AP-Monoamine L 184
Figure A3. 3 The TEM images of (a) AP-Gylcidoxy, (b) AP-Mercapto, (c) AP-Ureido, (d) AP-Diamine, and (e) AP-Triamine 185

Figure A4. 1 FTIR-ATR spectra of pristine (black) and 1 min permanganate treated (red) polyimide film. The spectra were collected from (a) 600-3600 cm^{-1} and (b) 600-1200 cm^{-1} 186

Figure A5. 1 FTIR-ATR spectra of KOH treated polyimide film.[169] The polyimide film was immersed into 1 M KOH solution at 80 °C for different immersion time 187

Figure A6. 1 The FTIR spectra of polyimide film treated with permanganate (black) and 4 g/L of *AP-Monoamine M* (red). The spectra were collected from (a) 600-3600 cm^{-1} and (b) 600-1800 cm^{-1} 188

Chapter 1 - General introduction

1.1. Technology trend of electronics industry

Since the invention of printed wiring technology by Eisler in 1936, several manufacturing methods and processes to produce PWB's (Printed Wiring Boards) have been revolutionized.[10] The electronics industry, driven largely by consumer demands, has produced devices capable of extreme functionality. However every new generation of products must be produced with a smaller form factor, faster data transmission and at lower cost. This has driven the electronics technology to find cost effective solutions when moving to higher interconnect densities.[11] As a consequence of this, the reduction in feature sizes, including conductor line width and space (L/S) is a prerequisite to increase the functionality of the electronic devices. As shown in Figure 1.1, the expected downscaling of the conductor L/S will challenge package substrate manufacturing.

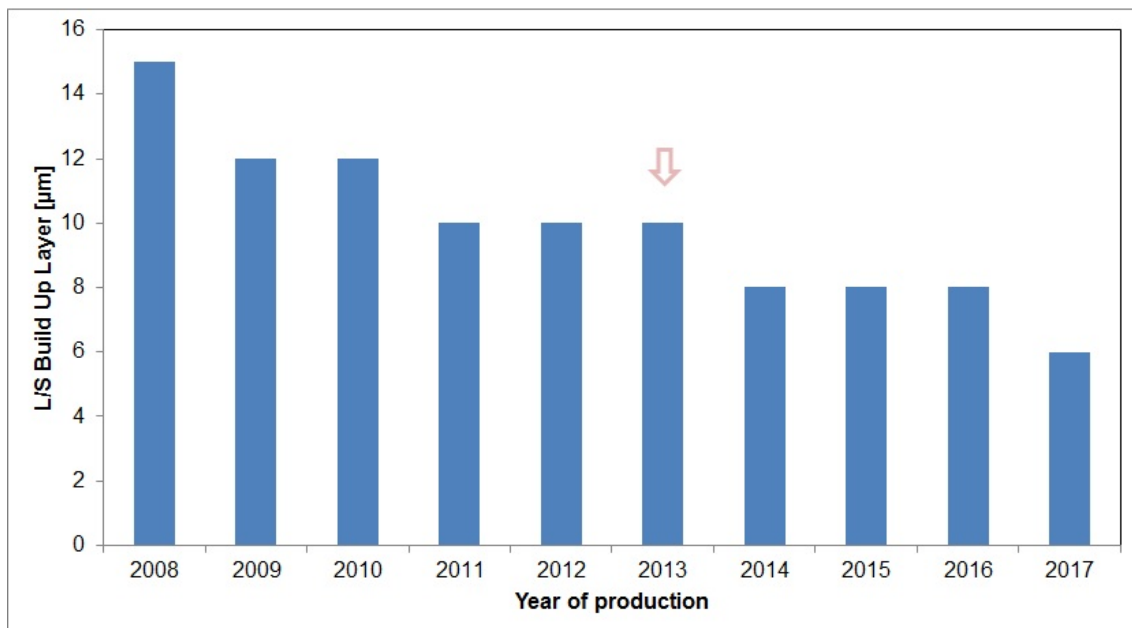

Figure 1.1 Following the technology development, conductor width and space size keeps on reducing gradually in PWB manufacturing. (Adapted from ITRS 2008[12])

The predictions for future growth in the electronics market, show significant growth in the areas where this trend will continue, thus driving L/S smaller and

transmission frequency higher, in particular in the case of smart phones and tablets as shown in Figure 1.2.

In order to realize the high density interconnect and high speed data transmissions for next generation electronics, further development will be required to ensure high yield manufacture in the future.

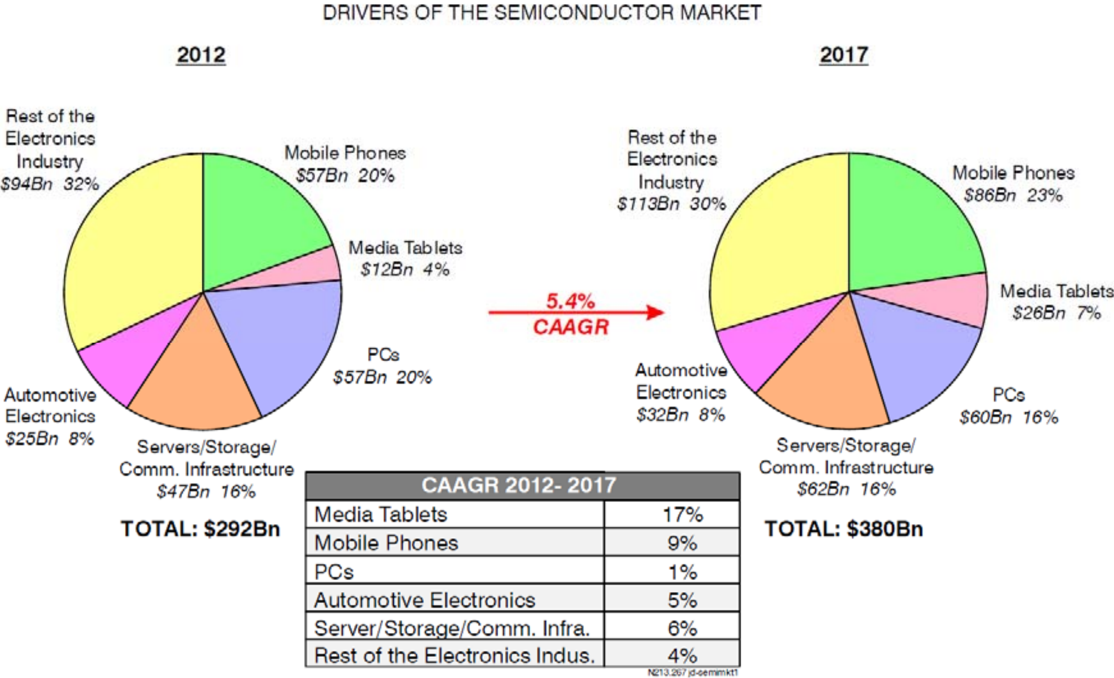

CAAGR 2012- 2017	
Media Tablets	17%
Mobile Phones	9%
PCs	1%
Automotive Electronics	5%
Server/Storage/Comm. Infra.	6%
Rest of the Electronics Indus.	4%

Figure 1.2 Semiconductor Industry Drivers Showing Compound Average Annual Growth Rates (CAAGR). (Source: Prismark Semiconductor Packaging Report Q1 2013[13])

Subtractive methods has been widely used for many years to create conductor lines, however the capability of this technique is extremely dependent on the copper thickness on the dielectric. This can vary from 35 to 2μm with significantly increasing cost for the lower copper thickness due to the difficulties to manufacture it. The Advanced Modified Semi Additive Process (AMSAP explained in Figure 1.4) typically has a copper thickness on the dielectric of 2μm however even this very thin copper layer is limited in high yield production to around 20μm L/S, which is already too high for the roadmap shown in Figure 1.3.

Typical production capabilities for the different manufacturing process are shown in Figure 1.3 below.

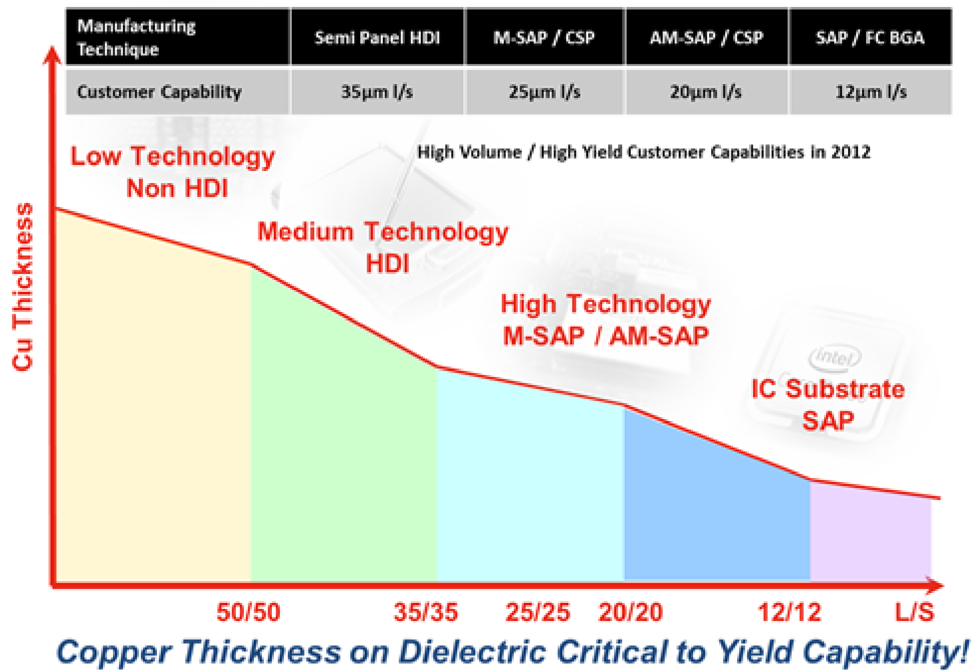

Figure 1.3 Line and space production capabilities dependent on manufacturing technique and copper thickness on the dielectric. (Source: Atotech Customer Survey 2012) HDI - High Density Interconnect, MSAP - Modified Semi Additive Process

As the conductor line width and space gets smaller, the lateral etching of copper during etching to create the circuit creates undercut beneath the etch resist causing line width reduction in any subtractive method.[14] This is primarily because most wet etching is isotropic in nature. This limits L/S capability as previously mentioned. To help to overcome this problem, the SAP process has been used for several years now to allow finer lines to be generated with a high yield for superior packaging reliability.[15]

AMSAP (Laminated laminated Dielectricdielectric) and SAP (Bare bare Dielectricdielectric) processes are compared in Figure 1.4. In Figure 1.4, note it can be seen that the laminated copper has higher roughness than the SAP version where it is attached to the dielectric. This roughness of typically 3-5 µm peak to valley maximum height which makes the copper removal from the surface more challenging and limits its L/S capability. The copper foil is plated onto a smooth drum which creates the smooth surface seen on the surface. On the back side of the copper foil, enhanced mechanical adhesion is created by plating microcrystalline copper then

typically zinc plating to ensure good adhesion to the dielectric material.

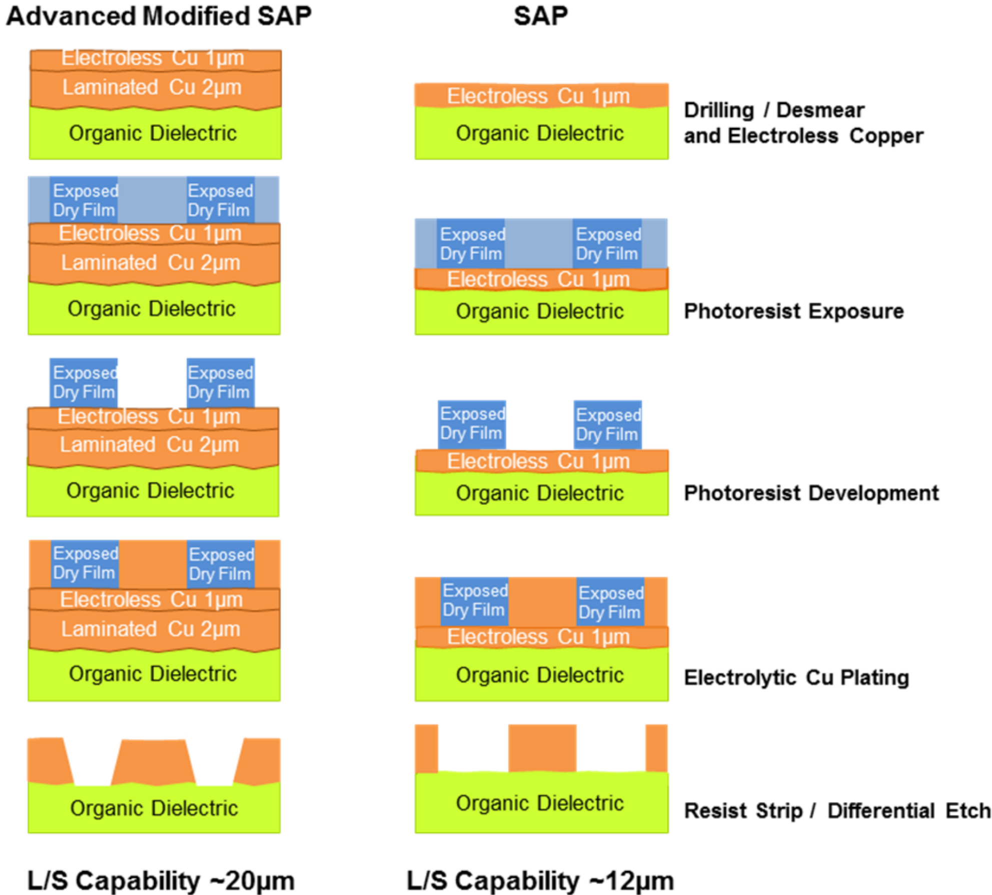

Figure 1.4 Comparison between the AMSAP subtractive process and the SAP process

Although the SAP process is being used very successfully to create fine line for IC substrate production, there are many more factors which will be influenced by the continued downscaling of the L/S going forward. As the signal frequency increases, the signal loss from the conductor is strongly dependent on the surface profile and roughness of both the copper and the dielectric layer. Since the adhesion of electroless copper used as a seed layer on the dielectric is essentially mechanical adhesion, reducing the dielectric roughness would certainly lead to lower adhesion or even blistering of the electroless copper from the dielectric material.

The specifications for the allowed roughness for IC substrate manufacturers come from Original Equipment Manufacturers (OEM's) who specify these details to their suppliers based on their future electrical requirements. An example of such a specification can be seen below in Figure 1.5.

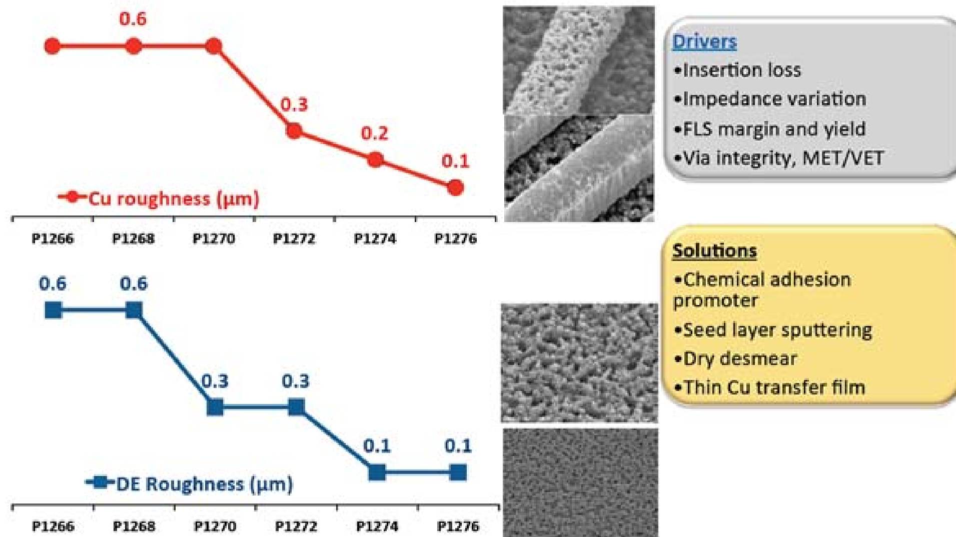

Figure 1.5 OEM Roadmap Showing Permitted Copper and Dielectric Roughness for Next Generation IC Substrates. (Extracted from Ref.[16])

The use of stress free electroless copper deposits minimizes the potential for blistering on these ultra-smooth substrates but as the dielectric roughness requirements are reduced alternative processes will be required.

1.2. Adhesion challenge in electronics industry

One of the major challenges in printed wiring boards (PWBs) manufacturing is the weak adhesion between conductor layers and dielectrics. Therefore, to improve the interfacial adhesion of plated metal on dielectric material, numerous methods for modifying dielectrics surface have been developed and applied. These methods have included wet chemical etching,[17-21] polymer grafting,[22-32] plasma treatment,[18, 33-35] and silane coupling agent treatment.[36-41] The current adhesion promotion methods will be summarized in chapter 2.

Due to simplicity and low cost, increasing the roughness of polymers surface via wet chemical etching has been one of the most common solutions to improve interfacial adhesion of metal plating on dielectric material. Through wet chemical etching process, cavities suitable for establishing mechanical interlocking with deposited conductor layer were created. Thus, having these ones a dominant effect on the adhesion strength of the electrodeposited copper on treated polymers surface.

Unfortunately, as the conductor L/S gets smaller (< 20 μm), the rough surface would induce several problems: excessive cross talk and increased noise.[11] Thus, there is a great risk of compromising the production yield. Furthermore, poor signal propagation become critical when high transmission frequencies were applied. The main causes of high frequency signal loss are the dielectric material and conductor which the signal travels along.[42] The dielectric constant and dissipation factor are the main contributors to signal loss in the dielectric material, while the signal loss in the conductor is strongly dependent on the surface profile and the roughness of the track.[42] A phenomenon call "skin effect" explains the way in which the signal flows on conductor surface. As signal frequency increases, skin depth gets thinner and the electrons tend to move exclusively on the surface of the conductor.

The conventional approach to ensure good adhesion of the conductor to the dielectric of roughening the dielectric to achieve mechanical adhesion is no longer applicable. A pre-requisite for the next generation, high frequency IC substrate, is a new way to enhance adhesion of the dielectric material to conductor. This must be independent of surface morphology or roughness.

On the basis of the above, the current work was conducted. This work describes a novel surface treatment method to promote the adhesion of metal films on the surface of the dielectric material without additional roughening, ensuring reduced signal losses whilst meeting industry standards for thermal reliability.

1.3. Objectives and outline of the thesis

In the present work, silica nanoparticles functionalized with various reactive groups are synthesized as well as characterized and deposited on epoxy substrate (ABF-GX92) and polyimide (Kapton®200 H) surface previously activated by permanganate or plasma. The modified polymer surfaces were activated with palladium prior to subsequent electroless deposition of copper. The functional groups on the surface of the silica nanoparticle serve as active groups which interact with the polymer surfaces and also act actively as ligands for the metal ions. Accordingly, functionalized silica nanoparticles have a tendency to introduce chemical adhesion between polymers and deposited metal layers. Thus, they enhance the interfacial adhesion without causing any surface roughening. To date and to our knowledge, there is no record of functionalized silica nanoparticle as an adhesion promoter between polymers and metals. Furthermore, one of the objectives of this work is the development of an understanding of the mechanisms responsible for adhesion at the interface between electroless copper and dielectric materials.

In detail, the thesis is structured as follows:

In *Chapter 1*, an overview of the motivation for the work is presented, as well as the objectives of the work. The relevant background information to understand the challenges are also described.

Chapter 2, several theories on the adhesion phenomenon of different material systems will be presented. The state of the art of the surface treatment methods to promote the adhesion between dielectrics and deposited metal layers are included. Since an electroless copper process is used for metallization, the basic principle of electroless copper deposition are described. Some insight into the dielectric materials used in this work, chemical structure and physical properties are also provided.

In *Chapter 3*, fundamentals of various analytical methods which applied in this work to investigate either functionalized silica nanoparticles or dielectric material surface are described.

In *Chapter 4*, the synthesis and characterization procedure for silica nanoparticles in various sizes and functionalities is described. The influence of the attached functional groups on the surface properties of silica nanoparticles (surface electrokinetic

potential, surface chemistry) is discussed. For silica nanoparticles modified with amine groups, the effect of the particles size and the organofunctional precursor on the amine density at the surface are discussed.

In *Chapter 5*, the adhesion behavior of electrolessly deposited copper on epoxy substrates (ABF-GX 92) modified with functionalized silica nanoparticles are investigated. Silica nanoparticles with various particles sizes and surface functionalities were used. The influence of various operation parameters during AP-*Monoamine M* treatment (annealing temperature, dip coating withdrawing speed, suspension temperature, substrate immersion time) on the adhesion strength are discussed as well. The adsorption of palladium, which is used as catalyst for electroless copper deposition on modified epoxy substrate surface, is investigated. Furthermore, suggestion of possible adhesion mechanism between copper and epoxy substrate in involving functionalized silica nanoparticles are also presented.

In *Chapter 6*, the adhesion behavior of electrolessly deposited copper on polyimide films (Kapton® 200 H) modified with aminopropyl functionalized silica nanoparticles are investigated. X-ray photoelectron spectroscopy is used to investigate the chemical interaction between aminopropyl functionalized silica nanoparticles and polyimide films. The correlation between particles coverage influenced by the dispersion concentration and the film immersion time, and the adhesion strength will be discussed. In combination with failure mode results, a possible adhesion mechanism between copper and polyimide film involving aminopropyl functionalized silica nanoparticles is suggested.

Finally, a summary of the entire thesis and an outlook for future work is given in *Chapter 7*.

Chapter 2 - Theoretical background

2.1. Polymer/metal adhesion mechanism

There are several theories on adhesion that adopted to explain the adhesion phenomenon of different material systems.[43] In the case of polymer/metal interfacial interactions, four main mechanisms of adhesion were considered, they are: physical adsorption, mechanical interlocking, chemical bonding and weak boundary layer.[18] In many cases, a combination of mechanisms is responsible for the overall adhesion observed between two materials.

Physical adsorption

This theory is the most widely used adhesion mechanism theory in explaining the adhesion behavior in the interface. The materials adhere to each other due to the interatomic and intermolecular forces between the atoms and molecules such as van der Waals forces, acid base interactions and hydrogen bonds (Figure 2.1).[44] The fundamental thermodynamics quantities such as surface free energy of adhesive and substrate is the general relation to describe the magnitude of these forces. The formation of adhesive joint in solid-liquid system usually goes to contact step. Therefore, in order to obtain a good adhesion of adhesive joint, a good wettability of liquid on solid is essential condition, although this is necessary but insufficient condition.

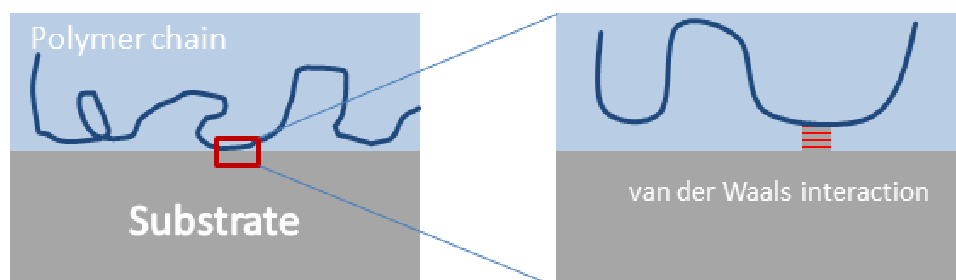

Figure 2.1 Schematic diagram of Van der waals interaction between polymer and metal

The relation between surface tension (gas/liquid: γ_{GS}, liquid/solid: γ_{LS}, and gas/solid: γ_{GS}) and wettability can be described according to Young's equation,[45] at three phase contacts the equilibrium contact angle (Θ) is written as,

$$\gamma_{GS} = \gamma_{LS} + \gamma_{GL} \cos\theta \tag{2. 1}$$

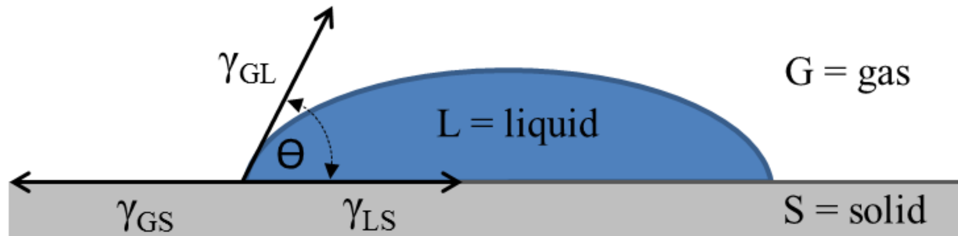

Figure 2.2 Contact angle of a drop of liquid on solid surface

The decrease of surface free energy of the solid in vacuum (γ_S) to the surface free energy of solid (γ_{GS}) after equilibrium adsorption of gas from the liquid can be defined as the spreading pressure π ($\pi = \gamma_S - \gamma_{GS}$). When the contact angle is Θ > 0 °, the liquid is not spreading over the solid surface. When the contact angle is Θ = 0 °, the liquid is spontaneously spread on the surface of the solid surface. Therefore, for spontaneous spread of liquid on solid surface is described as,

$$\gamma_S \geq \gamma_{LS} + \gamma_{GL} \tag{2. 2}$$

The adhesion energy for solid-liquid system (W_{LS}) based on Dupré's relationship could show that wettability of adhesive on substrate surface is the important criterion to the adhesion.

$$W_{LS} = \gamma_{GS} + \gamma_{GL} - \gamma_{LS} = \gamma_{GL}(1+\cos\theta) \tag{2. 3}$$

Therefore, good adhesion can result from high surface wettability as the contact angle is small. While poor adhesion can result from low surface wettability as the contact angle is large.

Mechanical interlocking

The theory of mechanical interlocking was first introduced by Mc. Bain and Hopkins[46] in 1925. This theory involves an anchoring of one material by filling the cavities, holes or irregular structure of the other material surface (Figure 2.3). In the most case of metallization of polymer surface, mechanical interlocking is still used as the main mechanism to elucidate the good adhesion of metal on rough polymer surface. However, possibility to obtained good adhesion between two smooth surfaces leads to the conclusion that mechanical interlocking theory cannot be considered as universal.[44]

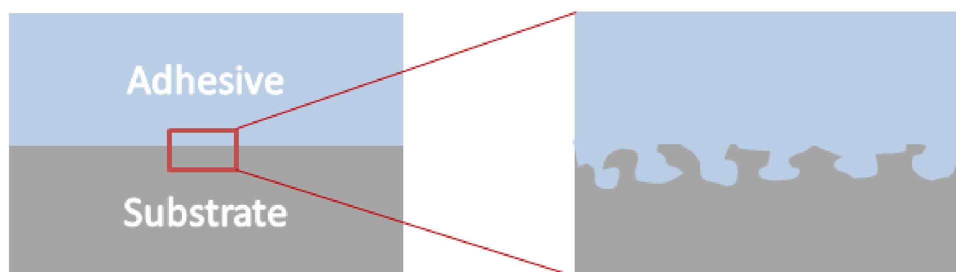

Figure 2.3 Schematic diagram of mechanical anchoring between polymer and metal

It is still debatable that the increase of adhesion strength from high surface area is due to the increase of mechanical interlocking or secondary bonding (surface wetting). Accordingly, Wake *et al*.,[47] suggested that the optimum joint strength is a combination of mechanical interlocking and interfacial chemical component as shown in bellow equation.

Optimum joint strength = (constant)

x (mechanical interlocking component) (2. 4)

x (interfacial chemical component)

Chemical bonding theory

The chemical bonding formed across two materials interface can give a great contribution to the adhesion strength between them. Primary chemical bonds are considered in chemical bonding mechanism. The schematic diagram of chemical bonding mechanism is shown in Figure 2.4. In comparison to secondary force

interactions such as van der Walls and hydrogen bonds, the primary chemical bonds has one order magnitude stronger bonding energies. Typically, the primary chemical bonds (ionic and covalent bonding) have energies ranging between 60-1000 kJ/mol, while the bonding energies of secondary force interactions are lower than 50 kJ/mol. The bonding energies of different types of bonding were summarized in Table 2.1.

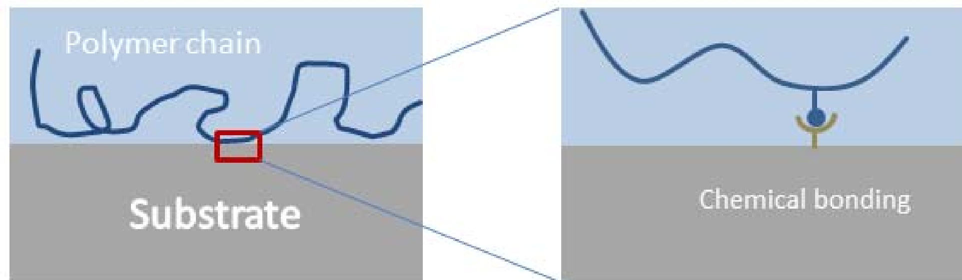

Figure 2.4 Schematic diagram of chemical bonding between polymer and metal

By introducing chemical bonds across the interface, the adhesion in the interface between two materials could be significantly improved. Moreover, the chemical bonding method is independent to the substrate surface morphology (roughness). Therefore, the chemical bonding is a favorable method to enhance the joint strength between polymer and metal.

Table 2.1 Typical bonding energies of various bonds type.[48-50]

Type	Bond Energy [kJ/mol]
Primary bonds	
Ionic	600-1100
Covalent	60-700
Metallic	110-350
Donor-acceptor bonds	
Brondsted acid-base interactions	Up to 1000
Lewis acid-base interactions	Up to 80
Secondary bonds	
Hydrogen bonds	
Hydrogen bonds involving fluorine	Up to 40
Hydrogen bonds excluding fluorine	10-25
Van der Waals bonds	
Permanent dipole-dipole interactions	4-20
Dipole induced dipole interactions	< 2
Dispersion (London) forces	0.08-40

Weak boundary layer

In the weak boundary layer theory, the degradation of adhesion due to the adhesion inhibitor at an interface was discussed. This theory was first introduced by Bikerman in 1967.[51] This theory suggested that the separation from the adhesion failure at the interface usually due to a cohesive break of a weak boundary layer. Weak boundary layer can arise from the environment, the adhesive and the substrate. It is not a rare case if the combination of any of the three would also form a weak boundary layer. The concept of weak boundary layer is shown in Figure 2.5.

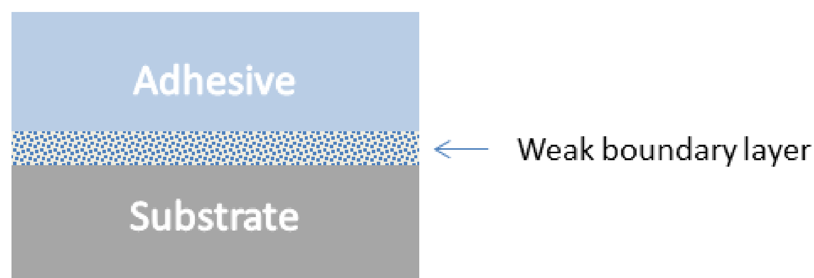

Figure 2.5 Schematic diagram of weak boundary layer in polymer/metal interface

The removal of weak boundary layer is essential to result good interfacial joint strength. In many cases, physical or chemical pretreatment is necessary to be implemented to obtain weak boundary layer free interface.[51]

2.2. Current dielectric/metal adhesion promoter methods

As mentioned before, to have a good adhesion of metal to the dielectric is a prime requirement for printed circuit board manufacturing. In order to achieve this, different pretreatment methods need to be performed prior to metallization. The conventional approach to solve adhesion problem describe above is to rough the surface, which can be done either by mechanical or chemical methods. To fulfill the electronics industry future requirement, metal plating on smooth dielectric surface, numerous research works have demonstrated several methods to enhance the chemical bonding at the interface. In this section we will focus on different kind of pretreatments to promote the adhesion between dielectrics and deposited metal layers.

2.2.1. Surface roughening with chemical etch

Increasing the roughness of dielectric material surface has been one of the most common solutions to improve interfacial adhesion of metal plating on dielectric material. Surface roughness may result from subtractive or additive roughening processes. Subtractive roughening process of dielectric material usually involves physical (mechanical abrasion) or chemical etching. As shown in Figure 2.6, through roughening processes, cavities suitable for establishing mechanical interlocking with deposited conductor layer are created. Additive roughening process may result in the buildup of rough texture surface on dielectric material.

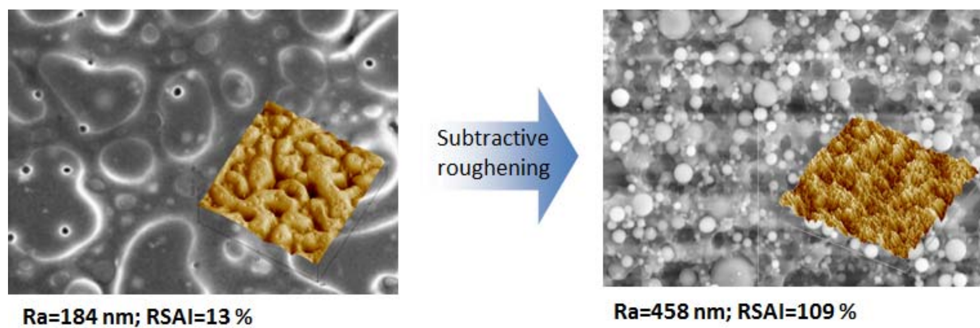

Figure 2.6 Surface morphology of ABF-GX 92 (epoxy resin/silica blend polymer) before (a) and after (b) subtractive roughening

In the last decade, numerous research works have reported the use of chemical treatment to promote the adhesion of plated metal on dielectric material.[17-21] Due to simplicity and low cost, wet chemical treatments are the most commonly used to roughening dielectric surface in subtractive method. These types of treatments commonly involve the oxidation of dielectric surface, usually implying sweller and oxidizing agents. On top of the roughened dielectric, the conductive metal is deposited and strong adhesion between them is obtained. The adhesion mechanism has two main contributions: On one side, surface roughness of the polymer and on the other side, the chemical composition of the surface. Very short exposure time with an oxidizing solution generates oxygen containing groups, which play an important role in enhancing the adhesion. Moreover, large number of microcavities are created during chemical treatment,[18] These groups have a dominant effect on the adhesion strength of the electrodeposited copper on the treated epoxy surface.

In a previous publication, Sam *et al.*[52-53] studied extensively the kinetic of epoxy polymer roughness with wet chemical treatment. Accordingly, the polymer oxidation mechanism due to chemical treatment was developed (Figure 2.7).[21] The uneven distribution of polar groups in polymer leads to the formation of different zones. Zones with a higher density of polar groups separate from zones with a lower density of polar groups creating regions called polar channels, Figure 2.7 (a). The diffusion of swellers into the free volume of polymer causes the polar groups to concentrate more in certain areas (polar channels), Figure 2.7 (b). As the polymer is exposed to an oxidizing agent, the area with higher density of polar groups (polar channel) will be oxidized faster and the etching on sideways is slower, see Figure 2.7 (c). As the channel is getting deeper, diffusional limitations become more important and the polymer breakdown groups move from the polar channel into polymer bulk (Figure 2.7 (d)).

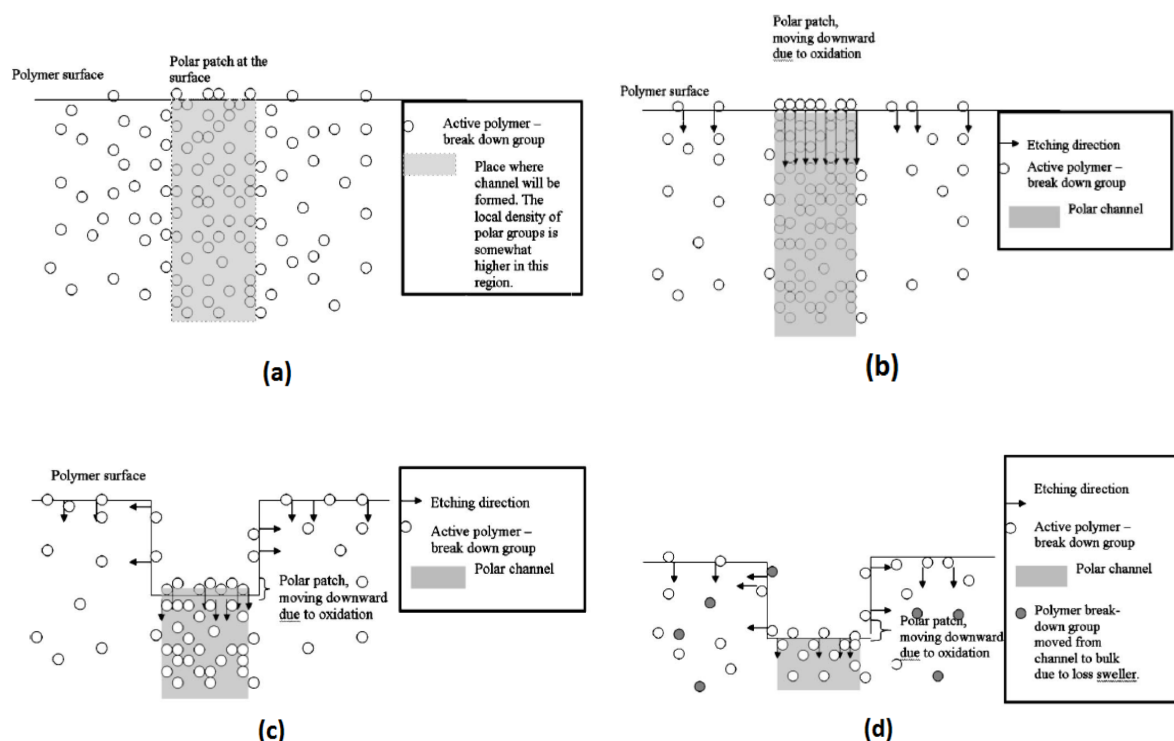

Figure 2.7 Illustration of the polymer oxidation mechanism in different process steps. (Extracted from Ref.[21])

As pointed out earlier by Schröer *et al.*,[17] the sweller and oxidizing agent treatment on epoxy polymer surface needs to be optimized to obtain a sufficient adhesion of metal films. The penetration of the sweller would lead to a partial solubilization of the polymer chain. Exposition of the polymer to an oxidizing agent leads to oxidative

decomposition of the polymer chains, increasing the surface roughness. However, an excessive etching reduces the roughness of the polymer. The author also pointed out that the surface profile of epoxy polymers is important for the adhesion strength of electrochemically deposited copper.

Nevertheless, depending on the nature of the substrate, the wet chemical etching treatment will behave in different way. Several dielectric materials with higher chemical resistance have been used in the past few years. As a result, the wet chemical treatment method to breakdown dielectric surface is not working efficiently anymore. Moreover, high degree of roughness on the dielectric surface which usually formed is already a concern for high density and high frequency electronics industry application in the future.

2.2.2. Polymer grafting on dielectrics

The grafting of polymer on dielectric surface has attracted considerable attention in electronics industry as this technique combines a variety of functional components in a single material.[54] This approach is attended to overcome the drawback of using permanganate chemical etching treatment. By choosing the proper monomers with appropriate functional groups, new molecular functionalities can be incorporated on the surface, which can serve as ligands for the metal ions for the electroless deposition. Consequently, the adhesion enhancement has two main contributions: On one hand, the mechanical interlocking due the formation of a rough texture of the surface and on the other hand chemical bonding due to the functional groups.

Grafting of polymer can be accomplished by either “grafting to” or “grafting from” approaches.[54] As shown in Figure 2.8,[55] in “grafting to” approach, end functionalized polymer chains are attached to a surface via physical adsorption or chemical reaction. On the other hand, “grafting from” is achieved by polymerization reaction from the surface via surface immobilized initiator.

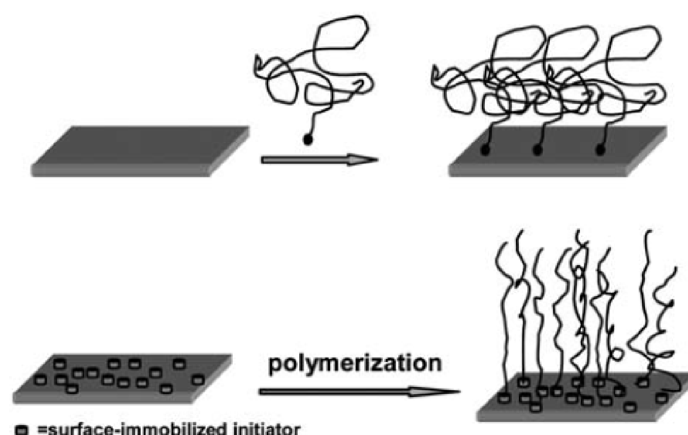

Figure 2.8 Schematic diagram of "grafting to" (top) and "grafting from" (bottom). (Extracted from Ref.[55])

Numerous research works have demonstrated the success in using polymer grafting method to improve the adhesion between polymer and plated metal layer. Inspired by the composition of adhesive proteins in mussels, Lee *et al*.[22] Liao *et al*.[23] and Schaubroeck *et al*.[24] demonstrated the use of self-polymerization of dopamine as an effective adhesion promoter between polymer substrate and electrochemically deposited copper. The polydopamine coating is able to be formed on wide variety of materials. Lancaster *et al*.,[25] described a method using block copolymers with one block designed to interpenetrate the substrate and the other one bearing chelating groups (such as polyacrylate) which were used to form host polymer film for electroless plating on various polymer substrate. With the aim to modify surface composition with minimal changes to the roughness of the surface, Siau *et al*.,[26] reported that the grafting of iminodiacetic and imidazole groups on epoxy surface enhances the adhesion of electroless plated copper.

New attempts were made by Yang *et al*.[27-28] Yu *et al*.[29-30] and Wang *et al*.[31] to demonstrated that UV or plasma induced surface graft copolymerization improves the adhesion of poly(tetrafluoroethylene) and polyimide films with the electrolessly deposited copper or nickel for flexible printed circuit boards. Those authors also reported that the deposited thin polymer film via UV or plasma graft polymerization can be used as chemisorption sites for the palladium complex during the activation process.

More recently, Garcia *et al*.[32] developed a new method to enhance the adhesion of ligand induced electroless plated copper (LIEP) on flexible and

transparent substrates. As shown in Figure 2.9, this process involves the photo-assisted reduction of aryldiazonium salt/acrylate monomer (GraftFast). The combination of polyacrylic acid graft polymerization and LIEP process was used to fabricate micrometric metal patterns with a good adhesion and promising electrical properties.

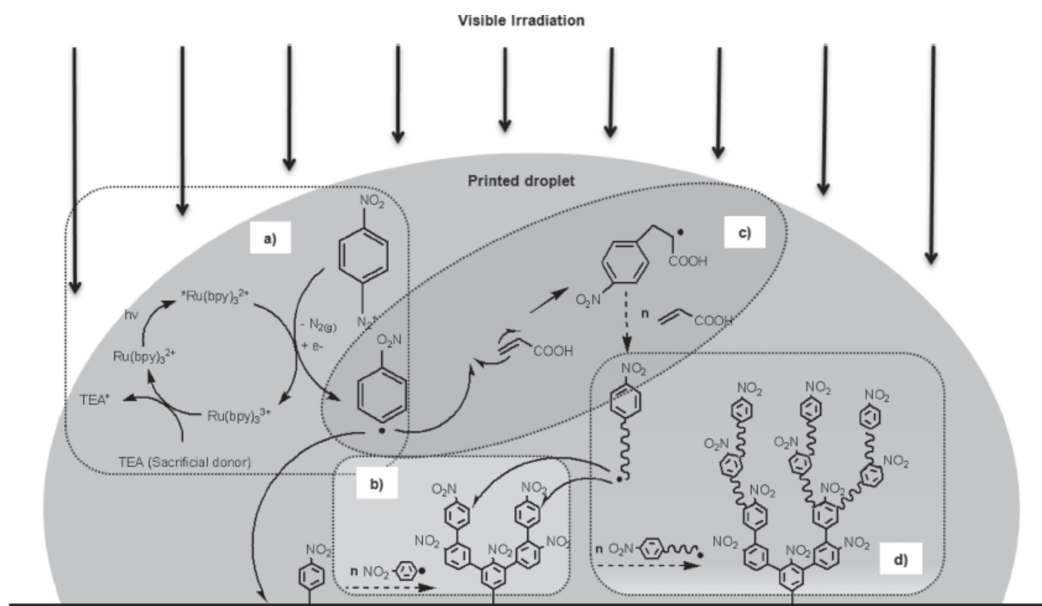

Figure 2.9 Mechanism of "GraftFast" process purposed by Garcia *et al.*,[32] The process involves four main process, (a) photo-assisted reduction of the aryldiazonium compound, (b) the resulting aryl radicals grafted onto the surface and at the same time polynitrophenylene multilayer grows, (c) aryl radicals initiate the polymerization of acrylic acid, (d) polyacrylic acid oligoradicals grafting onto polynitrophenylene layer

Despite the fact that polymer grafting processes can be used to enhance the adhesion between dielectrics and plated conductive metal layer, most of them lead to complex and expensive processes. Similar to the chemical etch process, rough surfaces which are usually formed, are already a big concern for high density and high frequency electronics industry application in the future. Additionally, the obtained adhesion is not sufficient enough to fulfill the industrial requirements.

2.2.3. Plasma treatment

As already mentioned above, polymer surface treatments for adhesion enhancement using only mechanical roughening have limited effectiveness. On the other hand, wet chemical treatment with organic solvents are becoming unacceptable due to environmental and safety considerations. Modification of polymer surface

using plasma treatment is a possible solution to overcome the drawbacks mentioned above. Depending on process gas and on the selected working conditions, plasma treatments may be used to produce etching, cross-linking, surface radical group formation, grafting of specific functional groups and thin film deposition (plasma polymerization).[56] Besides, numerous research works have demonstrated the effect of plasma modification on the adhesion between conductive metal layers and polymer substrates.[18, 33-35]

Because of the mentioned reasons above, plasma treatments have been gaining wide acceptance over the years in diverse industrial application especially in electronics industry. In the late 70's Burkstrand *et al*.[57] showed the reaction of evaporated metals with polymer surfaces treated with oxygen plasma. In these work, the author addressed that metal-oxygen-carbon (M-O-C) were formed. Further after, Gerenser *et al*.[58] studied the interaction between plasma (Ar, O_2, N_2 and mixed gas) treated polyethylene (PE) and vacuum evaporated Ag. For this particular system, Ag on PE, the adhesion is shown to increase in the following order: Ar plasma < O_2 plasma < N_2 plasma.

The effect of different plasma treatments for the electroless platting of polymer have been studied extensively by Charbonnier and coworkers.[59] During NH_3 plasma treatment process, nitrogen bearing groups were grafted on the surface. These nitrogen bearing groups are used to chemisorb the catalytic species (Pd (II)) and initiate the electroless deposition of autocatalytic metals (Ni, Cu, Au and Ag).

Table 2.2 summarized the selected literature regarding plasma treatment on polymer surface to enhance adhesion with deposited conductive metal layer.

Although plasma treatments are clean and environmental friendly processes, most of the processes need to be carried out in a controlled atmosphere. Accordingly, plasma treatment processes are difficult to industrialize. Moreover, the effectiveness of plasma treatment on adhesion enhancement strongly depends on the nature of polymer substrates. Additionally, in most of the cases, the obtained adhesion is not sufficient enough to fulfill the industry requirement.

Table 2.2 List of selected literature regarding plasma treatment on polymer surface to enhance adhesion with deposited conductive metal layer

Polymer	Plasma treatment	Metal	Peel strength of deposited metal films		Surface investigation method	Ref
			Untreated	Treated		
Photodefinable epoxy	O_2 RF plasma	e-less Cu	5 MPa	11 MPa	SEM, XPS, AFM	[18]
Liquid crystalline polymer (LCP)	O_2 RF plasma	e-less Cu	5 MPa	6.5 MPa	SEM, XPS, AFM	[19]
Vecstar®OC	Ar, O_2, N_2, NH_3 RF plasma	Thermal evaporation Cu	0.1 N/cm	0.8 N/cm (Ar and O_2) 1.2 N/cm (N_2, NH_3)	XPS, AFM	[35]
Polypropylene, polycarbonate	O_2, N_2, NH_3 RF plasma	e-less Ni-P	Not pass Scotch® tape test	Pass Scotch® tape test	XPS	[34]
Polycarbonate (PC), polyimide Kapton®HN, polypropylene (PP), poly(butyleneterephthalate) (PBT)	Ar and H_2 RF plasma	e-less Ni-P	Not pass Scotch® tape test	Pass Scotch® tape test	XPS	[60]

2.2.4. Silane coupling agents

Silane coupling agents are organosilicone compounds consisting of a hydrolysable group on silicone (siloxane) and an organofunctional group (amino, vinyl, glyxidoxy and etc).[61] Surface treatment using silane is a well-known method to modify the physical and chemical surface properties.[62] In recent years, various research works have demonstrated the success in using silane coupling agents as adhesion promoter between dielectrics and deposited conductive metal layers.[36-41]

The reaction of silane coupling agents with dielectrics surface involves four steps (Figure 2.10).[63] Initially, a hydrolysis reaction occurs in the presence of water or ethanol, converting siloxane groups into silanol groups. The condensation reaction between silanol groups leads to the formation of oligomers. The reactive hydrogen group from the silanol group forms hydrogen bonds with the hydroxyl group on the substrate. Finally, during the curing step, covalent bonds with the substrate surface are formed and water is released. For most of the polymers, an oxidation step of the surface needs to be carried out in order to bring a sufficient amount of hydroxyl groups close to the surface.[64]

By choosing the right organofunctional groups, the formation of thin film of organofunctional silane on the substrate does not only enable the adsorption of metal species but also improves the adhesion of the deposited metal film to the substrate. Therefore, some research works report the use of nitrogen bearing organofunctional silane to chemisorb Pd (II) species as catalyst of electroless deposition process.[36-38, 41]

Moreover, Gandhi *et al.*,[39] investigated the use of a sulfur bearing organofunctional silane (mercaptopropyltrimethoxysilane) at a silicon dioxide-sputter copper interface, thereby, the influence of post-annealing after copper deposition was also discussed. Moreover, the author also reported the formation of stable siloxane bridges at the methoxysilane/SiO_2 interface upon annealing above 400 °C. Hence, strong chemical bonds are formed at both Cu/MPTMS and MPTMS/SiO_2 interfaces.

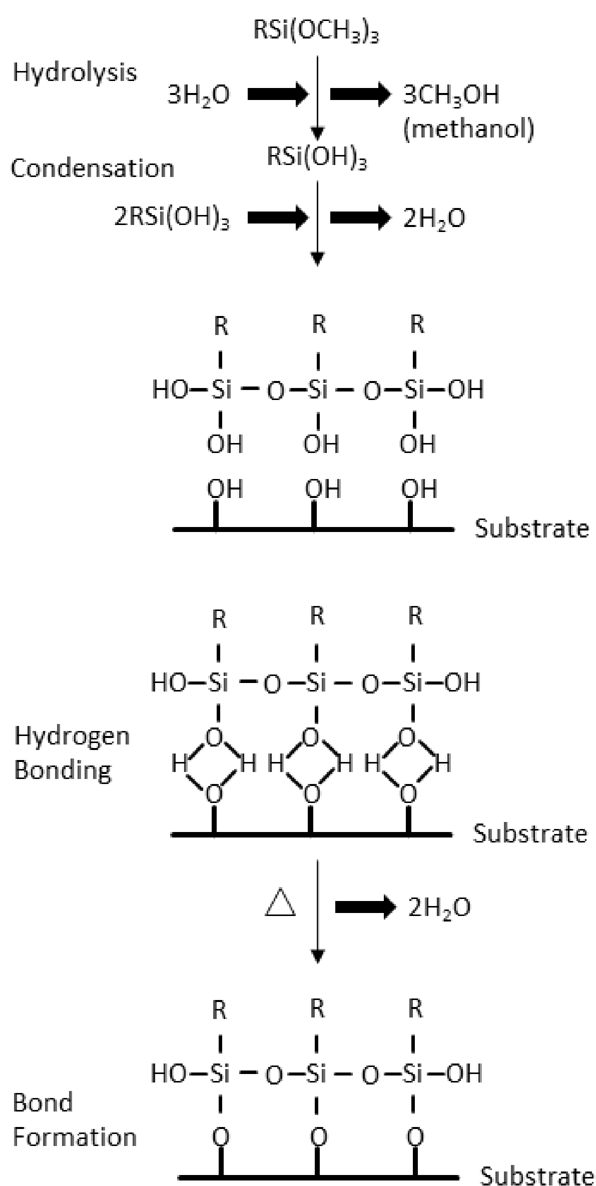

Figure 2.10 Reaction scheme of silane coupling on the surface of dielectrics. (Adapted from Ref.[63])

More recently, Mori and coworkers[40] demonstrated the use of 6-(3-triethoxysilylpropylamino)-1,3,5-triazine-2,4-dithiol (TES) as coupling agent in dielectrics metallization process. The adhesion enhancement has two main contributions: On one hand, the strong interaction between coupling agent silanol groups and substrate hydroxyl groups and on the other hand, the strong and direct bonding between sulfur atoms and copper metal.

Some drawbacks exist in using silane coupling agents. First, a uniform self-assembled monolayer (SAM) of silanes is difficult to obtain. Second, the moisture sensitivity of trialkoxysilane leads to uncontrolled hydrolysis and self-condensation.

Third, although silane coupling agents enhance the interface adhesion, this is still not strong enough to fulfill the industrial requirements. Therefore, silane coupling agents are not widely used in industry to solve polymer/metal interface adhesion.

2.2.5. Conclusions

Since decades, various adhesion promoter methods have been developed to enhance the adhesion between dielectrics and deposited metal layers. Unfortunately, none of these methods are suitable for high density and high frequency electronics industry application in the future. Accordingly, there is an urgent need to find a new adhesion promoter method without roughening the surface, while a good adhesion is obtained.

2.3. Metallization of polymer surface

Metallization of non-conducting surface such as polymers have gained a huge interest in industry and is widely used in various technological applications, ranging from food packing to microelectronics.[65-69] Numerous metallization methods have been developed in order to produce adherent metallic layers on polymer surfaces for different applications.[70] Among them, electroless deposition is the most widely used metallization method due to two main reasons, a simple process and a high cost efficiency. The compositions of electroless deposition baths are typically: metal salt, reducing agent, stabilizer, and metal complexer.

In printed circuit board production, electroless copper deposition has become one of the most used methods to create a conducting layers on substrate surfaces.[71] Similar to the other electroless deposition processes, this plating process involves the deposition of metals on catalytic surface of non-conducting substrates.[71] Therefore, activation steps have to be preceded in order to introduce catalytic species (Pd atoms and ions) on the polymer surface. Since palladium is only active as catalyst in form of metallic species (Pd^0), a reduction step of Pd (II) to Pd (0) with a reducing agent such as DMAB (dimethylaminoborane) needs to be performed. The reduction reaction of Pd (II) to Pd (0) consists of a few reactions which occurs simultaneously,[72]

1. *Pd (II)* ions reduction by DMAB

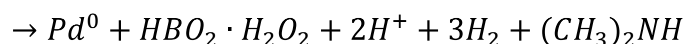

$$Pd^{2+} + (CH_3)_2NHBH_3 + 4H_2O \rightarrow Pd^0 + HBO_2 \cdot H_2O_2 + 2H^+ + 3H_2 + (CH_3)_2NH \quad (2.5)$$

2. *Pd (II)* ions reduction by gaseous H_2

$$Pd^{2+} + H_2 \rightarrow Pd^0 + 2H^+ \quad (2.6)$$

3. Oxidation of metallic Palladium by $H_2BO_2 \cdot H_2O_2$

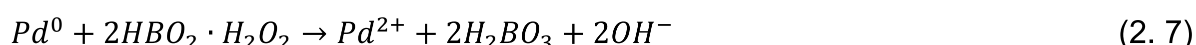

$$Pd^0 + 2HBO_2 \cdot H_2O_2 \rightarrow Pd^{2+} + 2H_2BO_3 + 2OH^- \quad (2.7)$$

Right after Palladium activation step, the substrates were introduced to electroless copper deposition process. As shown in Figure 2.11, with the help of reducing agents (formaldehyde), reduction reaction of Copper ions Cu (II) to metallic copper Cu (0) on the surface of catalytic substrate can be obtained.[72]

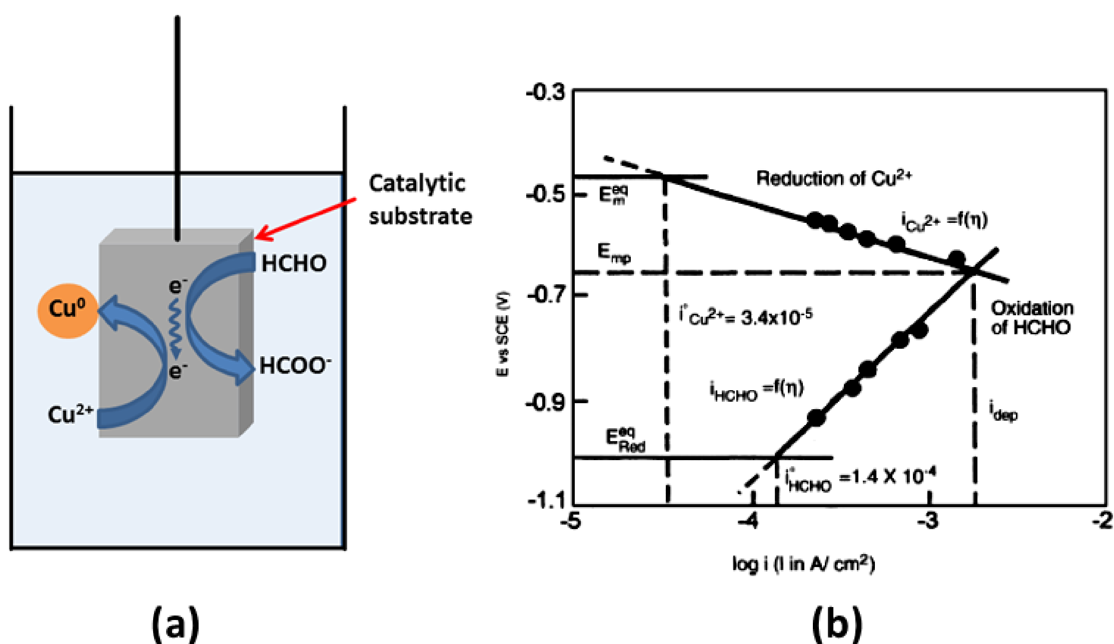

Figure 2.11 Process scheme of electroless copper deposition (a) and Evan's diagram[73] (b) as a brief way to describe the electroless deposition process of copper

The overall reaction for electroless copper deposition on catalytic surface with copper sulfate as copper ions source and formaldehyde (HCHO) as reduction agent is as follow,[73]

$$CuSO_4 + 2HCHO + 4NaOH \rightarrow Cu^0 + 2NaHCOO + 2H_2O + H_2 \quad (2.\ 8)$$

This reaction can be decomposed into:

1. Cathodic partial reaction (reduction)

$$Cu^{2+}_{solution} + 2e^- \rightarrow Cu^0_{lattice} \quad (2.\ 9)$$

2. Anodic partial reaction (oxidation)

$$HCHO + 3OH^- \rightarrow HCOO^- + 2H_2O + 2e^- \quad (2.\ 10)$$

According to mixed-potential theory, the overall reaction of electroless copper deposition can be described electrochemically by using current-potential curve. The kinetic parameter of partial anodic and cathodic reduction can be used to predict and characterize the overall reaction of electroless copper deposition. Figure 2.11 (b) shows the mixed potential diagram of electroless copper deposition with formaldehyde as the reducing agent (Evan's diagram).[73]

2.4. Polymer substrates for printed circuit board

In the last decade, the use of polymer has hugely increased due to the specific properties such as light weight, design flexibility and low cost of manufacturing. Specifically for printed circuit board industry, epoxy/glass fiber FR 4 is widely used as dielectrics substrate. As chip and package performance continue to increase (decrease feature size and increase signal frequency), this polymer substrate is not suitable to use anymore. This is due to two main reasons: first, the high dielectric constant of polymer substrate results to considerable amount of signal loss in high frequency signal transmission; second, it is nearly impossible to create fine conductor line (< 10 μm line/space) on high surface roughness morphology of polymer substrate. Thus, lower dielectric constant of polymer substrates with smooth surface have been developed recently.

The build-up film ABF-GX 92 is an epoxy resin/silica blend polymer produced by Ajinomoto Film Technology Company, Inc. Japan. Low dielectric constant, 3.2 and smooth surface morphology brings this polymer as one of the most used dielectrics material for IC (Integrated Circuit) substrate production. This polymer is based upon epoxy resin and phenol hardener. The chemical structure of this polymer is represented in Figure 2.12. The physical properties of ABF-GX92 were listed in Table 2.3.

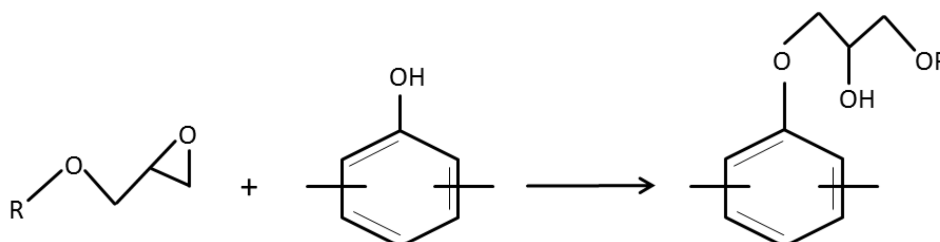

Figure 2.12 Chemical structure of ABF-GX92 substrate. (Extracted from Ref.[74])

Table 2.3 The physical properties of epoxy polymer film ABF-GX92. (Extracted from Ref.[75])

Properties		
CTE x-y (ppm: 25-150 °C) (Tensile TMA)		39
CTE x-y (ppm: 150-240 °C) (Tensile TMA)		117
Tg (°C, Tensile TMA)		153
Tg (°C, DMA)		168
Young's modulus (GPa)	23 °C	5
Tensile strength (MPa)	23 °C	98
Elongation (%)	23 °C	5.6
Dielectric constant (Cavity perturbation, 5.8 GHz)		3.2
Loss tangent (Cavity perturbation, 5.8 GHz)		0.017
Water absorption 100 °C, 1 h (wt%)		1

Polyimides have been widely used as dielectrics in microelectronics production due to it many outstanding properties, such as good thermal stability, low dielectric constant, low dissipation factors and implicit surface inertness. Poly [*N, N'*-(oxydiphenylene)pyromellitimide] or mostly known as Kapton®200 H is produced by DuPont. It is produce from the condensation of pyromellitic dianhydride (PMDA) and

4,4’-oxydianiline (ODA) in dipolar aprotic solvent such as *N*-methylpyrrolidone (NMP) or *N,N*-dimethylacetamide (DMAc). Reaction scheme of polyimide formation is shown in Figure 2.13. The physical properties of polyimide Kapton®HN is shown in Table 2.4.

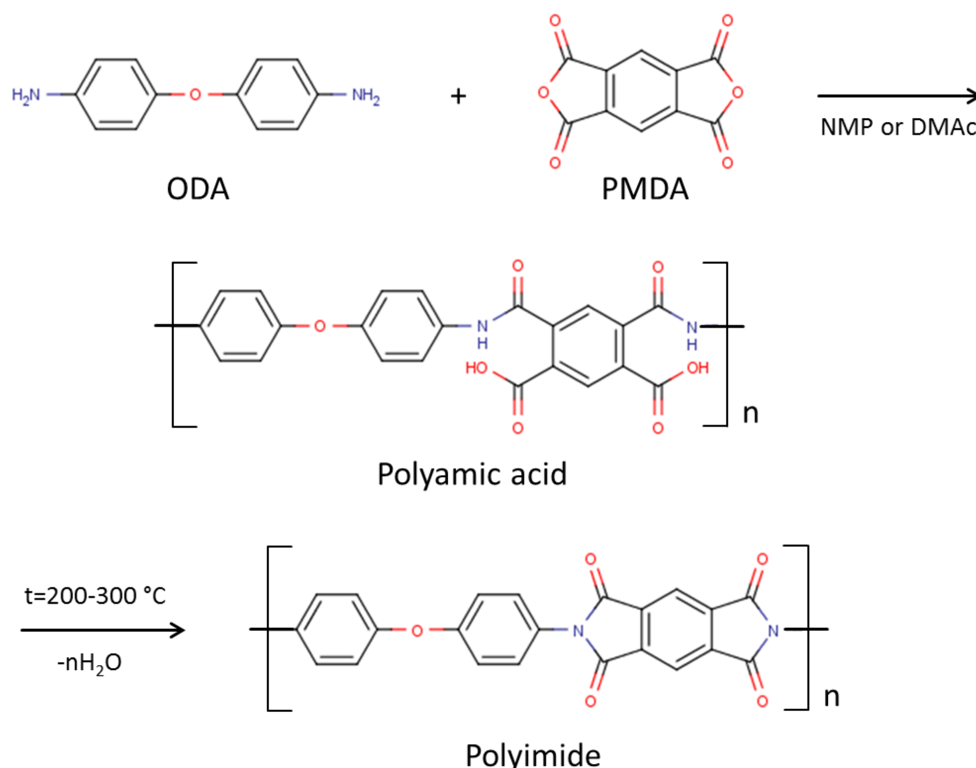

Figure 2.13 Reaction between ODA and PMDA to polyamic acid following with dehydration to polyimide. (Adapted from Ref.[76])

Table 2.4 The physical properties of poly [N, N'-(oxydiphenylene)pyromellitimide] Kapton®HN. (Data extracted from Ref.[77])

Properties		
CTE x-y (ppm: 30-100 °C)		17
CTE x-y (ppm: 100-200 °C)		32
Tg (°C)		360-410
Young’s modulus (GPa)	23 °C	2.5
Tensile strength (MPa)	23 °C	231
Elongation (%)	23 °C	72
Dielectric constant (1 kHz)		3.4
Dissipation factor (1 kHz)		0.0018
Water absorption 23 °C, 24 h (wt%)		2.8

Chapter 3 - Fundamentals of applied techniques

3.1 Dynamic Light Scattering (DLS)

Dynamic light scattering (DLS), also known as photon correlation spectroscopy (PCS) or quasi-elastic light scattering (QELS), is a powerful technique for measuring particles sizes of colloidal particles suspended in solution.[78] This technique can give information on particles sizes in the range of few nanometers to 5 micrometers. DLS measured the velocity of Brownian motion and relates this to the size of particles. Brownian motion is the random movement of the particles, as a result from the bombardment by the surrounding solvent molecules. This motion is influence by the temperature, viscosity of the solvent, and especially by the size of the particles. The larger the particle, the slower the Brownian motion. The velocity of Brownian motion is defined by the property known as the translation diffusion coefficient (D_T). For a spherical particle, the diameter of particle is calculated from the translation diffusion coefficient, by using *Stokes-Einstein relationship*

$$d_h = \frac{kT}{3\pi\eta D_T} \qquad (3.\ 1)$$

where k is Boltzmann's constant, T is the suspension temperature, and η is the viscosity of the medium. It needs to be noted that the particle diameter defined by DLS is the hydrodynamic diameter. The obtained particle size is the size of a sphere that has the same translational diffusion coefficient as the measured particle.

In DLS, a monochromatic light source, usually a laser is shot through a polarizer and into a sample. The light illuminates the sample and the small particle inside the sample scatters the light in all directions. The scattered light signal is collected by the one of the photomultiplier detectors, either at 90 ° or 173 ° scattering angle. The incoming data is processed in real time by a device known as correlator, deconvoluted by alogarithms to determine the size distribution of the sample. The schematic of DLS measurement is shown in Figure 3. 1.

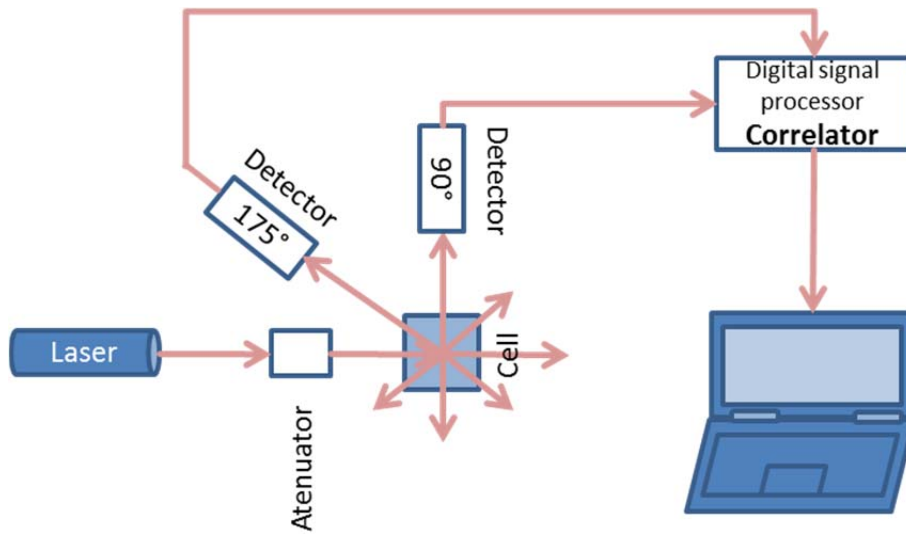

Figure 3. 1 Schematic of a DLS instrument (adapted from Ref.[79])

Because all particles in solution continuously move and diffuse with Brownian motion, there will be a change in the scattered light intensity. The small particles that can move faster cause the light intensity fluctuate more rapidly than large particles (Figure 3. 2).

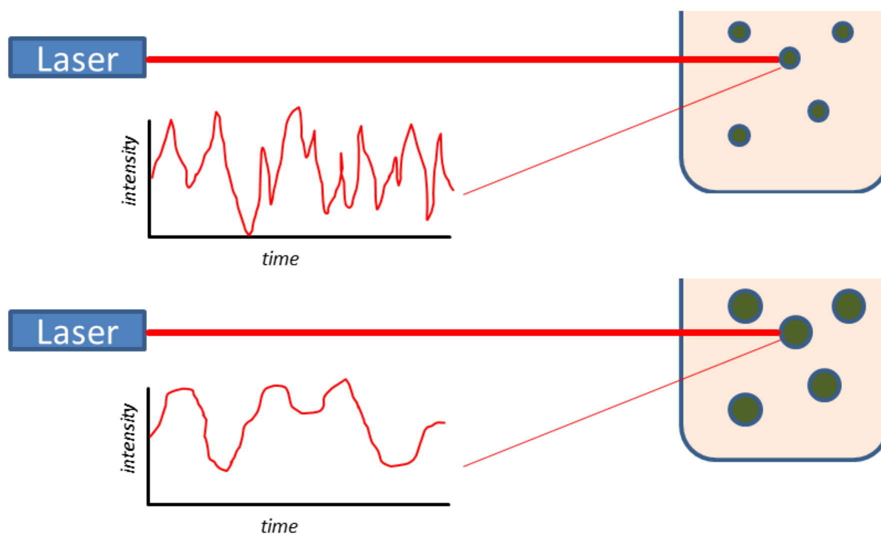

Figure 3. 2 The fluctuation of scattered light intensity as a function of time on different particle sizes (adapted from Ref.[80])

The correlator constructs the correlation function $G(\tau)$ of the detected intensity as shown below.

$$G(\tau) = \langle n(t) \cdot \mathrm{n}(t+\tau) \rangle \tag{3. 2}$$

where *n(t)* is the scattering intensity at time *t*, *τ* is the delay time and the angular brackets indicate that the product is the average over the duration of measurement time.

For a large number of mono-disperse particles in Brownian motion, the correlation function the exponential decaying function of the corellator time delay *τ* and described as,[81]

$$G(\tau) = B(1 + \beta e^{-2\Gamma\tau}) \tag{3. 3}$$

where *B* is the baseline of the correlation function, *β* is the intercept of the correlation function, Γ is the decay constant given by

$$\Gamma = D_T q^2 \tag{3. 4}$$

where *q* is the modulus of scattering vector, given by

$$q = \frac{4\pi n}{\lambda} \sin\left(\frac{\theta}{2}\right) \tag{3. 5}$$

n is the refractive index of the suspension, *Θ* is the scattering angle, and *λ* is the laser wavelength. Therefore, by inserting D_T into the Stokes-Einstein, the hydrodynamic diameter of the measured particle can be obtained.

Z-Average, also known as cummulant mean, is derived from cumulants analysis of the measured correlation curve. It is the fit of polynomial to the log of the G(1) correlation function.[80]

$$Ln[G(1)] = a + bt + ct^2 + dt^3 + et^4 + \ldots\ldots \tag{3. 6}$$

where *b* is the second order cumulant or the Z-average diffusion coefficient. By using the dispersant viscosity and some instrumental constants, the size was calculated. It is important to note that the result is valid only if the sample is monomodal, spherical and monodisperse.

3.2 Zeta Potential

A particle in solution with a net charge attracts a thin layer of ions of opposite charge, forming an electrical double layer, which consist of two parts (Figure 3. 3).[79] The inner part of the electrical double layer is strongly bound to the surface, and is referred as the Stern layer. The second part, which is less firmly associated is referred as diffuse layer. As the particle diffuse through the solution (e.g. due to gravity, kinetic energy, etc.), a boundary between the ions that move with the particles and ions that stay with bulk dispersant is formed. The electrostatic potential at this boundary is called zeta potential (ζ).

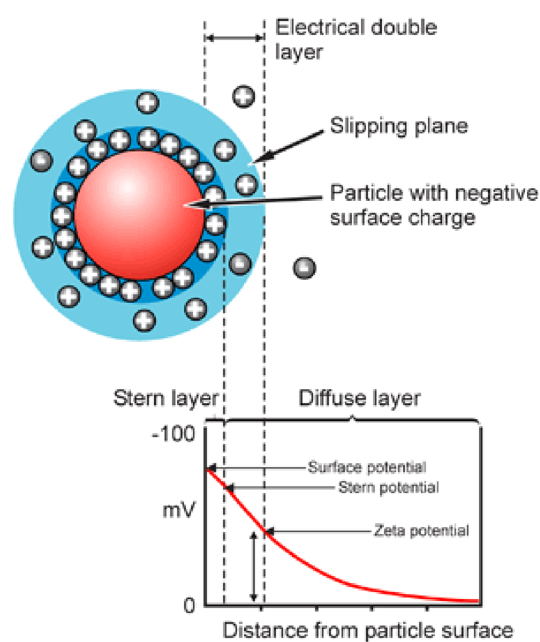

Figure 3. 3 Electrical double layer surrounding the surface of particle. (Reprinted from Ref.**[79]**)

The magnitude of zeta potential can be used to describe the stability of a colloidal system. When the particles in suspension have a large negative or positive zeta potential, they repeal each other. As a result, the suspension would remain stable, and no flocculation between particles would occur. Particles with zeta potential of > +30 mV or < -30 mV are considered stable.[79] There are three factors that can affect the zeta potential: pH of the suspension, conductivity of the suspension, and the concentration of the particles in suspension. The pH of the suspension is the most important factor that affects the zeta potential. At low pH (acidic), more positive zeta potential is obtained because of the addition of positive

charge from the acid. On the other hand, the increase of negative charge in solution at high pH (basic) results in more negative zeta potential. As the zeta potential change from positive to negative, there is a point where the zero zeta potential is crossed. This point is called the isoelectric point. Usually a particle suspension will be least stable when the zeta potential is close to this point (Figure 3. 4).

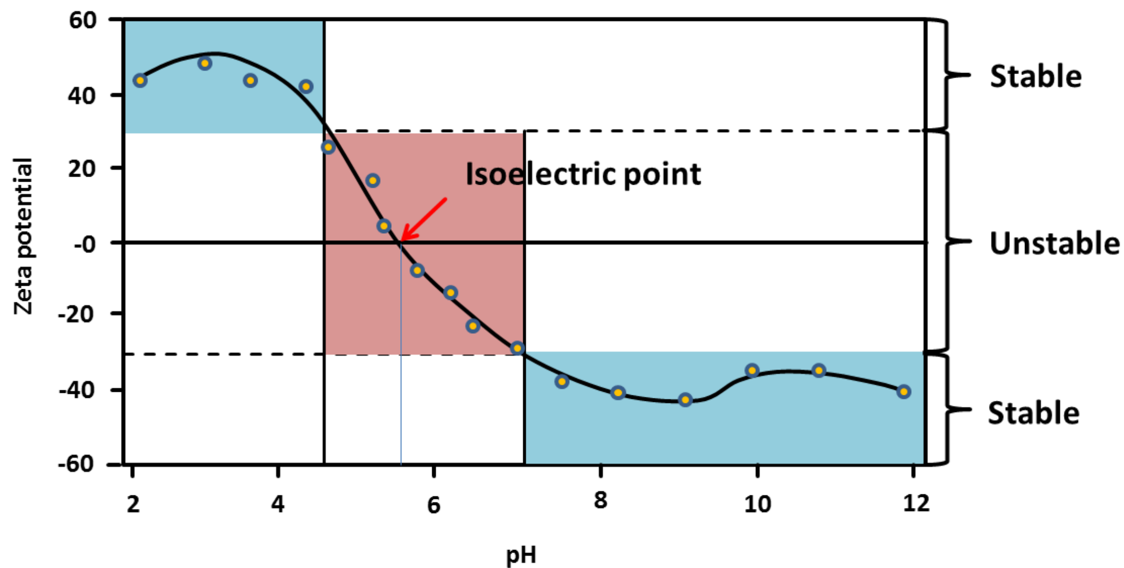

Figure 3. 4 Zeta potential of particles as a function of pH showing the range where the particles should remain stable. (Extracted from Ref.[79])

Another possible factor leading to surface charging is the dissociation of the surface chemical group.[82] Thus, at different pH, as the concentration of hydrogen ions changes, so does the surface charge of the particles. Because of this, zeta potential measurement technique has been used widely for monitoring surface chemical group on particle surface. The change of zeta potential with pH of silica particles carrying different surface chemical group is shown in Figure 3. 5, -OH for bare silica and $–NH_2$ for APTES functionalized silica.

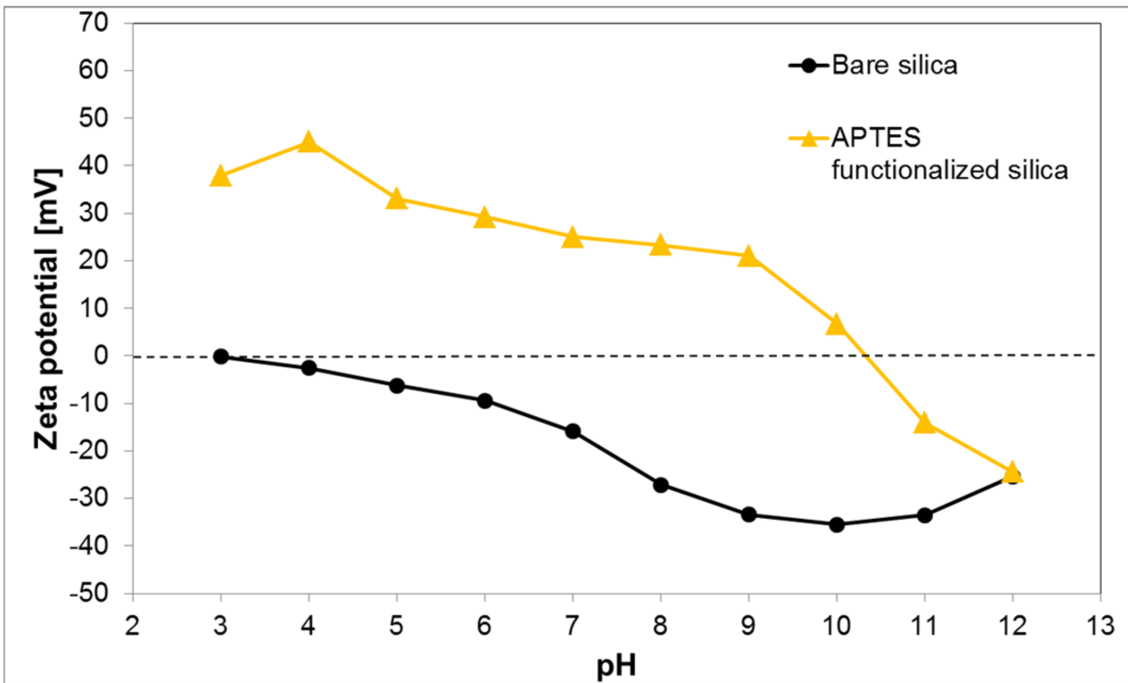

Figure 3. 5 The change of zeta potential with pH of silica particles carrying different surface chemical group, -OH for bare silica and –NH_2 for APTES functionalized silica

Zeta potential is not measureable directly but it can be calculated from the electrophoretic mobility of the particle.[83] The electrophoretic mobility is obtained by measuring the velocity of the particles using laser doppler velocimetry (LDV), while an electric field is applied across the sample (electrophoresis). The Henry equation is used to calculate the zeta potential, ζ:

$$U_E = \frac{2\varepsilon\zeta f(\kappa a)}{3\eta} \tag{3. 7}$$

Where U_E is the electrophoretic mobility, ζ is the zeta potential, ε is the dielectric constant of the solvent, η is the viscosity of the solvent, and $f(\kappa a)$ is Henry's function in which κa is the ratio of the particle radius to the electrical double layer thickness. Two values are generally used as an approximation for the $f(\kappa a)$.[80] For measurements in aqueous media with the particle size larger than 200 nm, 1.5 is used and referred to as Smoluchowski approximation. For small particle measure in non-aqueous media, $f(\kappa a) = 1$ is used and referred to Huckel approximation.

3.3. C, H, N, S Elemental Analysis (EA)

C, H, N, S elemental analysis is a relatively simple analysis method to detect different elements (atoms and ions) in a sample. This technique is based upon the combustion process (furnace temperature higher than 1000 °C) of carbon into carbon dioxide, hydrogen to water, nitrogen to nitrogen gas/oxides of nitrogen and sulfur to sulfur dioxide. CO_2, H_2O and SO_2 are specifically adsorbed while passing through the adsorption columns, while N_2 gets to the detector. After the detection of N_2, the adsorption columns were heated up one after the other, in order to release and detect the remaining gases. Typical instrumentation arrangement of CHNS elemental analyzer is shown in Figure 3. 6.

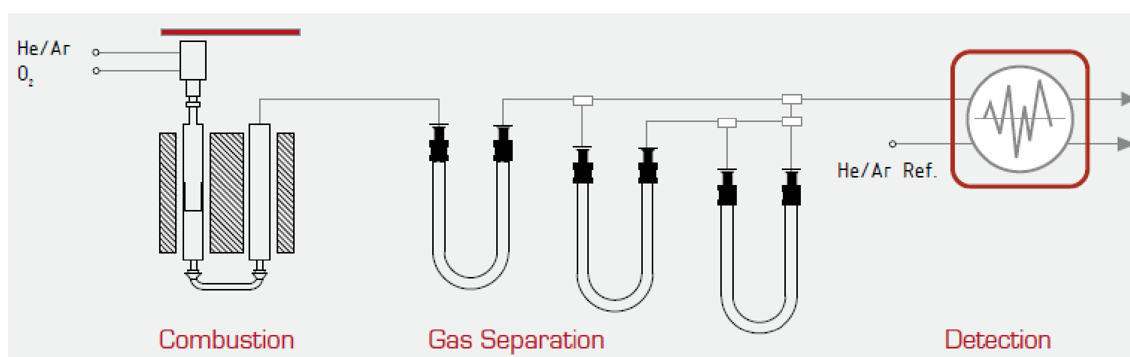

Figure 3. 6 Typical instrumentation arrangement of CHNS elemental analyzer. (Reprinted from Ref.[84])

In using this measurement, one thing we need to keep in mind is that the results are a measure of the total amount of combustible amount in the sample, regardless it is because of one component or many. Under the condition of mineralization, fluorine is reacting to form HF, which reacts with the silica tube as source of error. Therefore, some measurement deviation occurs when analyzing fluorine containing samples. The important consideration in using this measurement method is that the highly viscous material can not be handled.

3.4. Ultraviolet/Visible Spectroscopy (UV-Vis)

Molecular absorption spectroscopy in the region of ultraviolet and visible spectral is widely used for the quantitative determination of large number of inorganic, organic, and biological species.[85] This absorption spectroscopy is based on the measurement of transmittance or absorbance of solution by using

electromagnetic radiation between 190 nm to 800 nm and is divided into ultraviolet (190-400 nm) and visible (400-800 nm). As stated in *Beer's Law* equation, the absorbance is directly proportional to the concentration of an absorbing species (*c*) and the path length (*b*).

$$A = \log\frac{P_0}{P} = \varepsilon bc \quad (3.\ 8)$$

In equation (3.8), *A* is the absorbance, P_o is the intensity of the incident light, *P* is the intensity of light transmitted through the sample, and ε is the constant of proportionality or molar absorptivity.

The method of external standards is the most often used method to establish the relationship between absorbance and concentration. In a consistent condition of analysis, the calibration curve is generated from a series of standard solutions that cover the concentration range expected from the sample.

UV-Vis spectroscopy in combination with chemical derivatization method was used to quantify the amount of free amine groups on the surface of silica (AP-Monoamine, AP-Diamine, and AP-Triamine). As mentioned in the literature,[86] salicylaldehyde easily reacts with primary amine groups. After the reaction, the color immediately turns bright yellow as salicylaldimine (Schiff's base), has a strong absorption in UV-Vis around 404 nm. A calibration curve as a function of APTES concentration was prepared (vide infra). The absorbance spectra of APTES after it was treated with salicylaldehyde were shown in Figure 3. 7. The appearance of isobestic point at 360 nm implies an equilibrium exist between the two species. Salicylaldehyde has a peak at 320 nm. The intensity of the peak at 320 nm decreases while the one at 404 nm increases with respect to APTES concentration, indicating that salicylaldehyde underwent condensation reaction with primary amine to form salicylaldimine. Previous investigation by Dutta et al.,[87] has suggested that the strong absorption in UV-Vis around 404 nm is because of the formation of zwiterionic species of salicylaldimine.

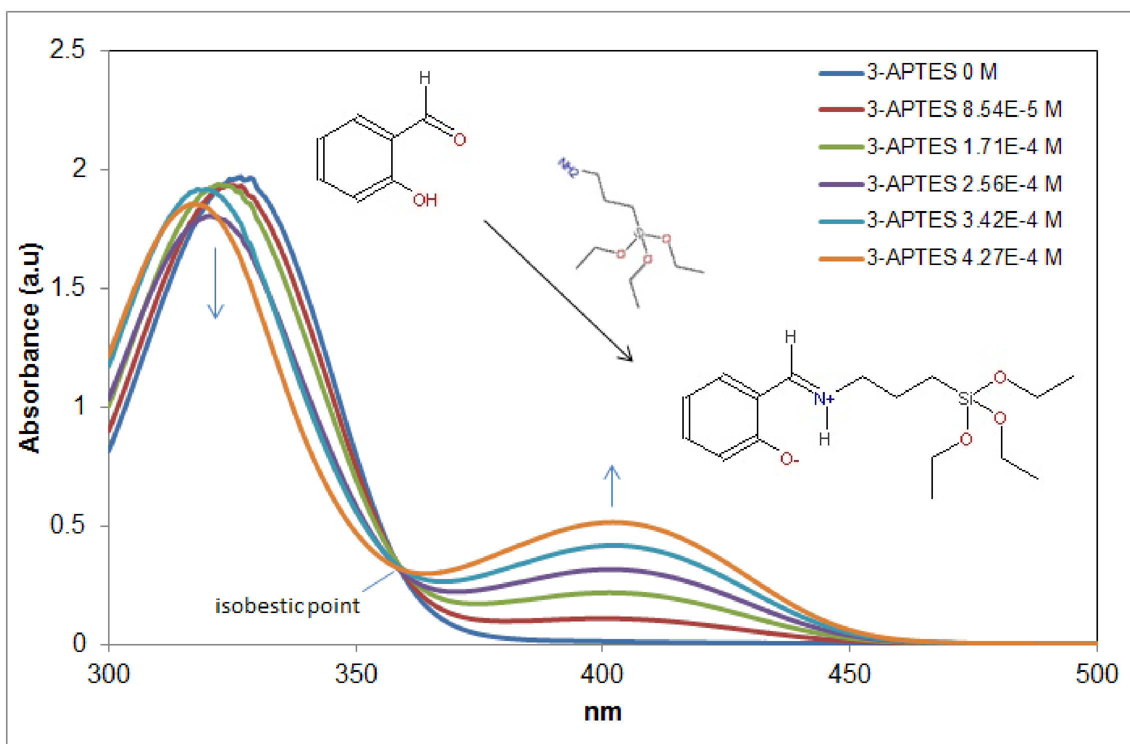

Figure 3. 7 The absorbance spectra of salicylaldehyde reacted with different concentration of 3-APTES

As shown in Figure 3. 8, a calibration curve was made by plotting absorbance intensity at 404 nm (A) versus concentration of APTES (C). Ethanol was used as the background for each measurement. The least square fitting gives a correlation equation, C = 1180.2 A + 0.0117 with coefficient of determination 0.99. Using absorbance-concentration correlation equation (calibration curve), measured particles size (DLS), and silica density ($\rho = 2.2$ g/cm^3)[88], the density of amine groups on the surface of silica in $-NH_2$ groups/nm^2 was determined. The calculation of the density of amine group is mentioned more in detail in Appendix 1.

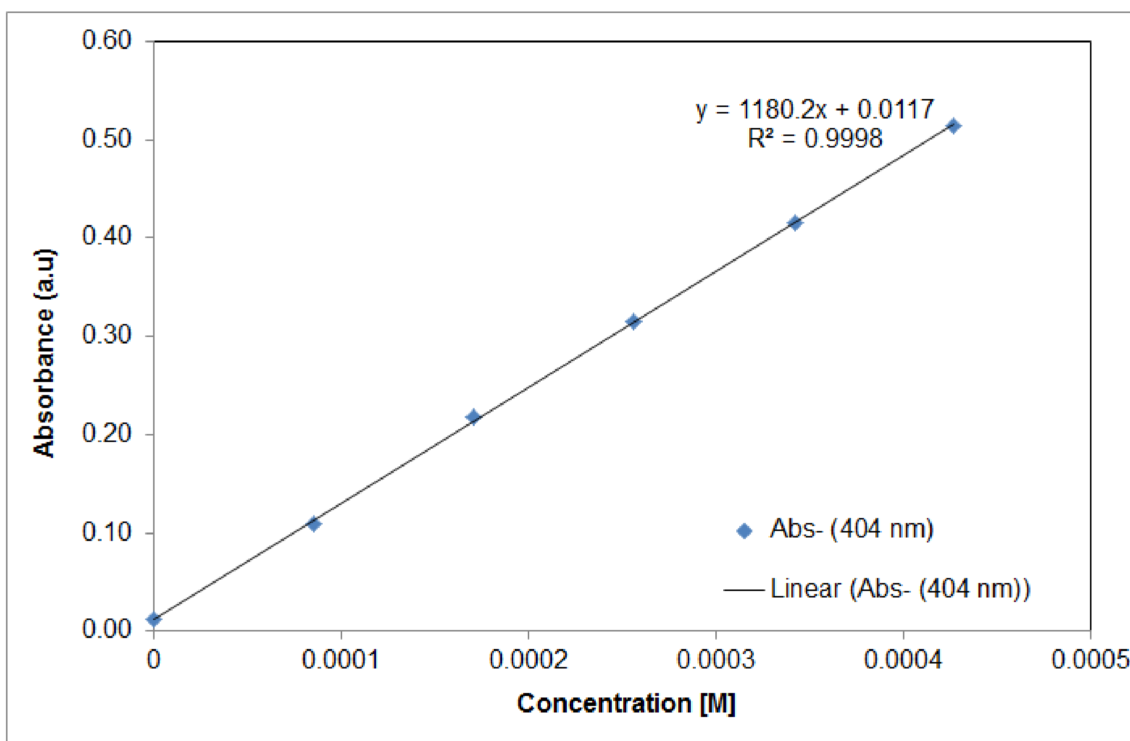

Figure 3. 8 A calibration curve showing the absorbance intensity at 404 nm vs. APTES concentration

3.5. Fourier Transform Infra-Red-Attenuated Total Reflectance (FTIR-ATR)

The infrared spectroscopy is one of the most versatile methods available for the characterization of the chemical structure of molecules. This vibrational spectroscopy technique covers the infrared region of electromagnetic spectrum (12800 to 10 cm^{-1}). The typical range of analysis in wavenumbers is from 4000 to 670 cm^{-1}.[89] Infrared spectroscopy exploits the fact that different functional groups absorb characteristic frequencies of IR radiation, when a molecule undergoes a net change in dipole moment as it vibrates or rotates. Since every non-linear molecule is able to move in three dimensional directions, a molecule containing N atoms has 3N degrees of freedom, which six of them are translations and rotations of the molecule itself. The remaining 3N-6 degrees of freedom represent the possible vibrations within the molecule.

Attenuated total reflectance (ATR) generally allows qualitative or quantitative analysis of sample with simple or no sample preparation. It is suitable for studying highly absorbing solid (non-transparent) and liquid materials such as polymer films, coatings, powders and aqueous samples.[90] ATR occurs when the beam of radiation

enters from a more-dense (higher refractive index, ATR crystals) to a less-dense medium (lower refractive index, samples) at an angle greater than the critical angle. The critical angle (θ_c) is defined as,

$$\theta_c = sin^{-1}\left(\frac{n_2}{n_1}\right) \tag{3. 9}$$

where n_1 is the refractive index of the crystal and n_2 is the refractive index of the sample. An evanescent field is formed at the interface between the two media, and penetrates into the sample. The depth of beam penetration in ATR spectroscopy is a function of the wavelength, λ, the refractive index of the crystal, n_1, the refractive index of the sample, n_2 and the angle of incident beam, Θ.

$$d_p = \frac{\lambda}{2\pi(n_1^2 sin^2\theta - n_2^2)^{1/2}} \tag{3. 10}$$

During the measurement, some of the evanescent wave is absorbed by the sample and the reflected radiation is returned to the detector. Figure 3. 9 represents the schematic of a single reflection ATR system.

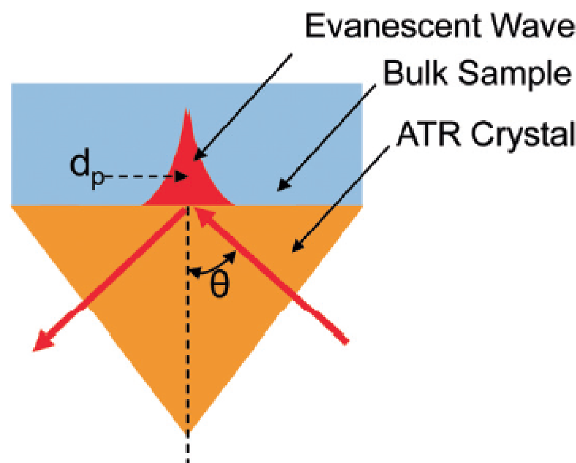

Figure 3. 9 Representation schematic of a single reflection ATR with Θ incidence angle. (Extracted from Ref.[91])

In particular, for the characterization of polymer substrates such as epoxy resin (ABF-GX92) and polyimide films (Kapton®HN), the penetration depth is strongly dependent on the refractive index of the substrate. Since the polyimide films are much more transparent than the epoxy resin, the refractive index of the polyimide film is lower than epoxy resin. The depth of IR beam penetration is greatly enhanced

relative to epoxy resin. For this reason, the intensity of reflected radiation back to the detector is lower in comparison with epoxy resin substrate.

3.6. X-ray Photoelectron Spectroscopy (XPS)

X-ray pthotoelectron spectroscopy (XPS), also known as electron spectroscopy for chemical analysis (ESCA) is a widely used technique to investigate the chemical composition of surfaces.[92] In XPS, the sample surface is irradiated with x-ray of known energy, hv in vacuum. According to the photoelectric effect, every atom has core electron that can be emitted at certain kinetic energy (E_k). This phenomenon is explained briefly below. When an x-ray photon hits an atom, the energy is absorbed by the core electron of an atom. If the photon energy is large enough, the core level electron will then be emitted out from the atom. This emitted electron with kinetic energy of E_k is referred to as photoelectron. At the same time, irradiation of solid surface using x-ray can also result to the emission of Auger electron (Figure 3. 10).

In electron spectrometer, the kinetic energy of emitted electron (E_k) is measured. The binding energy of the electron (E_b) is calculated by using equation described as,

$$E_k = hv - E_b - \phi \tag{3. 11}$$

Where hv is the x-ray photon energy ($hv = 1486.6\ eV$ for Al K_α) and ϕ is the work function induced by the analyzer. The energy of emitted photoelectrons is analyzed in order to identify and determine the composition of materials surface. Because of the poor penetrating power of electrons, atomic and molecular compositions of the outermost 3-10 nm layers of the surface were analyzed in XPS.

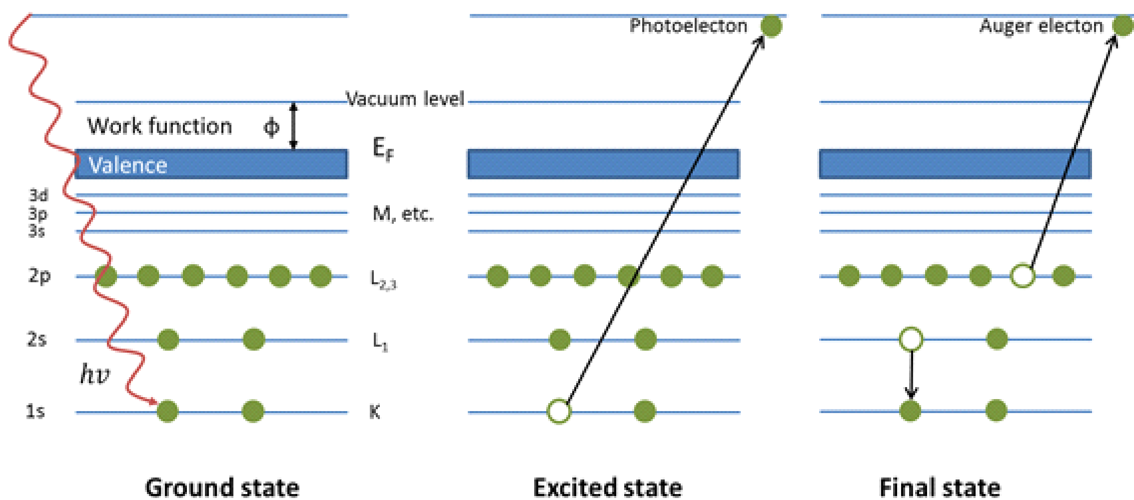

Figure 3. 10 Schematic diagram of photoelectron and auger electron emission process

Electron spectrometers are made up of different components. These components include (1) an x-ray source, (2) sample holder, (3) analyzer, and (4) detector. A simple schematic drawing of electron spectrometer instrumentation is described in Figure 3. 11. The sample is irradiated by shooting a short wavelength of x-ray on at the surface. The energy of these x-rays is absorbed and electrons are emitted from the inner core shell of an atom at the surface of the sample. These emitted electrons called photoelectrons. The kinetic energy carried by the photoelectrons is measured by the energy analyzer, while the number of emitted electrons is measured by the detector.

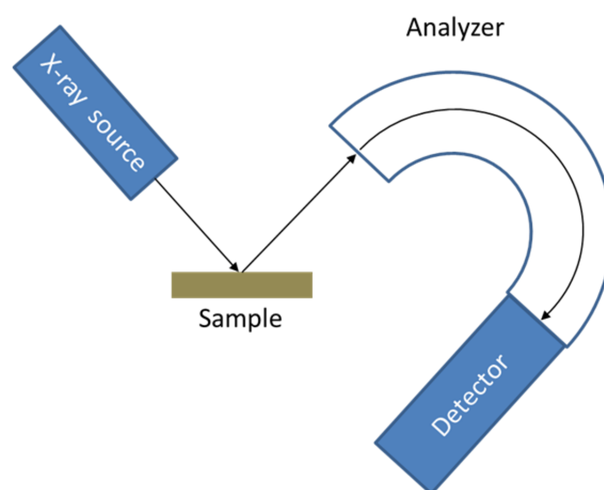

Figure 3. 11 Schematic drawing of XPS using a monochromatic x-ray source

For insulating sample such as organic polymers, surface charge is builds on the surface during irradiation of X-ray. Surface charge leads to energy kinetic loss of emitted electron. As a result, XPS binding energy peak is shifted. In order to overcome this problem, an additional source of electron is implemented during the X-ray irradiation to compensate the positive charge buildup from photoelectron emission. This can be done by flooding the sample with a monoenergetic source of low energy (< 20 eV) electron,[93] also known as low energy electron flood gun. However, since the vacuum level of the sample is in electrical equilibrium with the energy of the sample, the measured E_b is dependent on the sample work function (ϕ_s) and the energy of the flooding electron (ϕ_e),

$$E_B^{Vac} = hv - E_k - \phi_e \qquad (3.\ 12)$$

Thus, it is difficult to measure the absolute E_B values for the insulating sample which is not in electrical contact with the spectrometer. Therefore, the use of internal reference is necessary to adjust the E_B scale, C_{1s} is typically set to 285.0 eV, and allow us to accurately measure the other E_B in the sample.

3.7. Atomic Force Microscope (AFM)

Atomic force microscopy is a very high resolution of scanning probe microscopy. AFM operate by measuring the kinetic force between a probe and the sample. In general, the probe is a sharp pyramid tip with height of around 5 μm with 15-40 nm end radius. In this technique, the tip is brought into proximity of a sample surface, and then indirectly measuring the deflection of the cantilever as a response to external force due to it interaction with the surface (Figure 3. 12).[94] In theory, the topography of any surface can be imaged down to atomic resolution with AFM. The applicability to measure non-conducting samples is the advantage of AFM among scanning electron microscope (SEM). Therefore, AFM is essential for studying surface topography at the nanoscale, having resolution far exceeding other optical based methods.

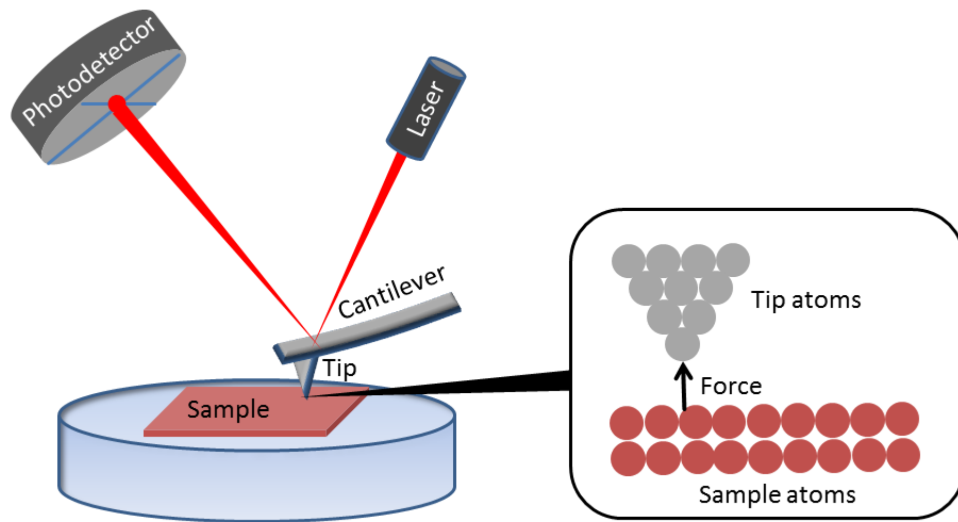

Figure 3. 12 Schematic drawing of the AFM set-up

Three modes are commonly used in AFM: contact, tapping and non-contact mode.[85] In contact mode, the end of the tip is in contact with the sample when it scanning. The tip scans at a constant force (fixed deflection of cantilever) and the motion of the scanner in z-direction is recorded. Constantly contact between the tip and the sample surface leads to surface damage especially for soft samples. Therefore, for polymer samples the tapping mode is mostly used. In this mode, the cantilever oscillates at a frequency of a few hundreds kilohertz (resonance frequency) and only periodically touch or "tapping" the sample.[95] As the tip approaches the surface, the oscillation amplitude is reduced due to the energy loss caused by the tip contacting the surface. This oscillation amplitude reduction is used to identify and measure feature of the surface.

AFM analysis produces three dimensional image of the samples that can be used to quantivy the surface roughness, by using root mean square (RMS) roughness calculations. Example of the three dimensional AFM image of polymer substrate is shown in Figure 3.13. The RMS is calculated using the following formula,

$$R_{rms} = \sqrt{\frac{1}{n}\sum_{i=1}^{n}(h(x_i) - \hbar)^2} \quad (3.\ 13)$$

Where n is the number of lattice points, $h(x_i)$ is the height function across the surface and $\hbar$ is the average height defined as,

$$\hbar = \frac{1}{n}\sum_{i=1}^{n} h(x_i) \quad (3.\ 14)$$

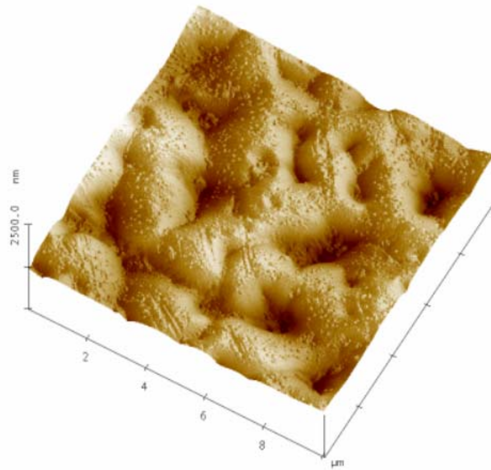

Figure 3.13 Three dimensional AFM image of polymer substrate

3.8. Field Emission Scanning Electron Microscope (FESEM)

Scanning electron microscope (SEM) is used widely in many scientific applications, enables the investigation of specimens with a resolution down to nanometer scale. In this technique, the beam of electrons (primary electrons) is generated by a suitable source such as tungsten filament. This electron beam is accelerated in a high voltage and pass through the system aperture and electromagnetic lenses to produce a thin beam of electron. Finally, the electron beam scans the surface of the specimen.

The interaction of a primary electron with the surface or bulk of the specimen leads to the emission of various energy signals that can provide information on structure and chemical composition of the specimen. Different signals that originate depending on the electron interaction volume or depth are shown in Figure 3. 14. For surface imaging in SEM, two types of signals are most commonly collected: secondary electron (SE) and backscattered electron (BSE). The characteristic x-ray signal is used in Energy Dispersed Spectroscopy (EDS) to determine the chemical composition of the specimen.

A field-emission cathode in the electron gun of a scanning electron microscope (FESEM) provides narrower probing beams at low as well as high electron energy, resulting in both improved spatial resolution and minimized sample charging and damage. FESEM is an essential instrument for surface imaging which demand the highest magnification possible.

Since SEM required conductive surface and most of the polymer specimen are not conductive enough for SEM investigation, a thin layer of metal such as gold, platinum or iridium need to be deposited on the surface by sputtering to increase the conductivity.

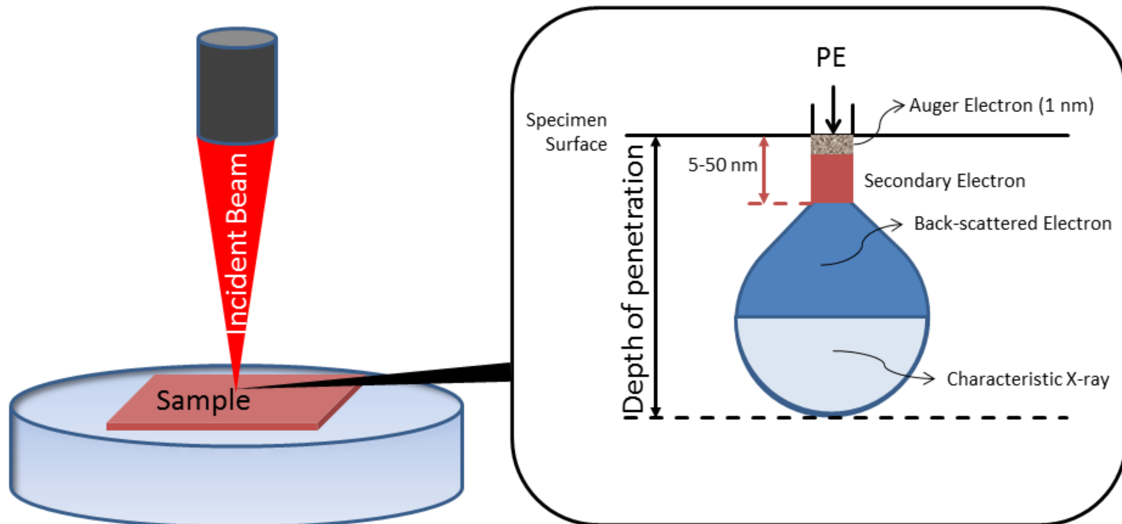

Figure 3. 14 Various signals generated as a result of primary electron interaction with surface or bulk of solid specimen

3.9. Inductively Coupled Plasma- Optical Emission Spectroscopy (ICP-OES)

ICP-OES is an analytical technique used for the detection of trace metals. This technique is based upon the emission of photons from atoms or ions which have been excited by using inductively coupled plasma (ICP) discharge.[96],[97] The emitted photons have characteristic wavelength which can be used to identify the elements from which they originated. The intensity of the emission indicates the concentration of the element in the sample.

In ICP-OES, liquid and gas samples can be introduced directly into the instrument, while an extraction step or dissolution in acid is required for the solid samples (metal samples), thereafter the analytes will be present in a solution. The solution converted into aerosol by using nebulizer and directed into the plasma discharge. High temperature (10,000 K) at the core of the ICP leads to immediate evaporation of the aerosol and at the same time photons from particular element are

emitted. With the help of photodetector, the particular wavelength exciting the monochromator is converted to an electrical signal.

The most important criteria of ICP-OES, is the detection limit of individual elements, from 100 µg/L to 0.1 µg/L. For high concentration of analytes, dilution step in aqueous solution is required, prior to the measurement.

Chapter 4 - Synthesis and characterization of functionalized silica nanoparticles

4.1. Introduction

Monodispersed spherical silica nanoparticles can be prepared from the hydrolysis of alkyl silicates, and condensation reaction of silicic acid in ammonia (catalyst) and water containing alcoholic solutions.[98-99] In general, the hydrolysis and condensation reaction of tetraethylorthosilicate (TEOS) will follow the reaction shown in Scheme 4. 1. For the base catalyzed hydrolysis reaction of TEOS, the hydroxide ions attack the TEOS molecules by a nucleophilic reaction mechanism, removing the first alkoxy group to produce silicic acid. The hydrolyzed intermediate undergoes condensation to eventually form silica. The resulting silica nanoparticles are stabilized by electrostatic repulsion from the ammonium (NH_4^+) ions in ammonia containing solution (Scheme 4. 2).

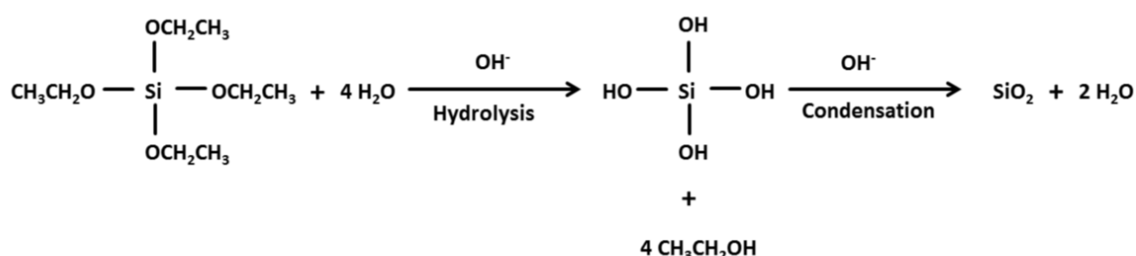

Scheme 4. 1 Base catalyzed hydrolysis and condensation reaction of TEOS

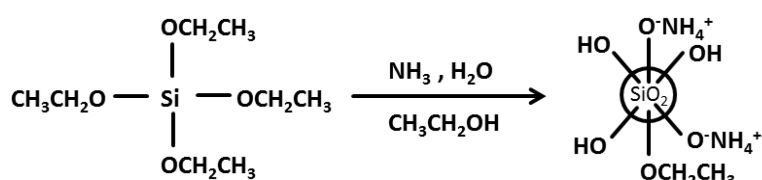

Scheme 4. 2 Silica nanoparticles stabilization in ammonia containing ethanolic solution. (Extracted from Ref.[100])

Many factors can affect the size of the resulting silica nanoparticles, such as the reaction temperature, the concentration of water, the alkyl silicates and the catalyst, and the reaction time.[98, 101] In the case of TEOS in ethanol with ammonia

as the catalyst, the diameter of the obtained particles (*d*) can be predicted by using the following equation:[98]

$$d = A[H_2O]^2 exp(-B[H_2O]) \quad (4.1)$$

where

$$A = [TEOS]^{-1/2}(-1.042 + 40.57[NH_3] - 9.313[NH_3]^2) \quad (4.2)$$

$$B = 0.3264 - 0.2727[TEOS] \quad (4.3)$$

The surfaces of bare silica nanoparticles (SiO_2) can be functionalized with polymer chains, either by chemical bonding or by physisorption.[100] Owing to its simplicity and low cost, particle surface modification by silanization with organosilanes is the most commonly used method to prepare functionalized silica nanoparticles. In order to obtain an optimal surface functionalization, these particles must be stable in the dispersion during the modification process. This is one of the biggest challenges in the modification of particle surfaces.

Particles collide because of their random motions known as Brownian motions.[102] When the repulsive forces between the particles are low, for example, when the particles have a low surface charge, they start to form larger chain or clusters consisting of many particles (coagulation) as a result of the interparticle collisions due to Brownian motion. At this point, the colloidal stability of the particles in the dispersion is low. Because the zeta potential is a function of pH, the stability of particles varies with pH.[103] As shown in Figure 4. 1, the stability of bare silica nanoparticles strongly depends on the pH of the dispersion. At elevated pH values, after the particles reach their critical size, the stability increases because of the mutual repulsion between them, decreasing the number of effective collisions between particles.[103] At around neutral pH, silica particles are least stable as the particles have low ionic charge on the surface, and the particles tend to aggregate and gel. The silica sols have a maximum temporary stability (metastable) around pH1.5-4.

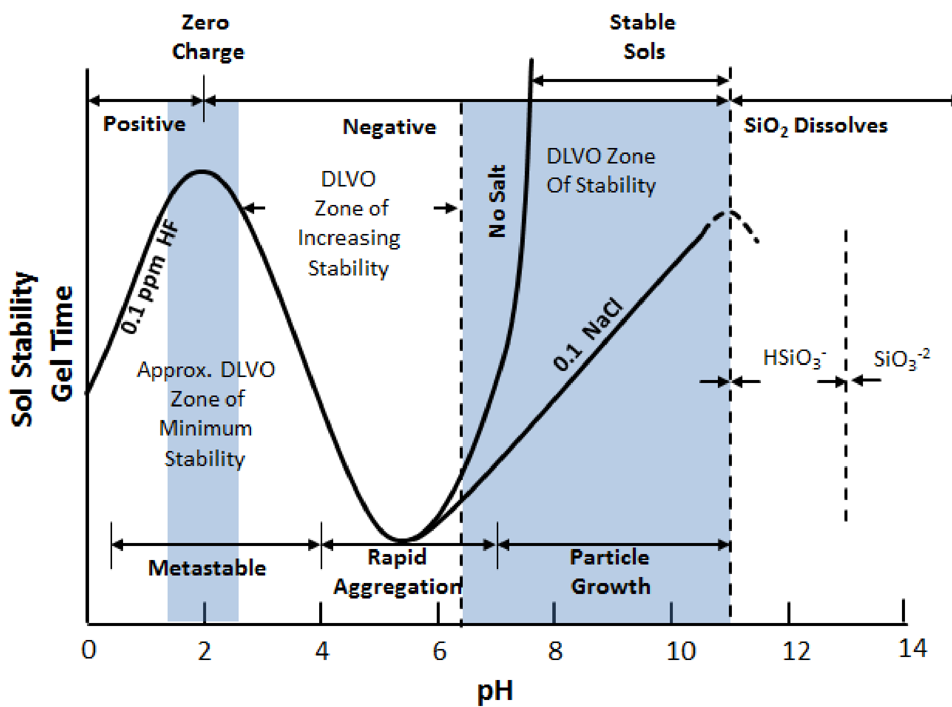

Figure 4. 1 Stability of colloidal silica sol as a function of pH. (Adapted from Ref.[103])

Our goal is to prepare colloidal dispersion of silica nanoparticles with functional groups on the surface. Narrow size distribution and stability of colloidal dispersion in alcoholic solution are desired. The obtained functionalized silica nanoparticle dispersion will be used for the treatment of dielectric substrates. They are applied to enhance the adhesion between copper and the dielectric substrate in printed circuit board productions.

4.2. Experimental

4.2.1. Materials

Tetraethoxyorthosilicate (TEOS, 99.9 %) was purchased from Alfa Aesar. Ammonium hydroxide (25 wt.%) was purchased from AppliChem. Absolute ethanol (99.9 %, analytical grade) was purchased from Merck. Acetic acid (99.8 %) was purchased from Sigma Aldrich. Ureidopropyltrimethoxysilane (UPMS, 97 %), (3-glycidoxypropyl)trimethoxysilane (3-GLYMO, 98 %), 3-mercaptopropyltriethoxysilane (3-MPTES, 92 %), 3-aminopropyltriethoxysilane (3-APTES, 98 %), N-(2-aminoethyl)-3-aminopropyltriethoxysilane (DPTES, 95 %), and N-(3-trimethoxysilylpropyl) diethylenetriamine (TPTMS, 95 %) were purchased from ABCR specialty chemicals. The chemicals were used as received without further purification. Dialysis membranes used to purify the functionalized silica nanoparticles were purchased from Spectrum Labs (Spectrapor®1 regenerated cellulose, pore size: 6-8 kDa).

4.2.2. Preparation of functionalized silica nanoparticles

The bare silica nanoparticles (*AP-Hydroxyl*) were prepared using the Stöber[99] process with tetraethoxyorthosilicate (TEOS). In this method, the aqueous ammonia served both as a reactant and a catalyst for the hydrolysis of TEOS. Six types of functionalized silica nanoparticles, aminopropyl (*AP-Monoamine*), N-(2-Aminoethyl)-3-Aminopropyl (*AP-Diamine*), 3-[2-(2-aminoethylamino)ethylamino]propyl (*AP-Triamine*), ureidopropyl (*AP-Ureido*), glycidoxypropyl (*AP-Glycidoxy*), and mercaptopropyl (*AP-Mercapto*) were prepared from *AP-Hydroxyl*. The synthesis details of each type are given below.

The synthesis was carried out in a 100 ml Mettler Toledo EasyMax™ synthesis work station controlled with the software iControl™ 5.2. Reactor temperature, stirring speed, dosing rate of chemicals, and heating/cooling rate were controlled in the same manner for all syntheses.

Bare Silica (AP-Hydroxyl)

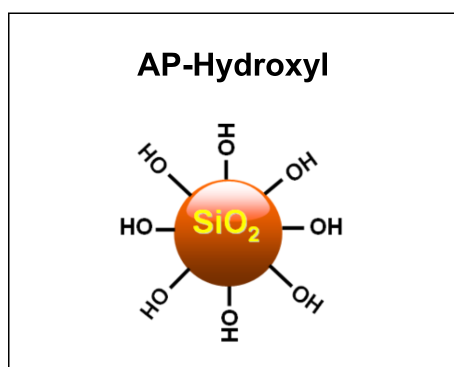

Table 4. **1** summarizes the reagents for the synthesis of *AP-Hydroxyl* with the size of 18 nm (obtained from DLS). The procedure for the synthesis is described below.

2.3 ml of 25 % ammonium hydroxide, 0.2 ml of deionized water, and 89 ml of absolute ethanol were added into a 100 ml EasyMax glass reactor. The mixture was stirred at 300 rpm at a reactor temperature (Tr) of 20 °C for 5 minutes. 8.9 ml of TEOS was added into the vessel and the mixture was stirred for 17 h. *AP-Hydroxyl* nanoparticles of around 18 nm in size were obtained and 100 % of product yield was assumed. A 2 ml aliquot of the sample was taken to determine the particle size distribution using Dynamic Light Scattering (DLS).

Table 4. 1 List of reagents and amounts were used for 100 mL scale synthesis of AP-Hydroxyl in ethanol

Chemicals	Concentration [mol/L]	Amount in 100 mL [mL]
Ammonium hydroxide, 25% aq. solution (12.8 M NH_3)	0.3 (NH_3)	2.3
Deionized water	0.1	0.2
Absolute ethanol	15.4	89.0
Tetraethoxyorthosilicate (TEOS)	0.4	8.9

Aminopropyl functionalized silica nanoparticles (AP-Monoamine)

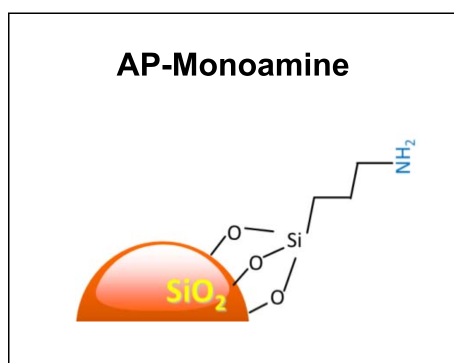

AP-Monoamine M

5.72 mL of acetic acid was dosed into 100 mL of *AP-Hydroxyl* suspension with a constant flow rate of 3 ml/min, stirring speed of 300 rpm and a reactor temperature (Tr) of 20 °C. After 2 minutes of stirring, 8 mL of 3-APTES was added slowly into the reactor with a flow rate of 3 mL/min. After stirring for 1 h, the reactor temperature was raised slowly from 20 °C to 75 °C at a ramping speed of 5 °C/min. The solution was refluxed for 3 h and was allowed to cool to room temperature. *AP-Monoamine* nanoparticles

of 52 nm diameter were obtained by this method. A list of reagents and volumes used in the synthesis are summarized in Table 4. 2.

Table 4. 2 List of reagents and amounts used for the synthesis of AP-Monoamine M

Chemicals	Concentration [mol/L]	Amount in 100 mL [mL]
AP-Hydroxyl	-	100
Acetic acid	1	5.7
3-Aminopropyltriethoxysilane (APTES)	0.34	8.0

AP-Monoamine S

To obtain *AP-Monoamine S*, *AP-Hydroxyl* was modified with APTES in the same manners as *AP-Monoamine M*. However, in the synthesis of *AP-Hydroxyl*, the amount of ammonium hydroxide in 100 mL synthesis was 1.9 mL (0.25 mol/L of NH_3) instead of 2.3 mL (0.3 mol of NH_3).

AP-Monoamine L

To obtain *AP-Monoamine L*, *AP-Hydroxyl* was modified with APTES in the same manner as *AP-Monoamine M*. However, in the synthesis of *AP-Hydroxyl*, the amount of ethanol was 45 mL (7.5 mol/L) instead of 89 mL (15.4 mol/L). Before the addition of acetic acid, an additional amount of 45 mL (7.5 mol/L) of absolute ethanol was added into the reaction mixture.

N-(2-Aminoethyl)-3-Aminopropyl functionalized silica nanoparticles (AP-Diamine)

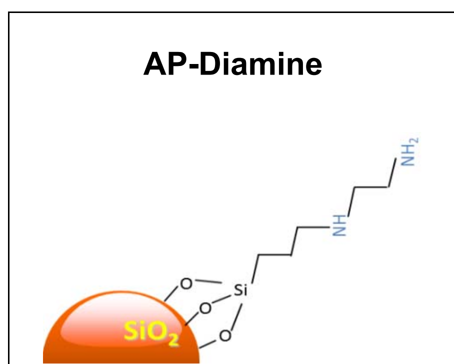

To obtain *AP-Diamine*, AP-Hydroxyl was modified in the same manners as *AP-Monoamine M*. However, DPTES was added instead of APTES. The molar amount was the same.

3-[2-(2-Aminoethylamino)ethylamino]propyl functionalized silica nanoparticles (AP-Triamine)

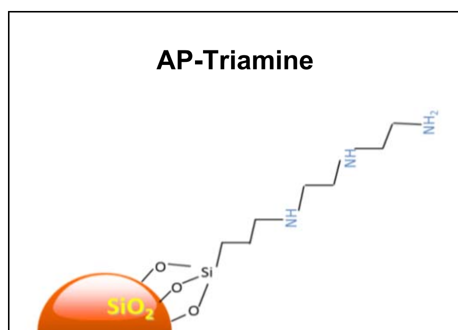

To obtain *AP-Triamine*, AP-Hydroxyl was modified in the same manner as *AP-Monoamine M*. However, TPTMS was added instead of APTES. The molar amount was the same.

Ureidopropyl functionalized silica nanoparticles (AP-Ureido)

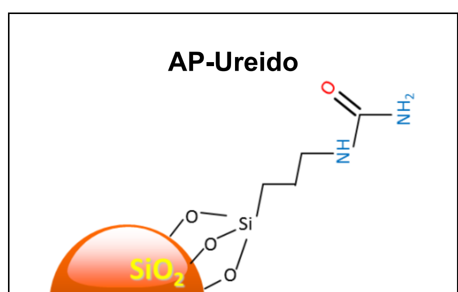

To obtain *AP-Ureido*, AP-Hydroxyl was modified in the same manner as *AP-Monoamine 50 M*. However, the UPMS was added instead of APTES. The molar amount was the same.

Glycidoxypropyl functionalized silica nanoparticles (AP-Glycidoxy)

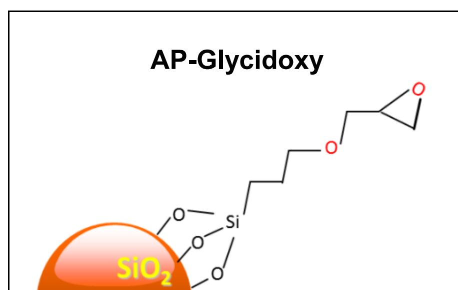

To obtain *AP-Glycidoxy*, AP-Hydroxyl was modified in the same manners as *AP-Monoamine M*. However, the 3-GLYMO was added instead of APTES. The molar amount was the same.

Mercaptopropyl functionalized silica nanoparticles (AP-Mercapto)

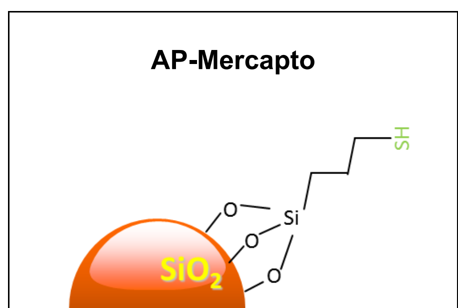

8 mL of 3-MPTES (0.34 mol/L) was added into 100 mL of a dispersion of *AP-Hydroxyl* with a flow rate of 3 mL/min, a stirring speed of 300 rpm, and at a reactor temperature (Tr) of 20 °C. After stirring for 1 h, the reactor temperature was raised slowly from 20 °C to 75 °C at a ramping speed of 5 °C/min. The solution was refluxed for 3 h and was allowed to cool to room temperature. 5.7 mL of acetic acid (1 mol/L) was added into the dispersion to increase the stability of suspension.

4.2.3. Purification of the functionalized silica sols by dialysis

20 mL of the functionalized silica sol was placed into a dialysis membrane tube. The sample was purified overnight in one liter of absolute ethanol (dialysate) at room temperature. The dialysate was replaced with fresh absolute ethanol, and purification was allowed to continue for another 3 h. The purified samples were carefully removed from the tube by using a Pasteur pipette.

4.2.4. Characterization

Dynamic Light Scattering (DLS)

The size distribution of particles is obtained by dynamic light scattering (DLS) using a Malvern Zetasizer nano zs with the software DTS v6.2. The instrument was equipped with a He-Ne laser (λ = 633 nm) and a back scattering detector at a fixed angle of 173 °. The laser power is automatically adjusted to an acceptable range of scattered light intensity. The average particle size (Z-average) is expressed as the intensity weighted harmonic mean size, derived from a cumulant analysis of the measured correlation curve (see Chapter 3).

Sample preparation:

The obtained nanoparticle samples were diluted to 2 g/L. The diluted sample was filtered through nylon membrane filters with a pore size of 0.45 µm. Disposable polystyrene cuvettes were used for all DLS measurements. The temperature of measurement chamber was kept at 20 °C, and the sample was allowed to stand in the compartment for the sample temperature to equilibrate, before the measurement was started. Further information regarding the measurement parameters and physical properties of materials can be found in Table 4. 3.

Table 4. 3 Measurement parameters for dynamic light scattering (DLS)

Conditions	
Laser Wavelength (nm)	633
Light Detection Angle (°)	173
Refractive Index of SiO_2	1.54 (Ghosh et al., 1999)[104]
Suspension absorption at 633 nm	0
Dispersant	Absolute ethanol
Dispersant Viscosity (cP)	1.1
Dispersant Refractive Index	1.36
Measurement Temperature (°C)	20
Number of Runs	10
Duration Time of Measurement (s)	20
Number of Measurements	5
Equilibration Time (s)	120

Atomic Force Microscopy (AFM)

Tapping mode AFM was performed using a Digital Instruments Nanoscope III microscope equipped with a Nanoscope III controller. All AFM measurements were made in ambient environment using Nanoscope cantilever with single crystal silicon tips (Nanosensors™). The properties of the cantilever is shown in Table 4. **4**.

Table 4. 4 The properties of cantilever with single crystal silicon tips used in AFM measurement

Property	Nominal Value	Specified Range
Thickness /μm	4	3.0 - 5.0
Mean Width /μm	30	22.5 - 37.5
Length /μm	125	115 - 135
Force Constant /(N/m)	42	10 - 130
Resonance Frequency /kHz	330	204 - 497

Sample preparation:

Polyimide Kapton®HN films were washed thoroughly with isopropanol to clean the surface and dried by purging with nitrogen gas purge. Diluted samples of nanoparticles (2 g/L) were deposited onto clean polyimide films by dip coating with a withdrawing speed of 180 mm/min. The films were annealed in an oven at 130 °C for 10 minutes to remove the remaining solvent.

Image processing:

From the obtained AFM images, we can determine the particle size distribution of silica nanoparticle with different particle sizes. To do this, an image processing software (Image J) was implemented to analyze the images. The comparison image before and after image processing with image J is shown in Figure 4.2. Particle size distribution was obtained by measuring 40 individual particles. The mean diameter of particle with the standard deviation is calculated.

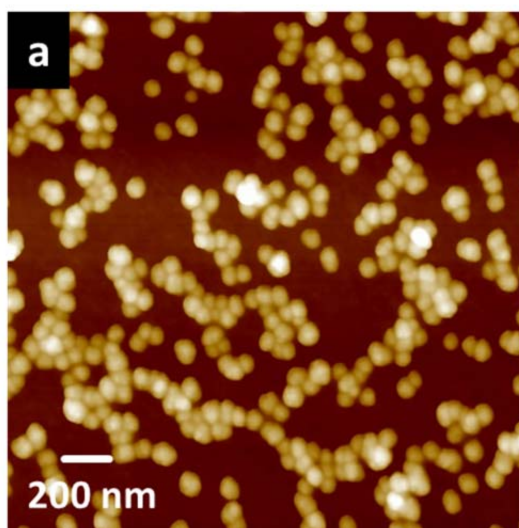

Figure 4.2 Image of silica nanoparticle obtained by AFM

Transmission Electron Microscope (TEM)

The obtained silica nanoparticles were also investigated under transmission electron microscope (TEM). The average diameter of the nanoparticles was analyzed. The TEM images were obtained using an EM 902A TEM from Philips. An acceleration voltage of 80 kV was applied.

Sample preparation:

The dispersions of particle were diluted up to 1 g/L in absolute ethanol. One drop (30 µL) of this dispersion solution was dropped on top of 300 mesh gold grid (Ted Pella Co.). This grid was coated with a ultrathin amorphous carbon film (~3 nm) on holey amorphous carbon film.

Image processing:

From the obtained TEM images, we can determine the particle size distribution of silica nanoparticles with different diameters. To do this, an image processing software (Image J) was implemented to analyze the images. Particle size distribution was obtained by measuring 100 individual particles. The mean diameter of particle and standard deviation were calculated.

Zeta Potential

The zeta potential of silica nanoparticles was measured with a Malvern Zetasizer nano zs with the software DTS v6.2. Measurements were made at different pH ranging from pH3 to pH12.

Sample preparation:

The samples were diluted to a concentration of 4 g/L with deionized water. The pH was first adjusted to pH3 with 0.1 M HCl. After every measurement, the pH was adjusted slowly up to the desired pH with 0.1 M NaOH

Fourier Transform Infra-Red-Attenuated Total Reflectance (FTIR-ATR)

The functional groups on silica nanoparticles after modification was determined qualitatively by FTIR-ATR spectroscopy using a Perkin Elmer Spectrum^{TM} 100 FTIR spectrometer equipped with a DTGS detector and a single reflection ATR unit with ZnSe-ATR element. The dried powder samples were introduced on the ATR crystal surface and measured between 4000-600 cm^{-1} with a resolution of 4 cm^{-1}. Each sample was scanned 32 times in air.

Elemental analysis (EA)

CHNS elemental analysis was used for the determination of the mass of carbon, hydrogen, nitrogen, and sulfur in the samples. The measurements of the elements were performed with an elemental analyzer “Vario EL Cube” (Elementar). The measurement device is equipped with two detectors, a wavelength detector for the determination of C, H, and N, and an infrared detector for the determination of S. Sulfanilic acid from Merck was used as the standard to check the performance of the device. The measurement uncertainty (MU) was calculated for each elements on basis of the sulfanilic acid measurements (Table 4. 5).

Table 4. 5 The MU of different elements on basis of sulfanilic acid measurements

Element	MU [%]
N	1.23
S	3.01
H	9.38
C	1.78

Functionalized silica nanoparticles were dried and weighed in tin foil. Around 2-5 mg of the dried sample was used. Each sample was measured at least twice. The combustion was performed with oxygen at a temperature at 1150 °C in a combustion tube for 90 s. For the evaluation of the data the EAS software from Elementar was used.

Ultraviolet/Visible Spectroscopy (UV-Vis)

UV/Visible spectra were obtained from Perkin Elmer Lambda 25 with the software Perkin Elmer UV WinLab. Silica nanoparticle samples with three different surface coating (*AP-Monoamine*, *AP-Diamine,* and *AP-Triamine*) were treated with salicylaldehyde after the purification step. Salicylaldehyde reacts with primary amine on silica nanoparticles, and allows for the quantification of the amount of primary amines on silica nanoparticles.[86]

Diluted dispersions of these nanoparticles were treated with excess salicylaldehyde to ensure that all the amines reacted. The concentration of the nanoparticles is 80 mg/L and the concentration of salicylaldehyde is 10 mM. After the reaction, the color of the dispersions turned bright yellow and showed strong absorption in the region of the visible light, with a maximum absorbance at around 404 nm.

A calibration curve was obtained by measuring the absorbance intensity of 3-APTES after reaction with salicylaldehyde (10 mM) as a function of concentration at 404 nm. *AP-Hydroxyl* was also measured as a reference. Using the calibration curve, the measured diameter of the particles (TEM), the density of silica (ρ = 2.2 g/cm^3), and the mass concentration of the particles in dispersion (g/L), the density of amine groups on the surface of silica in numbers of NH_2/nm^2 was determined.

4.3. Experimental results and discussions

4.3.1. Aminopropyl functionalized silica nanoparticles (*AP-Monoamine*)

The aminopropyl functionalized silica nanoparticles prepared in an one pot reaction process show a narrow particle size distribution (see below). The dispersions remained stable for over half year of storage at room temperature. No precipitation was observed. Aminopropyl functionalized silica nanoparticles in three different sizes were synthesized. The obtained particle diameters measured by DLS, TEM and AFM are shown in Table 4. 6. The diameter of the particle measured by AFM is only shown for the particles after functionalization with APTES. The TEM and AFM images of *AP-Monoamine* are shown in Figure 4. 3. The diameter of the particle in TEM and AFM is averaged value of at least 100 individual particles. Agglomerates are neglected. Please refer to the Appendix 3 for TEM images. As expected, the obtained Z-average in DLS shows larger particle diameter than the mean diameter in TEM and AFM. Unlike the microscopy method, dynamic light scattering measures the hydrodynamic diameter.[105] The translational diffusion coefficient depends not only on the size of particle's core but also on the surface structure (attached APTES molecules). Furthermore, the presence of aggregates or coalesced particles can be one of the reasons for larger diameter measured in DLS. The particle diameter in AFM is for all *AP-Monoamine* larger than the particle diameter in TEM. This discrepancy can be result from various reasons: 1.The particle change to smaller size because of the bombardment of highly energetic electrons during the measurement[106] (80kV), 2. The radius and geometry of the tip of AFM does affect the overall representation of the surface feature.[107]

Table 4. 6 Particle sizes of aminopropyl functionalized silica nanoparticles (*AP-Monoamine*) measured by DLS, TEM and AFM

Name	Bare silica		APTES functionalized silica		
	Z-average DLS [nm]	Diameter TEM [nm]	Z-average DLS [nm]	Diameter TEM [nm]	Diameter AFM [nm]
AP-Monoamine S	16 ± 2	11 ± 2	38 ± 1	14 ± 3	21 ± 4
AP-Monoamine M	18 ± 2	13 ± 2	52 ± 1	18 ± 3	26 ± 3
AP-Monoamine L	52 ± 2	37 ± 7	92 ± 2	44 ± 6	68 ± 7

*The diameter of the particle in TEM and AFM is averaged value of at least 100 individual particles

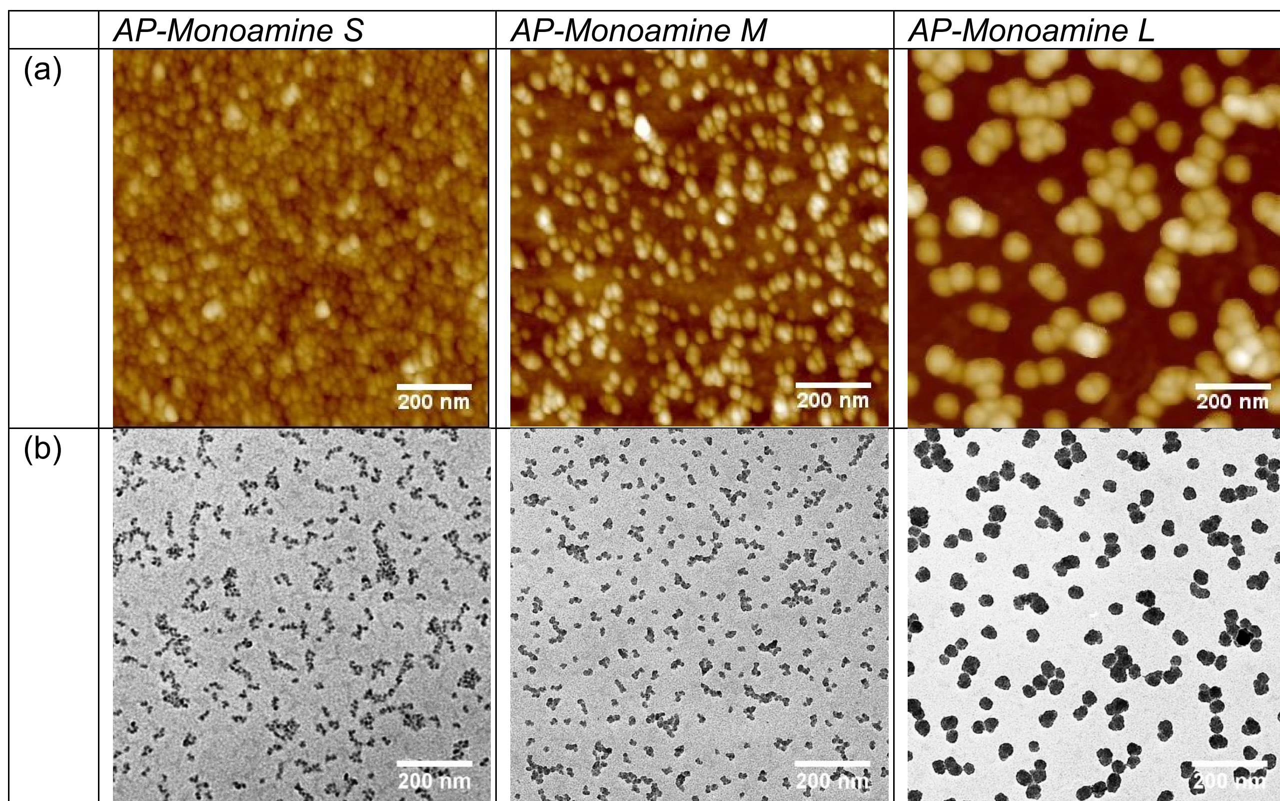

Figure 4. 3 AFM images (a) and TEM images (b) of *AP-Monoamine S, M*, and *L* after functionalization with 3-APTES

As shown in the DLS measurements result in Table 4. 6, the size of the silica colloids increases after the modification step with APTES, from 16±2 nm to 38±1 nm for *AP-Monoamine S*, from 18±2 nm to 52±1 nm for *AP-Monoamine M* and from 52±2 nm to 92±2 nm for *AP-Monoamine L*. For comparison, the TEM measured an increase of particle size from 11±2 nm to 14±3 nm for *AP-Monoamine S,* from 13±2 nm to 18±3 nm for *AP-Monoamine M,* and from 37±7 nm to 44±6 nm for *AP-Monoamine L*. The enormous increase in particle size measured by DLS after modification with APTES is because of the coagulation of silica particles when the pH of suspension changed to pH4. The bare silica particles are least stable under acidic conditions, leading to rapid gelling in solution.[103] Bare silica reaches it minimum stability when the pH is within 4-7. However, as mentioned in a previous work by Choi *et al.*,[108] the silanol groups of APTES in aqueous solution are relatively stable under acidic conditions. The APTES in the pH range of 3-6 exists as zwitterions ($^{-}O(HO)_2Si-CH_2CH_2CH_2NH_3^{+}$).[109] The formation of zwitterions prevents the continuous hydrolysis and self-condensation of APTES. Hence, silica nanoparticles with high APTES coverage on the surface were obtained.

Another possible explanation to the increase of particle size after the modification step is the reaction time. As described by Waddell *et al.*,[86] for long reaction time, multilayered condensation aggregates of APTES are formed around bare silica colloids. Moreover, as demonstrated in the literature,[110] refluxing the suspension resulted in irregular APTES deposition, polymerization, and covalent bonding to the bare silica surface. This can be observed from the increase in particle size measured by TEM after modification of bare silica with APTES. In additional, poly-condensation bridges between particles might form because of interactions between surface amino groups with neighboring silanol groups.

Based on above result, the thickness of the layer of APTES at silica surface can be calculated. It is ~3 nm, ~5 nm, and ~7 nm for *AP-Monoamine S*, *AP-Monoamine M*, and *AP-Monoamine L* respectively. This increase in particle size shows that more than a monolayer of APTES attached on the surface of silica (the length of one APTES molecule is ~1 nm). This computation is including the strongly and loosely attached APTES on the surface of silica. As the surface area for larger particles is lower, the interaction side for condensation between APTES and silica –OH groups is also lower. APTES in the solution condensates on top of ready attached APTES on silica surface. The layer of APTES will continue to growth until all APTES molecules are consumed. The thickness of the layer of APTES increases with an increasing average diameter of nanoparticles.

The change in zeta potential of bare (*AP-Hydroxyl*) and aminopropyl (*AP-Monoamine M*) silica nanoparticles with pH are shown in Figure 4. 4. The surface charge of *AP-Hydroxyl* becomes more negative with increasing pH due to the dissociation of protons from the silanol groups.[111] The zeta potential of the *AP-Monoamine* nanoparticles with different diameters shows a similar behavior. The surface charge of *AP-Monoamine M* is positive when the pH is lower than 10.5 (Isoelectric point) due to protonation of amine groups on the surface ($–NH_3^+$). This value is adjacent to the pKa of primary amine (pKa10.6).[112] This value is higher than that found in previous work by Pálmai *et al.*,[113] (pH 6.2), for a monolayer APTES on bare silica surface. The difference between our measured value of isoelectric point and the one from the literature can be explained by the difference in the number of amino groups near the surface of silica particles. Considering the large amount of APTES (excess amount) added for surface modification in our case, a considerable

degree of poly-condensation of aminopropyl silane near the silica surface can be expected. Thus, likely no silanol group (-OH) from the bare silica particle are present on the surface. In the case of the work of Pálmai *et al.*,[113] incomplete surface modification of bare silica nanoparticles was assumed. Some of the silanol (-OH) groups from bare silica nanoparticles may still be present. Hence, the isoelectric point (IEP) for such particles is the combination of two oppositely charged functional group.

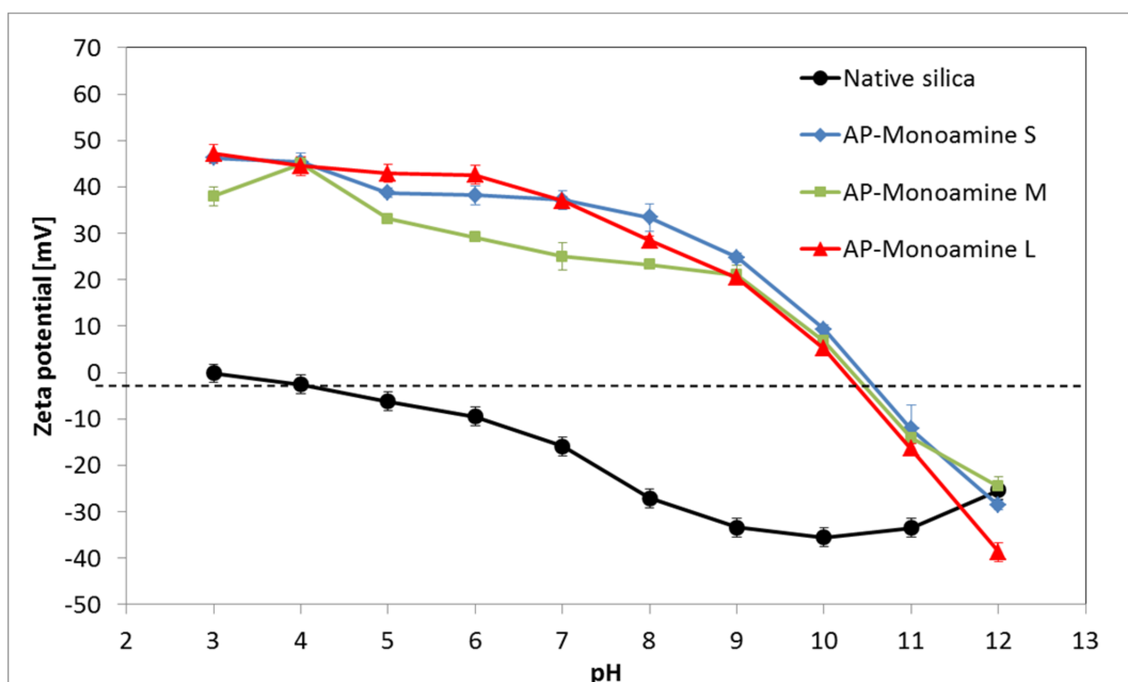

Figure 4. 4 The change of zeta potential of bare and aminopropyl silica nanoparticles with pH. The pH was set to pH3 with 0.1 M HCl and was slowly increased to higher pH with 0.1 M NaOH

As shown in the FTIR-ATR spectra (Figure 4. 5), *AP-Hydroxyl* exhibits a strong absorption band of Si-O asymmetric vibration (1080 cm^{-1}), Si-OH asymmetric vibration (973 cm^{-1}), Si-O symmetric vibration (815 cm^{-1}), and broad absorption band around 3500 cm^{-1} that corresponds to O-H stretching, in agreement with a previously published measurement.[1] It was also shown that the *AP-Hydroxyl* surface contained some ethoxy groups from incomplete hydrolysis reaction of the starting material. A further evidence for the incomplete hydrolysis of ethoxysilane is provided by the appearance of C-H stretching (3000-2850 cm^{-1}) and bending vibrational bands (1450-1350 cm^{-1}). Costa *et al.*[4] have reported the presence of ethoxy groups on a silica surface obtained by the Stöber method when a low concentration of the base catalyst (NH_3) was used.

For *AP-Monoamine M*, the presence of APTES on the surface of silica is confirmed by additional weak broad bands: NH_2 asymmetric stretch vibration (3386 cm^{-1}), NH_2 symmetric stretch vibration (3291 cm^{-1}), and the strong band of the NH_2 deformation mode (1541 cm^{-1}) of free amino groups.[3] Moreover, a strong vibration peak at 1410 cm^{-1} corresponding to the bending mode of methylene bonded to Si in 3-APTES (Si-CH_2),[8] and the C-H bending of ethoxy group from APTES at 1370 cm^{-1} were observed.

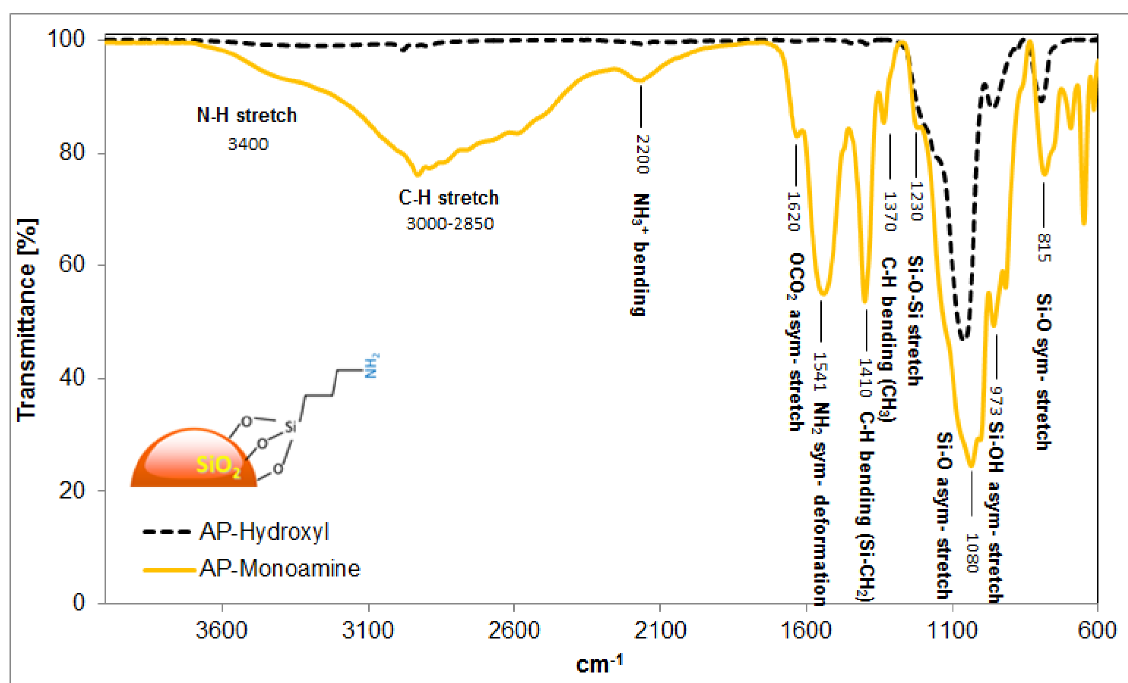

Figure 4. 5 FTIR-ATR spectra of bare (*AP-Hydroxyl*) and aminopropyl functionalized (*AP-Monoamine*) silica nanoparticle. The spectra were taken with resolution of 4 cm^{-1}

As reported previously by Culler *et al.*,[6] the vibrational modes at 2200 and 1620 cm^{-1} would arise when the silica surface amino groups interact with the atmosphere CO_2 to form ammonium bicarbonate (Figure 4. 6). In this work, the dried powder samples were introduced on the ATR crystal surface. The vibrational mode at 2200 cm^{-1} corresponds to the bending mode of NH_3^+, and the peak at 1620 cm^{-1} corresponds to the asymmetric stretching mode of OCO_2 from CO_2 interaction with APTES. Moreover, the existence of ammonium bicarbonate on the surface generates broad underlying background from 3500 to 2000 cm^{-1}. The formation of a covalent bond between 3-APTES and Si-OH of the silica surface can be confirmed by the change of intensity of the shoulder band at around 1230 cm^{-1} (Si-O-Si stretch).[9] Characteristic bands of *AP-Hydroxyl* and *AP-Monoamine* are compared with the

literature and are summarized in Table 4. 7. The FTIR-ATR spectra for different sizes of *AP-Monoamine* were identical to the one shown in Figure 4. 5. Therefore, these spectra are not discussed in more detail.

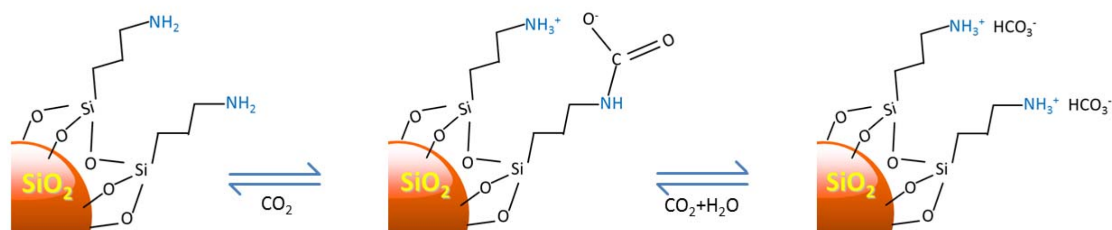

Figure 4. 6 The IR spectrum of amino-terminated silica particles may contain NH_3^+ and HCO_3^-. The reaction between surface amino groups atmosphere carbon dioxide can explain the reason for this observation. (Adapted from Ref.[114])

Table 4. 7 Characteristic bands of bare and aminopropyl silica (*AP-Monoamine*), obtained by FTIR-ATR

Assignment	Absorption Band [cm^{-1}]			
	Literature		This work	
	Bare	Aminopropyl	Bare	Aminopropyl
O-H stretch	3500[1]	-	3550	3500
N-H asy- stretch	-	3386[2-3]	-	3400
N-H sy- stretch	-	3290[2-3]	-	3291
C-H stretch	3000-2800[4]	3000-2800[4]	3000-2850	3000-2850
NH_3^+ bending	-	2260[6]	-	2200
OCO_2 asym- stretch	-	1630[6]	-	1620
NH_2 sy- deformation	-	1575[2-3]	-	1541
C-H bending (Si-CH_2)	-	1400[8]	-	1410
C-H bending	1450-1350[4]	1370[4]	1450-1350	1370
Si-O-Si stretch	1250[9]	1250[9]	1230	1230
Si-O asym- stretch	1050[1]	1050[1]	1080	1080
Si-OH asym- stretch	970[1]	970[1]	973	973
Si-O sym- stretch	810[1]	810[1]	815	815

UV-Vis spectroscopy in combination with chemical derivatization method was used to quantify the amount of free amine groups on the surface of silica. Salicylaldehyde reacts with primary amine on silica nanoparticles, and allows for the quantification of the amount of primary amines on silica nanoparticles.[86] The UV-Vis

spectra of bare and aminopropyl-functionalized silica nanoparticles of different sizes after reaction with salicylaldehyde are shown in Figure 4. 7.

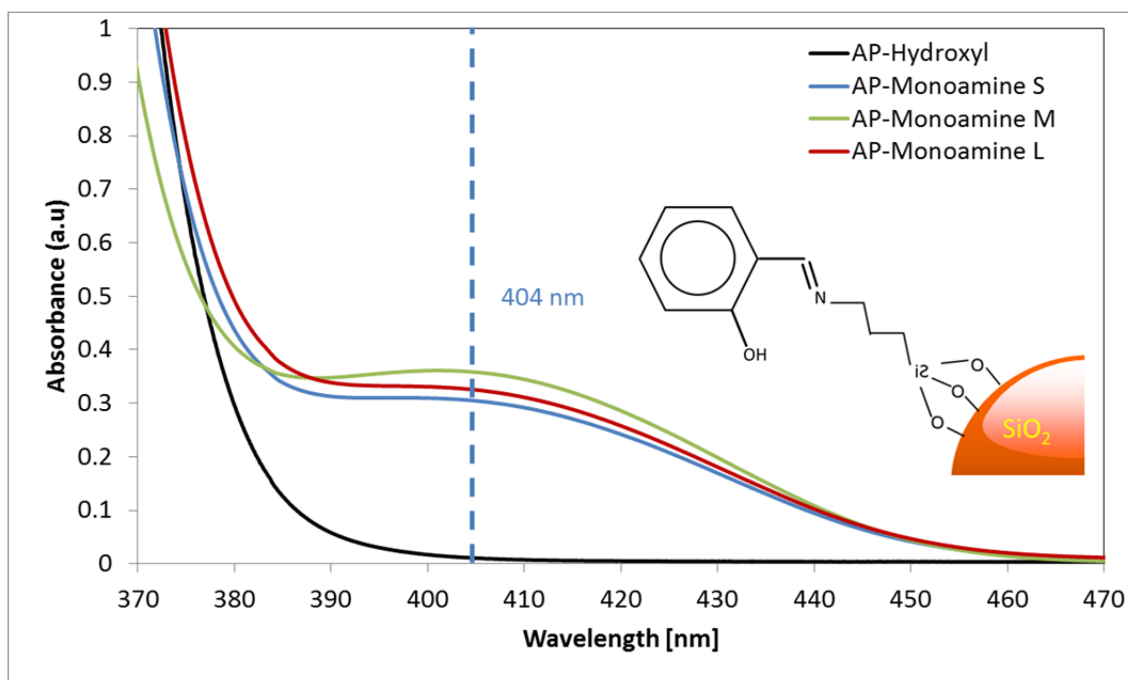

Figure 4. 7 UV-Vis spectra of bare and aminopropyl functionalized silica nanoparticles after chemical derivatization with salicylaldehyde. Bright yellow color was observed after reaction and the sample showed a strong absorption band around 404 nm

The density of amine groups on the surface of silica was determined from the UV-Vis measurement, using the absorbance-concentration (calibration curve), measured particles size (TEM), and the density of silica (ρ = 2.2 g/cm^3)[88]. The numbers of amine groups on the surface of silica were determined for different particle sizes: 12±2 $-NH_2$ groups/nm^2 for *AP-Monoamine S*, 16±1 $-NH_2$ groups/nm^2 for *AP-Monoamine M* and 39±2 $-NH_2$ groups/nm^2 for *AP-Monoamine L*. Refer to the Appendix 1 for the detail of calculation. These value are higher than obtained in previous investigation.[115],[116],[117],[118] Moreover, if one assumes that the surface density of –OH groups on the silica surface lies within the range of 4.2 – 5.7 –OH groups/nm^2,[119] and that one molecules of APTES reacts with one –OH group, a monolayer coverage by APTES of silica surface would result in 2-3 of $-NH_2$ groups/nm^2 (the length of triethoxysilicon is 0.8 nm). Our measurements yield a higher value for the number of $-NH_2$/nm^2, indicating the possibility of multilayer formation or a high degree of APTES condensation. A similar result was also

obtained by Chen and coworkers,[108] when an identical synthetic route as in this thesis was used to functionalize the silica nanoparticle surface with excess APTES.

The results of the DLS, zeta potential, FTIR-ATR, and UV-Vis measurements of the samples give clear indications of the presence of an APTES coating on the surface of the silica nanoparticles. From the UV-Vis measurements, it was deduced that APTES underwent multiple condensation reactions that led to a surface density that is higher than what is expected from a monolayer of aminopropylsilane covering the silica surface. An excess amount of APTES was used to synthesize the nanoparticles, and it is assumed that the excess APTES continued to extend the siloxane network, via the hydroxyl groups in APTES, until the reaction was quenched.

4.3.2. *AP-Diamine* and *AP-Triamine* functionalized silica

The particle size distributions of *AP-Diamine* and *AP-Triamine* obtained from DLS and TEM are shown in Table 4. 8. The TEM measurement shows that the *AP-Diamine* (19 ± 3 nm) and *AP-Triamine* (17 ± 3 nm) have a similar particle diameter as *AP-Monoamine M* (18 ± 3 nm). *AP-Hydroxyl* with a particle size of 13 ± 2 nm was used as the core for all syntheses. In the DLS measurements, the *AP Diamine* (53 ± 1 nm) showed a similar Z-average particle size with the *AP-Monoamine M* (52 ± 1 nm), while a smaller Z-average was obtained for *AP-Triamine* (37 ± 1 nm). The difference in particle size distributions (measured by DLS) of *AP-Monoamine M*, *AP-Diamine*, and *AP-Triamine* most likely originated from several reasons as discussed below.

Table 4. 8 Particle sizes of *AP-Monoamine, AP-Diamine and AP-Triamine* measured by TEM and DLS

Name	Bare silica			Functionalized silica		
	Z-average DLS [nm]	PDI	Diameter TEM [nm]	Z-average DLS [nm]	PDI	Diameter TEM [nm]
AP-Monoamine M	18 ± 2	0.16	13 ± 2	52 ± 1	0.13	18 ± 3
AP-Diamine				53 ± 1	0.16	19 ± 3
AP-Triamine				37 ± 1	0.09	17 ± 3

*The diameter of the particle in TEM is averaged value of at least 100 individual particles

The hydrolysis and self-condensation reaction of aminoalkoxysilane are catalyzed by the basic character of the silane.[120] Thus, the hydrolysis and self-

condensation of aminoalkoxysilanes with more than one amine group, DPTES and TPTMS are greatly enhanced relative to that of APTES. The high reactivity toward hydrolysis and self-condensation reactions generates a high proportion of three dimensional networks of polysiloxanes. These three dimensional networks tended to precipitate as colloidal gel-like particles, and thus become unavailable for adsorption. Because of this reason, the maximum coverage of the TPTMS precursor is significantly lower than the APTES and DPTES precursors.[121] As a result, the particle size measured by DLS of *AP-Triamine* is smaller than *AP-Diamine* and *AP-Monoamine M* because a thinner layer of TPTMS is formed on the surface.

Another possible explanation is steric hindrance because of the size of the aminoalkoxysilane precursor. This significantly reduces the diffusivity of the molecules onto the surface of silica nanoparticle. Thus, the silanol groups of the TPTMS precursors are hindered from interacting and covalently bonding to the hydroxyl group of the surface. The surface coverage is lower than in the case of APTES and DPTES precursors. As a result, the particle size of *AP-Triamine* is smaller than that of *AP-Monoamine M* and *AP-Diamine*.

The change in zeta potential of *AP-Diamine* and *AP-Triamine* with pH is shown in Figure 4. 8. In comparison to *AP-Monoamine M*, a nearly identical behavior of the zeta potential was observed. The surface charge of *AP-Diamine* and *AP-Triamine* silica is positive when the pH is lower than 10.5 (isoelectric point) due to protonation of amine groups on the surface ($–NH_2$ to $–NH_3^+$ and –NH– to $–NH_2^+–$). This result is in good agreement with previous work by Chan *et al*.[122] A similar maximum at pH 3 and isoelectric point at pH 10.5 might indicate that an identical amount of accessible amino groups ($–NH_2$ and –NH–) are present on the surface of the silica nanoparticles in case of *AP-Monoamine M*, *AP-Diamine,* and *AP-Triamine*. Since additional protonated secondary amino groups ($–NH_2^+–$) of DPTES and TPTMS should also contribute to the positive charge on the silica nanoparticle surface, and a similar maximum zeta potential for *AP-Monoamine M*, *AP-Diamine,* and *AP-Triamine* , lower coverage of DPTES and TPTMS than APTES would be expected.

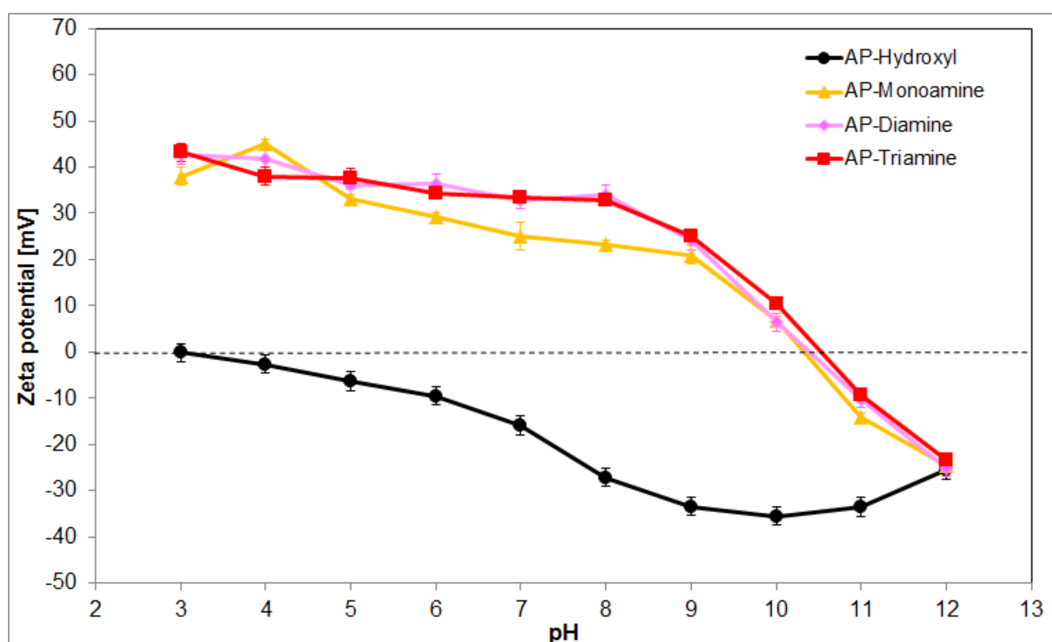

Figure 4. 8 The change in zeta potential of bare and aminopropyl-functionalized (*AP-Monoamine M, AP-Diamine and AP-Triamine*) silica nanoparticles with pH. The pH was set to pH 3 with 0.1 M HCl and slowly increased to higher pH with 0.1 M NaOH

As shown in Figure 4. 9, the resolved FTIR-ATR spectra for *AP-Diamine* and *AP-Triamine* were comparable to that of *AP-Monoamine M*. In contrast to the FTIR-ATR spectra of *AP-Monoamine M*, an N-H asymmetric stretching band around 3300 cm^{-1} was observed for *AP-Triamine*. This band was assigned to the secondary amine (–NH–) of the triamine, and this band was almost invisible in *AP-Diamine*, possibly because of the fewer number of secondary amines in the diamine molecule. Furthermore, the asymmetric stretch of the precursor silanol group Si-OH (973 cm^{-1}), of *AP-Diamine* and *AP-Triamine* is lower than the one of *AP-Monoamine M*. This may indicate a lower coverage of DPTES and TPTMS precursor than APTES on the surface of silica nanoparticles.

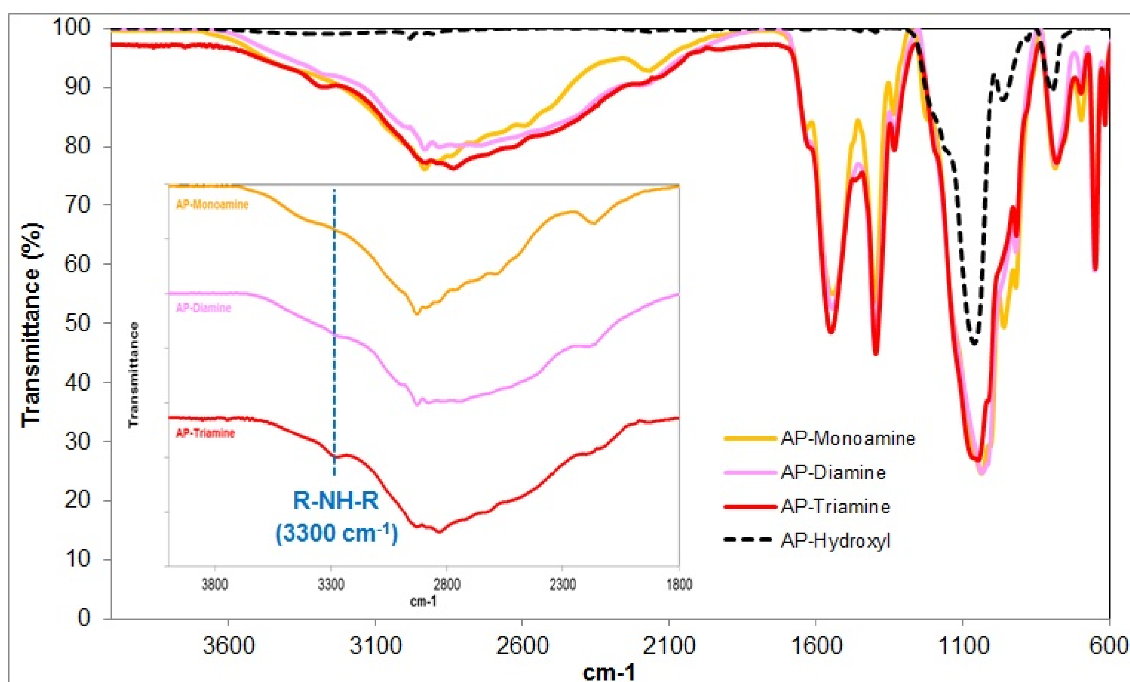

Figure 4. 9 FTIR-ATR spectra of *AP-Monoamine M, AP-Diamine, and AP-Triamine*. The spectra were taken with resolution of 4 cm^{-1}

In the same way as described for *AP-Monoamine M*, the amount of amino groups on the silica surface was measured (Figure 4. 10). The density of amino groups on the surface of silica was determined from the UV-Vis measurement in ethanol, using the relation between absorbance and concentration (calibration curve), the measured particle size (TEM) and the density of silica (ρ = 2.2 g/cm^3)[88]. The calculated number of amine groups is 6±1 $-NH_2$ groups/nm^2 for *AP-Diamine* and 5±1 $-NH_2$ groups/nm^2 for *AP-Triamine*. The amount of amine groups on the surface is lower than *AP-Monoamine M* (16±1 $-NH_2$ groups/nm^2). The lower density of amino groups could result from lesser adsorption of the precursors on the silica surface, especially TPTMS. This is because of the high reactivity towards hydrolysis and self-condensation, and also steric hindrance because of the size of the molecules.

Care must be taken when interpreting the UV-Vis results. As illustrated in Scheme 4. 3, aldehyde undergoes nucleophilic addition and dehydration reactions with primary amines to give substituted imines (bright yellow solution). On the other hand, nucleophilic addition and dehydration reactions of aldehyde with secondary amines results in the formation of examine (colorless solution), with absorption around 320 nm. Therefore, the absorption measured at 404 nm in UV-Vis should be independent from the concentration of secondary amines.

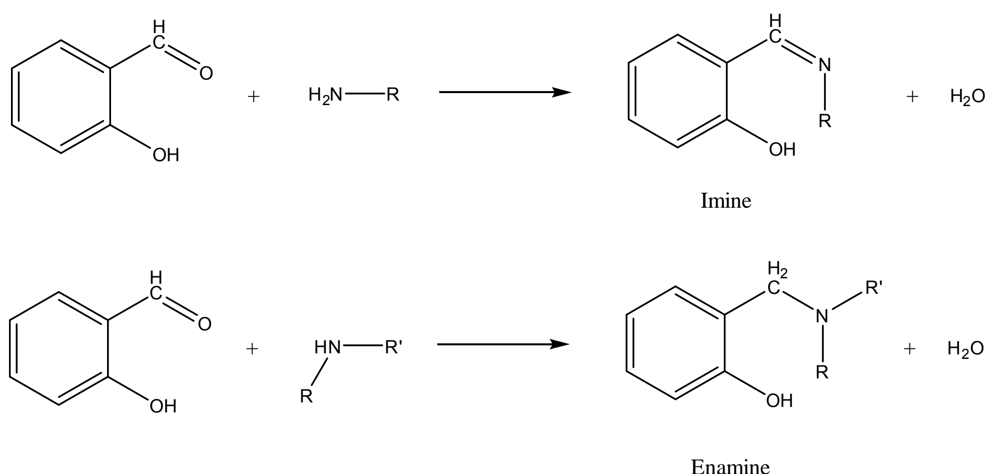

Scheme 4. 3 Reaction of aromatic aldehyde with primary amine to produce imine (bright yellow) and with secondary amine to produce enamine (colorless)

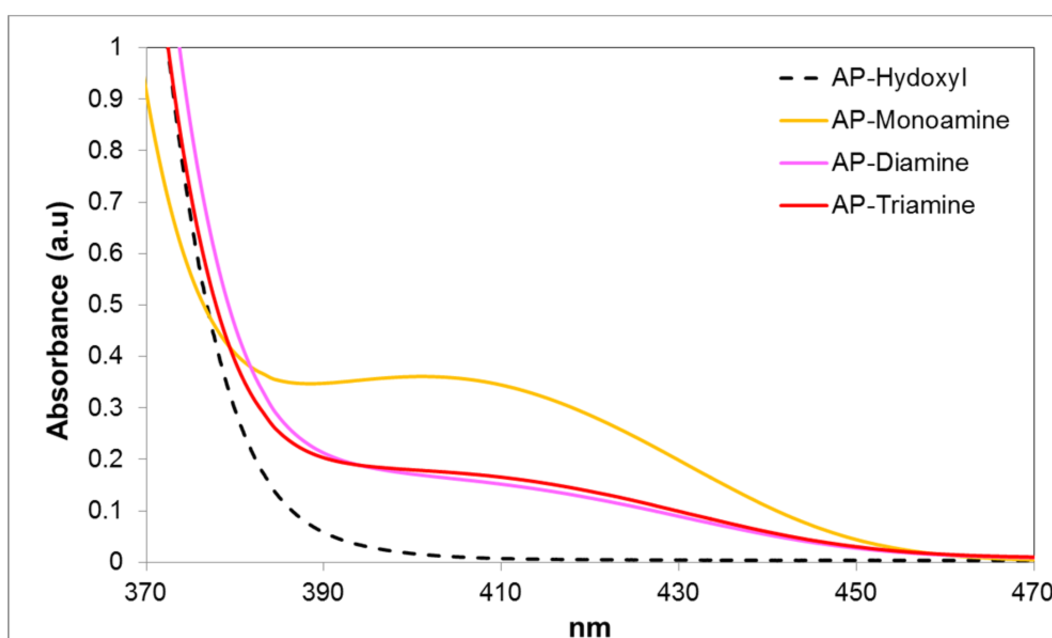

Figure 4. 10 UV-Vis spectra of *AP-Hydoxyl* (bare silica), *AP-Monoamine M, AP-Diamine* and *AP-Triamine* after chemical derivatization with salicylaldehyde. Bright yellow color results after the reaction and has a strong absorption at 404 nm

The elemental analysis measurements results for *AP-Monoamine M*, *AP-Diamine*, and *AP-Triamine* are shown in Table 4. 9. Using the measured mass percentage, measured particles size (TEM), and silica density (ρ = 2.2 g/cm^3)[88], the numbers of functional groups on the surface of silica were determined. The calculated number of primary amine group (NH_2) is 14 ± 2 –NH_2 molecules/nm^2 for *AP-Monoamine M*, 12 ± 2 –NH_2 molecules/nm^2 for *AP-Diamine*, and 10 ± 2 –NH_2 molecules/nm^2 for *AP-Triamine*. The amount of molecules showed here, already

divided by 2 for *AP-Diamine* and divided by 3 for *AP-Triamine*. Please refer to the Appendix 2 for details of the calculation. For *AP-Monoamine M*, the obtained number of amino groups is similar with the one that was measured with UV-Vis. In the case of *AP-Diamine* and *AP-Triamine*, the calculated amount of amine groups with elemental analysis is almost two times higher than the one obtained from UV-Vis. This is maybe because of structural irregularity features of the DPTES layer on the surface of the silica nanoparticles. The densely packed DPTES precursor inhibits the accessibility of salicylaldehyde into the surface. Hence, some of the DPTES are not accessible for the reaction with salicylaldehyde. Since elemental analysis has been done by combustion process, all compositions on the surface of silica are fully resolved.

Table 4. 9 Elemental analysis data of *AP-Monoamine M*, *AP-Diamine*, and *AP-Triamine*

	C [%]	H [%]	N [%]
AP-Hydroxyl	4.24	2.00	0.00
AP-Monoamine M	20.70	6.00	5.00
AP-Diamine	32.20	7.50	9.00
AP-Triamine	32.40	7.40	9.70

4.3.3. Silica nanoparticles modified with different functional groups

Table 4. 10 shows the particle size of silica nanoparticles modified with different groups measured with DLS and TEM. *AP-Hydroxyl* with the size of 13 ± 2 nm (TEM) was used as the core for all synthesis. The particle size of the aminopropyl silica nanoparticle (*AP-Monoamine M*) is included for comparison. According to the TEM measurement, all functionalized particles have similar average particle sizes. Average particle size of 17 ± 3 nm for *AP-Ureido*, 20 ± 3 nm for *AP-Glycidoxy* and 20 ± 3 for *AP-Mercapto* are found. According the DLS measurement, nanoparticles with a hydrodynamic diameter (Z-average) of 68 ± 1 nm (*AP-Ureido*), 55 ± 1 nm (*AP-Glycidoxy*), 38 ± 2 nm (*AP-Mercapto*) were obtained. The discrepancy between both measurement (DLS and TEM) is because of the presence of aggregates or coalesced particles discussed previously for *AP-Monoamine*.

Table 4. 10 Particle sizes of *AP-Monoamine M, AP-Ureido, AP-Glycidoxy and AP-Mercapto* measured by TEM and DLS

Name	Bare silica			Functionalized silica		
	Z-average DLS [nm]	PDI	Diameter TEM [nm]	Z-average DLS [nm]	PDI	Diameter TEM [nm]
AP-Monoamine M	18 ± 2	0.16	13 ± 2	52 ± 1	0.13	18 ± 3
AP-Ureido				68 ± 1	0.14	17 ± 3
AP-Glycidoxy				55 ± 1	0.15	20 ± 3
AP-Mercapto				38 ± 2	0.11	20 ± 3

Table 4. 11 shows the surface coverage of the mercaptopropyl on silica nanoparticle surface, determined by elemental analysis of sulfur. AP-Mercapto had a surface coverage of 2.18±0.1 mmol/1 g of silica particles, corresponding to only 50 % binding of the added MPTES (4.25 mmol/1 g of silica particles). Please refer to Appendix 2 for details of the calculation of the elemental analysis results. Unlike aminoalkoxysilane, 3-mercaptopropyltriethoxysilane has no capability of self-catalyzing.[123] Because of this reason, the rate of hydrolysis and condensation of 3-mercaptopropyltriethoxysilane at the surface of the silica nanoparticles is low. This suggests that there may be some MPTES precursors that were not adsorbed on the surface and formed particle clusters instead.

Table 4. 11 The elemental analysis data of silica nanoparticles modified with different functional groups

	C [%]	H [%]	N [%]	S [%]
AP-Ureido	22.95±1.00	5.40±0.22	11.11±0.85	0.00
AP-Glycidoxy	26.42±0.11	5.10±0.21	0.36±0	0.00
AP-Mercapto	15.40±0.15	2.90±0.20	0.00	7.00±0.31

The elemental analysis data in Table 4. 11 shows a surface coverage of 3.96±0.2 mmol/1 g of silica particles, corresponding to 93% binding of the added UPMS (4.25 mmol/1 g of silica particles). This is may be because of the strong interaction between ureido groups on the surface and also un-adsorbed precursor,

giving an addition to the inter-particle covalent bridges. Thus, the particles tend to aggregate. Consecutive aggregation of *AP-Ureido* leads to gel formation. Precipitation was observed after three days of storage at room temperature. This result has a good agreement with the measurement results of TEM and DLS.

In order to investigate the influence of different functional groups on the surface charge of silica at different pH values, zeta potential measurements were carried out. The change of the zeta potential of silica nanoparticles modified with different functional group as a function of pH is shown in Figure 4. 11. The zeta potentials of the bare (*AP-Hydroxyl*) and aminopropyl (*AP-Monoamine M*) silica nanoparticles are also shown for comparison.

The zeta potential of *AP-Ureido* is positive when the pH is lower than 6.5 (isoelectric point) and negative when the pH is higher than 6.5. Compared with amines, ureido groups are less basic because of the carbonyl group, and they form a negatively charged conjugated base on the silica surface for pH > 6.5 (which follows from our zeta potential measurements). The unexpected IEP, which is higher than the pKa of urea (0.18)[124] is maybe because of the presence of the protonated amino groups, wherein proton transfer occurs from the silanol groups to the amino groups, via the hydrogen bond between amine and hydroxyl moieties. Hence, the IEP was shifted to a higher pH. In the case of *AP-Glycidoxy*, the oxirane readily reacts with diverse compounds with the opening of the ring. The acid catalyzed hydrolysis reaction of the oxirane ring generated ethylene glycols.[125-126] Also the S_N2 nucleophilic addition reaction with ammonium hydroxide (from the *AP-Hydroxyl* preparation step) generated ethanolamine,[127] as shown by the presence of a small amount of nitrogen in the elemental analysis data, 0.26 mmol/g (Table 4. 11). The possible reaction scheme of ring opening of oxirane by acid catalyzed hydrolysis and ammonium hydroxide S_N2 nucleophilic addition reaction is shown in Scheme 4. 4. Therefore, positively charged *AP-Glycidoxy* was observed when the pH was lower than pH 8 (Isoelectric point), because of the protonation of the amino groups on the surface ($–NH_3^+$). A negative surface charge was observed for pH higher than 8 because of the deprotonation of the –OH groups of ethylene glycols to form $–O^-$. The IEP of *AP-Glycidoxy* was expected to be lower than the pKa of ethanolamine (pKa = 9.5). This is because two oppositely charged groups (ethylene glycol and ethanolamine) were present on the surface.

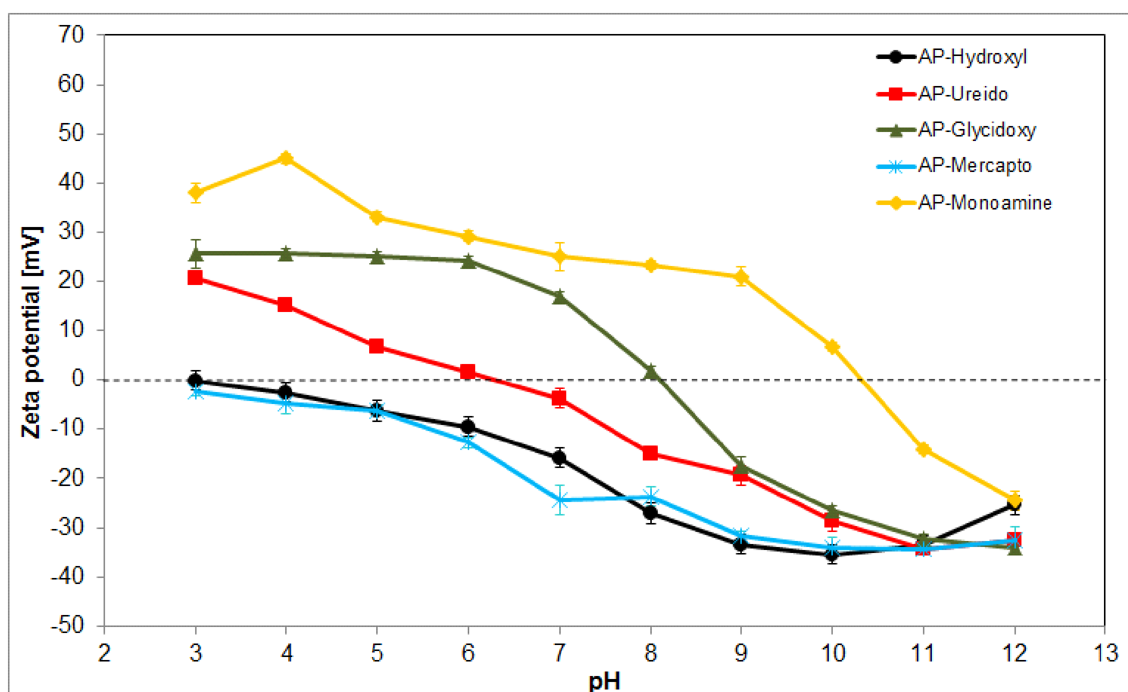

Figure 4. 11 The zeta potential of various functionalized silica nanoparticles as a function of the pH. The pH was set to 3 with 0.1 M HCl and slowly increased by the addition of 0.1 M NaOH

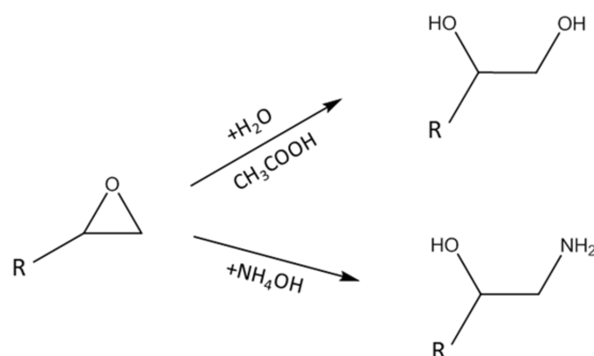

Scheme 4. 4 The ring opening reactions of oxirane by acid catalyzed hydrolysis and by nucleophilic ammonium hydroxide addition S_N2 reaction

The zeta potential of *AP-Mercapto* shows a similar pH dependent behavior as the *AP-Hydroxyl* (bare silica nanoparticles), here no isoelectric point was observed. Since the –SH group is a weak acid, its negatively charged conjugate base should be formed on silica surface.[128] Moreover, because 3-mercaptopropyltriethoxysilane has a low reactivity, some of the Si-OH from bare silica nanoparticles may still be present.[123] Accordingly, the surface charge of *AP-Mercapto* becomes more negative with increasing pH.

The FTIR-ATR spectra of silica nanoparticles functionalized with different functional groups are shown in Figure 4. 12. The FTIR-ATR spectra of the bare (*AP-Hydroxyl*) and aminopropyl silica (*AP-Monoamine M*) nanoparticles are also shown for comparison. The characteristic bands to indicate the existence of ureidopropyl groups on silica nanoparticles were found at 3342 cm^{-1} (N-H asymmetric stretch), 3240 cm^{-1} (N-H symmetric stretch), 3000-2850 cm^{-1} (C-H stretch), 1645 cm^{-1} (C=O stretch), 1603 cm^{-1} (NH_2 asymmetric deformation), 1558 cm^{-1} (NH_2 symmetric deformation), 1395 cm^{-1} (C-H bending from Si-CH_2)[8].

The characteristic bands to indicate the presence of glycidoxypropyl groups on silica nanoparticles were found at 3000-2850 cm^{-1} (C-H stretch), 1738 cm^{-1} (C=O stretch) and 1395 cm^{-1} (C-H bending from Si-CH_2). Because the silanization step was carried out under acidic condition with the addition of acetic acid, diol monoester groups should have formed. Carboxylic acid provides a direct reaction route with epoxides to form 1,2 diol monoesters.[129] Hence, a strong stretching mode of C=O at 1738 cm^{-1} was observed.

The S-H stretch (2590-2580 cm^{-1}) and C-S stretch (705-570 cm^{-1}) are characteristic signatures of mercaptans, but these bands are weak in the infrared (Figure 4. 12 (b)).[130] Additional characteristic bands such as C-H stretch (3000-2850 cm^{-1}) and C-H bending from Si-CH_2 (1391 cm^{-1}) indicate the presence of mercaptopropyl groups on silica particles. As mentioned before, 3-mercaptopropyl triethoxysilane has significantly lower hydrolysis and condensation rates than self-catalyzing aminoalkoxysilane precursors used in this study. Furthermore, the starting material 3-MPTES 92 % was not purified before used, and it is possible that it contained disulfides. Thus, low adsorption of MPTES on silica, as well as a low degree of condensation of MPTES was expected. As a result, the obtained FTIR-ATR spectrum shows only a small alteration to the one from *AP-Hydroxyl* nanoparticles. The assigned characteristic bands were listed in Table 4. 12. The elemental analysis data in Table 4. 11 confirmed the existence of 3-mercaptopropyl groups on silica nanoparticles surface. The high ratio of C to S (C / S = 6 / 1) indicates the presence of high amount of ethoxy groups on the silica surface, from the un-hydrolyzed MPTES.

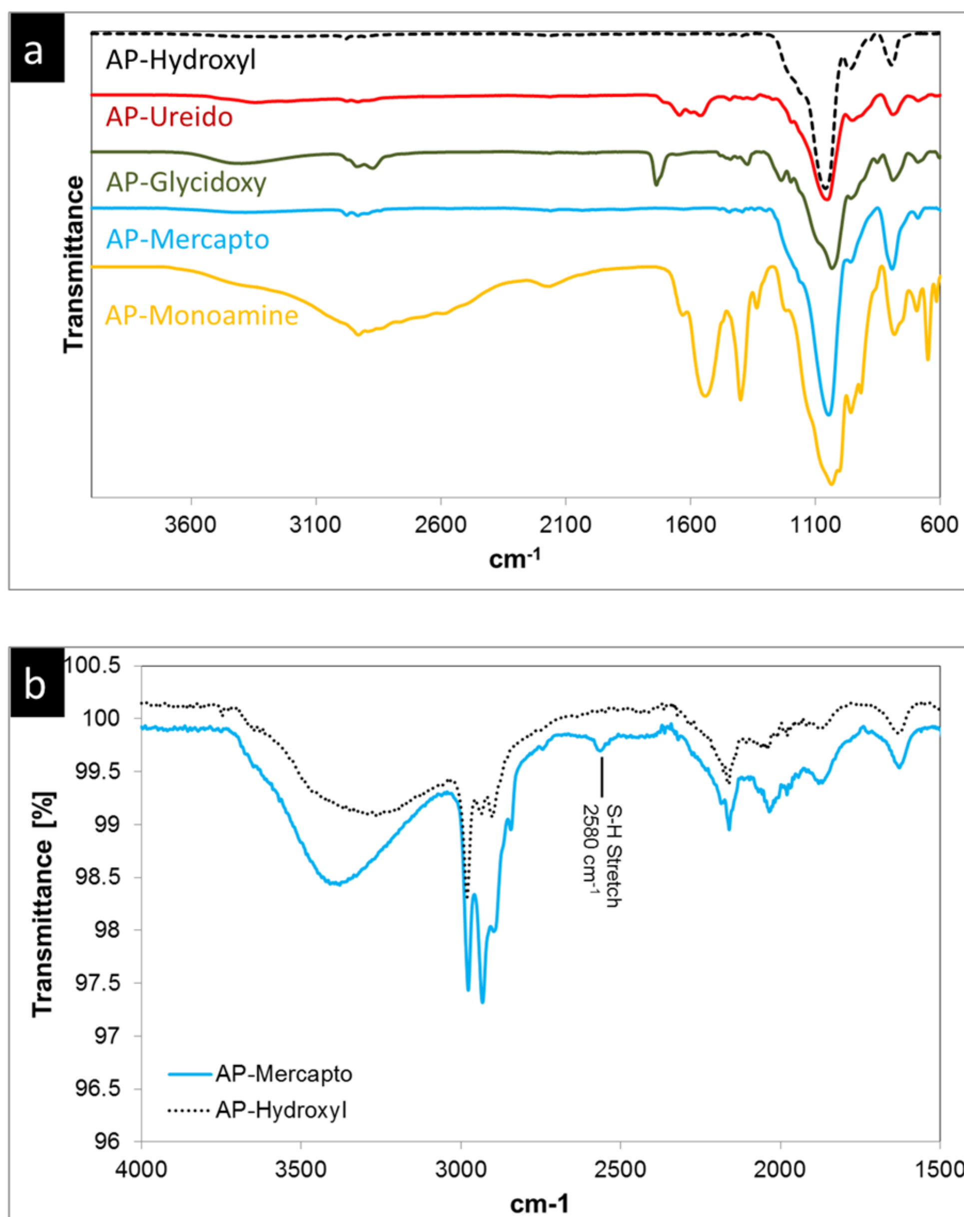

Figure 4. 12 FTIR-ATR spectra of silica nanoparticles functionalized with different functional groups (a) and magnified view of the *AP-Mercapto* spectrum for better comparison (b). The spectra were taken with resolution of 4 cm^{-1}

4.4. Conclusions

Silica nanoparticles of desired size and surface functionalization were synthesized by Stöber process and simple silanization with organosilane. *AP-Monoamine*, *AP-Diamine*, *AP-Triamine*, *AP-Ureido*, *AP-Glycidoxy* and *AP-Mercapto* were prepared. Although the presence of aggregates or coalesced particles in dispersion was observed, stable colloids in the size range 15-45 nm (measured by TEM) have been obtained. The reactivity of organosilane (hydrolysis and condensation) used for modification has strong influence on the attachment of the functional groups at silica surface. Hence, functionalized silica nanoparticles with different degree of coverage of functional group were obtained. Aminopropyl functionalized silica (*AP-Monoamine*) with a high density of surface amino groups was obtained. *AP-Monoamine* with different particles size shows an isoelectric point at pH 10.5. The result of different characterization methods (zeta potential measurements, DLS, FTIR-ATR, and UV-Vis spectroscopy) indicates that multilayers of amine organosilane form on the silica surface.

Chapter 5 - Modification of epoxy substrate (ABF-GX92) surface for adhesion enhancement with deposited copper films

5.1. Introduction

As it was mentioned before (see Chapter 1), it is well known that dielectric substrates and copper have a very poor adhesion between each other. To increase the adhesion between those materials has become a challenging topic for several decades. Increasing the substrate surface roughness (R_{rms} > 1 μm) was the most common solution for adhesion problems. R_{rms} is the root mean square roughness (see Chapter 3). A rough surface creates interlocking connections between dielectric substrate and copper which increases the adhesion significantly (Figure 5. 1(a)). Due to the development of printed circuit board production for high density and high frequency applications, rough surface substrates are not anymore suitable for these new functions. Instead, smooth surface substrates (R_{rms} < 0.1 μm) are required, for which a new surface pretreatment method is need to be developed to enhance the adhesion of metal films on the surface of dielectric substrate, without additional roughening.

One method to eliminate mechanical anchoring while keeping a good adhesion value (N/cm) is to increase the chemical adhesion. Additional pretreatment prior to metallization processes is utilized to introduce more active chemical groups on polymer surfaces. Different techniques have been developed such as plasma treatments[18, 33-35] for chemical and physical modifications of the polymer surface, or graft polymerization and silane coupling agents to incorporate new functional groups on the polymer surface.[22-25, 28-29, 31-32, 40-41] These techniques have been applied with different outcome, having all of them their own advantages and limitations (see Chapter 2).

One of the most common approaches among these methods is to introduce nitrogen containing functional groups such as amines on the polymer surface. By using the strong interaction of these groups with the palladium catalyst, which is used for electroless copper deposition, and to copper itself,[131-134] the adhesion enhancement between electroless copper and dielectric material can be achieved.

Nonetheless, the achieved adhesion enhancement is still not good enough for the electronics industry requirement. Furthermore, the details of interaction between nitrogen containing groups and palladium catalyst and or copper layer are still unclear.

In this chapter, it is described a new process of modifying epoxy polymer substrate for copper metallization. Silica nanoparticles functionalized with aminopropyl groups were used to modify the surface of epoxy substrate, increasing the adhesion with the metal films, without roughening the substrate surface (R_{rms} < 0.1 μm). This chemical modification generates peel strength as large as 9 N/cm, two times higher than the result of traditional way (variation from 4-5 N/cm),[17, 20] with much higher surface roughness (R_{rms} > 0.3 μm). In order to have better understanding of adhesion mechanism, in this work, the use of different functional groups of silica nanoparticles as adhesion promoter was also described. The process using functionalized silica as adhesion promoter is described briefly in Figure 5. 1(b).

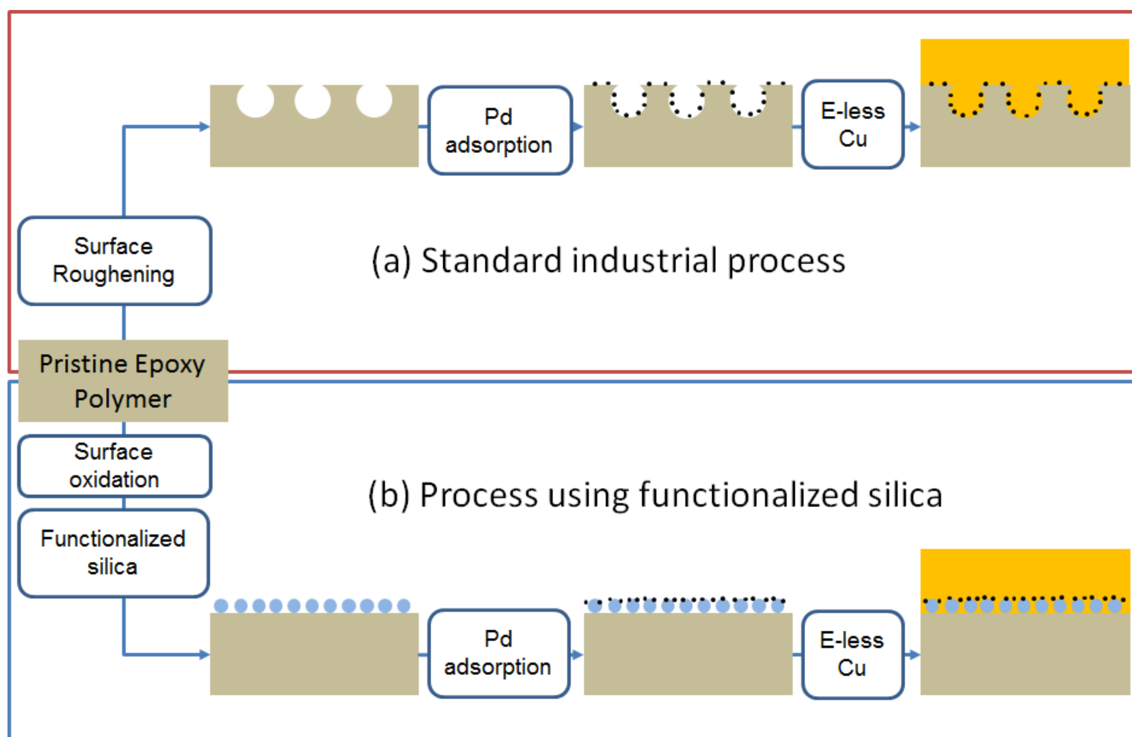

Figure 5. 1 Surface preparation of epoxy polymer for copper metallization by (a) Standard industrial PCB production process and (b) Functionalized silica process (this work)

5.2. Experimental

5.2.1. Materials

Epoxy polymer substrate

On top of a copper cladded FR 4 epoxy glass fiber substrate a 40 µm buildup layer of epoxy polymer film (ABF-GX 92) was laminated. The lamination of the buildup film was done by Ajinomoto Film Technology Company, Inc. Japan. The overall thickness of the laminated panel was 1 mm. The epoxy polymer substrates were cut with dimension of 4.4 cm x 7.7 cm in size.

Chemicals

Isopropanol was purchased from Merck chemicals. Functionalized silica nanoparticles were used to modify epoxy polymer surface. Preparation and characterization are explained in Chapter 4. Pretreatment and plating reagents were provided by Atotech Deutschland GmbH and listed as:

1. Atotech palladium chloride solution (4 %w/w)
2. Atotech Securiganth P 500 permanganate etch ($NaMnO_4$ and NaOH)
3. Atotech reduction solution Securiganth P 500 (manganese oxide reducer)
4. Atotech Neoganth 834 activator (ionic palladium)
5. Atotech Neoganth WA reducer (palladium reducer, dimethylaminoborane)
6. Atotech Printoganth PV (electroless copper, formaldehyde reduction agent)
7. Atotech Cupracid TLC (galvanic copper)

5.2.2. Sample preparation

The surface of epoxy substrate was cleaned with isopropanol in an ultrasonic bath for 5 min at room temperature before use. Two different ways of surface activation were performed using permanganate (strong oxidation agent) or plasma (Ar, O_2).

Permanganate pretreatment

Atotech Securiganth P 500 permanganate etch (alkaline oxidizing solution) was used. The substrates were treated at 80 °C for variable amount of time to oxidize

the surface. Thin layer of permanganate and manganese oxide remaining on the polymer surface was removed by immersing into Atotech P 500 reduction solution (contains hydroxyl ammonium sulfate and sulfuric acid) at 50 °C for a set amount of time. The substrates were rinsed with copious amount of distilled water after every step. The panels were dried with dry air.

Plasma pretreatment

The prepared substrate was inserted into a cylindrical discharge cell, model Zepto PC XP manufactured by Diener electronics, plasma-surface technology. The reaction chamber was evacuated to 0.1 mbar, and either Ar or O_2 gas was introduced into the reaction chamber with a constant flow rate. The plasma treatment was performed at a power discharge of 37.5 and 75 W at a system pressure of 0.5 mbar for a set period of time.

Treatment of functionalized silica nanoparticles on polymer surfaces

After surface activation step, the substrates were fixed onto dip coater and immersed into freshly prepared solution containing functionalized silica nanoparticles at various concentrations (in ethanol; pH4-5) and operating temperatures. After immersing the substrates for a known period of time, the substrates were withdrawn from functionalized silica nanoparticles solution with a speed of 120 to 240 mm/min. The panels were finally annealed in an oven temperature range from 80 to 160 °C for 10 min.

Electroless deposition of copper on modified epoxy substrate

After modification with functionalized silica nanoparticles, the polymer substrates were activated with a palladium catalyst prior to electroless copper deposition. The commercially available ionic palladium catalyst solution Atotech Neoganth 834 activator (palladium catalyst solution in an alkaline media) was used in this work. The surface modified epoxy polymer panels were immersed into the prepared palladium catalyst solutions for 4 min at 40 °C, and then rinsed three times with distilled water. The adsorbed palladium ions Pd (II) on modified epoxy polymer surface were reduced to Pd^0 by using Atotech Neoganth WA reducer (palladium reduction solution containing dimethylaminoborane) followed by rinsing with distilled water. The typical immersion time for this reduction step is 3 min at 30 °C.

Electroless copper plating was then carried out by using a commercially available electroless plating bath Printoganth PV from Atotech Deutschland GmbH. The typical plating condition is a temperature of 35 °C and 15 min immersion time. A copper layer of about 800 nm was deposited by this condition. After electroless plating, the substrates were washed in copious amount of distilled water for three times, dried and annealed at 150 °C for 1 h. Table 5. 1 shows the process sequence of electroless copper plating on modified polymer substrates.

Table 5. 1 Process sequences of electroless copper plating on modified polymer substrates

Step	Chemistry	Operation Temperature (°C)	Immersion Time (min)
1	Atotech Neoganth 834 activator	40	4
2	Atotech Neoganth WA reducer	30	3
3	Atotech Printoganth PV	35	15

Galvanic copper plating on polymer substrate with electroless copper

Galvanic copper plating was performed using a commercial electrolytic copper plating bath (Atotech Cupracid TLC) at room temperature for 90 min with a current density of 2 A/dm^2. The thickness of plated galvanic copper is around 40 µm. This additional copper layer serves as an anchoring layer for peeling the underlying electrolessly deposited copper. The electroless copper plated polymer substrates were immersed into diluted sulfuric acid (10 w/w% H_2SO_4; 25 °C; 1 min) prior to galvanic plating to remove the existing oxides layer from the surface. Immediately after galvanic copper plating, the films were washed thoroughly with distilled water before annealing at 180 °C for 1 h.

5.2.3. Characterization

Fourier Transform Infra-red-Attenuated Total Reflectance (FTIR-ATR)

The chemical structure of polymer surface was characterized with an FTIR-ATR spectrometer (Perkin Elmer Spectrum™ 100 FTIR) equipped with a DTGS (deuterated triglycine sulfate) detector and a single reflection Ge-ATR (attenuated

total reflectance with Germanium crystal) unit. The angle of incident of the beam is 45 °. In general, pristine and modified polymer substrates were measured from 4000-600 cm^{-1} with resolution of 4 cm^{-1}. Each sample was scanned for 32 times.

Atomic Force Microscopy (AFM)

Taping mode AFM was performed using a Digital Instruments Nanoscope III microscope. All AFM measurements were made in ambient environment condition using nanocsope cantilever with single crystal silicon tips. The properties of the cantilever are summirized in Table 5. 2. The surface roughness was quantified by using root mean square (R_{rms}) roughness calculations (see Chapter 3).

Table 5. 2 The property of cantilever with single crystal silicon tips used in AFM measurement

Property	Nominal Value	Specified Range
Thickness /µm	4	3.0 - 5.0
Mean Width /µm	30	22.5 - 37.5
Length /µm	125	115 - 135
Force Constant /(N/m)	42	10 - 130
Resonance Frequency /kHz	330	204 - 497

Field Emission Scanning Electron Microscopy (FESEM)

The surface topography of epoxy polymer surface observation with field emission scanning electron microscope was obtained using Carl Zeiss Microscopy Supra® series. All images were collected in ultrahigh vacuum with an acceleration potential between 1 kV and 10 kV. Secondary electron and back scatter electron mode detectors were used to record the images. Considering that most of the polymer samples are highly insulating (volume resistivity $\approx 10^{15}$-10^{20} Ω·cm), the accumulation of localized excessive electrons will cause abnormal contrast, image distortion and shift. To overcome this problem, a thin layer of iridium (few nanometers) was deposited on the surface by sputtering to increase the conductivity. Thus, the excess electrons can be conducted.

Scanning Transmission Electron Microscopy (STEM)

Transmission electron microscope images were obtained on a Helios Nanolab™ Dualbeam™. A thick layer of Pt was deposited on the top of the sample prior to sample cutting. Ultrathin samples (lamella) are cut from the surface by using

Ga^+ ion beam. The interface between the copper layer and the epoxy substrate was investigated, in order to observe the presence of nanoparticles.

Inductively Coupled Plasma-Optical Emission Spectroscopy (ICP-OES)

The amount of adsorbed palladium ions on the surface of polymers was determined by using inductively coupled plasma optical emission spectroscopy (ICP-OES), Varian 720-ES ICP Optical Emission Spectrometer.

Epoxy substrates with polished edges with dimension of 10x10 cm were immersed into palladium solution (Atotech Neoganth 834 activator) for about 4 min at 40 °C and then rinsed three times with distilled water. Thereafter, the panels were immersed into Atotech Neoganth WA reducer solution for 3 min at 30 °C to reduce the adsorbed Pd (II) species on the surface to Pd (0). After rinsing with distilled water, the panels were dried using heat gun. The extraction of palladium from the substrate surface was carried by immersing the sample into 50 ml diluted aquaregia solution (37 % HCl : 65 % HNO_3 : H_2O = 3:1:4) at room temperature for 5 min. The extracted sample was diluted to five times the original volume with Milli Q water for ICP-OES measurement.

Evaluation of adhesion strength

The adhesion strength between deposited copper layers and epoxy polymer substrate was studied quantitatively on LTCM-6 series from Chatillon. Standard ASTM D6862 90 ° peel strength test[135] was conducted for adhesion evaluation. All measurements were carried out at peeling speed of 45 mm/min. Each adhesion strength result is the average of at least two measurements for every sample. Normally the results from each measurement should not vary more than 0.5 N/cm.

A number of experiments were performed to test the reliability of adhesion of copper layers aminopropyl functionalized silica treated epoxy substrate under a variety of stress conditions, Highly Accelerated Stress Test (HAST) or infrared reflow oven test (IR reflow) was conducted. The HAST parameter followed a standard classification JESD22-A110-B.[136] The samples were subjected into oven heat chamber at 130 °C and relative humidity (RH) of 85 % for 96 hours. The IR reflow test was carried out five times in an IR reflow oven (Compact nitro B 2100-400), with

a temperature profile setup of a standard classification IPC/JEDEC J-STD-020D.[137] The peel strength evaluation was performed after every stress test.

5.2.4. The optimization of process parameters

Different operation parameters influence the adhesion of copper on *AP-Monoamine M* treated epoxy substrate. Therefore, for simplification, some of the parameters were need to be optimized. The experiment was planned using the Box-Behnken, response surface design of the JMP 10 package (SAS Institute Inc.).[138-139] Box Behnken Design (BBD)[138] is class of second order design, which based on three-level incomplete factorial design. The number of experiments required for the BBD is defined as $N=2k(k-1)+C_0$. Where k is the number of factors and C_0 is the number of central points.

In this experimental design, the concentration of *AP-Monoamine M* (4 g/L), immersion time (5 min) and the annealing time after particle treatment (10 min) are constant. The adhesion strengths (N/cm) of copper on the epoxy substrate were evaluated by varying the *AP-Monoamine M* dispersion temperature, substrate withdrawing speed, and the annealing temperature after particle treatment, on the basis of Box-Behnken design.

The obtained experimental results were also analyzed using the JMP 10 package software.[140] The distribution of analyzed data was represented in quantile plot (Figure 5. 2), with the following options added to the plot,

a. The median sample value showing the median of each level
b. The 25 % and 75 % quantiles describing the 25 % and 75 % quartiles respectively
c. The whisker extending the end of the box to the outermost data point

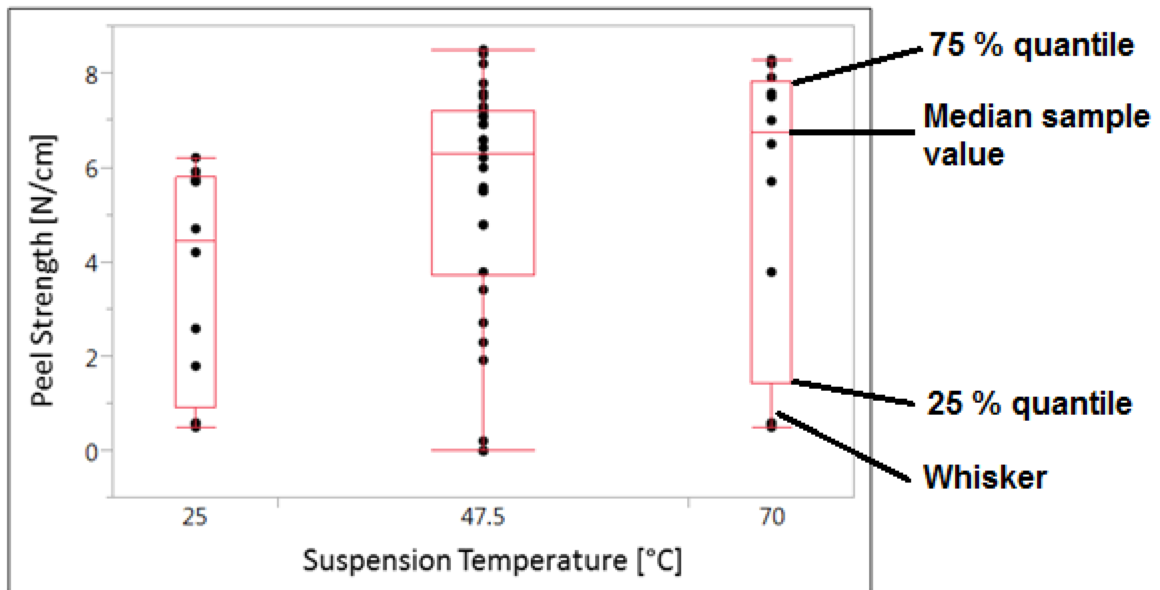

Figure 5. 2 Example of quantile plots

5.3. Results and discussions

5.3.1. Activation of the surface of epoxy substrate

To study the influence of the surface activation step on the epoxy substrate surface. The substrates were treated with permanganate solution (Atotech Securiganth P 500 permanganate etch) for different periods of time. In Figure 5. 3, it can be seen, some holes with the diameter of around 200 nm were found at the surface of epoxy substrate, before surface activation step. It was believed, these holes were created during the lamination and curing process of epoxy films.

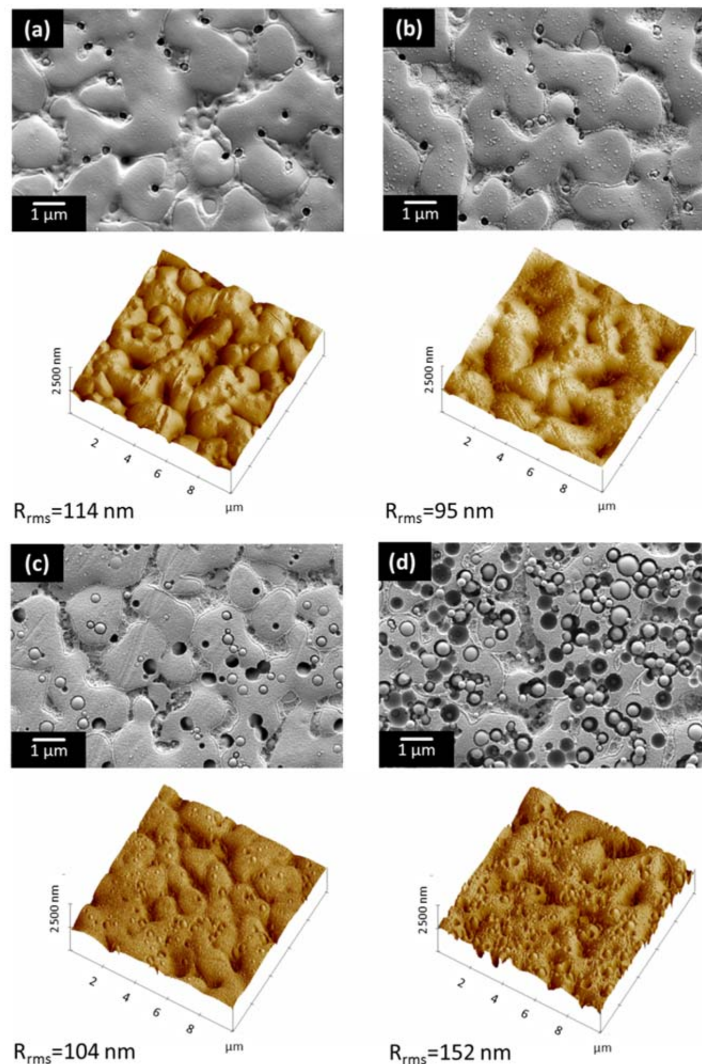

Figure 5. 3 FE-SEM and AFM surface topography image of epoxy substrate treated with permanganate in different periods of time, (a) 0 min, (b) 1 min, (c) 5 min, and (c) 15 min

It is noticeable that the root mean square roughness (R_{rms}) measured in atomic force microscope (AFM) of epoxy polymer surface was slightly decreased from R_{rms} = 114±6 nm to 95±3 nm for one minute treatment in permanganate, and increased gradually to R_{rms} = 104±5 nm for 5 min, and R_{rms} = 152±2 nm for 15 min (Figure 5. 3). This is because of the epoxy substrate which is used in this work has an ether linkage located in the backbone of the polymer, which is formed by the opening of the epoxide ring during the curing process.[52] The permanganate etch attacks the polymer via this ether linkage, removed a small segment of the polymer chain and exposed the next linkage for the subsequent etch attack. In this manner, the permanganate etch removes the entire chain of the polymer, and forming pores on the surface. The proposed etch mechanism of epoxy substrate by permanganate is shown in Figure 5. 4.

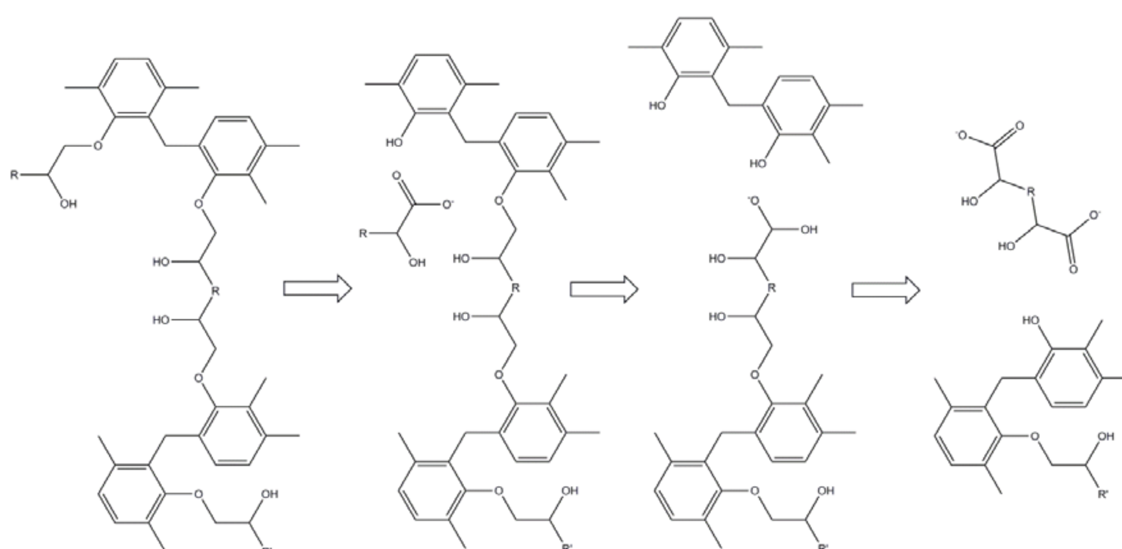

Figure 5. 4 The scheme of proposed mechanism of the degradation of epoxy polymer chain by permanganate, adapted from the work of Sam et al., 2004[53]

The changes in the chemical composition of the epoxy substrate surface were investigated by FTIR-ATR. The FTIR-ATR spectrum of pristine epoxy substrate (ABF-GX 92) is shown in Figure 5. 5, with the assignment of the characteristic bands were summarized in Table 5. 3. The pristine epoxy polymer shows characteristic absorption band due to the diglycidyl ether bisphenol A (DGEBA) component of copolymer[141] (3500, 3057, 2965-2873, 1608, 1509, 1036, 916, 827, and 755 cm^{-1}), the characteristic bands of the incorporated silica filler at (1070-1090 cm^{-1}), and a band characteristic of acrylates (1740 cm^{-1}).

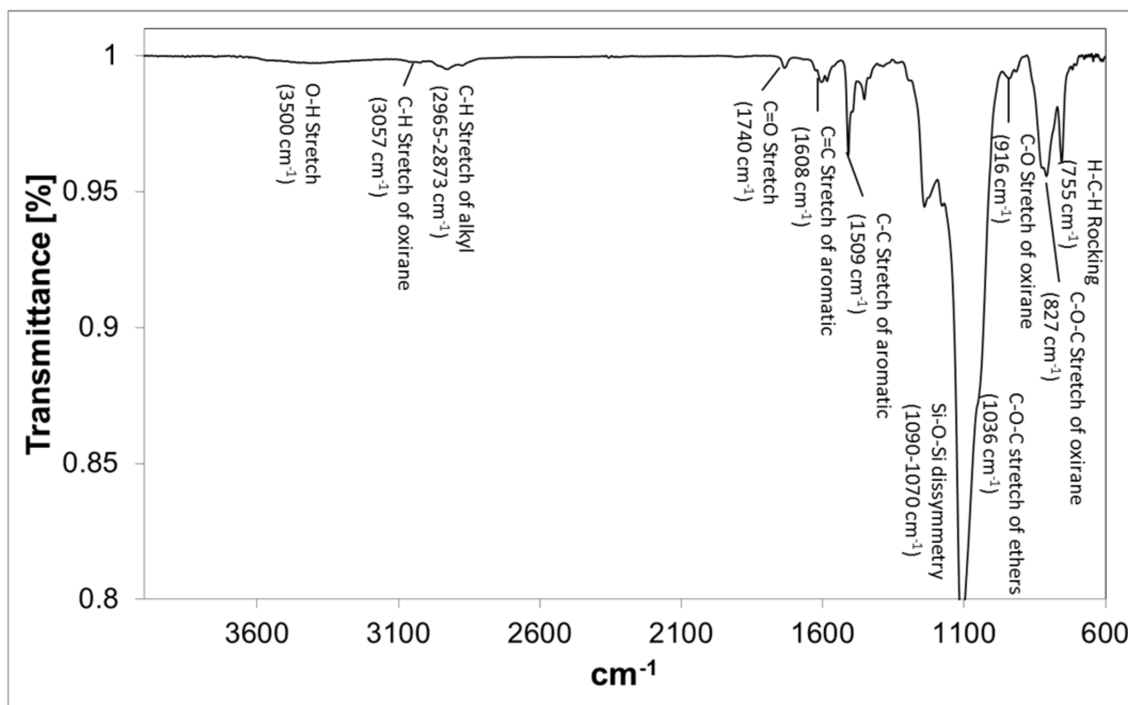

Figure 5. 5 FTIR-ATR spectra of the pristine epoxy substrate

Table 5. 3 Characteristic bands of the epoxy substrate, obtained by FTIR-ATR.[141]

Assignment	Absorption band (cm^{-1})
O-H stretch	3500
C-H stretch of oxirane ring	3057
C-H stretch of alkyl	2965-2873
C=O stretch	1740
C=C stretch of aromatic	1608
C-C stretch of aromatic	1509
Si-O-Si dissymmetry vibration	1070-1090
C-O-C stretch of ethers	1036
C-O stretch of oxirane group	916
C-O-C stretch of oxirane group	827
H-C-H rocking	755

The recorded spectra of permanganate treated epoxy substrate are shown in Figure 5. 6. All characteristic absorption band intensities are gradually reduced with increasing permanganates treatment time. This is maybe because of the increase of the roughness of the surface of epoxy substrate. The increase of surface roughness leads to loss of IR reflectance energy. Therefore, all recorded spectra were normalized to the highest peak (1100 cm^{-1}). In Figure 5. 6, it could be seen that the

broad absorption band around 3100-3600 cm^{-1} (O-H stretch) was gradually reduced with longer treatment time. Instead, the intensities of the broad absorption band around 2750-2850 cm^{-1} (C-H stretch from aldehyde) and absorption band at 1740 cm^{-1} (C=O stretch) increased. This result can be explained in the following way. The cured novolac epoxy resin contains functional groups, such as secondary alcohol (R-OH-R') and ether (R-O-R'). Through the oxidation reaction with permanganate, these functional groups will break-down into ketone and primary alcohol groups. The primary alcohol can be oxidized further to form aldehydes and carboxylic acid or carboxylate ions (alkaline solution). Thus, the signal intensity of the O-H stretch reduces, followed by the increase of the C-H stretch and C=O stretch signal intensities. These groups will remain on the surface, serves as active groups, which then react with functionalized silica nanoparticles.

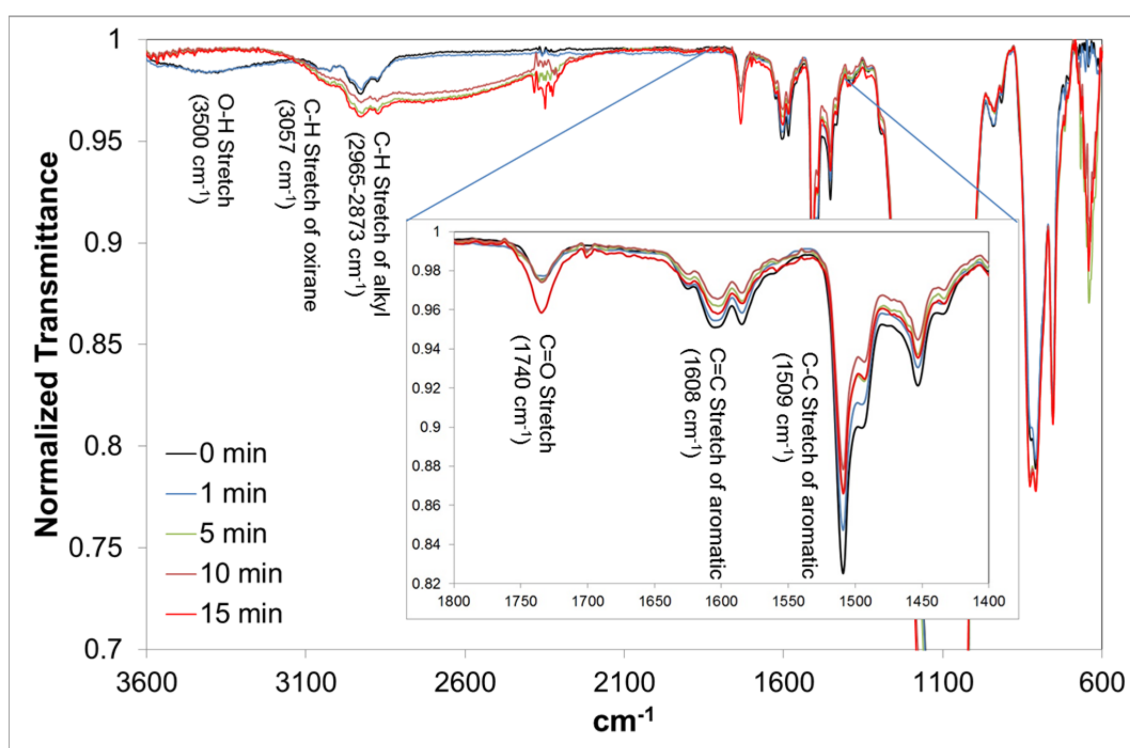

Figure 5. 6 FTIR-ATR spectra of epoxy polymer surface treated with permanganate at different period of time

The surface activation treatment with permanganate resulted in remarkable modification on the surface of epoxy polymer chemical composition and morphology. In short period of treatment time, after 1 min of immersion, certain functional groups, such as aldehyde, ketone, and carboxylic acid were generated. Long immersion into permanganate etch solution (15 min), result in the break-down of the polymer chain,

which then rough surface was created (R_{rms} > 0.1 µm). Since the aim of this work is to keep a low surface roughness (R_{rms} < 0.1 µm), one min treatment time into permanganate solution was used as surface activation step, prior to functionalized silica nanoparticles treatment step.

5.3.2. Epoxy polymer surface modification with aminopropyl functionalized silica nanoparticles (*AP-Monoamine M*)

Based on previous section, the surface chemistry of epoxy substrate can be modified by using strong oxidation agent, such as permanganate. One minute treatment time into permanganate solution was used as surface activation step, followed by manganese oxide removal step. After these two steps, the activated epoxy substrates were immersed into a solution of functionalized silica.

The changes in surface morphology of epoxy substrate after modification by functionalized silica nanoparticles were studied by FE-SEM (Field Emission-Scanning Electron Microscope) and AFM (Atomic Force Microscope). The FE-SEM images of activated epoxy substrate and the activated epoxy substrate treated with *AP-Monoamine M* are shown in Figure 5. 7. These images were taken after drying the sample in atmospheric environment. Some particles were observed on the surface of the epoxy substrate after activation step (Figure 5. 7 (a)). Those particles can be defined as the remains of manganese oxide particle, from improper cleaning of the substrate after the permanganate treatment. Example of manganese oxide particles were circled in yellow. On the other hand, polymer particles as the decomposition product of epoxy resin is also need to be considered. Some holes with the size of around 200 nm have been found also at the surface of the blank epoxy substrate (no permanganate treatment). The reason for this was explained in the previous section 5.3.1. A dense and uniform nano-granulate structure was formed on the surface of epoxy substrate surface treated with 4 g/L of *AP-Monoamine M*, Figure 5. 7(b). The nanoparticles spread over the surface with a high uniformity, a minor agglomeration was observed.

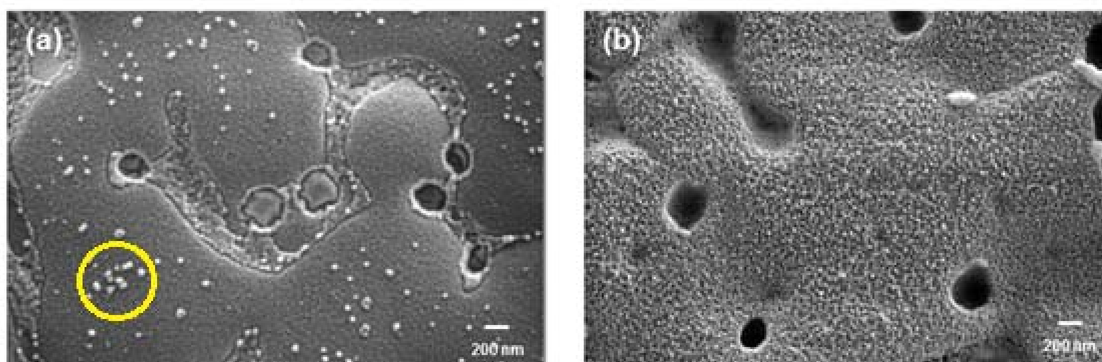

Figure 5. 7 FE-SEM Surface morphology images of activated epoxy substrate before (a) and after (b) 4 g/L *AP-Monoamine M* treatment

Figure 5. 8 shows FTIR-ATR spectra of activated epoxy substrate treated in different concentration of *AP-monoamine M* dispersions. The samples were prepared by immersing the epoxy substrate, and subsequently dried in atmospheric environment. The presence of *AP-Monoamine M* on the surface could be confirmed by three absorption bands: 2800-2950 cm^{-1} (C-H stretch), 1740 cm^{-1} (C=O stretch) and 1640-1690 cm^{-1} (C=N stretch). The fingerprint region with wavelength smaller than 1400 cm^{-1} remains approximately the same for all spectra. Slight changes could be observed for the absorption band in the region between 2800-2950 cm^{-1} (C-H stretch), the absorption band at 1740 cm^{-1} (C=O stretch) and the broad absorption band in the region 1640-1690 cm^{-1} (C=N stretch). The change of intensity ratio of the C=O to C=C aromatic stretch and C=N to C=C aromatic stretch is shown in Figure 5. 9. It is well known that primary amine has a good affinity to react with ketones and aldehydes.[142] As mentioned previously, an aldehydes and ketones rich surface was formed on epoxy substrate after permanganate treatment. Primary amine on functionalized silica undergoes nucleophile addition with aldehydes and ketones to give substituted imines. This reaction will lead to a decrease in C=O stretch and an increase of C=N stretch absorption band intensity. An increase in absorption band intensity around 2800-2950 cm^{-1} might correspond to the propyl chain on silica nanoparticles surface, these peaks are used for qualitative discussion only.

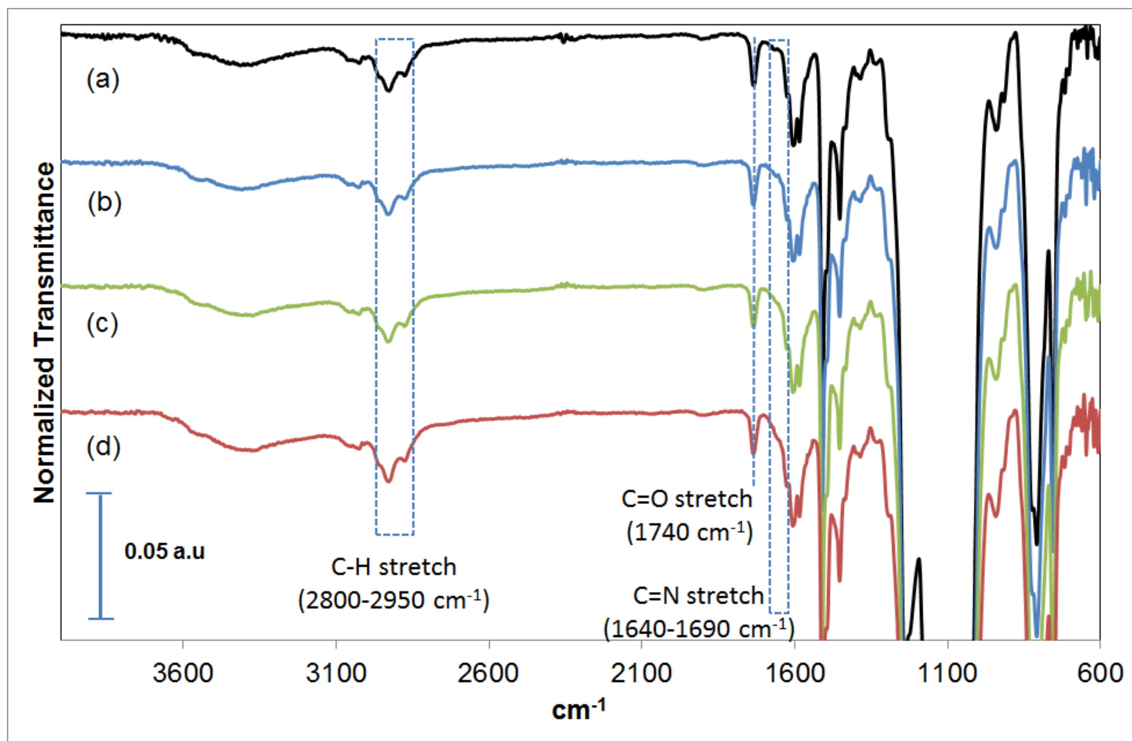

Figure 5. 8 FTIR-ATR spectra of epoxy polymer surface treated with (a) 0 g/L, (b) 2 g/L, (c) 4 g/L and (d) 8 g/L of *AP-Monoamine M*

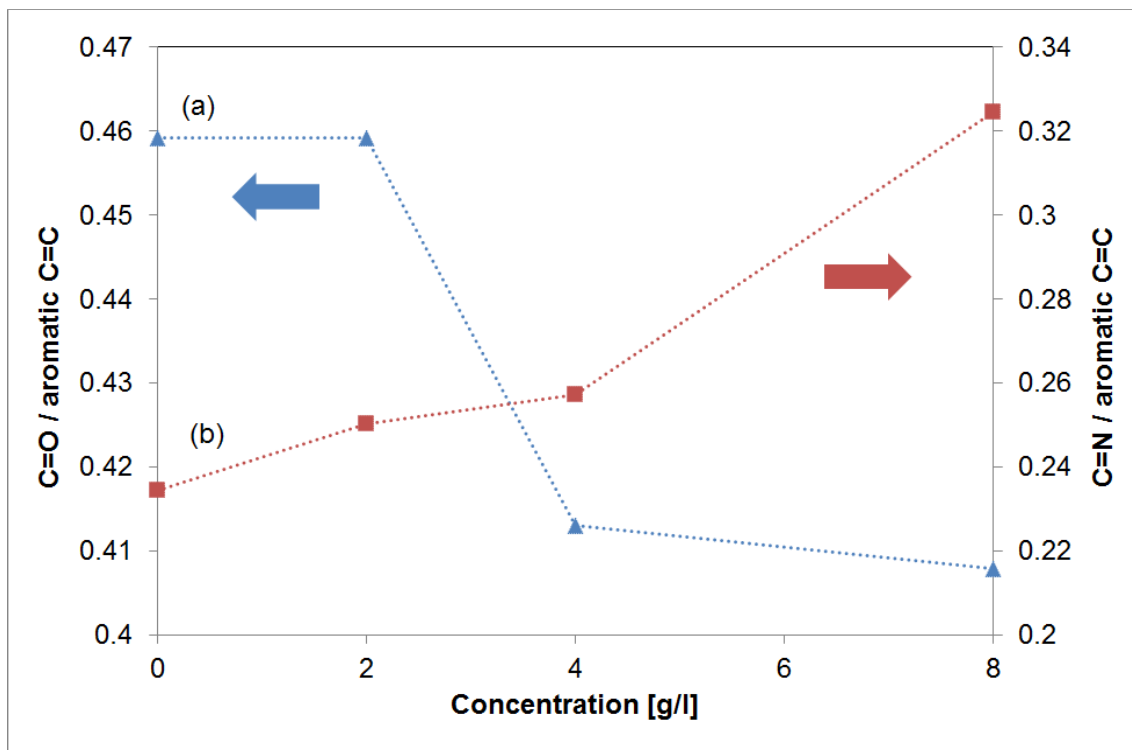

Figure 5. 9 The change of intensity ratio of (a) C=O to C=C aromatic stretch and (b) C=N to C=C aromatic stretch

5.3.3. Electroless copper deposition on epoxy substrate surface modified with aminopropyl functionalized silica

For the further study bellow, the surface of epoxy substrates were subjected into permanganate pretreatment for 1 min, before treated with 4g/L of *AP-Monoamine M*. The only permanganate treated and *AP-Monoamine M* modified epoxy substrates were activated in palladium solution prior to electroless copper deposition. The amount of palladium uptake on the resulting surfaces was analyzed by ICP-OES. The measured palladium uptake for the substrate treated with *AP-Monoamine M* is significantly higher than that of the only permanganate treated epoxy substrate, 1±0.2 mg/m^2 and 3.25±0.2 mg/m^2 for the only permanganate treated and *AP-Monoamine M* treated substrate respectively. These results suggest that the surface of epoxy substrate treated with *AP-Monoamine M* has a strong ability to retain palladium species from the palladium solution (Atotech Neoganth 834 activator).

The surface morphology of the epoxy substrates, after a short time immersion into e-less copper solution were observed by FE-SEM, see Figure 5. 10. The surface was already covered by copper after 1 min immersion time. The thickness of the copper deposit is expected to be less than 100 nm. It is noticeable that nodular electroless copper with small grain size was deposited on both surfaces. The coverage of deposited copper on the surface of epoxy substrate treated with only permanganate (Figure 5. 10(a)) is less dense than the one on the surface of epoxy substrate treated with *AP-Monoamine M* (Figure 5. 10 (b)), porous copper layer was observed. Some holes originated from the preparation of epoxy substrate were still visible on the surface of only permanganate treated substrate. These holes circled with orange color on the image. On the other hand, those holes were not visible anymore for *AP-Monoamine M* treated substrate. The reason of this maybe because of the surface of epoxy substrate treated with *AP-Monoamine M* has a stronger ability to retain palladium species from the palladium solution, by forming amine-palladium complexes.[26, 29] Electroless copper deposition process is catalyzed by palladium. Hence, denser layer of copper was formed with *AP-Monoamine M* treatment. Nonetheless, for both cases, a coherent layer of copper was formed

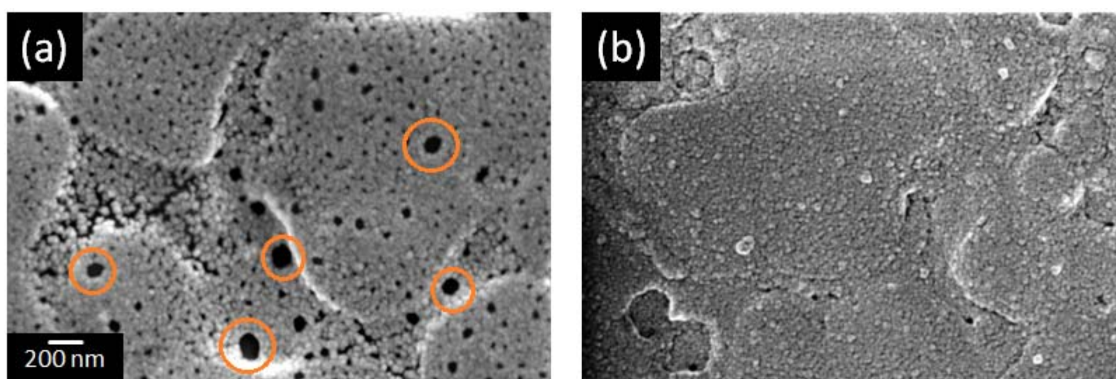

Figure 5. 10 The FESEM images of pristine (a) and 4 g/L *AP-Monoamine M* treated (b) ABF-GX92, after 1 min immersion in electroless copper solution. All images were taken with the same magnification

Figure 5. 11 shows cross-sectional STEM images of electroless copper deposited on (a) only permanganate treated, (b) with a 4 g/L dispersion of *AP-Monoamine M* treated epoxy substrates. The epoxy substrates were immersed into electroless copper solution for 15 min. The thickness of the copper deposit is around 500 nm. By investigating the interface between the epoxy substrate and the deposited copper layer, the existence of *AP-Monoamine M* in the interface could be proven. As shown in Figure 5. 11 (b), a semi-transparent layer of about 20-30 nm thickness was observed. This layer is not visible for copper deposited on permanganate activated only epoxy substrate image, Figure 5. 11 (a). Thus, it can be concluded that *AP-Monoamine M* layer was imbedded in the interface of epoxy substrate surface and copper deposit.

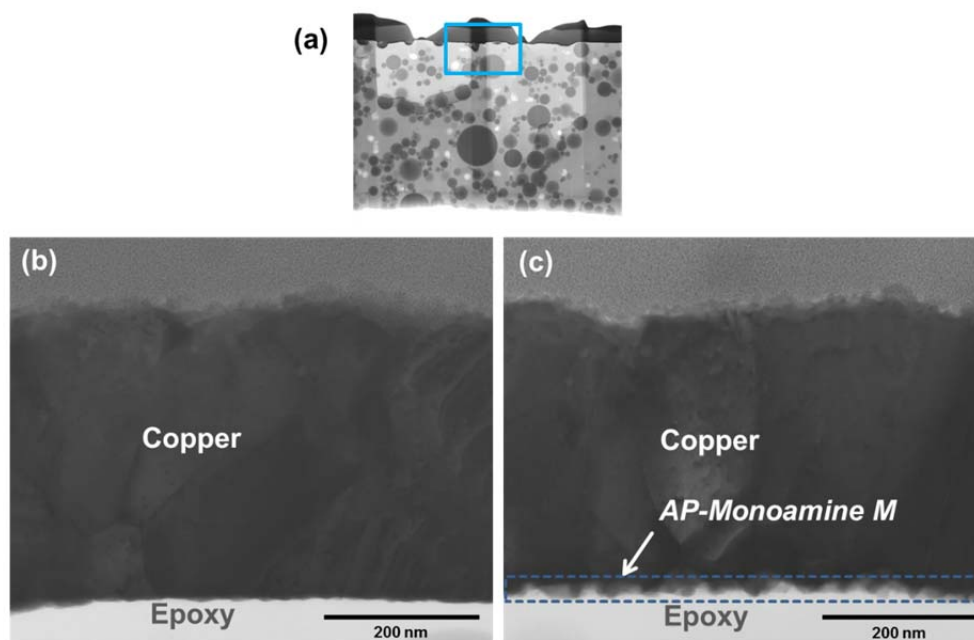

Figure 5. 11 Cross-sectional STEM image of electroless deposited copper on (b) only permanganate treated and (c) 4 g/L *AP-Monoamine M* treated epoxy polymer surface. (a) The low magnification STEM image shows the area where the interface was zoomed (blue square)

5.3.4. Evaluation of adhesion of deposited copper layer on *AP-Monoamine M* modified epoxy substrate

The adhesion performance of deposited copper on polymer surface is the main concern in electronics production.[11] Different operation parameters influence the adhesion of copper on *AP-Monoamine M* treated epoxy substrate. Therefore, for simplification, the optimization of three parameters (*AP-Monoamine M* dispersion temperature, epoxy substrate withdrawing speed, and annealing temperature after *AP-Monoamine M* treatment) was first performed. Then after, these three parameters were fixed and the optimized samples were used to investigate the influence of other parameters, such as the concentration of *AP-Monoamine M* and the immersion time of substrate in *AP-Monoamine M*.

5.3.4.1. The optimization of AP-Monoamine M suspension temperature, epoxy substrate withdrawing speed, and annealing temperature after particle treatment

The optimization of three factors: *AP-Monoamine M* dispersion temperature, substrate withdrawing speed, and annealing temperature after particle treatment

were shown in Figure 5. 12. An *AP-Monoamine M* concentration of 4 g/L, immersion time (in *AP-Monoamine M* dispersion) of 5 min, and annealing time after particle treatment of 10 min was used. Correlation analysis among those three factors was performed using JMP software package. From JMP data analysis, the desirable effect of the factors on the peel strength is examined.

A first analysis of the data leads to the conclusion that the annealing temperature (after *AP-Monoamine M* treatment) is the factor with the most relevant effect. Low adhesion strength was obtained (around 2±0.5 N/cm), when no annealing step was applied (the data is not included in the graph). The withdrawing speed does not seem to has relevant impact on the peel strength, while the dispersion temperature shows relevant impact only when the annealing temperature after the *AP-Monoamine M* treatment is 130 °C.

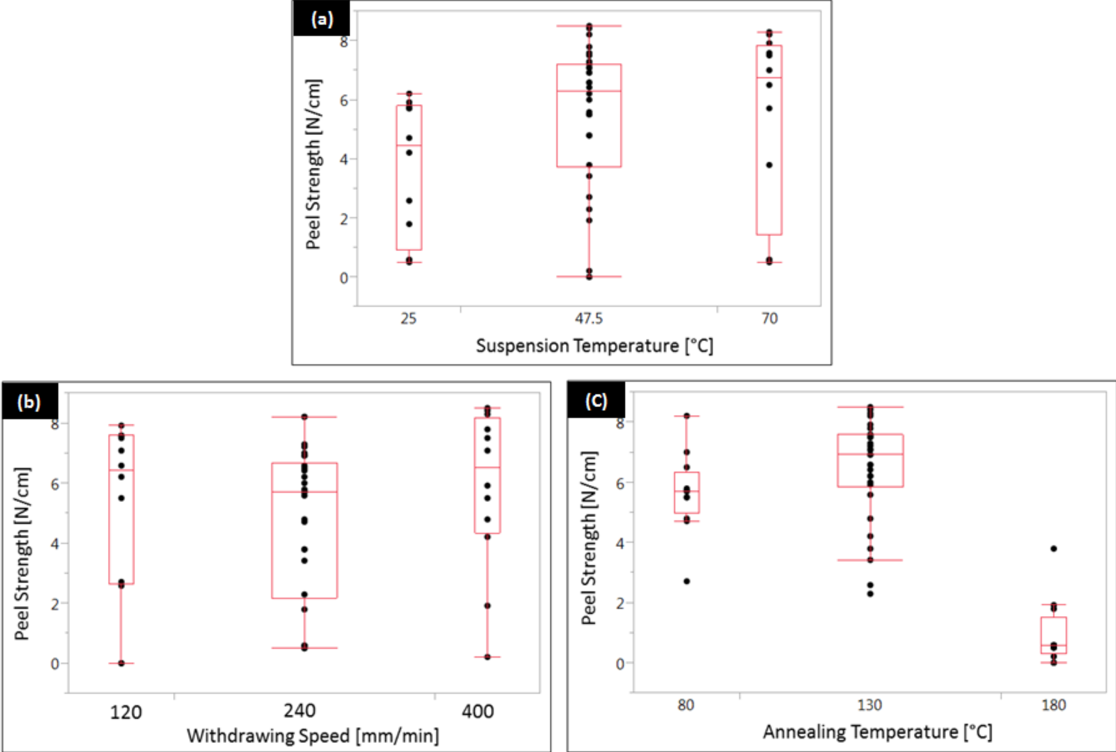

Figure 5. 12 The influence of *AP-Monoamine M* dispersion temperature (a), withdrawing speed (b), and annealing temperature after treatment with *AP-Monoamine M* (c) on the peel strength. *AP-Monoamine M* dispersion with a concentration of 4 g/L, an immersion time of 5 min, and an annealing time of 10 min were used

The increase in peel strength by annealing at either 80 °C or 130 °C maybe explained by assuming that the annealing step initiates the covalent bonding between epoxy substrate surface carbonyl groups and the amine groups of *AP-Monoamine M*, which then enhances the adhesion of copper on the surface of the epoxy substrate. Nonetheless, the annealing temperature has a strong negative impact, when the annealing temperature is 180 °C. A sharp drop of adhesion to almost 0.5±0.1 N/cm was obtained. A possible explanation for this weakening in peel strength can be the large difference in thermal expansion between epoxy substrate above the glass transition temperature (Tg), (1.3 ppm/°C)[75] and silica (0.55 ppm/°C).[143] At elevated temperature, the epoxy substrate expands the volume in all directions more than the silica. Thus, it results a tensile stress across the interface and which leads to extensive loosening of *AP-Monoamine M* from epoxy substrate surface.

Increasing the *AP-Monoamine M* dispersion temperature has a positive impact on the peel strength. Higher dispersion temperature results in higher peel strengths. This is can be because of the coverage of nanoparticles on epoxy substrate surface is more evenly distributed at higher dispersion temperature (Figure 5. 13 (b)), which consequence of the higher evaporation rate of ethanol at elevated temperature. As reported by Jung *et al*.,[144] the increase in evaporation rate of the solvent would increase the particle convective flux near the substrate surface. Thus, a highly uniform coverage of the substrate surface by particles is achieved, and higher peel strengths can be obtained. Furthermore, it can be noticed in Figure 5. 13(a), that a local variation in particle coverage was found at the surface of an epoxy substrate treated with *AP-Monoamine M* dispersion at 25 °C. Because of the non-uniformity of particle coverage, the obtained peel strength is lower than the one of epoxy substrate treated with *AP-Monoamine M* dispersion at 70 °C.

The best peel strength was obtained when the optimum condition was used. These are: dispersion temperature of *AP-Monoamine M* between 47.5 °C and 70 °C, substrate withdrawing speed between 120 and 240 mm/min, and annealing temperature of 130 °C. Since the boiling point of ethanol with the concentration of 96 % is about 78 °C, the temperature of the suspension of 60 °C was chosen. The middle point 180 mm/min was chosen as withdrawing speed. These parameters will

be adjusted to the above number and remained unchanged for the further investigation.

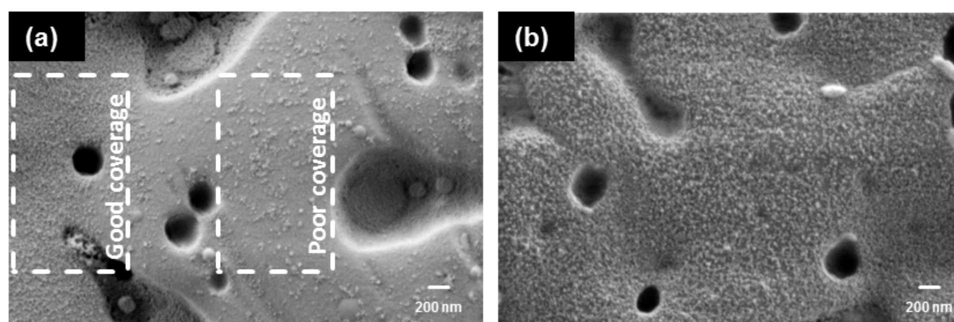

Figure 5. 13 FE-SEM images of epoxy substrate surfaces treated with a dispersion of *AP-Monoamine M* (c=4 g/L) at (a) 25 and (b) 70 °C. A withdrawing speed of 180 mm/min and immersion time of 5 min were used

5.3.4.2. The effect of plasma surface activation on adhesion strength

Alternatively, the samples were treated with argon or oxygen plasma to activate the surface instead of permanganate. The morphology of the surface of epoxy substrates after plasma treatment remained the same as original.

Figure 5. **14** shows peel strengths of copper deposited on *AP-Monoamine M* (c=4 g/L) modified epoxy substrates. Different exposure energy and time did not show a significant impact on the peel strength. In general, substrates treated with oxygen plasma shows higher adhesion strengths than those treated with argon plasma. As demonstrated in a work on an aromatic polymer (Vecstar OC®), [35] a higher amount of C=O groups are formed on the outermost layer of the polymer by the plasma modification, especially with oxygen plasma. As mentioned before, amine groups has a high reactivity toward C=O groups. Amine groups of *AP-Monoamine M* undergo nucleophile addition with surface C=O groups of the surface to give imines. Therefore, strong adhesion of copper on *AP-Monoamine M* treated epoxy polymer was obtained. Thus, the peel strength is comparable with those of epoxy substrates activated with permanganate (9.2±0.3 N/cm).

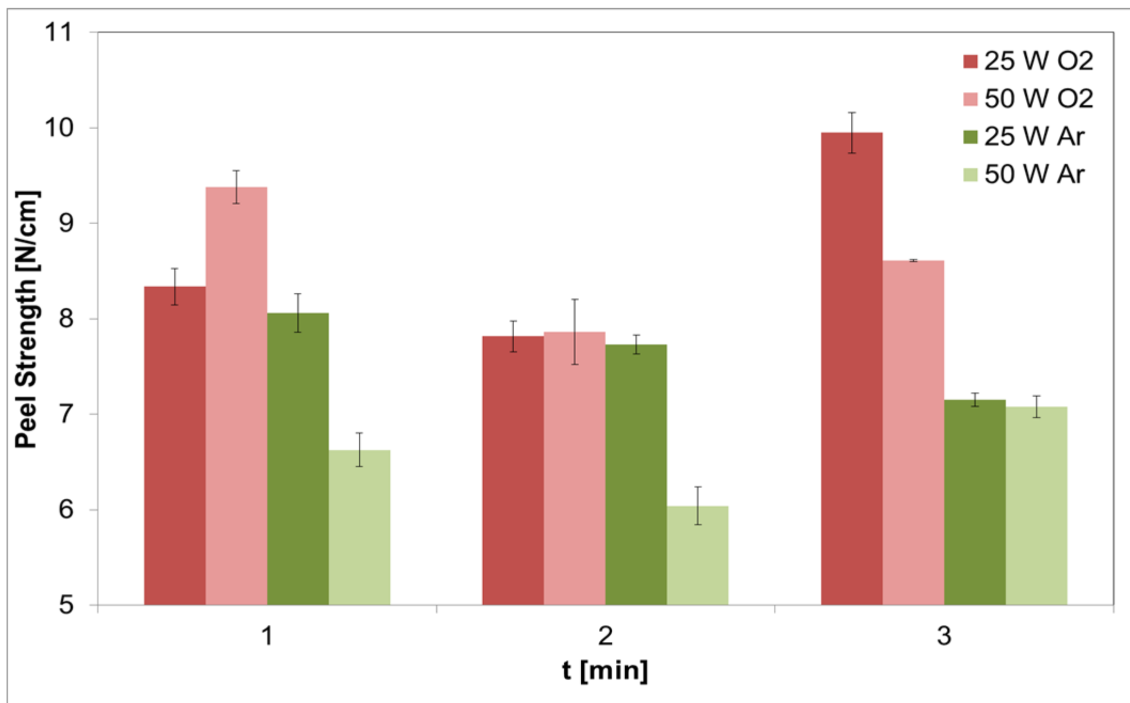

Figure 5. 14 Peel strength of deposited copper on epoxy substrate modified with 4 g/L of *AP-Monoamine 50 nm* at 60 °C for 5 min. Argon or oxygen plasma was used as surface activation step

Based on above results, for the further work, permanganate will be used for surface activation of epoxy substrate.

5.3.4.3. The effect of concentration of AP-Monoamine M on adhesion strength

The peel strength of copper on only permanganate treated epoxy substrate is very low, 0.6±0.1 N/cm. The peel strength increases significantly with *AP-Monoamine M* treatment. The dependence of the peel strength of deposited copper on *AP-Monoamine M* treated epoxy substrate with different is shown in Figure 5.15, having maximal peel strength of about 9.2±0.3 N/cm. When the concentration of *AP-Monoamine M* is lower than 4 g/L, the concentration has a strong impact on the peel strength result. Because of the increase of nanoparticle coverage on epoxy substrate surface (Figure 5.16). Further increase in *AP-Monoamine M* concentration, exceeding 4 g/L does not have significant increase on the peel strength. The surface of epoxy substrate is fully covered (Figure 5.16) after treatment with *AP-Monoamine M* with a concentration of 4 g/L. Insignificant changes of particle coverage on epoxy substrate surface occur at higher concentration which lead to similar peel strengths.

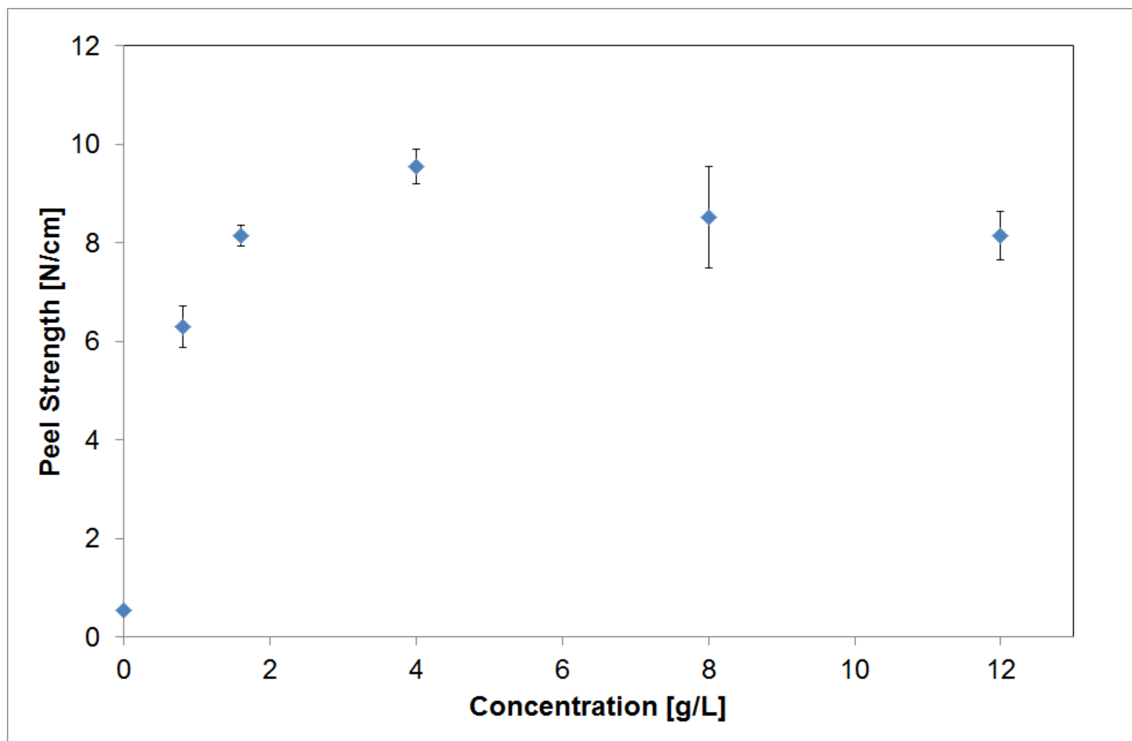

Figure 5.15 The peel strength of deposited copper on epoxy polymer substrate as a function of the concentration of *AP-Monoamine M.* The treatment was carried out at 60 °C for 5 min

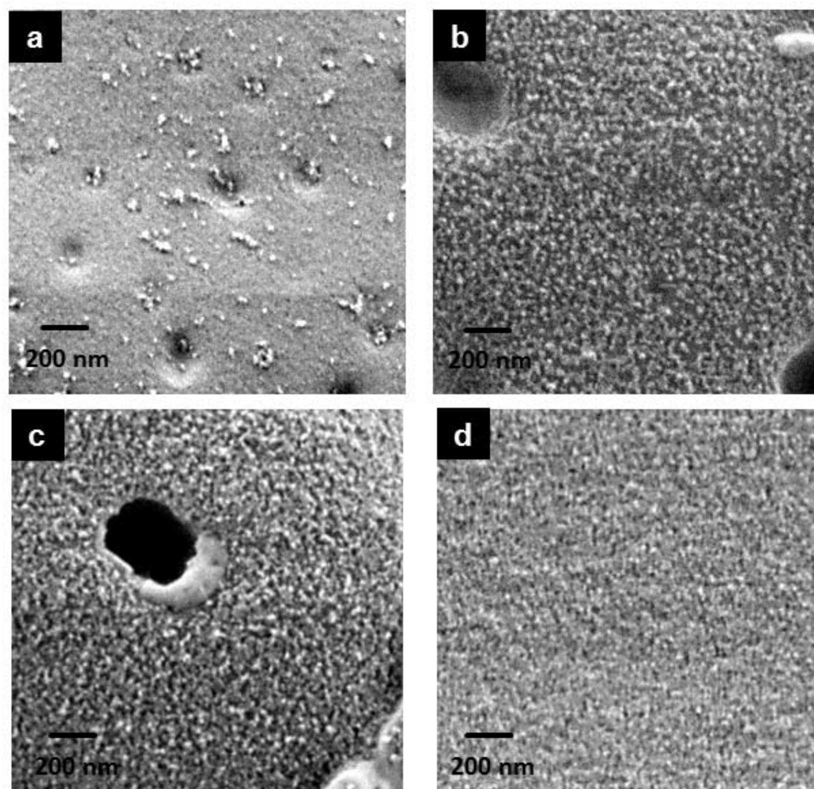

Figure 5.16 FESEM surface image of epoxy substrate treated with 0.4 (a), 2 (b), 4 (c), and 8 (d) g/L of *AP-Monoamine M* at 60 °C for 5 min

5.3.4.4. *The effect of substrate immersion time in AP-Monoamine M dispersion on adhesion strength*

Figure 5.17 shows the dependence of the adhesion strength of deposited copper layers on modified epoxy polymer substrates on the immersion time in *AP-Monoamine M* dispersion. The effect of the immersion time on the peel strength was more significant at low concentration, 0.8 g/L. The peel strength is increasing from 2.7±0.2 N/cm to 6.9±0.1 N/cm for 10 s and 600 s of immersion time respectively. For a low concentration of *AP-Monoamine M*, there are fewer nanoparticles per unit volume in the dispersion. This leads to low coverage of nanoparticles. Longer immersion time gives more probability for the particle to interact with the substrate surface. As a result, denser coverage of nanoparticles was obtained for longer immersion time (Figure 5.18). Hence, at low particle concentration, higher peel strength of copper on epoxy substrates can be achieved with longer immersion times.

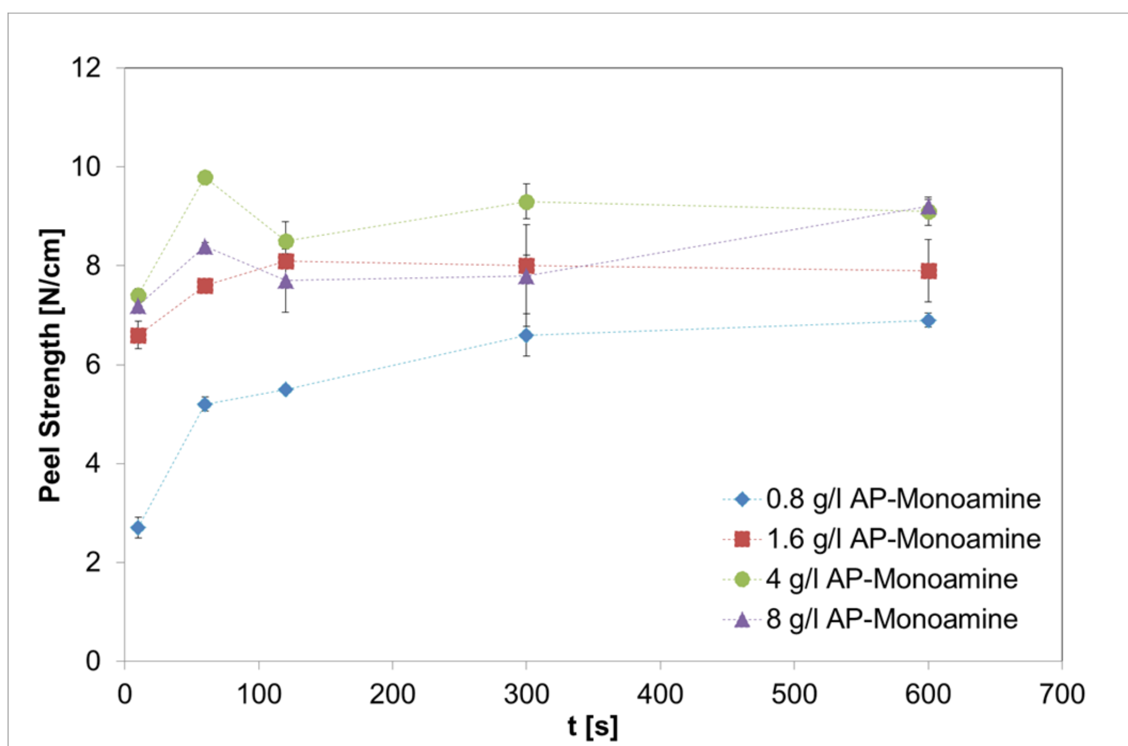

Figure 5.17 The dependence of adhesion strength of deposited copper on modified epoxy substrate on the immersion time in *AP-Monoamine M* dispersion with different concentrations. The dashed lines are guides to the eye

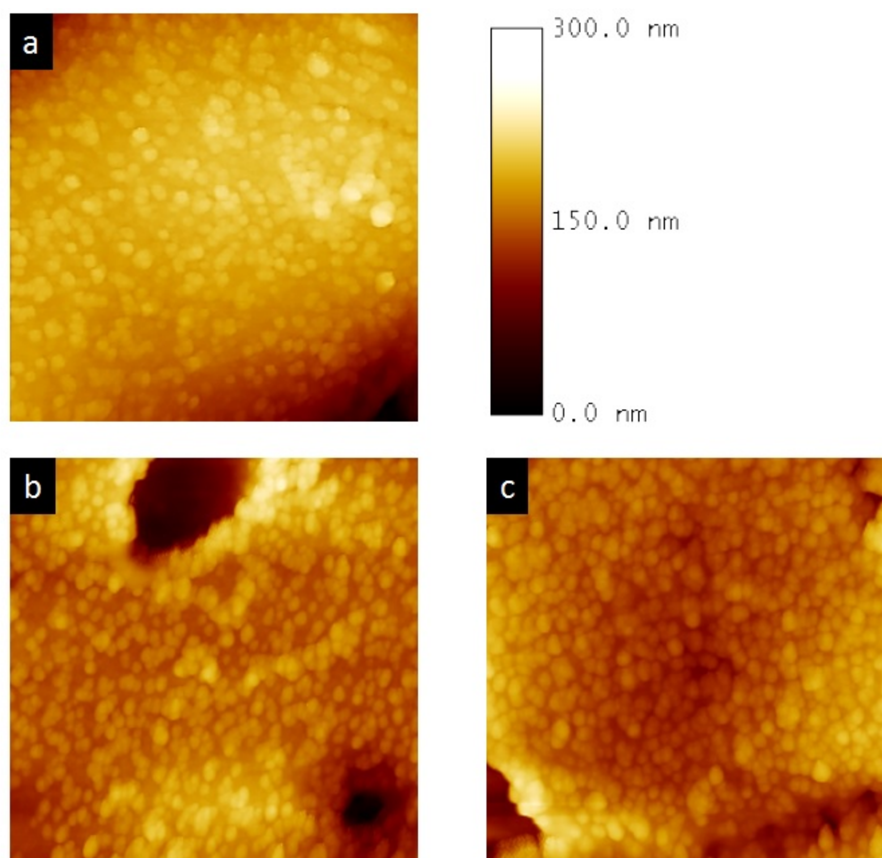

Figure 5.18 AFM surface morphology images of epoxy polymer treated with *AP-Monoamine M* dispersion with c= 0.8 g/L at 60 °C for 10 (a), 300 (b), 600 (c) s of immersion time. The measurement window size is 1 x 1 μm^2

Furthermore, as the concentration of *AP-Monoamine M* increases (4 g/L and 8 g/L), only a short time (120 s) of immersion is needed to achieve the maximal peel strength. With increasing concentration of the *AP-Monoamine M* dispersion, the number density of nanoparticles also increases. This leads to higher probability of attraction between the particles and the surface of the substrate, resulting in denser coverage of particles on the surface. Thus, high peel strengths can be readily achieved in short immersion time, values up to 9.2±0.3 N/cm for immersion time of 60 s are obtained.

5.3.4.5. The effect of particle size of AP-Monoamine on the adhesion strength

In order to study the influence of particles size on the adhesion strength, three different sizes of aminopropyl functionalized silica particles (*AP-Monoamine S, M* and *L*) at a concentration of 4 g/L were used to modify the epoxy substrate surface. The epoxy substrates were treated with permanganate at 80 °C for one minute prior to

the immersion into nanoparticle dispersions. A substrate withdrawing speed of 180 mm/min, a dispersion temperature of 60 °C, an immersion time of 5 min, and an annealing temperature of 130 °C for 10 min were used. The adhesion strength of copper on epoxy substrate modified with different sized *AP-Monoamine* particle shown in Figure 5.19. The FE-SEM images of the particles on epoxy substrate surfaces are shown in Figure 5.20. Comparable peel strengths were obtained for substrates modified with *AP-Monoamine S* (8.8±0.2 N/cm) and *AP-Monoamine M* (9.2±0.3 N/cm). In contrast, lower adhesion strengths for epoxy substrate treated with *AP-Monoamine L* (4.7±1.1 N/cm) are found. This is can be because of low *AP-Monoamine L* particle coverage on the surface of epoxy substrate (Figure 5.20 (c)).

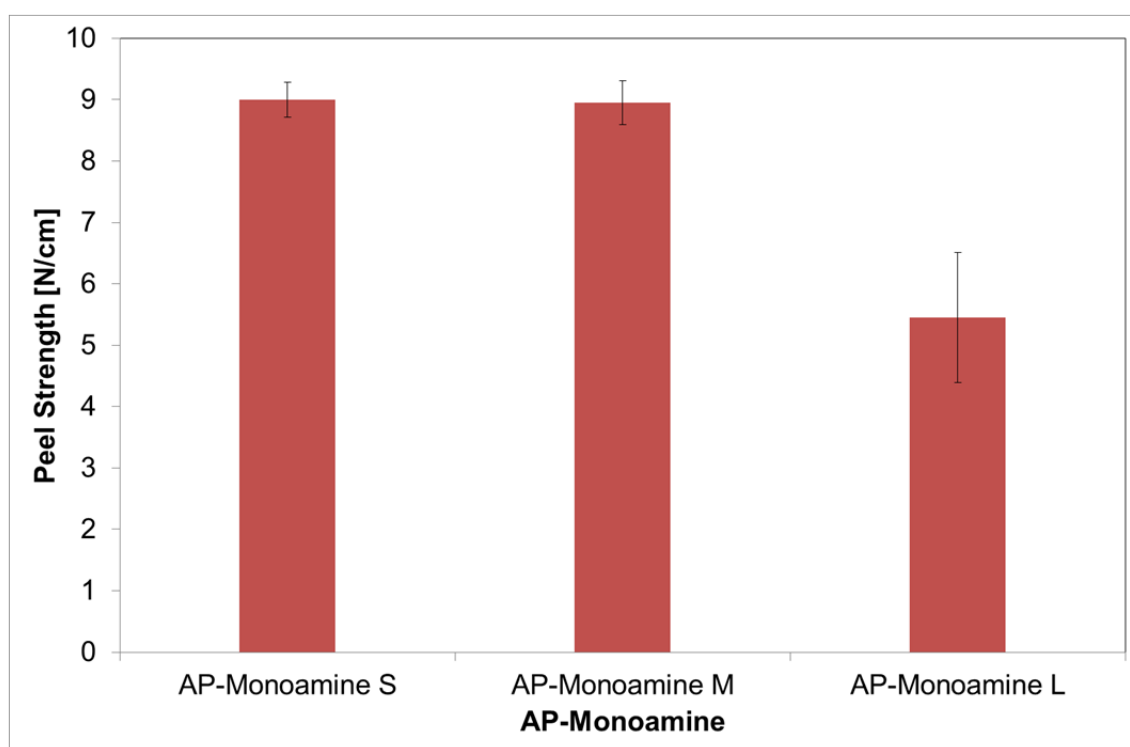

Figure 5.19 Influence of the *AP-Monoamine* particle size on the adhesion strength. *AP-Monoamine S* (Z-average in DLS= 38±1 nm; diameter TEM= 14±3 nm), *AP-Monoamine M* (Z-average in DLS= 52±1 nm; diameter TEM= 18±3 nm) and *AP-Monoamine L* (Z-average in DLS= 92±2 nm; diameter TEM= 68±7 nm) were used

As shown previously in Figure 4.7, the amount of amine groups on the silica nanoparticles increases with increasing particles size. This might suggest that higher aminopropyl polymeric chains were formed on the surface of larger silica nanoparticles. The adsorbed polymer chain keeps the particles away from each other. The van der Waals interaction in ethanol is not strong enough to cause aggregation.[145] At low pH, positively charged amine groups on the surface would

result in higher electrostatic repulsion between the particles. This leads to increasing of shear or slipping plane between aminopropyl functionalized silica. As a result, the distance between two positively charged particles were increased and lower particle coverage on the epoxy substrate surface was obtained.

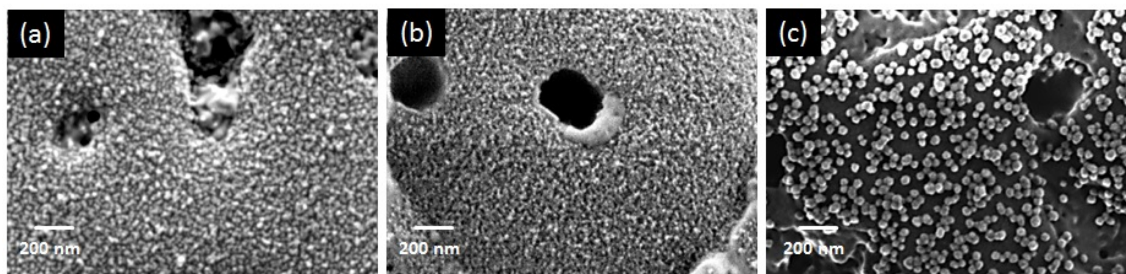

Figure 5.20 FE-SEM image of epoxy substrate surface treated with *AP-Monoamine S* (a), *M* (b), and *L* (c)

5.3.4.6. The effect of surface functional group of silica nanoparticles on adhesion strength

Dispersions of nanoparticles solution with different surface groups (*AP-Hydroxyl, AP-Ureido, AP-Glycidoxy, AP-Mercapto*) with a concentration of 4 g/L in ethanol (pH4) were prepared. The epoxy substrates were treated with permanganate at 80 °C for 1 min prior to the immersion into the nanoparticle dispersions. A substrate withdrawing speed of 180 mm/min, dispersion temperature of 60 °C, an immersion time of 5 min, and an annealing temperature of 130 °C for 10 min were used.

The adsorption characteristics of functionalized silica nanoparticles on epoxy substrate surface are shown in the FE-SEM images in Figure 5.21. Ureidopropyl and glycidoxypropyl functionalized silica nanoparticles were able to adsorb on the surface, while mercaptopropyl functionalized and native silica nanoparticles were hardly found on the substrate surface.

Zeta potential measurements of the particles show that (Figure 4.14) the surface charge of ureidopropyl and glycidoxypropyl functionalized silica nanoparticles were positive at low pH, while mercaptopropyl functionalized and native silica nanoparticles have a negative zeta potential under these conditions. Surface

activation of epoxy substrate using either permanganate or plasma results to the occurrence of negatively charged oxygen species on the surface.[53] Consequently, *AP-Mercapto* and *AP-Hydroxyl* were hardly adsorbed on the surface of epoxy polymer (Figure 5.21). This is mainly due to the electrostatic repulsion between the negatively charged functionalized silica nanoparticles and the epoxy substrate surface. Electrostatic interaction occurs between silica nanoparticles surface and epoxy substrate surface. Depending on the charge of interacting species, this interaction can be either attractive or repulsive. This interaction between particles and substrate surface as the precondition for functionalized silica to attracted on the substrate surface before further interaction, such as chemical bonding interaction.

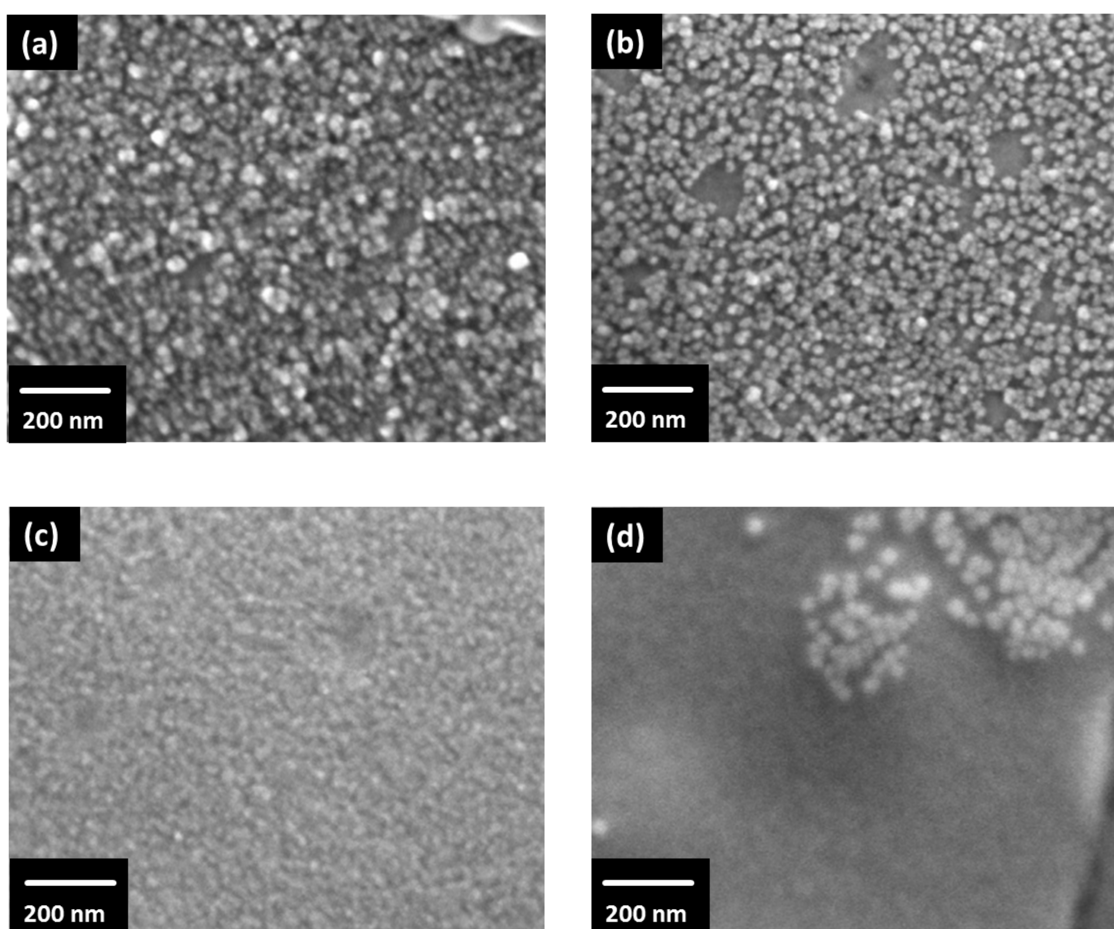

Figure 5.21 FE-SEM image of epoxy substrate surface covered with (a) *AP-Ureido* (Z-average in DLS= 68±1 nm, (b) *AP-Glycidoxy* (Z-average in DLS= 55±1 nm), (c) *AP-Mercapto* (Z-average in DLS= 38±2 nm), and (d) Native silica nanoparticles (Z-average in DLS= 52±2 nm)

The adhesion strength of copper on epoxy substrate surface modified with different functional groups is shown in Figure 5.22. Compare to the adhesion of copper on only permanganate treated epoxy substrate (0.6±0.1 N/cm), epoxy substrate treated with *AP-Ureido* and *AP-Glycidoxy* shows only small adhesion improvement, while *AP-Mercapto* and *AP-Hydroxyl* treated epoxy substrate show no adhesion improvement.

Contrary to AP-Mercapto and AP-Hydroxyl, AP-Ureido and AP-Glycidoxy were able to be adsorbed on the surface of epoxy substrate. The positive surface charge of nanoparticles at acidic pH builds electrostatic interaction with negative surface charge of epoxy substrate surface. Though *AP-Ureido* and *AP-Glycidoxy* are present on the surface of epoxy substrate surface, the adhesion strength is relatively low, 2.2±0.2 and 1±0.1 N/cm for *AP-Ureido* and *AP-Glycidoxy* modified epoxy polymer respectively. This might be due to the fact that 1, 2-diol (glycidoxy ring opening) and ureido functional groups formed weaker metal ligands to copper than primary amine. Log K_f = 3.75 for 1, 2-diol-copper[146] and log K_f = 7.5 for Ureido-Copper,[147] while Log K_f = 20.1 for primary amine-copper.[148]

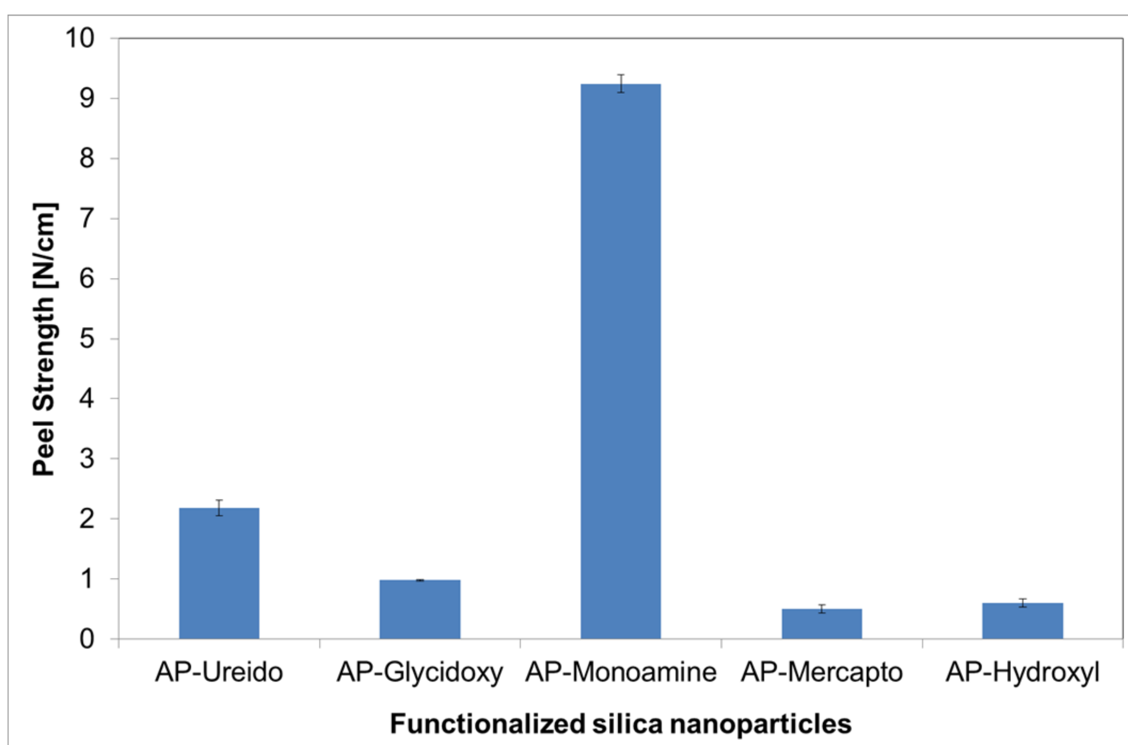

Figure 5.22 Effect of different functional groups on functionalized silica nanoparticles on the adhesion strength of the copper layer

5.3.4.7. The effect of functional group chain length on adhesion strength

Additionally, a series of silica nanoparticles functionalized with aminoalkoxysilanes having more than one amine group (diamines and triamines) were used to modify the epoxy substrate surface. Nanoparticle dispersions of *AP-Diamine* and *AP-Triamine* with concentration of 4 g/L in ethanol (pH4) were prepared. The epoxy substrates were treated with permanganate at 80 °C for 1 min prior to the immersion into nanoparticles dispersion. A substrate withdrawing speed of 180 mm/min, dispersion temperature of 60 °C, an immersion time of 5 minutes, and an annealing temperature of 130 °C for 10 min were used.

Figure 5.23 shows the adhesion strength of copper on epoxy substrate modified with a dispersion (c= 4 g/L) of *AP-Monoamine* ($-NH_2$), *AP-Diamine* ($-NH-NH_2$) and *AP-Triamine* ($-NH-NH-NH_2$). It was noticed that the obtained peel strength has strong dependence on the number of amine moieties, following the order: *AP-Monoamine* (8.3±1 N/cm) > *AP-Diamine* (5.9±0.6 N/cm) > *AP-Triamine* (4.4±0.1 N/cm). The lower adhesion strength of *AP-Triamine* modified epoxy polymer could result from: (1) Lower amine group density due to lower coverage of *AP-Triamine* precursor on the silica nanoparticles surface (Chapter 4), (2) The steric hindrance of the amine group from triamine which could suppress the reactivity with either epoxy substrate surface or deposited copper. The coverage efficiency of aminoalkoxysilanes on surface of silica is highly dependent on the number of amine moieties and whether the amine is sterically or electrostatically hindered.[121]

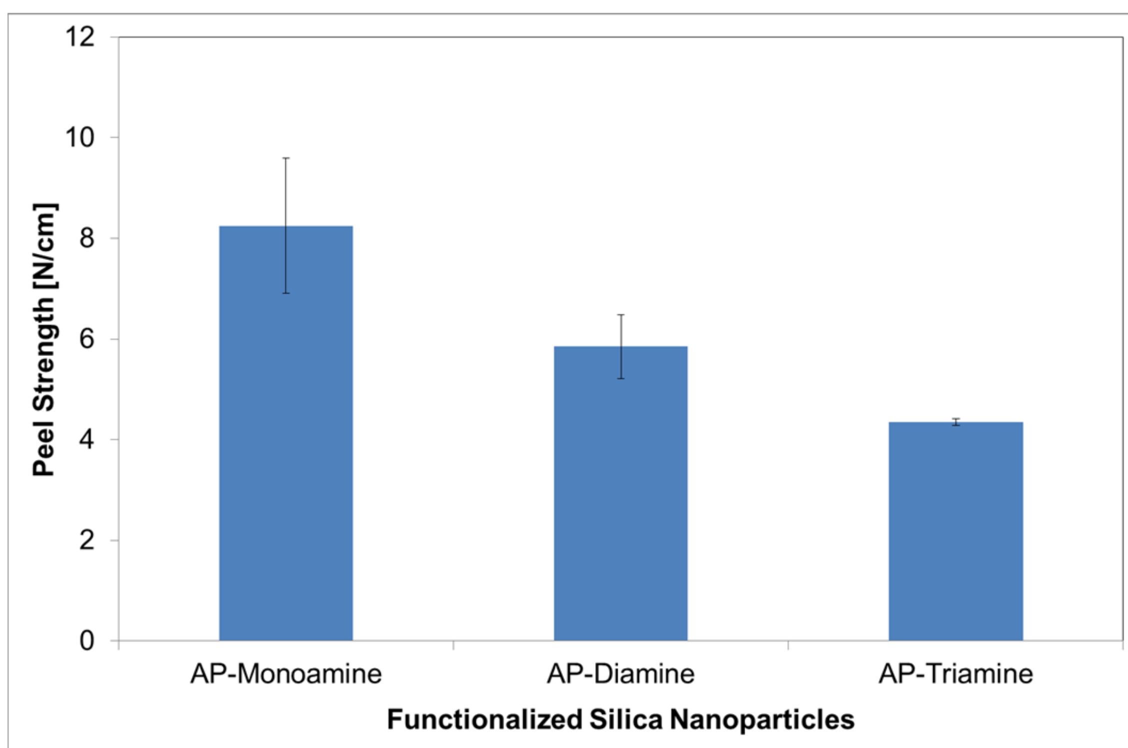

Figure 5.23 The peel strength of copper on different amine chain functionalized silica modified epoxy substrate

5.3.5. Failure mode of deposited copper layers on AP-Monoamine modified epoxy substrate

In the investigation of adhesion between metal and polymer, study of the locus of adhesion failure is beneficial. The peeled epoxy substrates and the copper surface morphology were investigated with FE-SEM and the chemical compositions were investigated with FTIR-ATR and EDX. Figure 5. 24 shows the FE-SEM surface morphology image of a peeled epoxy substrate (a) and copper (b) from a sample that underwent the *AP-Monoamine M* adhesion promoter process, here the peel strength was 9.2±0.3 N/cm. The EDX spectrum of the peeled copper surface (the surface from Figure 5. 24 (b)) is shown in Figure 5. 24 (c). Some parts of the epoxy substrate seem be removed and transferred to the copper surface after peeling. The Kα silicon (1.74 keV) and carbon (0.277 keV)) signals give strong evidence for the presence of epoxy polymer traces on the peeled copper surface.

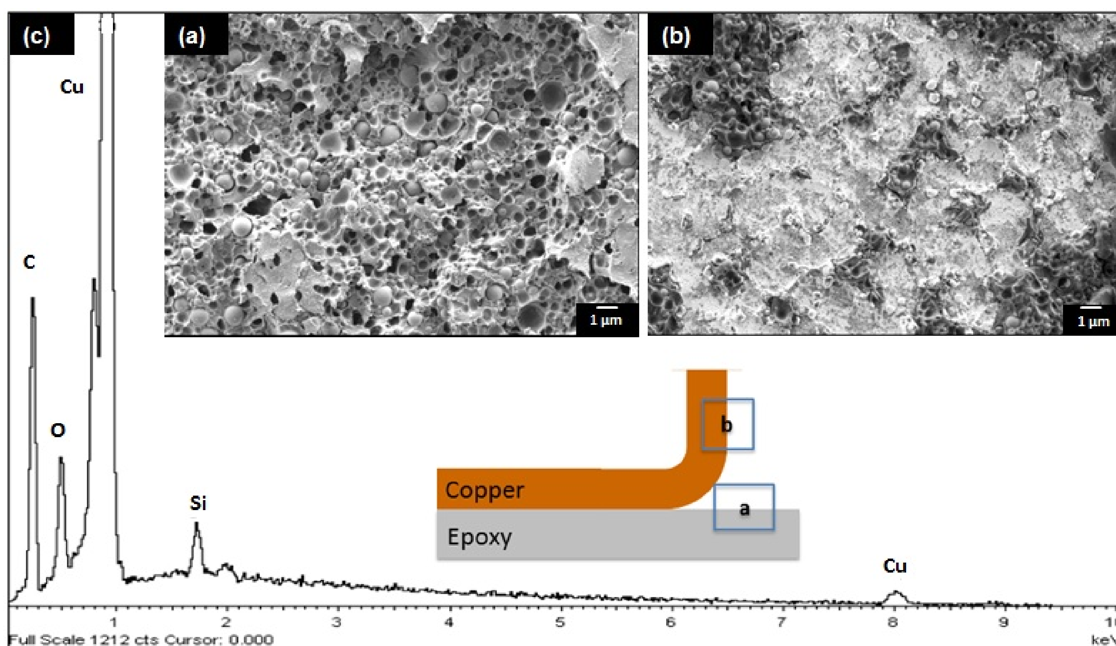

Figure 5. 24 FE-SEM images of the surface morphology of peeled off epoxy polymer treated with *AP-Monoamine M* (a) and copper (b) surface after adhesion evaluation. EDX spectra of peeled copper surface (c)

Furthermore, the peeled copper surfaces from samples treated with 4 g/L *AP-Monoamine M* were characterized by FTIR-ATR spectroscopy. As shown in Figure 5. 25, FTIR-ATR spectra clearly indicate the presence of epoxy polymer residue on delaminated copper surface. Characteristic absorption bands from the pristine epoxy polymer substrate were also found on delaminated copper surface, although the intensity is comparatively lower. Absorption bands at 2965-2873, 1608, 1509, 1036, 915, 831, and 772 cm^{-1} indicate the presence of diglycidyl ether bisphenol A (DGEBA), while broad absorption band at 1070-1090 cm^{-1} corroborate the presence of silica on the peeled copper surface. The obtained FTIR-ATR spectra show a good agreement with electron microscope and EDX results.

The results suggest that the adhesion failure mode is the cohesive failure within the epoxy polymer networks. The strong interaction of amines on the surface of nanoparticles with the epoxy substrate surface, and deposited copper layer results in this strong adhesion. The adhesion is strong enough that the epoxy substrate was destroyed. Consequently, chemical adhesion (chemical bonding interaction) considered as the main contributor to the adhesion enhancement between *AP-Monoamine M* treated epoxy substrates and deposited copper layers.

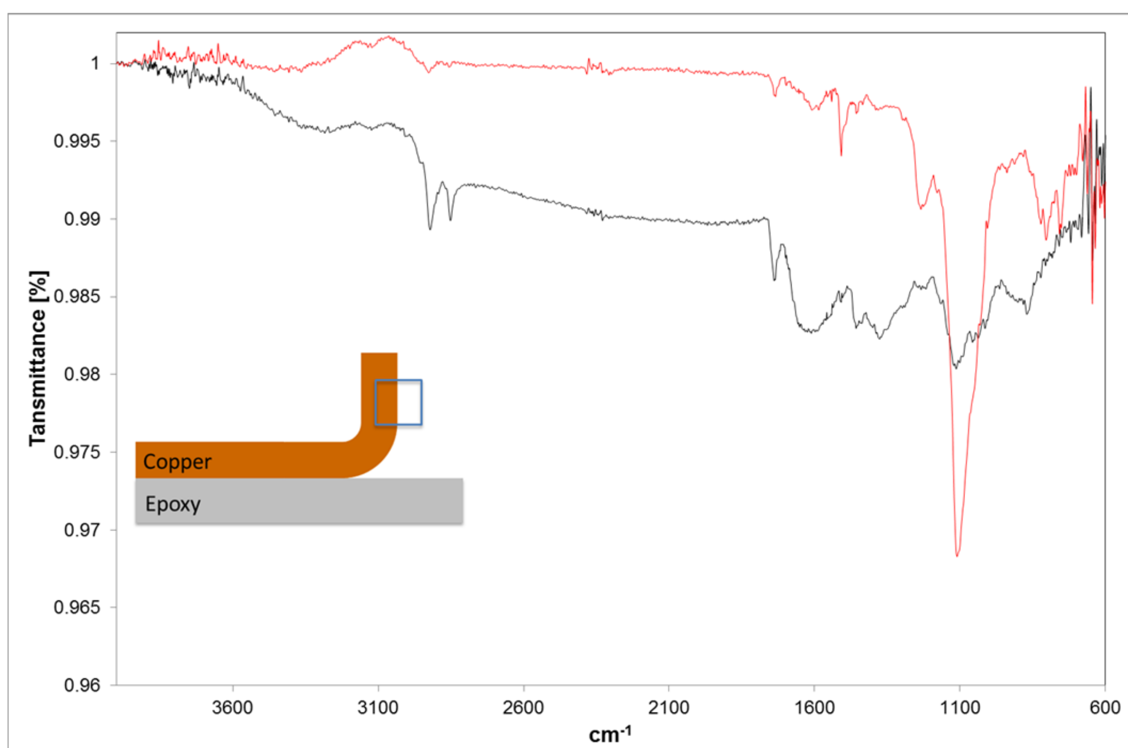

Figure 5. 25 FTIR-ATR spectra of peeled copper surface from sample involving copper deposited on *AP-Monoamine M* treated (red line) and only permanganate treated (black line) of epoxy substrate

The adhesion failure of copper plated on *AP-Monoamine L* treated epoxy substrate was also investigated. The surface of the epoxy substrate after peeling showed minor damage, Figure 5. 26(a). Polymer traces were hardly found on peeled copper surfaces, Figure 5. 26(b). From the back scattered electron signal of scanning electron microscope on the peeled copper surface, it can be seen that the *AP-Monoamine L* particles were imbedded inside the copper layer, see Figure 5. 26(b). Additionally, the EDX signal of the Silicon Kα line at 1.74 keV was visible on the peeled copper layer (Figure 5. 26(c)). This gives clear evidence that *AP-Monoamine L* particle is present on the peeled copper surface.

Contrary to the *AP-Monoamine M*, the adhesion failure of copper on *AP-Monoamine L* treated epoxy substrate involves fracture failure in the epoxy substrate and adhesion failure at *AP-Monoamine L*-epoxy substrate interface. This is mainly due to the low particles coverage on the surface, see Figure 5.20. The amount of attached amine groups on the surface of the silica particles is not high enough to generate high adhesive strength beyond the cohesive strength of the polymer network.

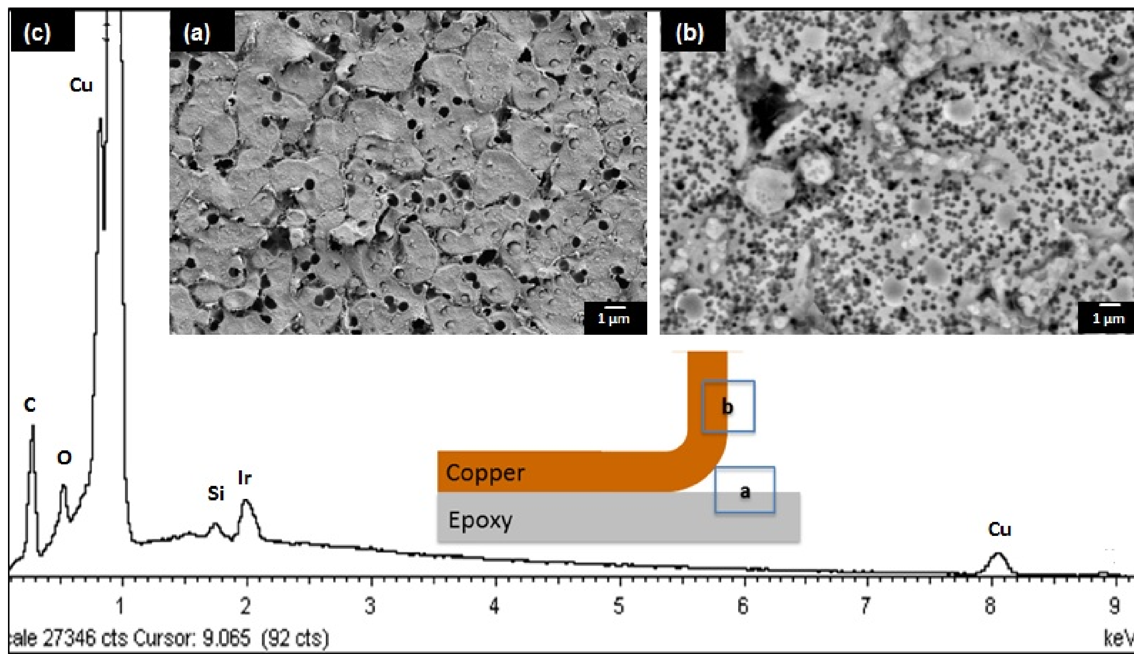

Figure 5. 26 FE-SEM surface morphology image of (a) peeled epoxy polymer treated with *AP-Monoamine L* and (b) the copper surface after adhesion evaluation. Figure (c) is the EDX spectrum of the peeled copper surface

5.3.6. Adhesion reliability of deposited copper on modified epoxy substrate surfaces after stress test

To achieve good adhesion of deposited copper on polymer surfaces, in the initial state is not enough for electronics production. The stability of adhesion during the production process and ageing by the time is one of the concerns in electronics production. In order to study the adhesion reliability of copper on *AP-Monoamine M* treated epoxy substrate, the high accelerated stress test (HAST) or the infra-red reflow test (IR reflow) was performed. In HAST, the plated samples are subjected into oven heat chamber at 130 °C and relative humidity (RH) of 85 % for 96 hours. In IR reflow, the platted samples are placed into an infra-red reflow oven for five times. Details regarding these parameters are described in experimental section (section 5.2.3).

Due to the extremely low peel strength (0.6±0.1 N/cm) of copper plated on only permanganate treated epoxy substrate samples, those samples were not subjected to any stress test. The peel strength of copper on *AP-Monoamine M* treated epoxy polymer after high accelerated stress test (HAST) and infra-red (IR)

reflow test are shown in Figure 5. 27. The sample shows remarkable degradation in peel strength after the test. The peel strength dropped to 4±0.4 N/cm after the sample was subjected to HAST. The sample subjected to IR reflow test exhibits severe degradation of peel strength, from 8.2±0.3 N/cm to 1±0.5 N/cm.

The degradation of the peel strength after the HAST is mainly induced by the water molecules in the humid oven chamber. The transport of water molecules along the polymer/metal interfaces is well documented.[149-151] Penetrated water molecules substitute the chemical bonding between *AP-Monoamine M* and copper, because of the higher interaction energy of water with the copper surface. The magnitude of chemical bonds between water and metal or oxide surfaces is typically in the range of 40 to 65 kJ/mol.[152] This can be seen in Figure 5. 28, where the majority of adhesion failure mode is adhesive failure between *AP-Monoamine M* and copper. Notwithstanding, the adhesion strength after the HAST is still strong enough to exceed the polymer cohesive strength. As a result, some traces of epoxy polymer are present on the peeled copper surface, see Figure 5. 28.

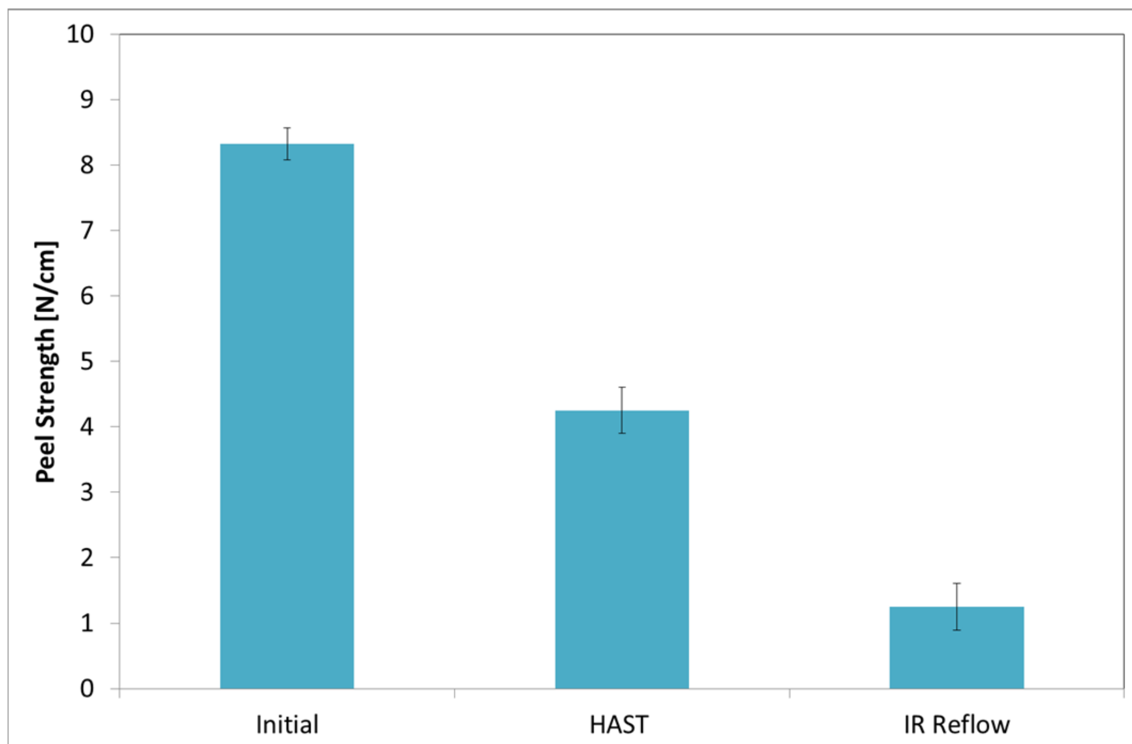

Figure 5. 27 Adhesion strength of copper on *AP-Monoamine M* treated epoxy substrate surfaces after HAST and IR reflow tests

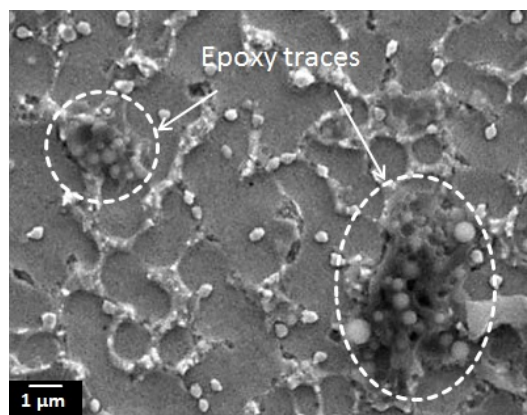

Figure 5. 28 FE-SEM surface morphology image of copper side after HAST. Some parts of epoxy have been removed and transferred to copper surface after peeling. The sample has peel strength of 4±0.4 N/cm

In case of the sample after IR reflow test, the adhesion failure is mainly due to the nature of the epoxy polymer and the copper. At higher temperature, polymer materials such as epoxy resin have a tendency to expand their volume in all directions. The degree of expansion with temperature is defined as the coefficient of thermal expansion (CTE). The difference in the thermal expansion coefficient between the epoxy polymer (α = 117 ppm/°C at 150-240 °C)[74] and the copper (α = 17 ppm/°C at 150-240 °C)[153] layer results in tensile stress across the interface, and leads to extensive coalescence of delamination. The FE-SEM surface morphology image of the peeled epoxy polymer and the copper surface after IR reflow stress test are shown in Figure 5. 29. It is apparent that the *AP-Monoamine M* remains on the epoxy substrate surface (Figure 5. 29 (a)). By looking at the FE-SEM image in Figure 5. 29(a) and (b), the failure locus suggests that adhesion failure between *AP-Monoamine M* and copper layer occurs. This can be confirmed from by the EDX spectrum of the peeled copper side after the IR reflow test (Figure 5. 29(c)), showing no evidence for the presence of silica on the peeled copper surface side. A sphere with the size of around 200 nm at the copper surface after peeling is the negative image of cooper plated inside the hole of the epoxy substrate.

The peel strength of copper on *AP-Monoamine L* modified epoxy polymer after the IR reflow test is very low (1±0.2 N/cm), in comparison with the initial peel strength (4.7±1.1 N/cm). The FE-SEM surface morphology image of peeled copper and *AP-Monoamine L* modified epoxy polymer after IR reflow stress test is shown in Figure 5. 30. Contrary to the *AP-Monoamine M* results, nearly no nanoparticles were observed

on the surface of the epoxy polymer after peeling (see Figure 5. 30(a)). When the volume of the polymer expands during the IR reflow, additional mechanical adhesion (an anchoring of one material by filling irregular structure of the other material surface) contributed from the anchoring between copper and *AP-Monoamine M* which is strong enough to overcome the strength of tensile stress across the interface (~150 N/m^2). The adhesion failure between *AP-Monoamine M* and copper can be avoided. Instead, the adhesion failure between epoxy polymer and *AP-Monoamine M* occurs due to the weaker adhesion strength.

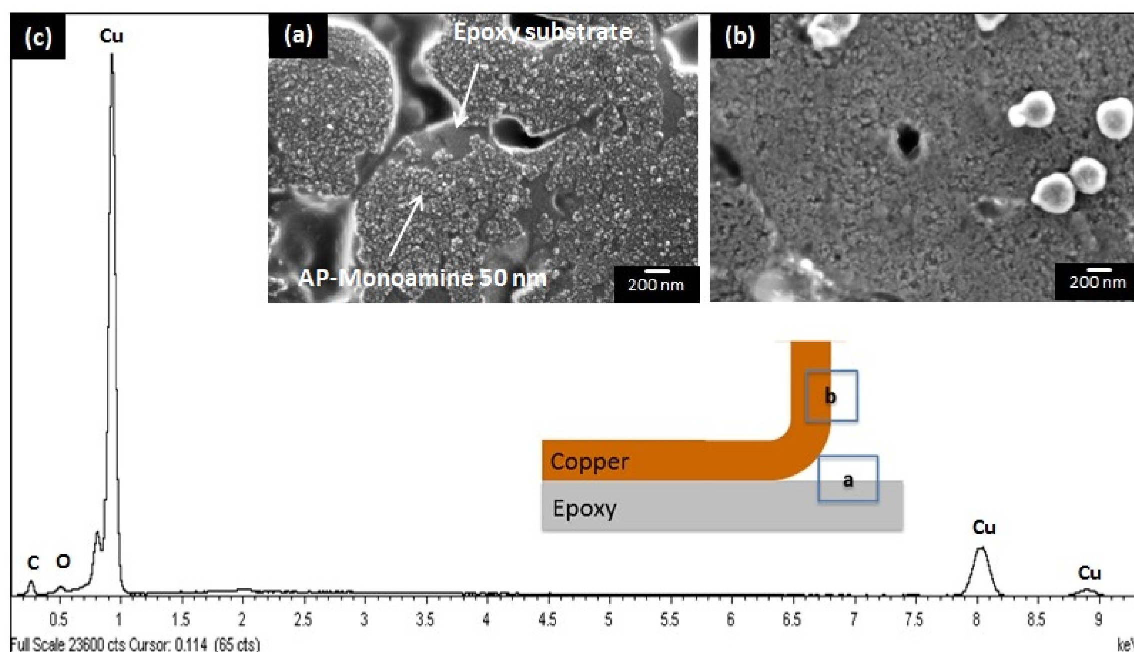

Figure 5. 29 Surface morphology of (a) the peeled epoxy polymer treated with *AP-Monoamine M* and (b) the copper surface after the IR reflow test. Figure (c) is the EDX spectrum of peeled copper surface

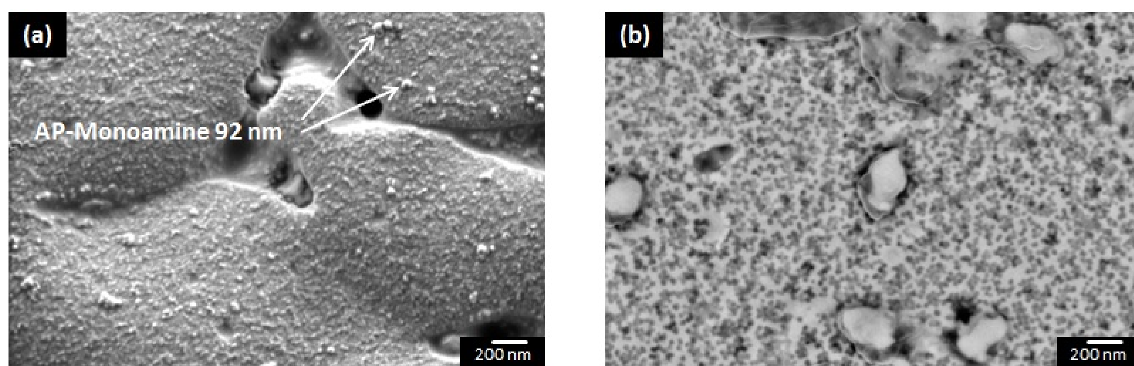

Figure 5. 30 Surface morphology of peeled off epoxy polymer treated with *AP-monoamine L* (a) and copper (b) surface after IR reflow test

5.3.7. The adsorption of palladium species on *AP-Monoamine M* modified epoxy substrate

Since the activation step has to be preceded in order to introduce catalytic species (palladium atoms and ions) on the substrate surface, a study of the interactions between *AP-Monoamine M* and palladium species gives beneficial information about the adhesion mechanism. Therefore, a model experiment was designed to study the influence of *AP-Monoamine M* on the adsorption of palladium species on the epoxy substrate surface, and also on the resulting adhesion strength. The palladium determination was conducted using inductively coupled plasma-optical emission spectroscopy (ICP-OES) and the adhesion strength was determined using a 90° peel strength test. To eliminate the possible effect of palladium ligands in the Neoganth 834 activator, $PdCl_2$ solution with concentration of 200 mg/L (pH1) was used. Figure 5. 31 shows the amount of palladium uptake on *AP-Monoamine M* modified substrate as a function of immersion time in a dispersion with of *AP-Monoamine M* with concentration of 0.8 g/L.

With increasing immersion time of the substrate in *AP-Monoamine M* dispersion, the amount of palladium uptake on the substrate surface also increases (see Figure 5. 31). As demonstrated previously by Charbonnier and coworkers,[33] the presence of nitrogen containing functional groups plays the key role in the adsorption of palladium on polymer surfaces. According to Cruywagen and Kriek,[154] in acidic chloride media (pH<5), $PdCl_4^{2-}$ ions are the main species in the solution. Since amines are always present in protonated form at a pH lower than the pKa of it conjugated acid, electrostatic interaction between $PdCl_4^{2-}$ ions and protonated amine groups ($R\text{-}NH_3^+$) takes place in aqueous solution (see Figure 5. 32). The reactivity of *AP-Monoamine M* treated substrate with the $PdCl_4^{2-}$ highly depends on the amount of amine groups on substrate surface, from higher particles coverage. Consequently, longer immersion time in *AP-Monoamine M* dispersion result in higher amount of palladium uptake on the polymer surface.

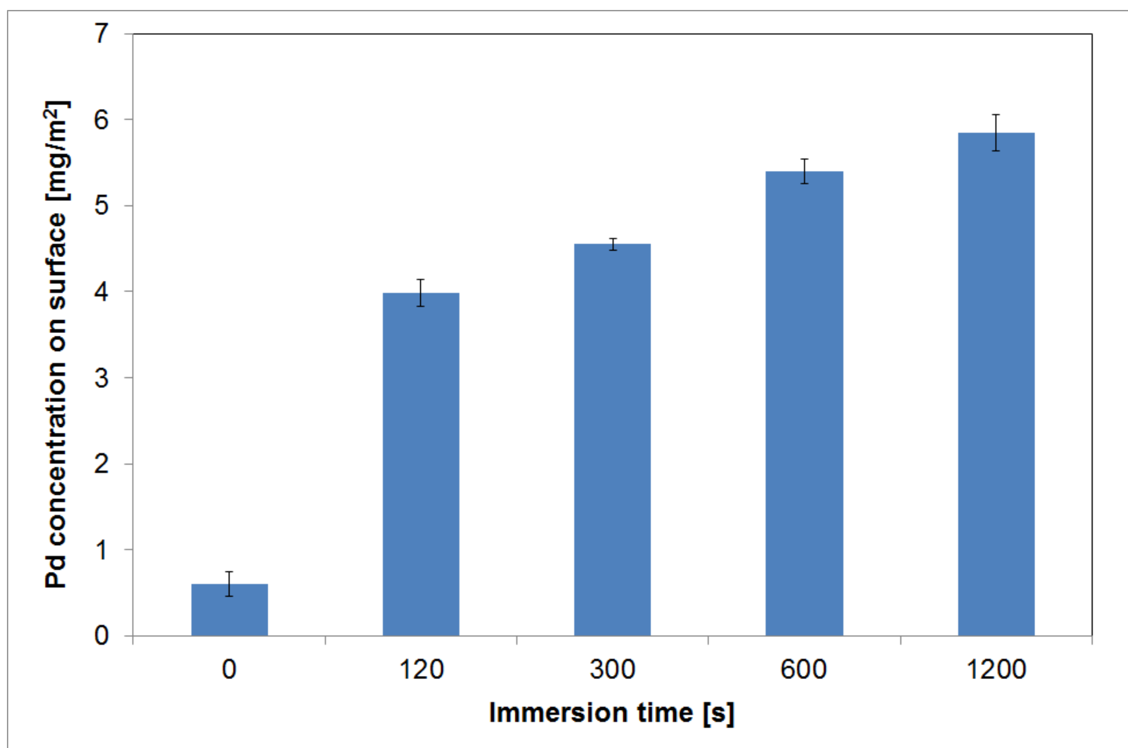

Figure 5. 31 Palladium ion concentrations on the epoxy substrate surface as a function of immersion time in AP-Monoamine solution. 0.8 g/L of *AP-Monoamine M* was used

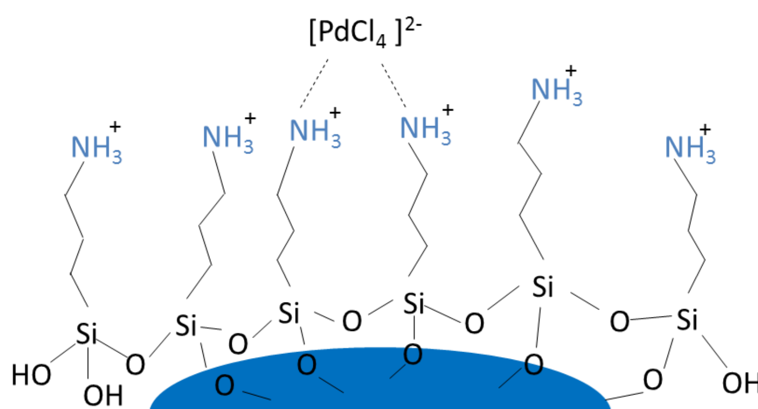

Figure 5. 32 Scheme of the reaction mechanism proposed for palladium chemisorption on epoxy substrate surfaces containing aminopropyl functionalized silica

Figure 5. 33 shows the change of palladium uptake and copper adhesion strength on an epoxy substrate surface treated with *AP-Monoamine M* (c= 4 g/L) as a function of the concentration of the palladium chloride solution. The amount of Pd on the surface gradually increases with increasing concentration of the palladium chloride solution and reaches a plateau when the concentration of the palladium

solutions is higher than 200 mg/L. Furthermore, similar adhesion behavior was obtained for complete concentrations range.

These results indicate that the chemical interaction between Pd (II) or Pd (0) species and aminopropyl groups of functionalized silica nanoparticles is not the only contributions to the adhesion strength enhancement. Since amine groups ($-NH_2$) have good affinity for the Cu (II), [134, 155] it is possible to get an interaction between amine and Cu (II) species as one of the contributions to the adhesion strength enhancement. Moreover, it was shown in the previous study,[156] that amine groups also have favorable interaction with Cu (0) species.

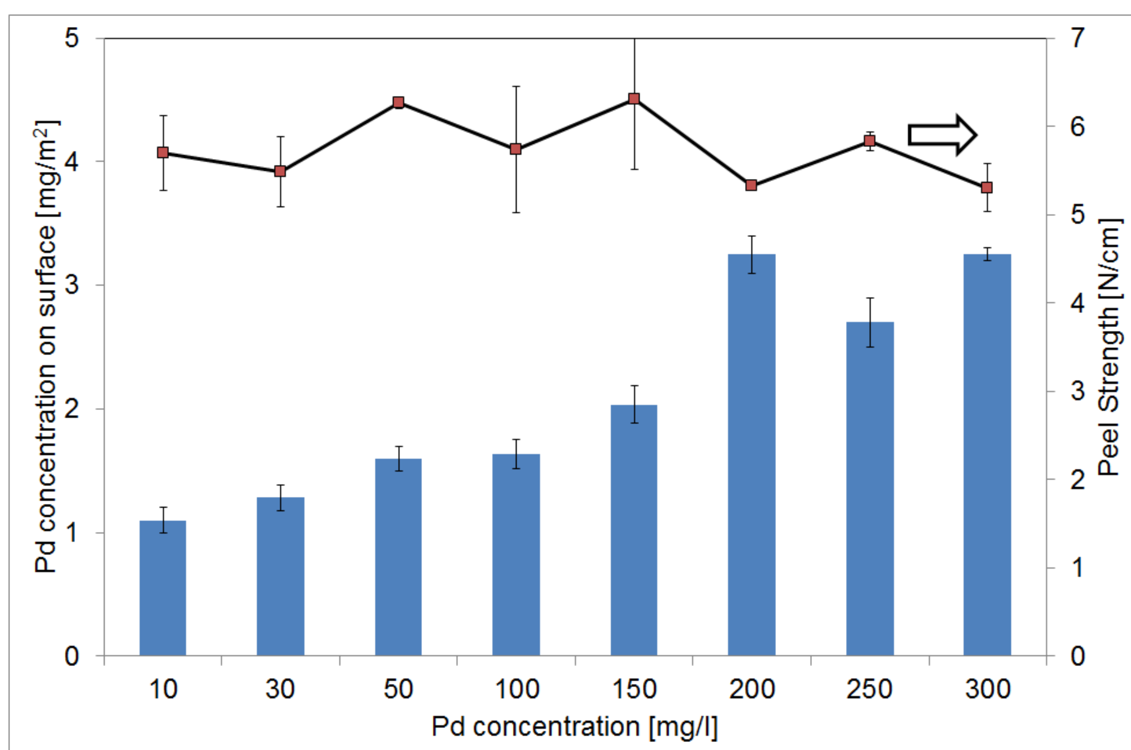

Figure 5. 33 Pd concentration on polymer surface (Bar) and adhesion peel strength (Line) as a function of the concentration of the palladium chloride solution. The polymer substrates were modified with a dispersion of *AP-Monoamine M* with concentration of 4 g/L

5.4. Conclusions

In this chapter, a new method for modifying epoxy substrate for copper metallization using functionalized silica nanoparticles was described. Functionalized silica nanoparticles were used to enhance the adhesion between copper and the modified epoxy substrate. Functionalized silica nanoparticles were coated on the surface of permanganate pretreated epoxy substrate prior to copper deposition. By choosing appropriate functional groups on the silica nanoparticles surface, chemical interactions between functionalized silica and the epoxy substrate can be obtained, incorporating new functionalities on the surface, which can serve as ligands to the metal ions for the electroless copper deposition, and thus enhanced the adhesion between the epoxy substrate and copper. The adhesion strength between copper and the epoxy substrate modified with aminopropyl functionalized silica nanoparticles (*AP-Monoamine M*) increases with the nanoparticles concentration, the nanoparticle dispersion temperature and the substrate immersion time during dip coating. A maximum peel adhesion strength of about 9.2±0.3 N/cm was achieved. As demonstrated, the adhesion strength is strongly depended on the *AP-Monoamine* particles coverage at the substrate surface. From the peeled samples, it was confirmed that the failure resulted in the destruction of epoxy resin. Furthermore, it was found that the uptake of palladium species on the epoxy substrate increases ten times the after treatment with aminopropyl functionalized silica nanoparticles (*AP-Monoamine*) compared to the only permanganate treated epoxy substrate.

Chapter 6 - Surface modification of polyimide films with aminopropyl functionalized silica nanoparticles for improvement of adhesion with deposited copper

6.1 Introduction

Polyimides are the most common thermoplastic material used as substrates in flexible printed circuit board production because they have good process ability, low dielectric constant, high thermal stability, low moisture adsoption, and high mechanical strength.[29, 77, 157] Nonetheless, because of the inertness of polyimide surface, the adhesion of metal deposited directly onto polyimide is poor. Numerous methods for modifying polyimide surface have been developed and applied. These methods include wet chemical treatment using alkaline solution such as KOH,[158-160] plasma treatment[157, 161-162], and polymer grafting.[29, 31] Wet chemical treatment in alkaline solution is the most common approach to solve the adhesion problem, because the process is simple and inexpensive. In particular, polyimide surface treated with KOH at elevated temperature, gives potassium polyamate surface, which is converted to polyamic acid by dilute HCl treatment, can improve the adhesion between deposited copper and polyimide films (Figure 6.1).[163]

Unfortunately, adhesion strength achieved by this treatment does not meet the requirement set by microelectronics industry (peel strength > 6N/cm). Moreover, this treatment does not only influence the polymer surface but also opening the imide ring in the bulk of the material.[164] As a result, retaining the metal film on polyimide with good adhesion is difficult, especially against humid conditions. Therefore, new ways to enhance the adhesion of copper to polyimide film are desired.

In this chapter, aminopropyl functionalized silica nanoparticles (*AP-Monoamine*) are adsorbed on the surface of permanganate treated polyimide film (Kapton® 200 H). The adhesion of electroless copper on *AP-Monoamine* modified polyimide film is investigated. Peel strength higher than 6 N/cm need to be achieved. *AP-Monoamine* treatment is use to introduce high concentrations of active amines to the polyimide surface. The primary amine groups of *AP-Monoamine* help this particles to be anchored, and are thought to interact with palladium catalyst used for electroless copper deposition, as well as the deposited electroless copper. Process

scheme of electroless copper deposition on *AP-Monoamine* modified polyimide film is described in Figure 6.2. After surface oxidation treatment by alkaline permanganate, *AP-Monoamine* is adsorbed on the surface of the film. Once the polyimide film treated with *AP-Monoamine*, palladium catalyst is adsorbed on the surface prior to electroless copper deposition step.

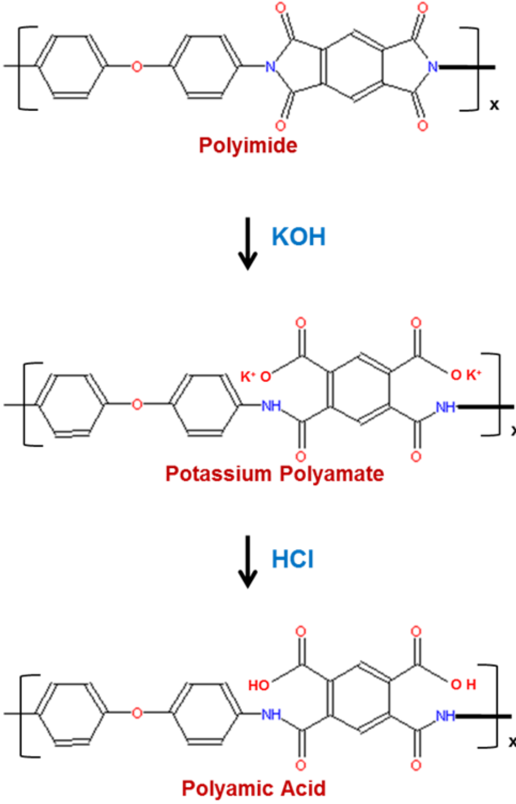

Figure 6.1 Polyimide surface treated with KOH at elevated temperature gives potassium polyamate, which is then converted to polyamic acid with diluted HCl, ligand for deposited metal adhesion.[163]

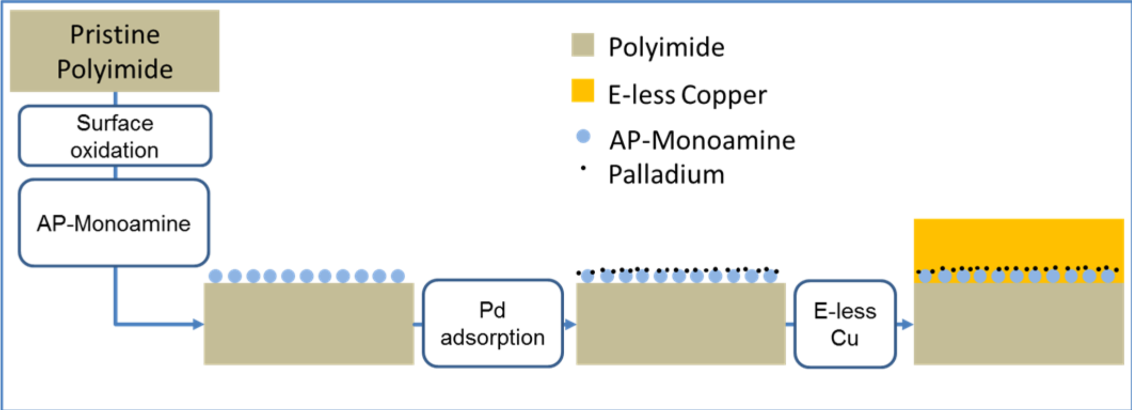

Figure 6.2 Process scheme of electroless copper deposition on *AP-Monoamine* modified polyimide film

6.2 Experimental

6.2.1 Materials

Polyimide films

The polyimide film used in this present work was poly [N, N'-(oxydiphenylene)pyromellitimide], Kapton® 200 H purchased from DuPont chemical company. It was received in a roll of 300 mm in width and 50 μm in thickness. The polyimide films were cut into dimensions of 44 cm x 77 cm. The polyimide films were adhered on rigid panels using a double sided polyimide tape (double coated Kapton® Polyimide film, Nitto Denko Co.) for further processability.

Chemicals

Isopropanol was purchased from Merck chemicals. Aminopropyl functionalized silica nanoparticles (*AP-Monoamine*) with the size of 14±3, 18±3, and 44±6 nm were used to modify polyimide film surface. Preparation and characterization are explained in Chapter 4. Pretreatment and plating chemistry were provided by Atotech Deutschland GmbH and listed as:

1. Atotech palladium chloride solution (4 %w/w)
2. Atotech Securiganth P 500 permanganate etch ($NaMnO_4$ and NaOH)
3. Atotech reduction solution Securiganth P 500 (manganese oxide reducer)
4. Atotech Neoganth 834 activator (ionic palladium)
5. Atotech Neoganth WA reducer (palladium reducer, dimethylaminoborane)
6. Atotech Printoganth PV (electroless copper, formaldehyde reduction agent)
7. Atotech Cupracid TLC (galvanic copper)

6.2.2 Sample preparation

The surface of polyimide film was cleaned with isopropanol in an ultrasonic bath for five minutes at room temperature before use.

Permanganate surface activation

The samples were immersed into a permanganate solution (Atotech Securiganth P 500 permanganate etch) at 80 °C for one minute, followed by immersion into an oxides removal solution (Atotech P 500 reduction solution) at 50

°C for 1 min. The samples were rinsed with DI water after every step. The samples were finally dried with dry air at room temperature.

Treatment of aminopropyl functionalized silica (AP-Monoamine) on polyimide film surface

Permanganate activated samples were immersed into freshly prepared solution containing aminopropyl functionalized silica nanoparticles (in ethanol; pH4-5) at various concentrations for various immersion times. The suspension temperature was kept constant at 60 °C. The samples were withdrawn from the suspension with a speed of 180 mm/min. The panels were finally annealed in an oven at 130 °C for 10 minutes.

Electroless and electrolytic deposition of copper on modified polyimide films

The samples were treated in similar way to those of epoxy substrate (Chapter 5), except of immersion time in electroless copper solution, 5 minute at 35 °C. A copper layer of about 200 nm was deposited by this condition.

After modification with functionalized silica nanoparticles, the polymer substrates were activated with a palladium catalyst prior to electroless copper deposition. The commercially available ionic palladium catalyst solution Atotech Neoganth 834 activator (palladium catalyst solution in an alkaline media) was used in this work. The surface modified epoxy polymer panels were immersed into the prepared palladium catalyst solutions for 4 min at 40 °C, and then rinsed three times with distilled water. The adsorbed palladium ions Pd (II) on modified epoxy polymer surface were reduced to Pd^0 by using Atotech Neoganth WA reducer (palladium reduction solution containing dimethylaminoborane) followed by rinsing with distilled water. The typical immersion time for this reduction step is 3 min at 30 °C.

Electroless copper plating was then carried out by using a commercially available electroless plating bath Printoganth PV from Atotech Deutschland GmbH. The typical plating condition is a temperature of 35 °C and 5 min immersion time. A copper layer of about 800 nm was deposited by this condition. After electroless plating, the substrates were washed in copious amount of distilled water for three times, dried and annealed at 150 °C for 1 h. Table 6. 1 shows the process sequence of electroless copper plating on modified polymer substrates.

Table 6. 1 Process sequences of electroless copper plating on modified polymer substrates

Step	Chemistry	Operation Temperature (°C)	Immersion Time (min)
1	Atotech Neoganth 834 activator	40	4
2	Atotech Neoganth WA reducer	30	3
3	Atotech Printoganth PV	35	15

Galvanic copper plating on polymer substrate with electroless copper

Galvanic copper plating was performed using a commercial electrolytic copper plating bath (Atotech Cupracid TLC) at room temperature for 90 min with a current density of 2 A/dm^2. The thickness of plated galvanic copper is around 40 µm. This additional copper layer serves as an anchoring layer for peeling the underlying electrolessly deposited copper. The electroless copper plated polymer substrates were immersed into diluted sulfuric acid (10 w/w% H_2SO_4; 25 °C; 1 min) prior to galvanic plating to remove the existing oxides layer from the surface. Immediately after galvanic copper plating, the films were washed thoroughly with distilled water before annealing at 180 °C for 1 h.

6.2.3 Surface characterization

Fourier Transform Infra-red-Attenuated Total Reflectance (FTIR-ATR)

The chemical structure of polymer surface was characterized with an FTIR-ATR spectrometer (Perkin Elmer Spectrum^{TM} 100 FTIR) equipped with a DTGS (deuterated triglycine sulfate) detector and a single reflection Ge-ATR (attenuated total reflectance with Germanium crystal) unit. The angle of incident of the beam is 45 °. In general, pristine and modified polymer substrates were measured from 4000-600 cm^{-1} with resolution of 4 cm^{-1}. Each sample was scanned for 32 times.

Atomic Force Microscopy (AFM)

Taping mode AFM was performed using a Digital Instruments Nanoscope III microscope. All AFM measurements were made in ambient environment condition

using nanocsope cantilever with single crystal silicon tips. The properties of the cantilever are summirized in Table 6. 2. The surface roughness was quantified by using root mean square (R_{rms}) roughness calculations (see Chapter 3).

Table 6. 2 The property of cantilever with single crystal silicon tips used in AFM measurement

Property	Nominal Value	Specified Range
Thickness /μm	4	3.0 - 5.0
Mean Width /μm	30	22.5 - 37.5
Length /μm	125	115 - 135
Force Constant /(N/m)	42	10 - 130
Resonance Frequency /kHz	330	204 - 497

Field Emission Scanning Electron Microscopy (FESEM)

The surface topography of epoxy polymer surface observation with field emission scanning electron microscope was obtained using Carl Zeiss Microscopy Supra® series. All images were collected in ultrahigh vacuum with an acceleration potential between 1 kV and 10 kV. Secondary electron and back scatter electron mode detectors were used to record the images. Considering that most of the polymer samples are highly insulating (volume resistivity $\approx 10^{15}$-10^{20} Ω·cm), the accumulation of localized excessive electrons will cause abnormal contrast, image distortion and shift. To overcome this problem, a thin layer of iridium (few nanometers) was deposited on the surface by sputtering to increase the conductivity. Thus, the excess electrons can be conducted.

X-ray Photoelectron Spectroscopy

The measurement was done at Case Western Reserve University (CWRU), Cleveland US. XPS measurements were carried out on a PHI-5000, VersaProbe Scanning X-Ray Microprobe with Al Kα monochromated X-ray source (1486.6 eV) at a constant energy step (0.4 eV, 25 ms/step) and 93.9 eV pass energy. In the case of multiplex scans of C1s, N1s, O1s and Si2p chemical states, energy step (0.1 eV, 45 ms/step) and 23.5 eV pass energy was used. The X-ray source was run at a reduced power of 65 W. The polyimide film samples were mounted on the sample holder with metal mask on the top of the sample. The core-level spectra were obtained at a photoelectron take-off angle of 45 ° with respect to the sample surface. The pressure

of the measurement chamber was maintained at 10^{-8} Torr. N1s was used as the charge reference and the binding energy of this line was set to 400.6 eV.[165]

Evaluation of adhesion strength

The adhesion strength between deposited copper layers and epoxy polymer substrate was studied quantitatively on LTCM-6 series from Chatillon. Standard ASTM D6862 90 ° peel strength test[135] was conducted for adhesion evaluation. All measurements were carried out at peeling speed of 45 mm/min. Each adhesion strength result is the average of at least two measurements for every sample. Normally the results from each measurement should not vary more than 0.5 N/cm.

A number of experiments were performed to test the reliability of adhesion of copper layers aminopropyl functionalized silica treated epoxy substrate under a variety of stress conditions, Highly Accelerated Stress Test (HAST) or infrared reflow oven test (IR reflow) was conducted. The HAST parameter followed a standard classification JESD22-A110-B.[136] The samples were subjected into oven heat chamber at 130 °C and relative humidity (RH) of 85 % for 96 hours. The IR reflow test was carried out five times in an IR reflow oven (Compact nitro B 2100-400), with a temperature profile setup of a standard classification IPC/JEDEC J-STD-020D.[137] The peel strength evaluation was performed after every stress test.

6.3 Results and discussions

6.3.1 Permanganate treatment on polyimide Kapton®200 H films

It was reported in the literature that the surface of polyimide can be modified by using permanganate solution under alkaline condition.[158, 160, 166] In those publications, the influence of alkaline permanganate treatment on the surface of different grade of polyimide films was studied. The chemical structure of three different grade of polyimide films investigated in the literature is shown in Figure 6. 3. Those polyimide films are Kapton®200 H, Upilex®-S, and Eymyd® L30N. For those three grades of polyimide films, alkaline permanganate treatment changes the properties of the film significantly, especially the surface morphology of the film.[158, 160, 166] The average surface roughness of the film increases when the polyimide film is treated with alkaline permanganate solution. Moreover, Baumgartner *et al.,* [166] reported that exposure to alkaline permanganate solution increases the total oxygen concentration at the surface of polyimide film Eymyd® L30N . This was proven by the increase in intensity of oxygen 1s in XPS measurement. He assumed that functional groups such as carboxyl groups and hydroxyl groups were formed on the surface.[166] Therefore, in this work, alkaline permanganate treatment was used for activation of polyimide film prior to *AP-Monoamine* treatment.

In order to understand the influence of alkaline permanganate on the surface chemistry of polyimide film, FTIR-ATR investigation was performed. In ATR techniques, the quantitative analysis is not straight forward, because the Lambert-Beer law is not generally valid.[167] However, by comparing the intensity ratios of bands shown in the same spectrum, some quantitative considerations are allowed.[167] In Figure 6.4, two FTIR-ATR spectra recorded from pristine and permanganate treated polyimide films are shown. After the permanganate solution treatment, the film was immersed into reduction solution for 1 min prior to FTIR-ATR investigation. This step is used to remove the MnO_2 residue which remained on the surface of film. The region with wavelength higher than 1800 cm^{-1} remains approximately the same for both spectra. Refer to appendix 4 (a) for the full FTIR-ATR spectra.

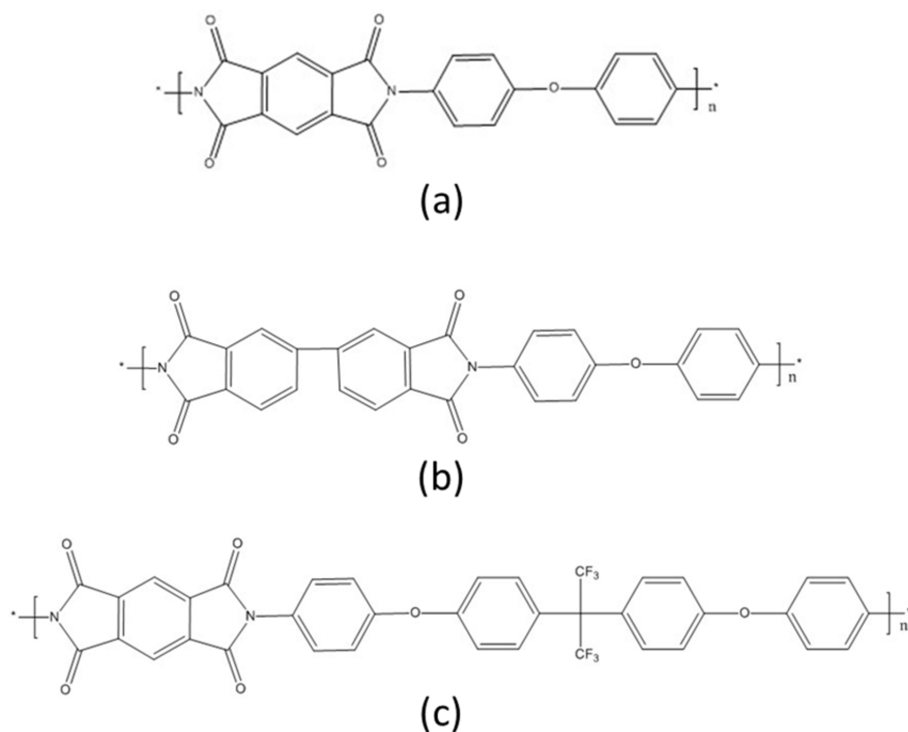

Figure 6. 3 Chemical structure of (a) Kapton®200 H, (b) Upilex®-S, and (c) Eymyd® L30N

The spectrum of pristine polyimide films (black line in Figure 6.4) shows characteristic absorption band due to pyromellitic dianhydride (PMDA) moiety[168] at 1777 cm^{-1} (υC=O in phase), 1717 cm^{-1} (υC=O out of phase), 1379 cm^{-1} (υC-N), 1116 cm^{-1} (υO-C) and 820 cm^{-1} (γ1,2,4,5-C_6H_2). In addition, 1501 cm^{-1} (υ1,4-C_6H_4) and 1248 cm^{-1} (υC-O-C) bands due to 4,4'-oxydianiline (ODA) moiety are observed.[168] The absorption band of the crystalline phase of polyimide was also observed at 1455 cm^{-1} ($\delta(CH_2)C_6H_{11}$). Table 6.3 lists the observed bands and the assignment for some bands. Because of the complex molecular structure of polyimide, some absorption bands are not assigned at this point.

The spectrum of polyimide films treated with permanganate (red line in Figure 6.4) shows characteristic absorption bands similar to those of pristine polyimide film. In general, it is not easy to identify the difference in the two spectra. The same difficulty has also been recognized by other working groups.[160, 169] Changes in absorption bands in between 950-600 cm^{-1} (aromatic C-H bending) were observed, but no further assignment was made. See Appendix 4 (b) for the zoomed view of the spectra. Because of the complexity of the chemical structure, the exact effect of permanganate on polyimide film surface is not clear from the ATR spectrum.

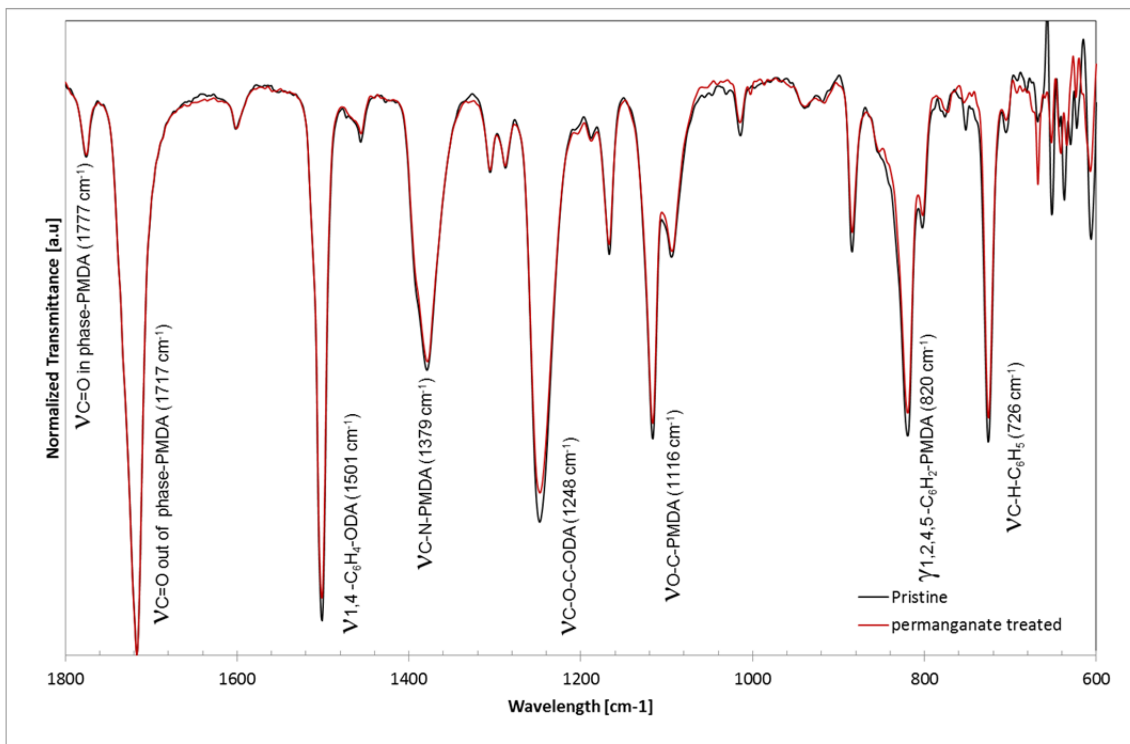

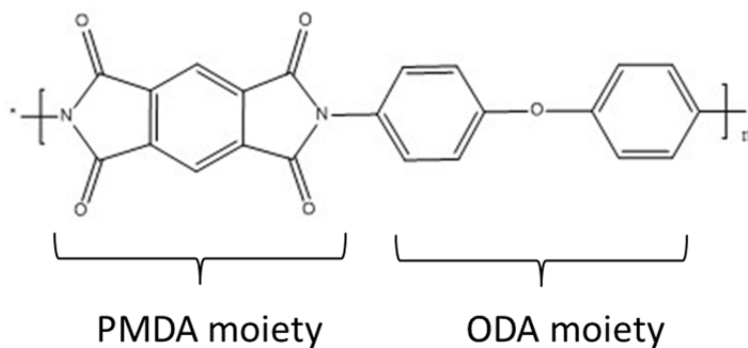

Figure 6.4 Normalized FTIR-ATR spectra of untreated (black) and 1 min permanganate treated (red) polyimide film. All peaks are normalized to the peak at 1717 cm^{-1}

Table 6.3 Characteristic bands of polyimide Kapton® 200 H before and after permanganate treatment, obtained by FTIR-ATR. The assignments are made according to reference[168]

Assignment	Absorption band [cm^{-1}]	
	Pristine	Permanganate treated
C=O stretch in phase (PMDA moiety)	1777	1777
C=O stretch out of phase (PMDA moiety)	1717	1717
C-H stretch (C_6H_5)	1601	1601
1,4-C_6H_4 stretch (ODA moiety)	1501	1501
(CH_2)C_6H_{11} bending[a]	1455	1455
C-N stretch (PMDA moiety)	1379	1379
	1307	1307
	1289	1289
C-O-C stretch (ODA moiety)	1248	1248
	1169	1169
C-O-C stretch (PMDA moiety)	1116	1116
1,2,4,5-C_6H_2 stretch	1017	1017
	883	883
1,2,4,5-C_6H_2 deformation (PMDA moiety)	820	820
	804	804
	778	773
	750	
C-H stretch (C_6H_5)	726	726
		670
	651	651
	638	
1,4-C_6H_4 stretch	606	606

[a]Absorption band assigned for crystalline phase of polyimide

In the ATR spectrum of polyimide film treated with alkaline permanganate, no evidence of the ring opening of imide in PMDA moiety was observed. The same finding has been reported by other working group.[158, 160, 166] The hydrolysis of polyimide to sodium polyamate is expected in alkaline permanganate solution (see

Figure 6. 5(a)). As reported by Kauer *et al.,* 2013[169] the formation of potassium polyamate was observed by FTIR-ATR, for the Kapton polyimide film treated in potassium hydroxide solution. See Appendix 5 for the FTIR-ATR spectra of potassium hydroxide treated polyimide film. In Kauer's work, the polyimide film was immersed into 1 M KOH solution at 80 °C for different immersion time (between 1-10 min). It can be clearly seen that the intensity of imide bands (1778, 1718, 1378, 1118, and 724 cm^{-1}) decreases significantly with increasing treatment time. At the same time, new absorption bands of C=O from amide (1650 and 1537 cm^{-1}) and N-H from amide (3635-3150 cm^{-1}) become more apparent. These observations strongly indicate the transformation of polyimide into potassium polyamate. Kauer observed changes in ATR spectra only when the polyimide films were treated in 1 M KOH solution for 5 min or longer. Since KOH and NaOH are strong bases with similar chemical properties, a similar ring opening effect on polyimide film expected in both KOH and in permanganate/NaOH solution.

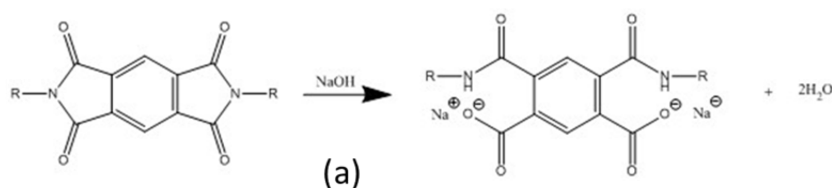

Figure 6. 5 Reaction scheme of hydrolysis of polyimide to sodium polyamate

In alkaline permanganate treatment process, the hydrolysis reaction of polyimide was not observed. This is likely because of the different kinetic of the reaction (hydrolysis by sodium hydroxide and etching by permanganate). With 1 min of treatment time, the etching of polyimide film by permanganate can be observed (in this work), while the hydrolysis of polyimide film can only be observed when the polyimide films were treated in 1 M KOH solution for 5 min or longer (Kauer's[169] work). With the process condition used in this work, the etch rate of the surface of polyimide film is faster than the hydrolysis reaction of the polyimide. Hence, there is no ring opening of imide in PMDA moiety was observed in ATR.

To support the FTIR-ATR results, the same polyimide samples were also characterized by monochromatized X-ray photoelectron spectroscopy. In Figure 6. **6**

the XPS survey scans of pristine and permanganate treated polyimide films are shown. Before permanganate treatment (pristine), the spectrum shows the presence of four elements, C1s (73.6 %), O1s (19.6 %), N1s (6.7 %), and Si2p (0.1 %). Following the permanganate treatment, three elements were present, C1s (74.6 %), O1s (18.7 %) and N1s (6.7 %). No Mn peaks from permanganate was observed. No major composition changes were observed. The appearance of trace amount of Si2p on the pristine polyimide film may be because of the contamination during storage of the film.

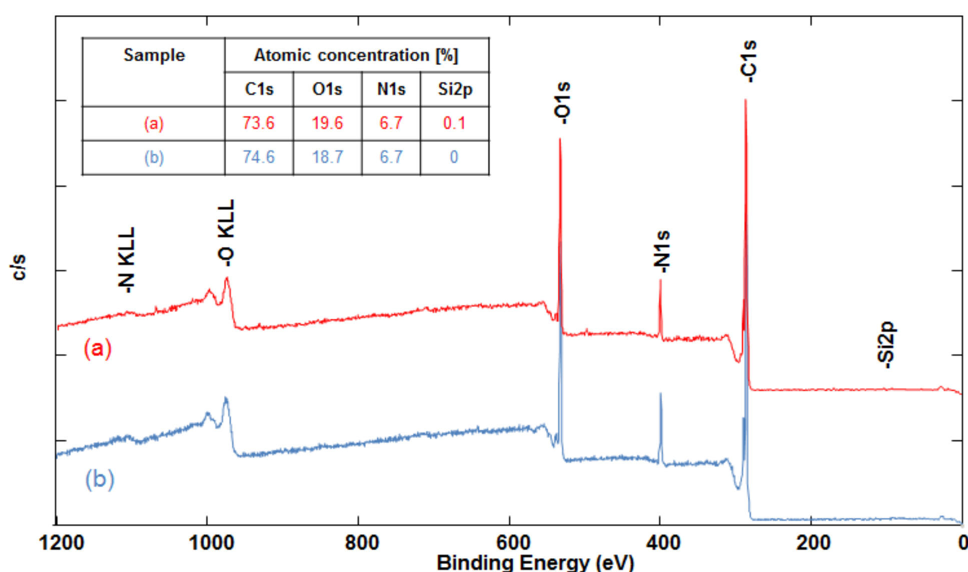

Figure 6. 6 XPS survey scan of (a) pristine and (b) permanganate treated polyimide films

A detailed analysis of the binding states and chemical shifts of the C1s, O1s and N1s signals of the pristine polyimide film are shown in Figure 6. 7 and Figure 6. 8. In general, the atomic and molecular compositions of the outermost 3-10 nm layers of the surface were analyzed. The obtained binding energies of C1s, O1s and N1s compared to those in the literature[170] are listed in Table 6. 4. Based on the schematic drawing of the repeat unit of PMDA-ODA (Figure 6. 7 (a)), the spectra were curve fitted and each curve was assigned to the corresponding environment of the polyimide. The separation of the C1s signal into six carbon species was not possible, because of the resolution of the spectrum (Figure 6. 7 (b)). Therefore, following the analysis by Wolany *et al.*,[165] the curve was fitted into only three C1s chemical states. The peak at 284.8 eV is attributed to the aromatic C-H of ODA (C1), 285.8 eV is attributed to the sum peak of the aromatic C-H of PMDA (C2), C-N (C3),

aromatic state of PMDA (C4) and C-O-C (C5), and the peak at 288.7 eV is attributed to the C=O state (C6). In Wolany's work, a similar polyimide film, Kapton 200 FPC-E was investigated.

In the high resolution analysis of O1s (Figure 6. 8 (a)), the O1s was resolved into two chemical states. The component 1 (O1) with higher binding energy at 533.4 eV corresponds to oxygen in C-O-C environment, and the component 2 (O2) with lower binding energy at 532.1 eV corresponds to oxygen in a C=O environment. The only peak that was obtained for N1s at 400.6 eV is attributed to C-N (N1), Figure 6. 8 (c).[170]

For the polyimide films treated with alkaline permanganate, no new species of C1s (Figure 6. 7 (c)), O1s (Figure 6. 8 (b)), and N1s (Figure 6. 8 (c)) were detected. The positions of the peaks of different chemical states were similar to those of the pristine polyimide film (see Table 6. 4). It was expected that alkaline permanganate treatment would lead to a ring opening and hydrolysis reaction of polyimide. Through this reaction, the imide groups of polyimide should be converted to carboxylic acid and amide groups (polyamic acid). This should lead to a substantial change in the C1s, O1s and N1s peaks in the XPS measurement.[165] Two carbonyl peaks at 287.9 eV (carboxylate carbon) and at 289 eV (amide carbon) are well separated in polyamic acid.[171] A higher energy O1s peak around 533 eV should also appear.[171] This peak is assigned to the hydroxyl oxygen in the carboxylate groups. The O1s peak for the carboxylate group is too close to the one at 533.4 eV (C-O-C), and it is therefore difficult to separate those peaks into two individual peaks. Furthermore, the N1s peak at 400.6 eV should be shifted to a lower binding energy of around 399.8 eV as a result of the conversion of imide to amide.[171]

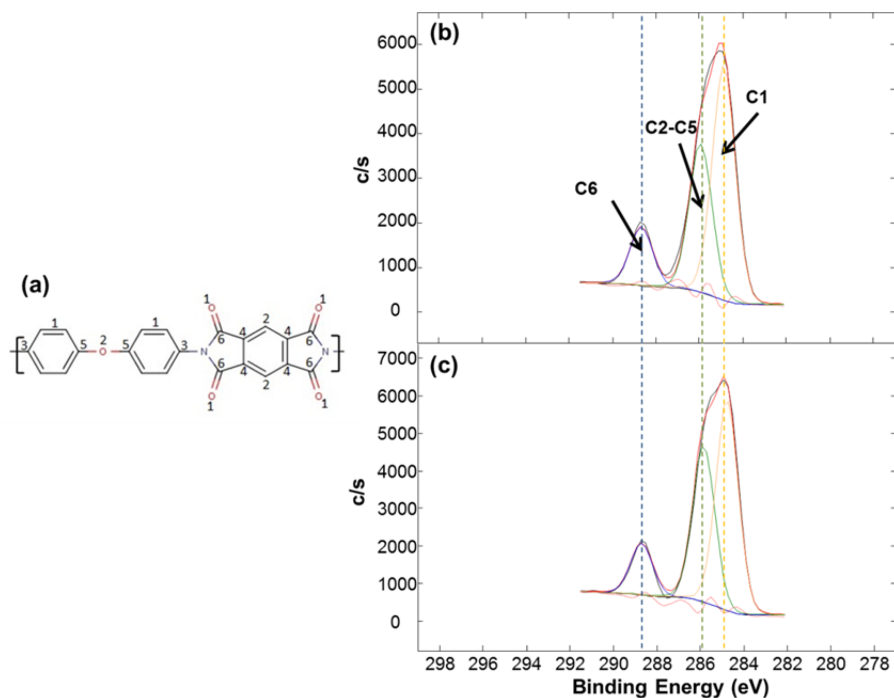

Figure 6. 7 (a) Binding state of the carbon and oxygen atoms in the polyimide repeat unit.[170] XPS C1s spectra for (b) pristine and (c) permanganate treated polyimide films. The dashed line is only shown for a better observation of the peak of the fitted lines

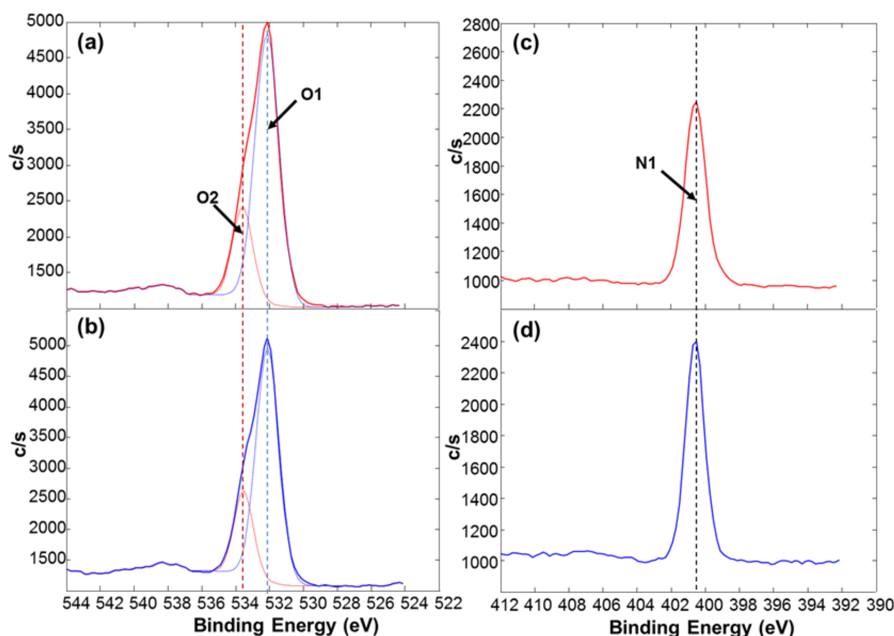

Figure 6. 8 The XPS O1s and N1s spectra of (a) and (c) pristine, and (b) and (d) permanganate treated polyimide films. The dashed line is only shown for a better observation of the peak of the fitted lines

Table 6. 4 XPS chemical states analysis for C1s, N1s and O1s signals of pristine polyimide Kapton® 200 H

Signal	Component	E_B [eV] Briggs *et al.*[170]	E_B [eV] Wolany et al.,[165]	E_B [eV] This work	
				Pristine	Permanganate treated
C1s	C1 (C-H aromatic ODA)	284.7	284.8	284.8	284.8
	C2 (C-H aromatic PMDA)	285.6			
	C3 (C-N)	285.7	285.6	285.8	285.9
	C4 (aromatic PMDA)	285.8			
	C5 (C-O-C)	286.3			
	C6 (C=O)	288.6	288.6	288.7	288.7
O1s	O1 (C=O)	532.0	532.0	532.1	532.1
	O2 (C-O-C)	533.3	533.3	533.4	533.4
N1s	N1 (C-N)	400.6	400.6	400.6	400.6

The component ratios, calculated from peak areas of pristine and polyimide films treated with permanganate are compared and shown in Table 6. 5. In general, the polyimide films treated with permanganate show similar component ratio to that of pristine polyimide. The measured ratios of C1s component C1 (C=O) relative to other C1s components of pristine polyimide films are lower than the theoretical value. The measured ratio was 13 % whereas the theoretical ratio was 18 %. The discrepancy in the measured C=O ratio was observed in the O1s component as well. The ratio between O1s O1 (C=O) to O2 (C-O-C) was 71 % to 29 %, which is 80 % and 20 % theoretically. The two components are separated by about 1.4 eV, and it may be difficult to conclude with definitive values for polymer samples such as ours. For pristine PMDA-ODA (pyromellitic dianhydride oxydianiline) and BPDA-ODA (biphenyl tetracarbocylic acid dianhydride-p-phenylene diaminophenyl) this difference was also observed by other research groups.[172-176] The lower value of carbonyl could originate from several causes. Firstly, polyimide with no broken bonds, chain formations or cross linking was assumed in calculated structure. The hydrogen bonding or crosslinking might exist in bulk of measured polyimide film.[172] Secondly, the presence of isoimide species.[173] The replacement of carbonyl oxygen by

nitrogen leads to reduction in carbonyl and ether oxygen ratio (Figure 6. 9). Thirdly, shake-up and shake-off satellite in C1s and O1s spectra in XPS measurement.[174] Lastly, the discrepancy can be result from the adsorption of environmental species on the surface (hydrocarbons contaminants).[175]

Table 6. 5 The component ratio of polyimide surface of pristine and permanganate treated films, and theoretical values

Signal	Component	Area [%]		
		Pristine	**Permanganate**	**Theoretical**
C1s	C1	53	50	36
	C2-C5	34	37	46
	C6	13	13	18
O1s	O1	71	70	80
	O2	29	30	20
N1s	N1	100	100	100

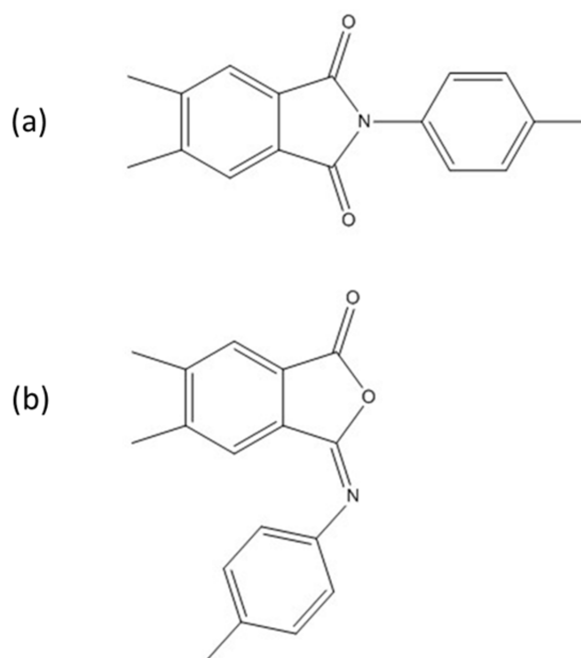

Figure 6. 9 Chemical structure of (a) imide and (b) isoimide.

Although changes of the chemical composition of the surface of polyimide film after permanganate treatment is not easy to be observed with FTIR-ATR or XPS, the surface morphology of the polyimide film shows a noticeable change in surface roughness after alkaline permanganate treatment. AFM images of the surface

morphology of untreated and permanganate treated polyimide film are shown in Figure 6.10. The root mean square roughness (R_{rms}) calculated.

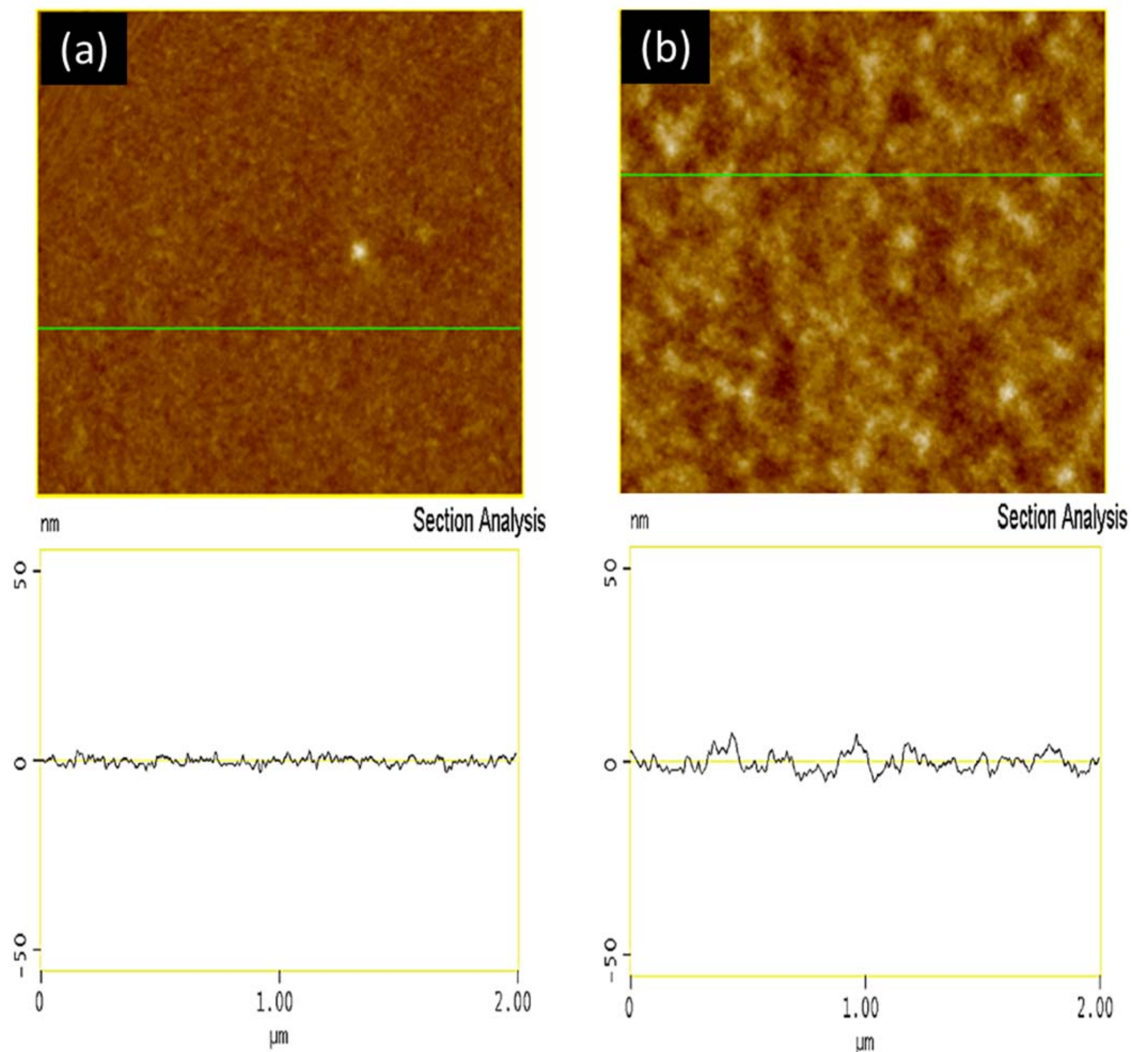

Figure 6.10 AFM images of the surface morphology of untreated (a) and permanganate treated for 1 min (b) Kapton®200 H polyimide film. A measuring window of 2x2 μm^2 was used. The surface roughness of the polyimide film increases after permanganate treatment from R_{rms} = 1.1±0.1 nm to R_{rms} = 2.6±0.3 nm

The surface of pristine polyimide film is very smooth, with R_{rms} = 1.1±0.1 nm (see Figure 6.10(a)). The polyimide film after permanganate treatment shows an increase in surface roughness, to R_{rms} = 2.6±0.3 nm (Figure 6.10(b)). The surface was etched uniformly, and some recesses were created on the film surface. It was also noted that the wettability of the polyimide film increased tremendously after 1 min of alkaline permanganate treatment. This was observed optically during a rinsing step with water after the permanganate treatment. Kauer *et al.,* 2013[169] have investigated the change of the contact angle of water on a polyimide film

(Kapton®200 H) surface. The water contact angle reduces from 77 ° to 45 ° after 1 min immersion in alkaline permanganate solution. With longer exposure, the contact angle does not change significantly. Additionally, Kauer *et al.,* 2013[169] have also observed that the weight of polyimide film decreased, to 11 % of its initial mass, after 1 h exposure in alkaline permanganate solution. In comparison, polyimide film exposed to 1 M KOH for 1 h showed no significant change in weight.

In alkaline permanganate solution, the polyimide film undergoes chain cleavage or etching rather than a simple reaction of ring opening of the imide (hydrolysis). This can be proven from the investigation result in AFM (surface roughness increase) after 1 min treatment. The etch rate of polyimide film by alkaline permanganate is much faster than the ring opening reaction of imide by base NaOH. Alkaline permanganate treatment at 80 °C for 1 min is sufficient to change the properties of the Kapton®200 H polyimide film surface. Through the treatment, the roughness and the wettability of the film surface increases. For hydrophilic nanoparticles like aminopropyl functionalized silica (*AP-Monoamine M*), the particle adsorption on the surface would influenced strongly by the wettability of the surface. The higher the wettability the better for *AP-Monoamine M* adsorbed on the surface.

6.3.2 Polyimide film surface modification with aminopropyl functionalized silica nanoparticles (*AP-Monoamine*)

In this section, polyimide films treated with permanganate were immersed into freshly prepared dispersion containing aminopropyl functionalized silica nanoparticles (*AP-Monoamine M*). As measured by TEM, the diameter of *AP-Monoamine M* is 18±3 nm. Please refer to Chapter 4 for the properties of *AP-Monoamine M*.[177] The *AP-Monoamine M* particles were deposited by dip-coating, and the process conditions were adapted from that for of ABF-GX 92 described in Chapter 5. The temperature of *AP-Monoamine M* dispersion was kept constant at 60 °C. The films were withdrawn from the suspension with a speed of 180 mm/min. The films were annealed in an oven at 130 °C for 10 min. The surface morphology of the films was investigated by AFM and FE-SEM, and the chemical composition of the surface was determined with FTIR and XPS.

Figure 6. 11 shows FE-SEM images of polyimide film treated with *AP-Monoamine M* dispersion at four different concentrations: 0.8 g/L, 1.6 g/L, 4 g/L and 8

g/L. The polyimide films treated with permanganate were immersed in an *AP-Monoamine M* dispersion for 5 min. As can be seen in Figure 6. 11, the particles distributed uniformly on the surface of film. At all four concentrations some aggregates of the particles were visible at the surface. The aggregates might have formed in the dispersion during the synthesis of *AP-Monoamine M* (discussed in Chapter 4), and this can be concluded from the much larger Z-average measured by DLS (52 ± 1 nm) than the average diameter measured by TEM (18 ± 3 nm). It was noticed that the particle coverage on the surface increases with the concentration. As the concentration of *AP-Monoamine M* increases, there are more particles per unit volume, and thus the probability of interaction between particles and the film surface. Hence, higher surface coverage of *AP-Monoamine M* particles can be obtained at higher concentration of *AP-Monoamine M*. When a concentration of 0.8 g/L was used, big parts of the surface of the film were not covered with *AP-Monoamine M* particle (Figure 6. 11(a)). When the concentration was doubled (1.6 g/L), the surface of the film is almost completely covered with nanoparticles, leaving only some areas open (Figure 6. 11 (b)). At a concentration of 4 g/L *AP-Monoamine M*, the surface appears to be completely coated, and at 8 g/L *AP-Monoamine M*, the FE-SEM image appears similar to that obtained for a concentration of 4 g/L, but maybe multilayer of nanoparticles has been formed (Figure 6. 11 (c) and (d)).

The interaction force between *AP-Monoamine M* particles and polyimide film is the electrostatic attraction. This attraction is between the positively charged protonated amino groups of *AP-Monoamine M* and the negatively charged Kapton® polyimide film surface[177] under acidic condition (pH<7). The pH of all dispersion in different concentrations used in Figure 6. 11 of *AP-Monoamine M* are between 4 and 6. The formation of multi-layer of particles on the surface of polyimide film treated with high concentration of *AP-Monoamine M* can be explained in two ways:

First, not all particles of *AP-Monoamine M* have the same amount of positive charge on the surface. The measured zeta potential in Chapter 4 described the average amount of surface charge of 4 g/L of *AP-Monoamine M* particles. It is possible that as a single particle, some of *AP-Monoamine M* particles have lower positive surface charge than the average of measured surface charge. At high concentration of *AP-Monoamine M*, the repulsive force between particles with low positive surface charge is not strong enough to provide sufficient repulsion against

the attractive van der Waals force to prevent aggregation. Hence, particles tend to aggregate in the dispersion and consequently aggregates are adsorbed on the surface. Min *et al.,* 2008[178] described the effect of concentration of the nanoparticle on the inter-particles forces.

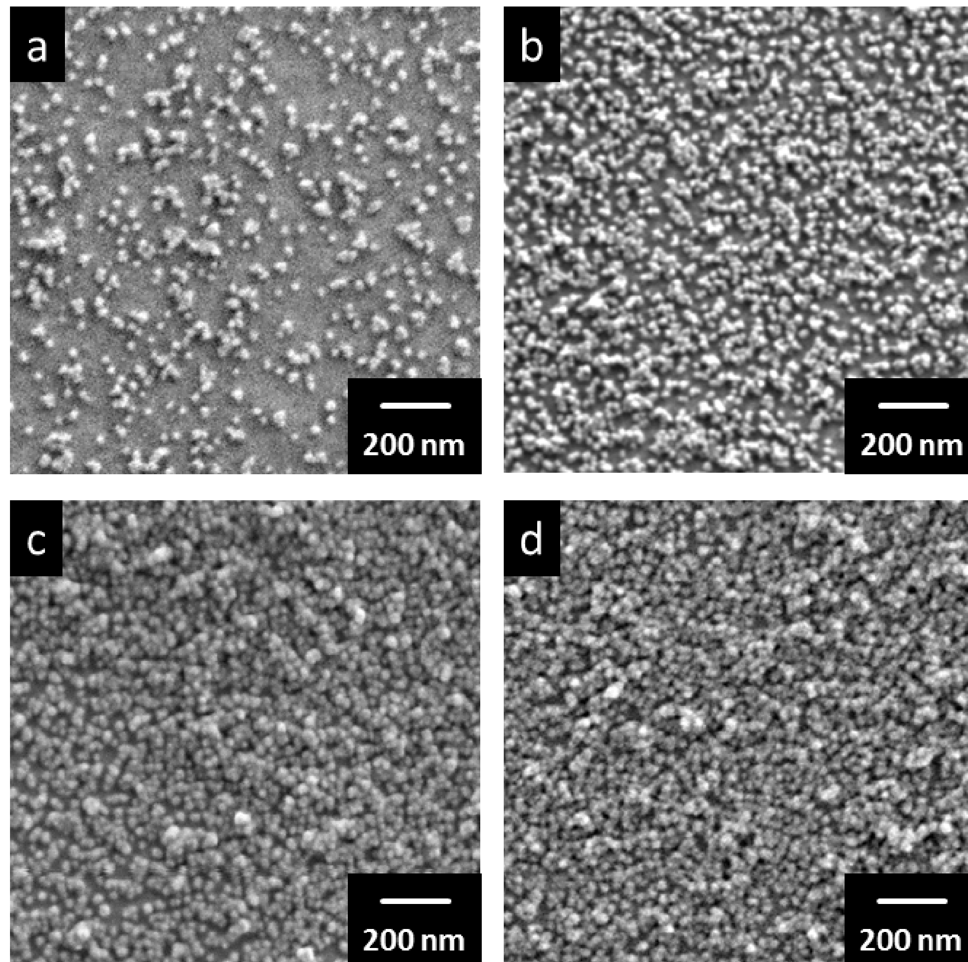

Figure 6. 11 FE-SEM images of the surface morphology of polyimide film treated with (a) 0.8, (b) 1.6, (c) 4 and (d) 8 g/L of *AP-Monoamine M*. The films were immersed into the suspension for at 60 °C for 5 min. The films were withdrawn from the suspension with a speed of 180 mm/min, and annealed in an oven at 130 °C for 10 min

Second, the increase of particle flux into the convective assembly at the meniscus. This meniscus was formed during the withdrawing step in dip-coating. In dip-coating, the particle layer formation is explained to be driven either by the direct adsorption from the solution or by convective assembly in the meniscus (see Figure 6. 12).[144, 179-181] The reasons for the convective assembly of particle in the meniscus are the evaporation of the solvent[144, 179] and the concentration of dispersion.[182] At high concentrations of *AP-Monoamine M*, particles become concentrated at the

meniscus. Because of the high speed of the evaporation of ethanol at 60 °C, the loosely adsorbed particles do not have enough time to adsorb on the polyimide surface, or to return into the solution, but instead, the particles tend to aggregates and form multilayer on the film surface.

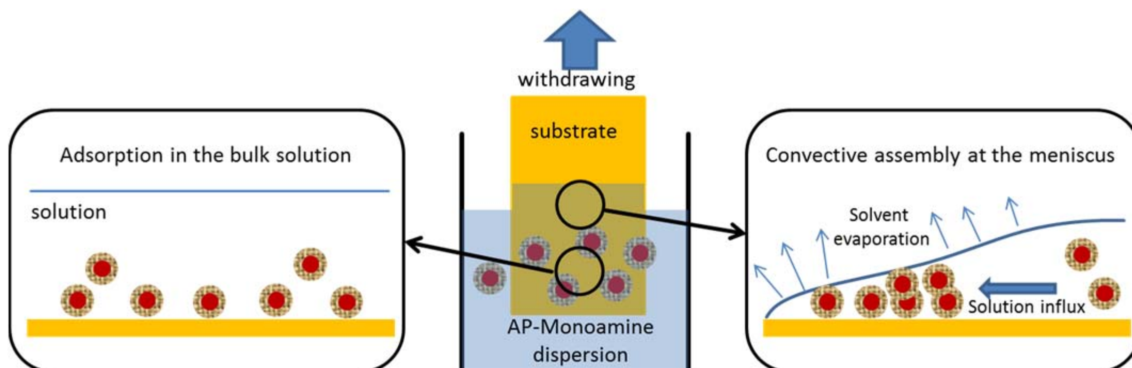

Figure 6. 12 The schematic illustration of particle layer formation in dip-coating driven by the direct adsorption from the solution and by the convective assembly in the meniscus. The figure was adapted from the publication of Jung *et al.,* 2009[144]

The AFM images of the surface morphology of polyimide film treated with 0.8 g/L of *AP-Monoamine M* at 60 °C for different immersion time is shown in Figure 6. 13. The surface coverage of *AP-Monoamine M* particles on the film surface in Figure 6. 13 were evaluated using image J, and shown in Figure 6. 14. In general, the treatment time of the polyimide film with *AP-Monoamine M* affects the coverage of particle. The surface coverage increases with longer immersion time. It was noticed in Figure 6. 14 that the coverage of the particles on the film surface reached its saturation point after an immersion time of 5 min. Longer immersion time than 5 min resulted in similar surface coverages even though huge parts of the film are not yet covered by particle. The decrease in surface coverage at 10 min of immersion time is smaller than the error bar observed for 2 and 5 min of immersion time, and this change is likely insignificant.

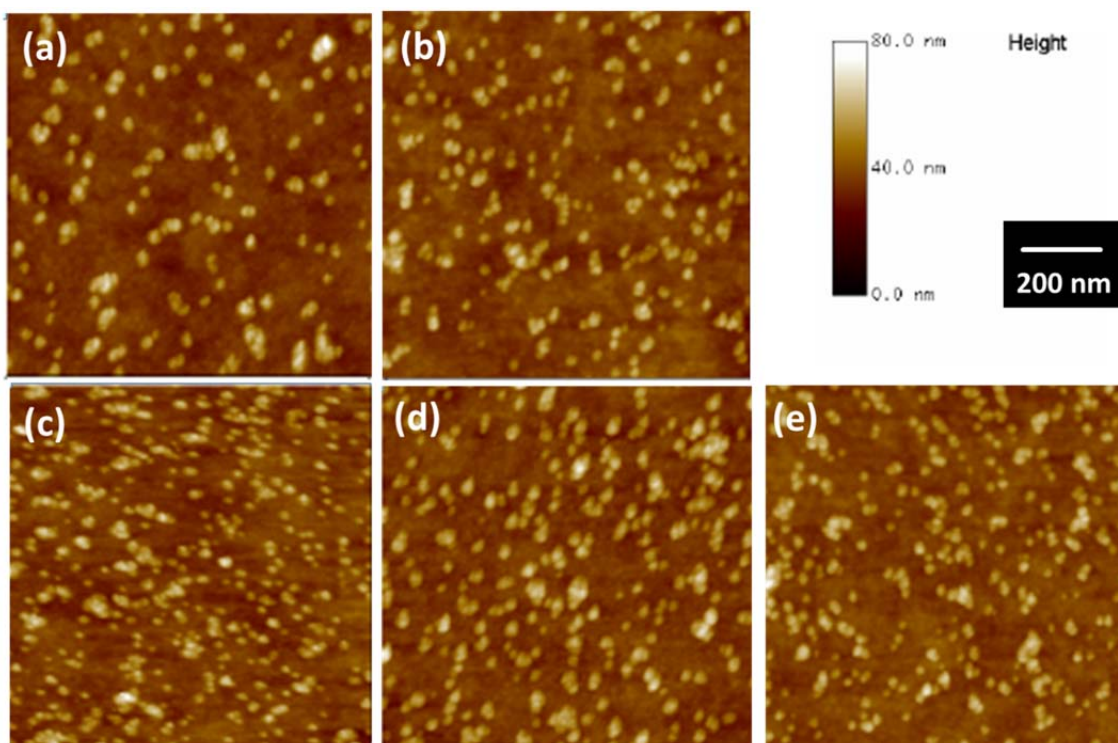

Figure 6. 13 AFM images of the surface morphology of polyimide film treated with 0.8 g/L of *AP-Monoamine M* for an immersion time of (a) 10, (b) 60, (c) 120, (d) 300 and (e) 600 s 60 °C. A measuring window of 1x1 μm^2 was used.

Electrostatic attraction has been defined as the interaction force for *AP-Monoamine M*/polyimide film assembly. A high probability of interaction between particle and film surface in *AP-Monoamine M* dispersion is essential for an optimum attraction. In dispersion with low concentration of *AP-Monoamine M*, particles have high degree of freedom to move around in the solution. In this condition, the probability for the particle to interact and adsorbed on the film surface is very low. Therefore, in a brief amount of time, it is not easy to have a high degree of particles coverage on the film surface. To achieve a high degree of particles coverage of the surface, other important factors need to be taken into account. One of those is the concentration of AP-*Monoamine M*.

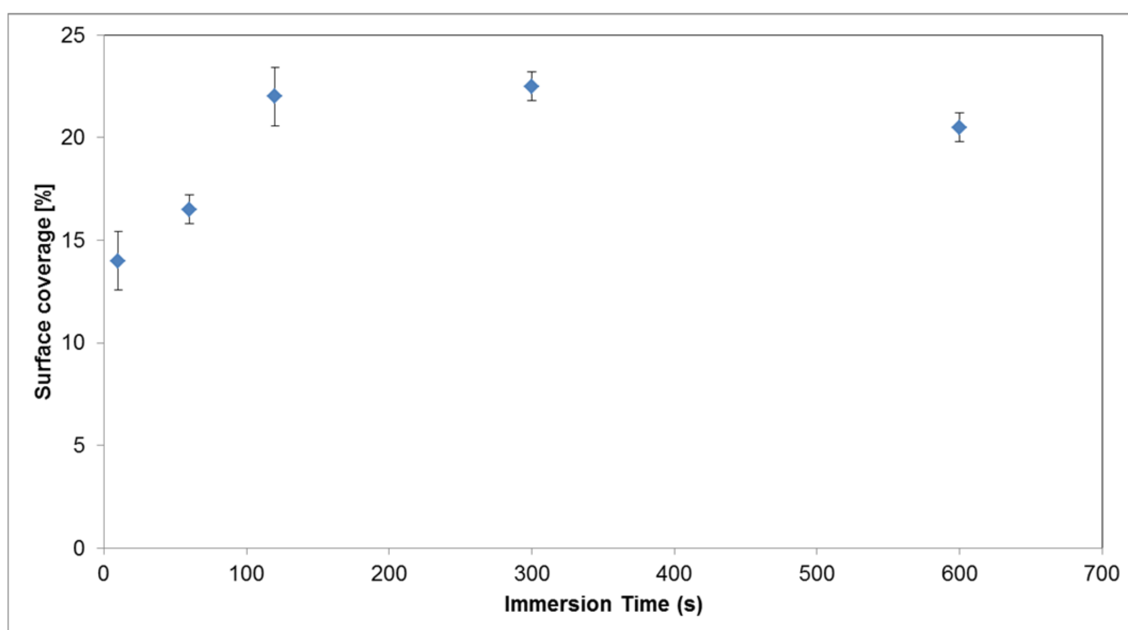

Figure 6. 14 Surface coverage of *AP-Monoamine M* particle on polyimide film surface as a function of immersion time. The film treated with 0.8 g/L *AP-Monoamine M* at 60 °C

Figure 6. 15 shows the surface morphology of polyimide films treated with 4 g/L of *AP-Monoamine M* for different immersion time obtained by AFM. After a short immersion time (10 s), the surface of the polyimide film is almost fully covered by the *AP-Monoamine M* particles. Only a small part of the polyimide film is still visible on the background (Figure 6. 15(a)). It needs only 60 s, for the surface is to be completely covered by *AP-Monoamine M.* At 60 °C polyimide film is not visible in the background (Figure 6. 15(b)). For immersion times of 120 s, 300 s, and 600 s, the AFM image appears similar to the one from immersion time of 60 s.

The chemical composition of the polyimide surface treated with 4 g/L of *AP-Monoamine M* for 5 min was investigated with FTIR-ATR. This condition was used in order to have complete coverage of particles on the film surface. The change of chemical composition on the surface is not fully verified because most of the characteristic bands of *AP-Monoamine M* overlapped with the polyimide film. There is no strong evidence of the presence of AP-Monoamine M on top of polyimide film. Moreover, because of the sampling depth of FTIR-ATR, most of the resolved characteristic bands are from the polyimide bulk. For this reason, the result of FTIR-ATR will not be discussed further in this section. Please refer to Appendix 6 for the

result of FTIR-ATR measurements. To overcome this problem, the samples were investigated with X-ray photoelectron spectroscopy (XPS).

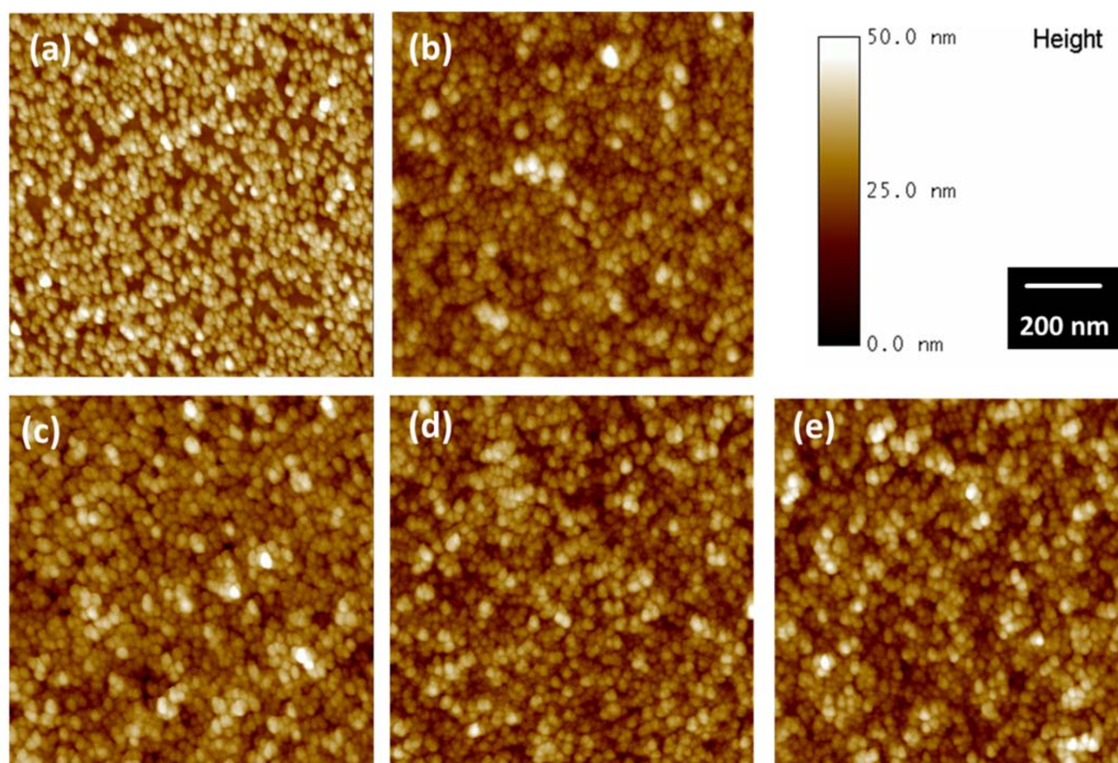

Figure 6. 15 AFM images of the surface morphology of polyimide film treated with 4 g/L of *AP-Monoamine M* for (a) 10, (b) 60, (c) 120, (d) 300 and (e) 600 s at 60 °C. A measuring window of 1x1 μm^2 was used

Figure 6.16 presents the XPS survey scans of polyimide films treated only with permanganate, and subsequently treated in 4 g/L of *AP-Monoamine M* dispersion for 5 min at 60 °C. The sample treated with *AP-Monoamine M* was annealed at 130 °C for 10 min prior to the XPS measurement. For the *AP-Monoamine M* treated film, the spectrum shows the presence of four elements, C1s (46.6 %), N1s (4.8 %), O1s (35.1 %), and Si2p (13.5 %). In comparison with the only permanganate treated one, the significant increase of atomic concentration of O1s from 18.7 % to 35.1 % and Si2p from 0.1 % to 13.5 % can be used as an evidence for the presence of *AP-Monoamine M* on the surface.

The detailed analysis of O1s, N1s and C1s core levels of the polyimide film coated with *AP-Monoamine M* and those from polyimide after permanganate treatment are shown in Figure 6.17 and Figure 6.18. The obtained binding energies are summarized in Table 6.6. For polyimide treated with *AP-Monoamine M*, in the O1s high resolution analysis, one new peak at 533 eV is observed (Figure 6.18). The

AP-Monoamine M treated sample shows new peaks in the O1s, N1s and C1s signals, in addition to the chemical state expected from the chemistry of the polyimide repeat unit. The change in the shapes of the O1s, N1s and C1s indicates the appearance of new binding states. In order to fit the line shape properly, additional binding states needed to be added, with the center of the peak at 286.8 eV (C7*), 533 eV (O3*) and 402.4 eV (N2*).

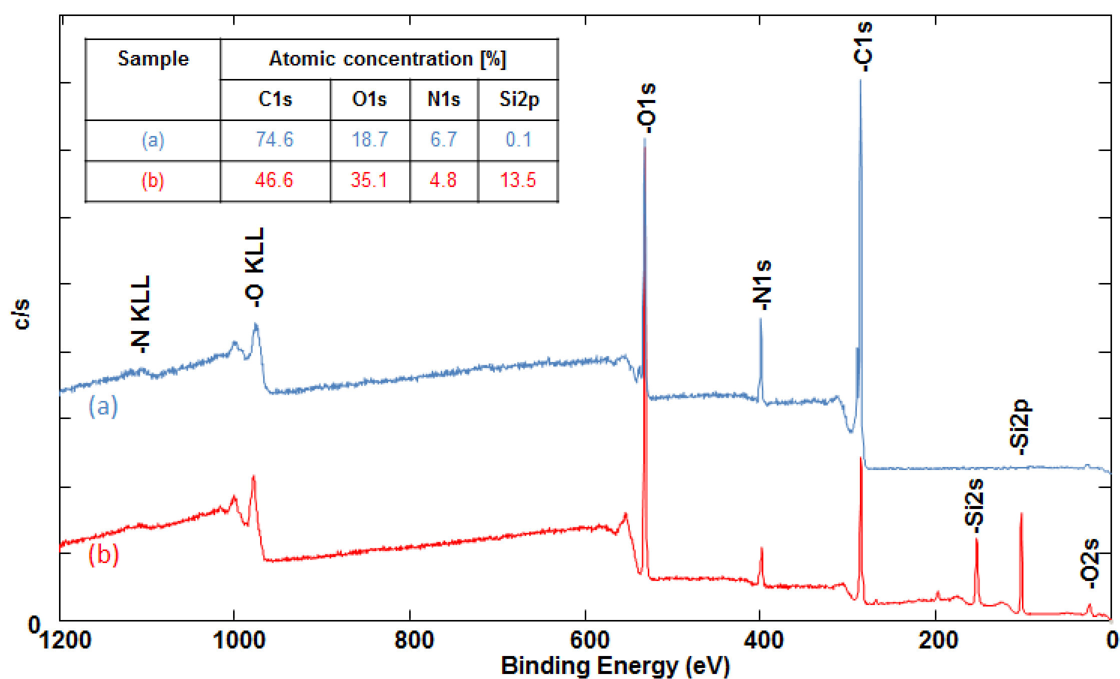

Figure 6.16 XPS survey scan of polyimide films treated (a) with permanganate and (b) subsequently treated with 4 g/L *AP-Monoamine M*

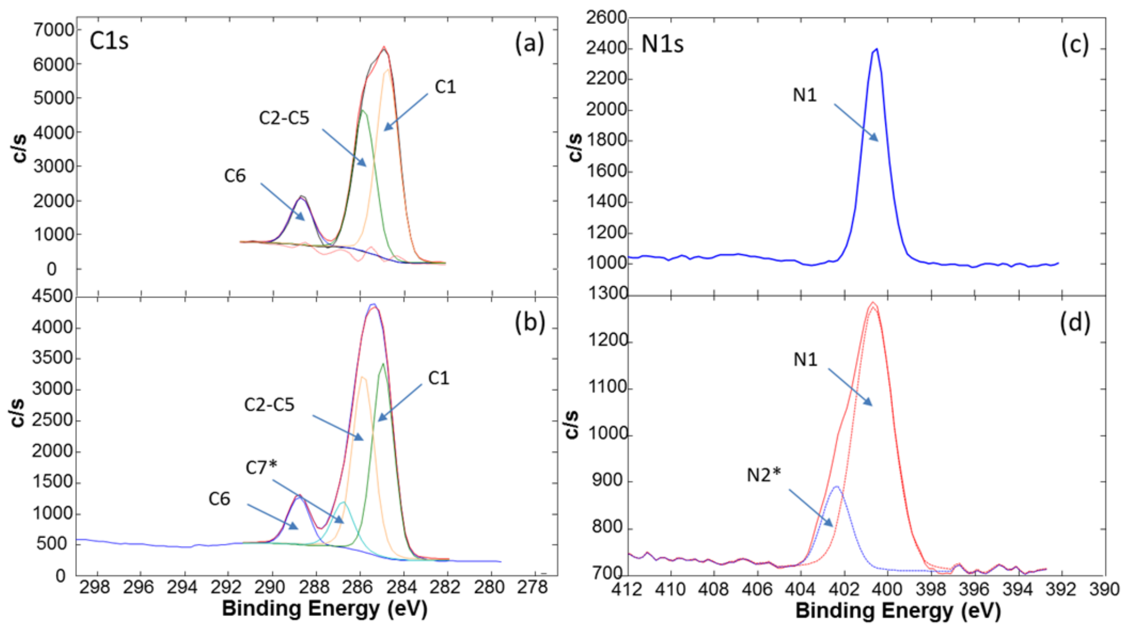

Figure 6.17 XPS C1s and N1s core level spectra of polyimide film treated with permanganate (a) and (c), and subsequently treated with of 4 g/L of *AP monoamine M* (b) and (d)

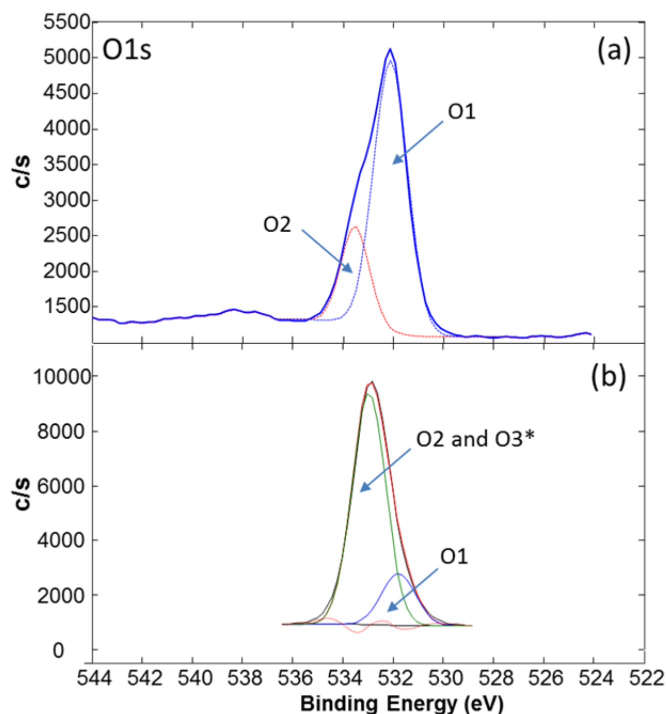

Figure 6.18 XPS O1s core level spectra of polyimide film treated (a) with permanganate and (b) subsequently treated with of 4 g/L of *AP monoamine M*

Table 6.6 XPS chemical states analysis for C1s, N1s and O1s signals of permanganate and *AP-Monoamine M* treated polyimide films

Signal	Component	Permanganate		*AP-Monoamine M*	
		E_B [eV]	Area [%]	E_B [eV]	Area [%]
C1s	C1 (C-H aromatic ODA)	284.8	50	284.9	40
	C2-C5	285.8	38	285.9	39
	C6 (C=O)	288.7	12	288.8	10
	C7* (C-NH_3^+)	-	-	286.8	11
O1s	O1 (C=O)	532.1	70	531.8	23
	O2 (C-O-C)	533.4	30	-	-
	O3* (Si-O Silica)	-	-	533	77
N1s	N1 (C-N imide)	400.6	100	400.7	84
	N2* (C-NH_3^+)	-	-	402.4	16

C2-C5: C2(C-H aromatic PMDA), C3 (C-N imide), C4 (aromatic PMDA) and C5 (C-O-C)

In the O1s analysis, the new component peak at 533 eV (O3*) is attributed to the Si-O from the silica. Since this peak is relatively close to the one at 533.4 eV (C-O-C), it is difficult to separate those peaks into individual peak. Therefore, the composition ratio showed in the Table 6.6 is the sum from those two binding states. Nonetheless, the chemical state for C=O at lower binding energy (531.8 eV) can still be distinguished. In the N1s spectra, the new component peak at 402.4 eV (N2*) is attributed to the protonated amine from *AP-Monoamine M* (-C-NH_3^+). The appearance of this species indicates that the amino groups of *AP-Monoamine M* are mostly in the protonated form when adsorbed on the surface of polyimide film.

Apart from these changes in oxygen and nitrogen chemical states, the C1s signal after *AP-Monoamine M* applied on the polyimide surface shows a new species at 286.8 eV (C7*). A similar binding state has been observed in synthesized polyimide film (6FDA-Durene) modified with polyamidoamine (PAMAM) dendrimers.[183] Xiao assigned this peak as carbon from amide (–NH-(C=O)–), from the reaction of some imide groups (-N$(C=O)_2$) of polyimide with amine groups of PAMAM. Through this reaction the decrease of component ratio of C=O from imide (C6) should also observed. As the aromatic ODA remains constant during *AP-Monoamine M* treatment process, the change in the C6/C1 area ratio can be used to indicate the reaction of imide groups (-N$(C=O)_2$) of polyimide with amine groups of

AP-Monoamine M to form amide groups –NH-(C=O)–. The area ratio of polyimide film treated only with permanganate (C6/C1=0.24) and the film coated with *AP-Monoamine M* (C6/C1=0.24) are similar. This indicates that likely there is no imide transformed to amide. The C7* (286.8 eV) can not be assigned as carbon from amide. This new component peak should be attributed to the protonated amine (-C-NH_3^+) from the *AP-Monoamine M*.

Despite there is no evidence of chemical interaction between imide groups of polyimide and amine groups of *AP-Monoamine M*, several publications[183-184] have proposed the ring opening of imide by amine as the possible chemical mechanism. Hence, a possible reaction mechanism of aminopropyl functionalized silica nanoparticles interaction with polyimide surface is proposed in Figure 6.19. It starts with the attraction between *AP-Monoamine M* and polyimide surface via electrostatic interaction. This is between the positively charged of protonated amino groups of *AP-Monoamine M* and the negatively charged of hydroxyl and carbonyl groups of hydrolysed polyimide. This charge complex holds the particles tightly at the surface. During annealing step, the amine groups of *AP-Monoamine M* react with some imide groups of polyimide film to form amide bonds.

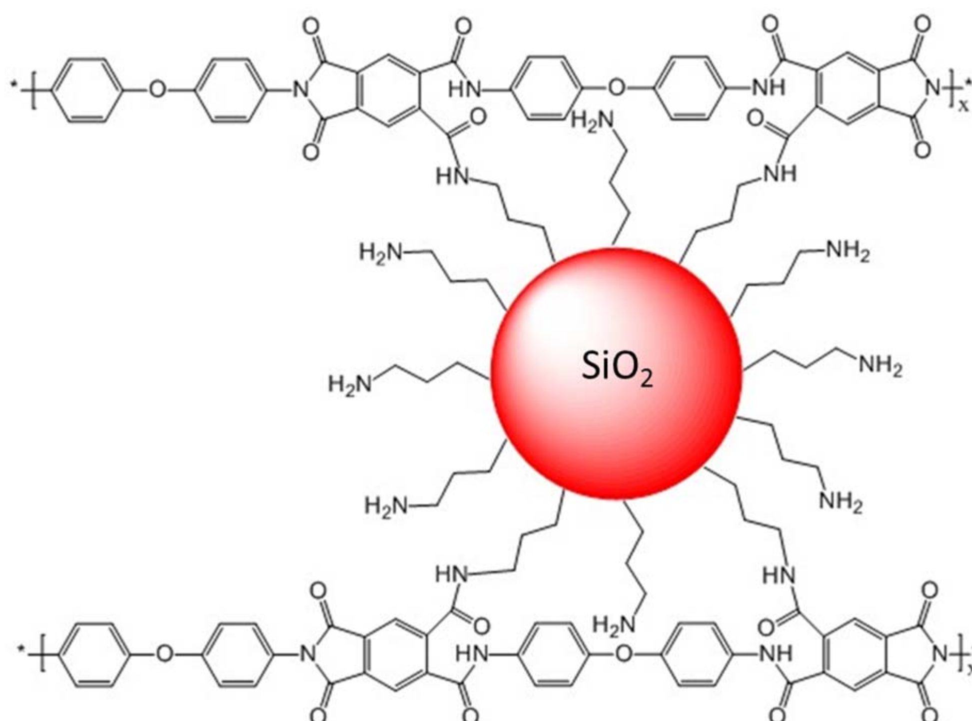

Figure 6.19 Possible reaction mechanism of aminopropyl functionalized silica nanoparticles (*AP-Monoamine M*) with polyimide film surface

6.3.3 Electroless copper deposition on *AP-Monoamine M* modified polyimide films

Prior to electroless copper plating on the polyimide film, the film is first activated with a palladium catalyst. Polyimide films treated only with alkaline permanganate, and that treated with alkaline permanganate and *AP-Monoamine M* were immersed into a solution containing Pd (II) ions for 4 min. The films were immersed subsequently into dimethylaminoborane (DMAB) solution for 3 min to reduce the Pd (II) ions to metallic Pd (0). Electroless copper plating was then carried out by using a commercially available electroless plating bath from Atotech Deutschland GmbH. With the help of reducing agents, the palladium metal (Pd (0)) catalyzes the reduction of copper in the electroless copper solution.[73]

The surface of polyimide film treated with solution containing Pd (II) ions (Neoganth palladium activator 834) was investigated by XPS. Prior to the XPS measurement, the polyimide films were rinsed with de-ionized water, and dried with dry air after immersion in Neoganth palladium activator 834 solution. The XPS survey scans are shown in Figure 6. 20 (spectrum (i) for *AP-Monoamine M* treated and spectrum (iii) for permanganate treatment only). The atomic concentration of elements is summarized in Table 6. 7. On the surface of both films, the presence of palladium species on the surface can be indicated by the appearance of the signal of Pd3d core-level in XPS survey scan. The atomic concentration ratio of Pd3d/C1s = 0.06 is the same for both samples (see Table 6. 7). This result indicates that the adsorption of the palladium species from neoganth 834 activator solution on the surface is independent from the nature of the polyimide film.

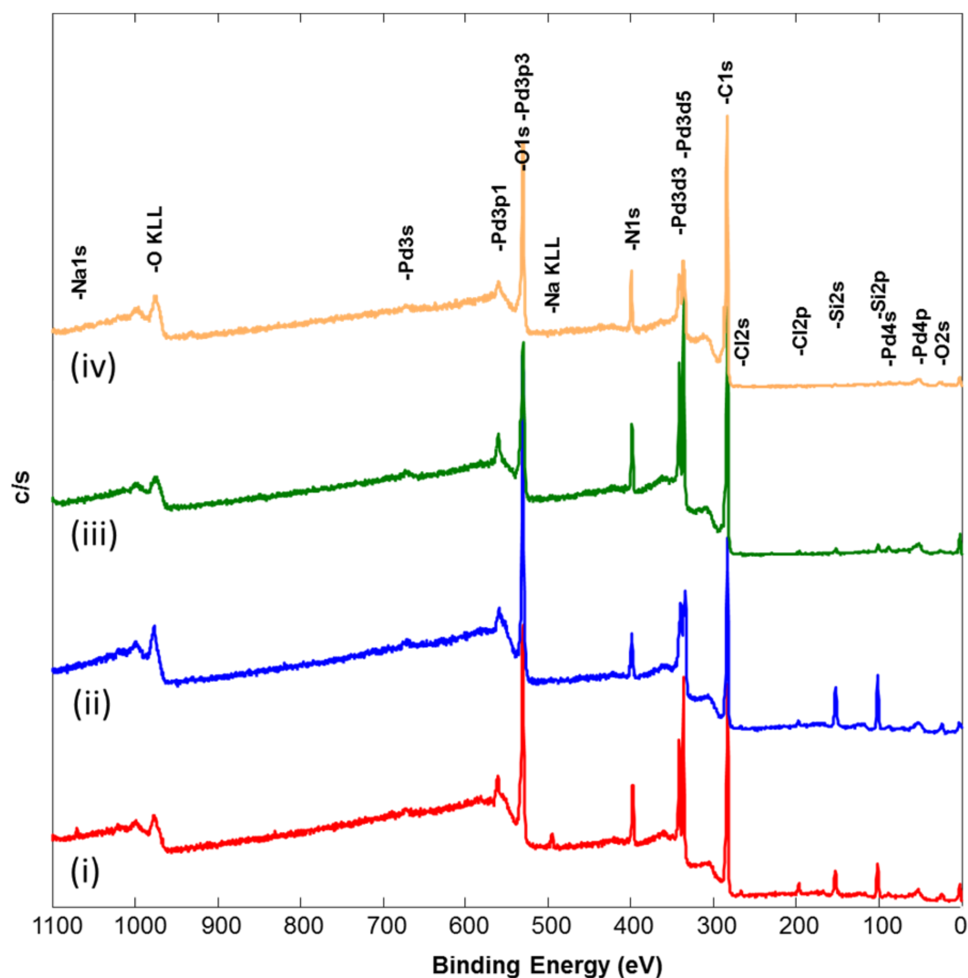

Figure 6. 20 XPS survey scan of polyimide film treated with *AP-Monoamine M* (4 g/L, 60 °C, 5 min) after the adsorption of Pd (II) ions (i), and after consecutive reduction of palladium from Pd (II) to Pd (0) (ii). Polyimide film treated only with permanganate after the adsorption of Pd (II) ions (iii), and after consecutive reduction of palladium from Pd (II) to Pd (0) (iv)

Table 6. 7 The atomic concentration of elements based on the spectra of surface scan in Figure 6. 20

Sample	**Atomic concentration [%]**						
	C1s (278 eV)	**N1s (291 eV)**	**O1s (533 eV)**	**Si2p (94 eV)**	**Pd3d (330 eV)**	**NaKLL (488 eV)**	**Cl2p (193 eV)**
(i)	51	10.6	26.9	5.9	3.2	1.6	0.9
(ii)	45.4	7.1	34.8	9	3.2	0.1	0.4
(iii)	60.4	10.3	23.9	1.6	3.6	0.1	0.1
(iv)	67.9	6.7	22.8	0.3	2.3	0.1	0.1

A detailed analysis of the binding states and chemical shifts of Pd3d and N1s signals are shown in Figure 6. 21 (polyimide film only treated with permanganate) and Figure 6. 22 (polyimide film treated with permanganate, then subsequently with *AP-Monoamine M*), and summarized in Table 6. 8. The obtained binding energies of Pd3d and N1s for both samples are the same. For Pd3d, the spectra can be curve-fitted with two spin orbit-split doublets. The lower binding energy doublet for the $Pd3d_{5/2}$ and $Pd3d_{3/2}$ peak component is lying at about 335 and 340 eV, respectively. Those signals are assigned to the Pd (0) species (denoted Pd2 in Figure 6. 21 and Figure 6. 22).[185] The higher binding energy doublet of $Pd3d_{5/2}$ and $Pd3d_{3/2}$ at about 338 and 343 eV, respectively, is attributed to the sum peak of Pd (II) and the Pd (II) complex species (denoted Pd1 in Figure 6. 21 and Figure 6. 22).[185] For N1s, The spectra are curve fitted as two N1s chemical states. The energy peak at higher binding energy at about 400 eV is assigned to the -C-N in imide component (N1).[165] The peak at lower binding energy at about 399 eV is assigned to the $-C-NH_2$ component (N3*). For polyimide film treated with *AP-Monoamine M*, the N2* ($C-NH_3^+$) component is not observed after the immersion step in the palladium solution. This change is attributed to the deprotonation of amine groups of *AP-Monoamine M* from NH_3^+ to NH_2 in alkaline palladium solution, in which the pH of the solution is 11.5, and the pKa of the amino group is 10.6.[112] Therefore, N3* component is presence instead of N2*. The presence of component N3* in only permanganate treated film indicates the existence of another nitrogen contained group in the palladium solution, presumably from the organic complexing agent used to maintain the stability of the palladium ions in the alkaline solution.

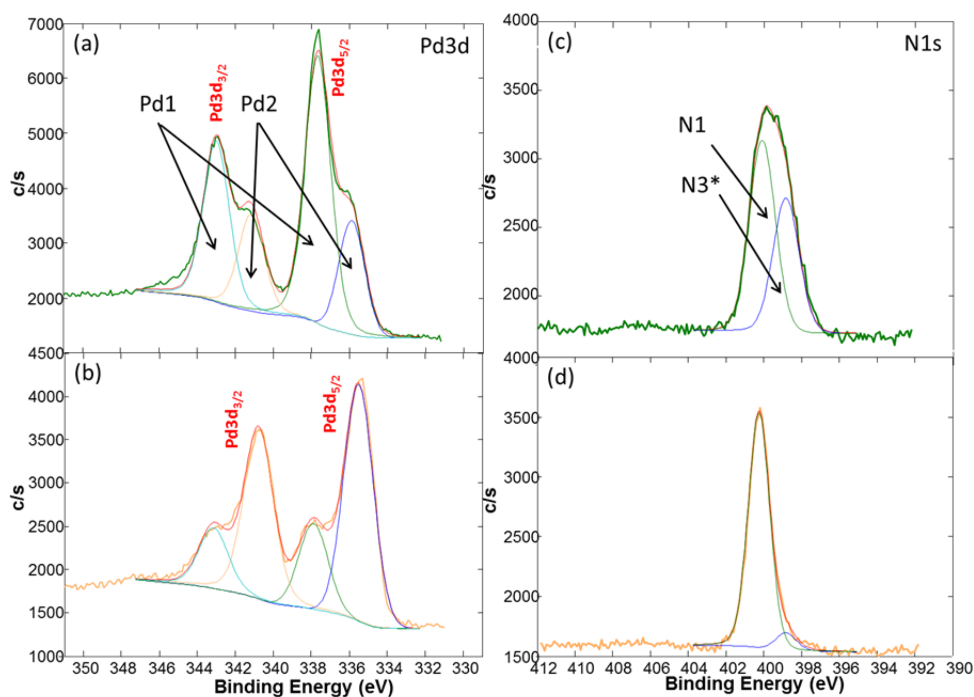

Figure 6. 21 XPS Pd3d and N1s spectra polyimide film treated with permanganate. (a), (c) followed by palladium activation step in Neoganth 834 activator, and (b), (d) after the sample underwent the Pd reduction step in DMAB solution

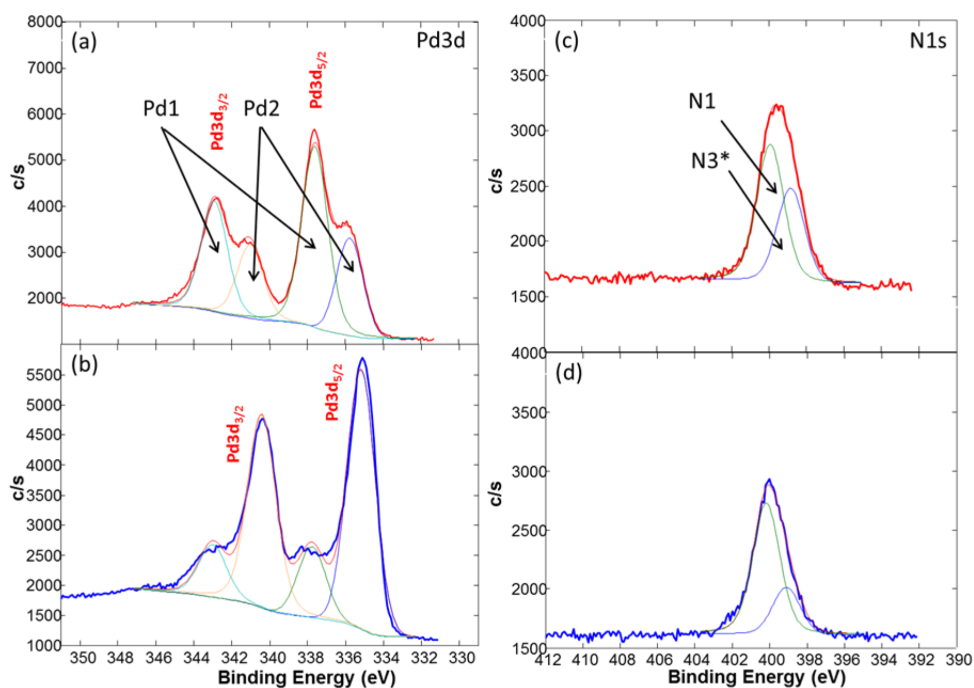

Figure 6. 22 XPS Pd3d and N1s spectra of *AP-Monoamine M* treated polyimide film (a), (c) followed by palladium activation step in Neoganth 834 activator, and (b), (d) after the sample underwent the Pd reduction step in DMAB solution

Table 6. 8 XPS chemical states analysis for Pd3d and N1s signals of polyimide films treated in alkaline permanganate solution and those treated with alkaline permanganate solution, then subsequently treated with *AP-Monoamine M*. In both cases, the sample were treated in Pd (II) ions solution (Neoganth activator 834), followed by reduction step in DMAB solution

Signal	Component	Permanganate treated		*AP-Monoamine M* treated	
		E_B [eV]	Area [%]	E_B [eV]	Area [%]
After immersion in palladium solution					
Pd3d	Pd1 (Pd (II))	337.7	43	337.6	40
		343	26	342.9	24
	Pd2 (Pd (0))	335.9	17	335.8	20
		341.2	15	341	16
N1s	N1 (C-N imide)	400.1	59	399.9	61
	N3* ($C-NH_2$)	398.84	41	398.8	39
After immersion in DMAB solution					
Pd3d	Pd1 (Pd (II))	337.9	15	337.8	12
		343.1	12	343	10
	Pd2 (Pd (0))	335.5	41	335.2	43
		340.8	32	340.4	35
N1s	N1 (C-N imide)	400.3	92	400.1	75
	N3* ($C-NH_2$)	398.8	8	399.1	25

After subsequent immersion in DMAB solution, the ratio of signal intensity of the Pd2/Pd1 component increases for both samples (Figure 6. 21(b) and Figure 6. 22(b)). This change indicates the reduction of the Pd (II) species to Pd (0) by DMAB. The presence of a small signal intensity of the Pd1 component in the XPS spectra after immersion in DMAB indicates that some Pd (II) species remained on the sample surface after the reduction step. The presence of weak signal intensity of N3* in the XPS spectra of polyimide film treated only with permanganate after reduction step, shows that the form of Pd species is maybe Pd (II)-complexing agent. Furthermore, it is likely that oxidation of Pd (0) to Pd (II) occured under atmospheric conditions during storage of the sample.

The decrease in atomic concentration ratio of Pd3d/C1s from 0.06 to 0.03 (Table 6. 7) has shown that some palladium atoms were removed from the surface of only permanganate treated film after the reduction of Pd (II) to Pd (0), while the

concentration of atomic palladium on the surface of *AP-Monoamine M* treated film remained the same (from the same atomic concentration ratio of Pd3d/C1s before and after reduction step). The electron configuration of Pd (0) is d10 and Pd (II) is d8. This shows that Pd (0) is very unfavorable energetic compared to Pd (II).[131-132] For this reason, the Pd (0)-N bond must be much weaker than Pd (II)-N bond, and thus the Pd (0) species can diffuse over the surface to form clusters.[131-132] Since there is no strong bond between Pd (0) clusters and polyimide film surface, some Pd (0) clusters could easily been removed from the surface by water rinsing. In the case of polyimide film treated with *AP-Monoamine M*, the clusters of Pd (0) species are trapped between the polymeric composites of *AP-Monoamine M* particle, and thus stabilized on the surface. Additionally, the reduction step of Pd (II) to Pd (0) leads to the release of Pd atoms from the complexing agent. The complexing agent is discharged from the surface of the film into the solution. This can be observed from the vigorous decreased of the ratio of N3* component after reduction step in Table 6. 8.

After the palladium activation step (Neoganth 834 activator followed by reduction in DMAB), the polyimide films were immersed into electroless copper solution at 35 °C. The reduction of Cu (II) ions to metallic Cu (0) on the surface was indicated by the prompt color change of the films from yellow to black after 30 s of immersion. The presence of the copper atoms on the surface of the *AP-Monoamine M* treated polyimide film is also indicated by the appearance of the copper signal in EDX spectrum (Figure 6. 23). The measured Kα copper (0.91 keV) signal in EDX gives strong evidence for the presence of copper on the film surface.

The electroless copper deposition on the polyimide film modified with *AP-Monoamine M* was also investigated with AFM. The evolution of the electroless copper growth as a function of the deposition time is shown in Figure 6.24. The particle size of *AP-Monoamine M* did not change after the Pd activation step (Figure 6.24(a)). The size of the Pd (0) clusters is too small to be observed by AFM. After immersion in copper solution for 10 s, the round structures that are ≥ 50 nm in diameter were observed. The area occupied by the particles is larger in Figure 6.24 (b). Moreover, the size of the particles is larger in Figure 6.24 (b), indicating the copper deposition process took place at the surface of Pd coated polyimide film. The deposition of copper was continued for another 20 s. Copper clusters are growing

further on top of particle, and are connecting particles with each other so that a continuous layer is formed, and finally a close layer of copper metal is obtained (Figure 6.24 (c)).

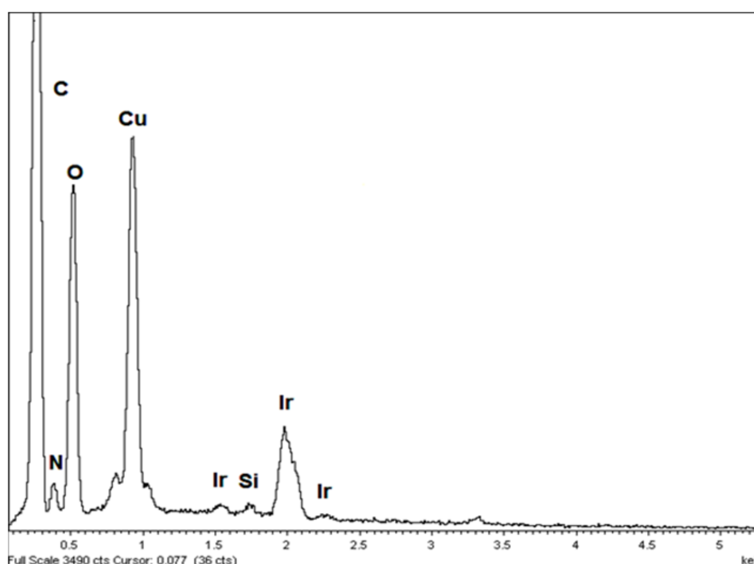

Figure 6. 23 EDX spectrum of an *AP-Monoamine M* treated polyimide film after electroless copper deposition. The sample was measured after 30 s immersion in electroless copper solution at 35 °C

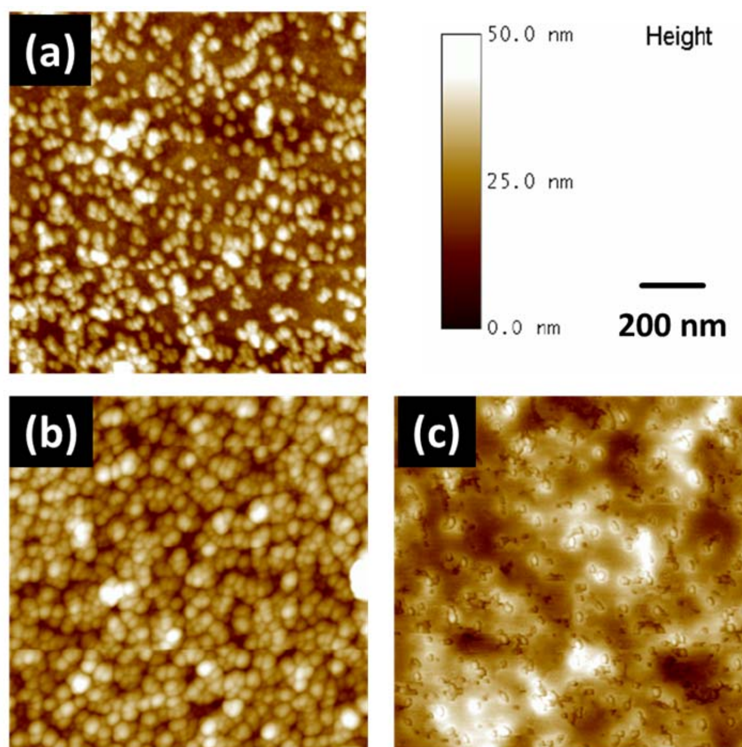

Figure 6.24 AFM image of *AP-Monoamine M* treated polyimide films deposited with electroless copper for (a) 0, (b) 10 and (c) 30 s. A measurement window of 1x1 µm was used

A possible reaction mechanism for electroless copper deposition on a polyimide surface treated with AP-Monoamine-M particles is proposed in Figure 6.25, starting with (a) the attraction of the complexed palladium ions by the nitrogen atoms of amino groups. The nitrogen atoms give their electron lone pairs to the adsorbed complexed palladium ions, and thus form amino-palladium complexes. (b) Subsequently, complexed palladium ions are reduced by DMAB from Pd (II) to Pd (0). The palladium atom clusters are formed immediately, and coordinated onto the *AP-Monoamine M* amino groups. (c) Finally, due to the presence of formaldehyde, copper cluster growths on the surrounding of palladium cluster.

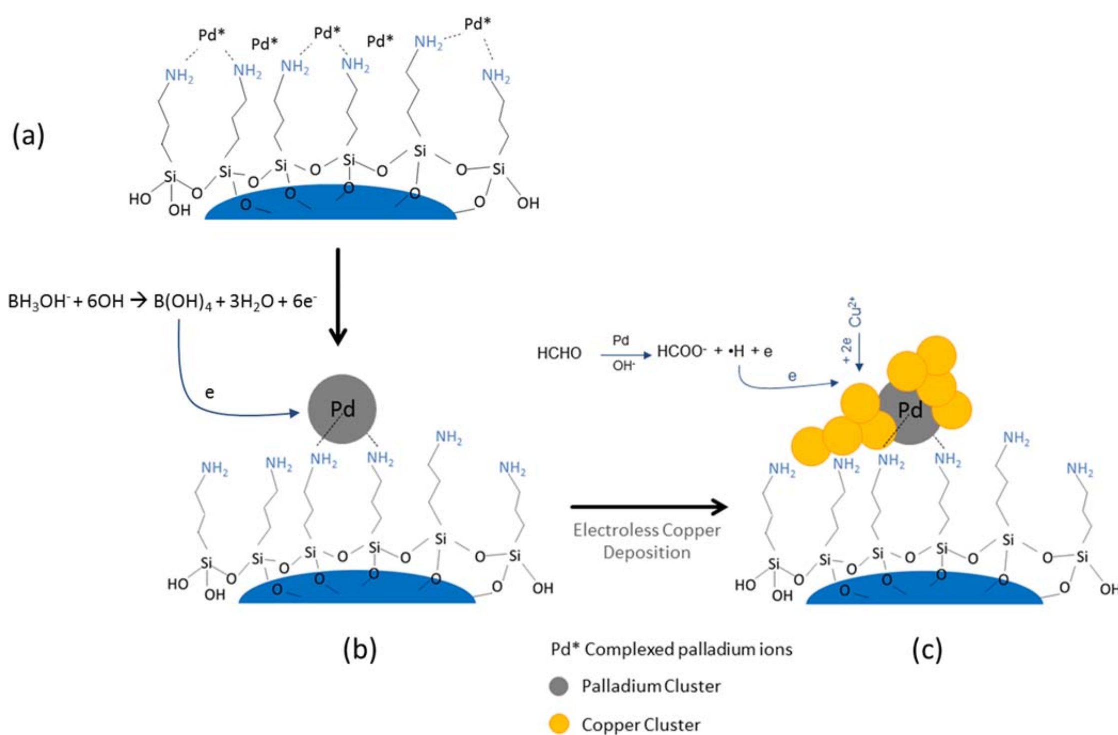

Figure 6.25 Possible reaction mechanism for the electroless copper deposition on polyimide film surface modified by *AP-Monoamine M*. (a) The strong electronegativity of the nitrogen atoms from amino group attracts the complexed palladium ions, so that they are adsorbed onto the surface of the particle, and form amino-palladium complexes; (b) complexed palladium ions are reduced by DMAB from Pd(II) to Pd(0). Subsequently, palladium clusters are formed and coordinated by the *AP-Monoamine M* amino groups; (c) Finally, growth of copper on the palladium clusters occurs

6.3.4 The evaluation of adhesion of deposited electroless copper layers on polyimide films modified by aminopropyl silica nanoparticles (*AP-Monoamine*)

The peel strength of electroless copper on polyimide which is not treated with permanganate is low (0.6±0.1 N/cm). *AP-Monoamine M* treatment without permanganate treatment results also in a low peel strength (0.9±0.1 N/cm). Therefore, in this section, all polyimide films were subjected to permanganate treatment prior to *AP-Monoamine M* treatment. Contrary to the epoxy polymer in Chapter 5, the peel strength of electrolessly deposited copper on polyimide films only treated with permanganate is higher than zero (3±0.3 N/cm). It was believed that the chemical interaction of copper with the carbonyl groups of the polyimide film leads to the formation of a Cu-O-C complex.[186] This complex formation is the main reason for the adhesion strength of copper on permanganate treated polyimide film. However, this adhesion strength does not meet the requirements set by the microelectronics industry. The peel strength should be >6 N/cm.

The effect of the immersion time in *AP-Monoamine M* dispersion on the peel strength of the copper deposited on the polyimide film is shown In Figure 6.26. The concentration of the *AP-Monoamine M* was 0.8 g/L. The *AP-Monoamine M* treatment time of the polyimide film affects both the degree of coverage with the particles (Figure 6. 13) and the peel strength (Figure 6.26). One can see the dependent of the peel strength to the surface coverage of particle on polyimide film. The increase in peel strength with *AP-Monoamine M* treatment time is attributable to the increase in the number of particle on the surface Follow the degree of the surface coverage of *AP-Monoamine M* particle, the peel strength increases from 3±0.3 N/cm to 9.8±0.4 N/cm. The peel strength result only varies slightly when the surface coverage of *AP-Monoamine M* particle reaches it saturation point (from 5 min to 10 min). The presence of *AP-Monoamine M* particle increases the bondability of electrolessly deposited copper to the polyimide film treated with permanganate. This is maybe related to the sum of all the intermolecular interactions (Cu/*AP-Monoamine M* and AP-Monoamine M/polyimide assembly). On one hand, the amine groups of *AP-Monoamine M* interaction to the imide groups of polyimide.[183-184] On the other hand, the direct interaction between amine groups and palladium or copper to form Pd-N or Cu-N bonds.[131-134]

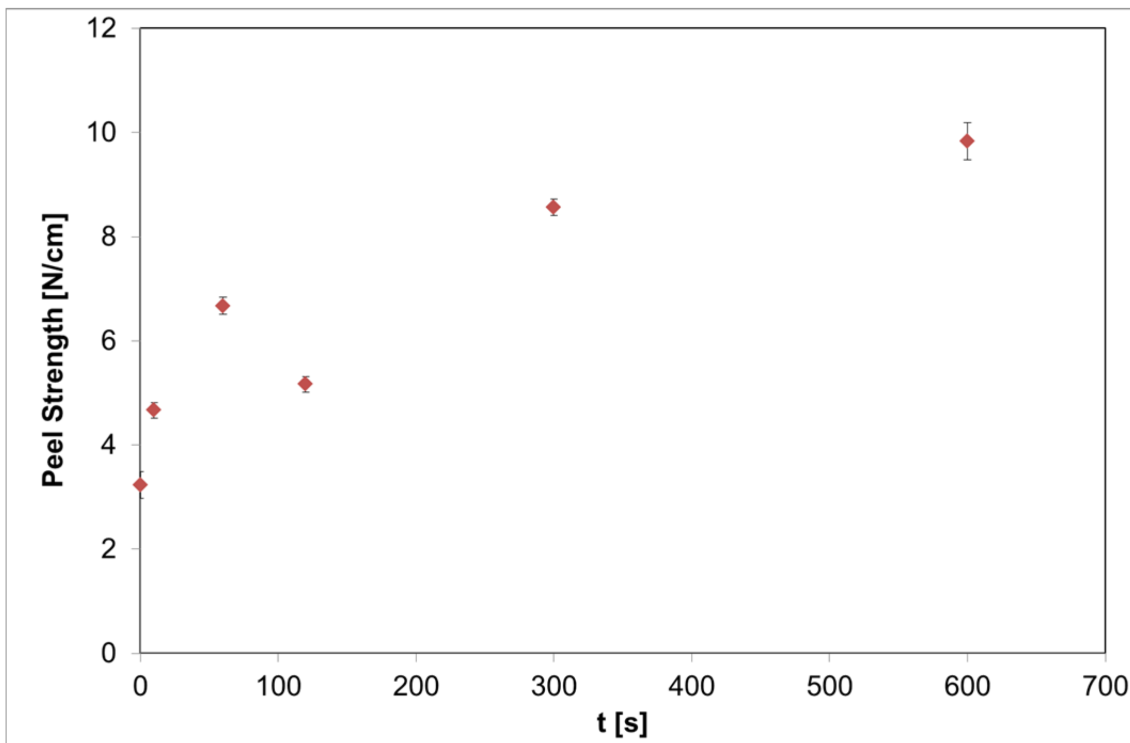

Figure 6.26 The dependence of the adhesion strength of the deposited copper on the modified polyimide as a function of immersion time. A 0.8 g/L *AP-Monoamine M* dispersion at 60 °C was used. The error bar shows the variation of the peel strength test within a single sample, peeled at three different positions

Figure 6.27 shows the dependence of the peel strength of the deposited copper on the polyimide film on the concentration of *AP-Monoamine M*. The adhesion strength increases with increasing *AP-Monoamine M* concentrations from 3±0.3 N/cm to 15±0.1 N/cm for concentrations between 0 g/L to 1.6 g/L. In this range of concentration, the dependent of the peel strength to the surface coverage of particle on polyimide film was observed. The surface coverage of AP-Monoamine M particle as function of concentration is shown in Figure 6. 11. At low particles coverage (0.8 g/L), the peel strength appears to be low (8.1±0.3 N/cm). The maximum adhesion strength is achieved when the optimum particles coverage is obtained, which is 15±0.1 N/cm for an *AP-Monoamine M* concentration of 1.6 g/L. A further increase of the *AP-Monoamine M* concentration above 1.6 g/L, results in a decrease in adhesion strength, and the peel strength eventually reaches 3.2±0.2 N/cm at a concentration of 8 g/L, a value comparable to the one of pristine polyimide film.

The decreasing of peel strength at high concentrations of *AP-Monoamine M* may be caused by the formation of the multilayer of particles on polyimide film

surface (Figure 6. 11(d)). The weak van der Waals attractions are the dominating interactions force between the particles. These interactions are not strong enough to hold the aggregated particles together. When the tensile force is applied to remove the copper layer (peeling), fracture arises from one to the next aggregated nanoparticles. Hence, low peel strength would obtain. Therefore, in this case, aggregated nanoparticles act as weak boundary layer in the polyimide-copper interface.

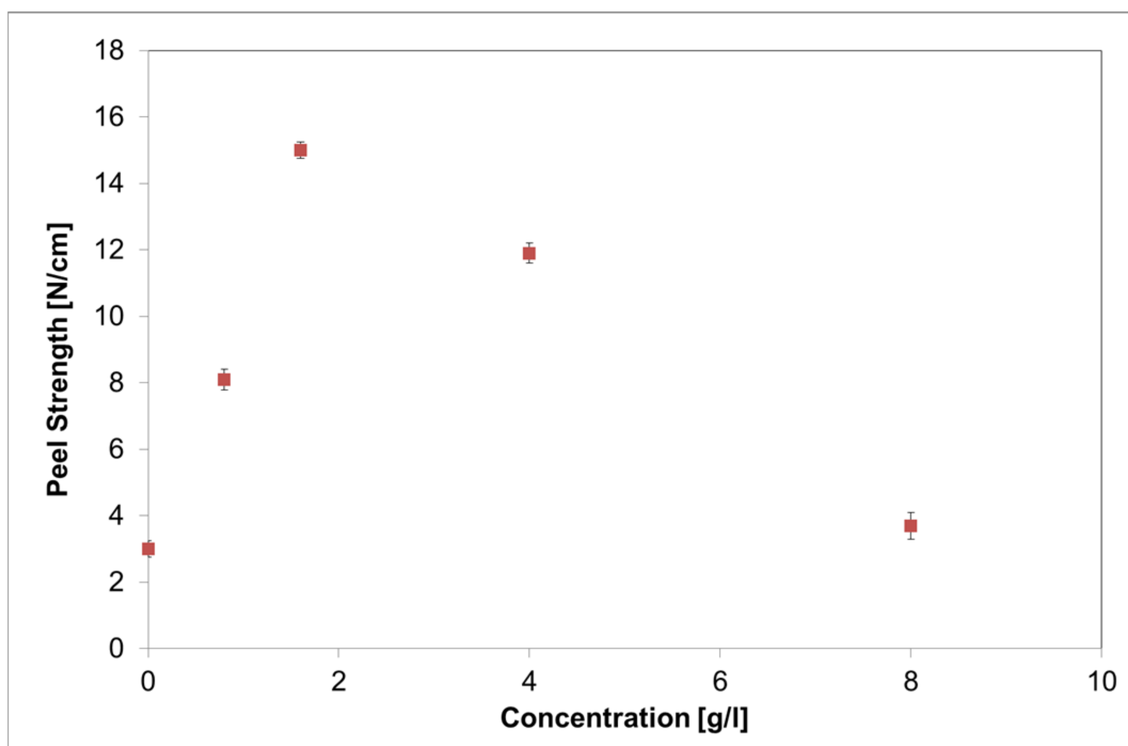

Figure 6.27 Dependence of the peel strength between deposited copper and modified polyimide films on the *AP-Monoamine M* concentration. The polyimide films were immersed in an *AP-Monoamine M* solution for 300 s at 60 °C. The error bar shows the variations of the peel strength within one sample, peeled at three different positions

The peel strength of electrolessly deposited copper increases significantly when *AP-Monoamine M* is applied onto the surface of polyimide films prior to metallization process. Values of up to 15±0.1 N/cm are reached. The corresponding increase in peel strength for the resulting Cu/*AP-Monoamine M*/polyimide assembly suggests that a functionalized silica nanoparticles induced adhesion enhancement is working. The strong adhesion of electroless copper layer on polyimide film treated with *AP-Monoamine M* is obtained from: 1. the amine groups of *AP-Monoamine M*

interaction to the imide groups of polyimide,[183-184] 2. Via a stable complex formation between amine groups of *AP-Monoamine M* and palladium or copper.[131-134]

In order to identified the contribution of surface morphology of polyimide film on the adhesion strength of copper to polyimide, three different sizes of aminopropyl functionalized silica *AP-Monoamine S* (TEM diameter = 14±3 nm), *M* (TEM diameter = 18±3 nm) and *L* (TEM diameter = 44±6 nm) were used to modify the polyimide films. The polyimide films were immersed into *AP-Monoamine* solution (4 g/L) for 5 min at 60 °C. The adhesion strength of copper deposited on polyimide film modified with different sizes of *AP-Monoamine* is shown in Figure 6.28. The AFM images of polyimide film surfaces covered with the three different nanoparticle species are shown in Figure 6.29. The root mean square roughness (R_{rms}), and the relative surface area increase (RSAI) were calculated. The values are summarized in Table 6.9.

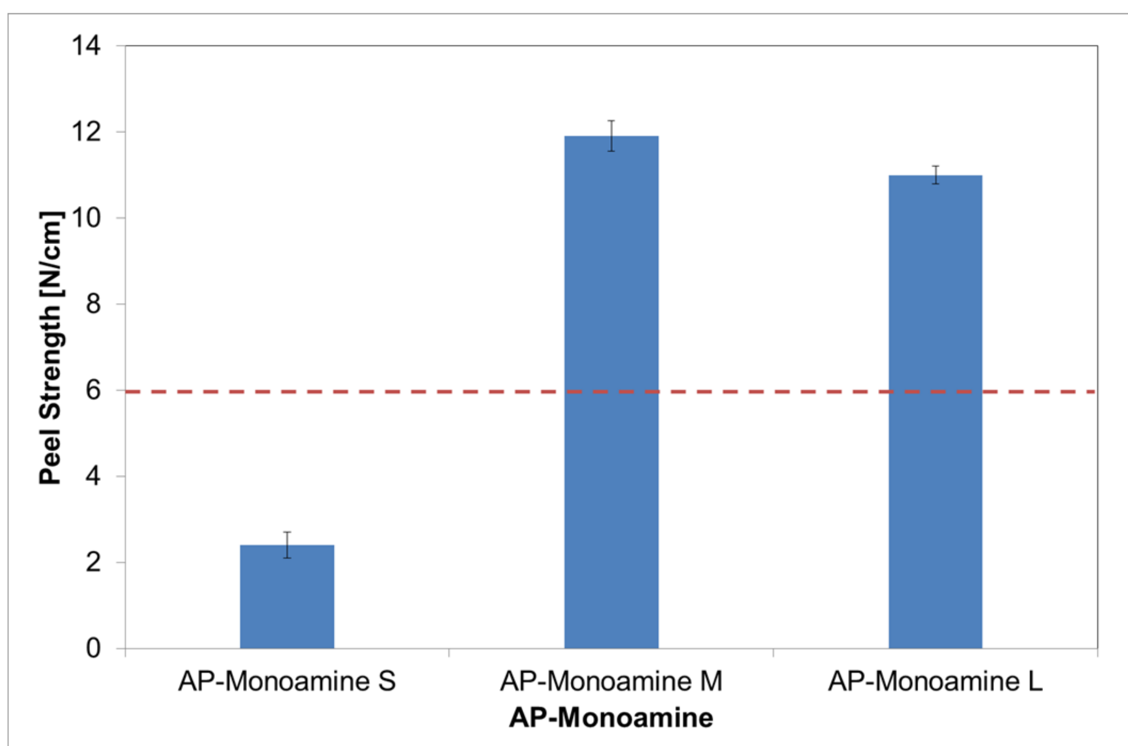

Figure 6.28 Adhesion strength of deposited copper on polyimide film modified with *AP-Monoamine S, M* and *L*. The vertical dash line is the border of the minimum peel strength needed to fulfill the industrial requirement (6 N/cm)

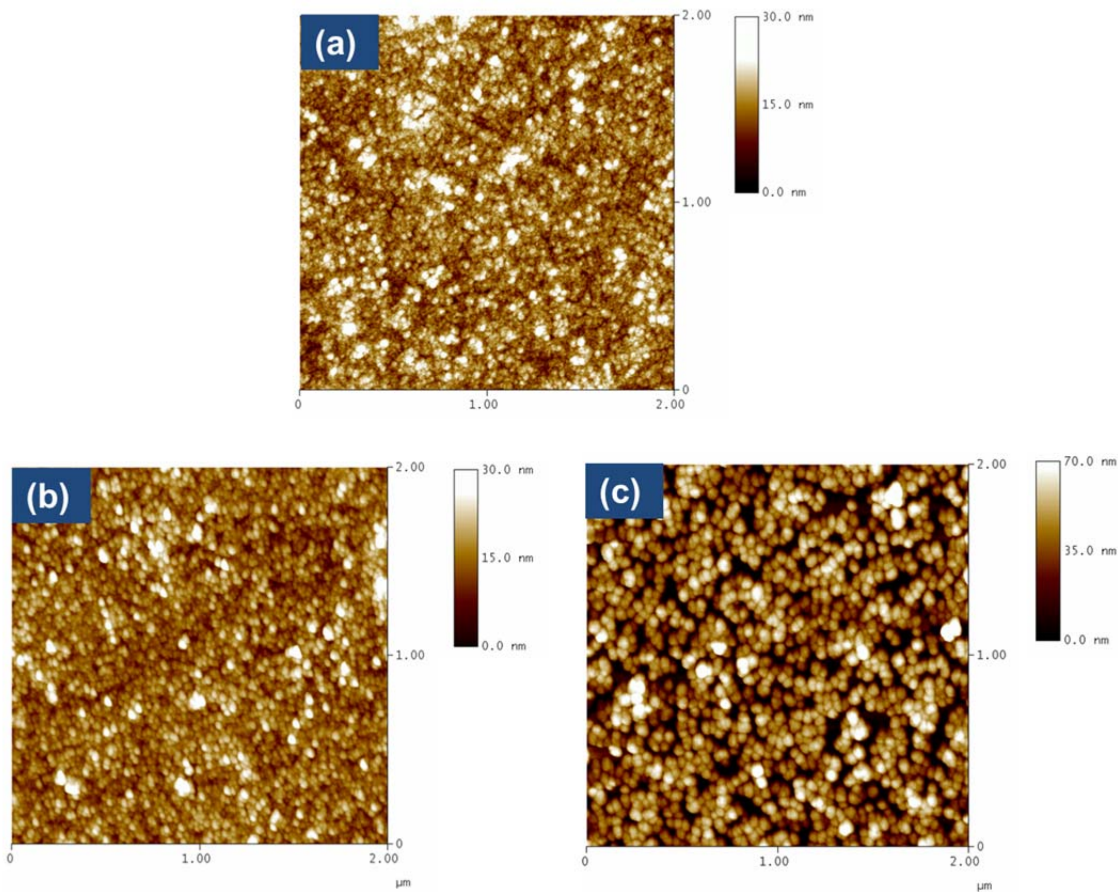

Figure 6.29 AFM images show the distribution of (a) *AP-Monoamine S*, (b) *AP-Monoamine M,* and (c) *AP-Monoamine L* on polyimide film surface. The Immersion time was 300 s and the temperature of the dispersion was 60 °C

Table 6.9 Surface roughness of polyimide films modified with different sizes of *AP-Monoamine*

Modification	R_{rms} [nm]	RSAI [%]
AP-Monoamine S	5.2±1	13.1±2
AP-Monoamine M	6.3±1	16.2±2
AP-Monoamine L	17.3±2	51.5±4
Permanganate treated Kapton® 200 H	2.6±0.3	1.5±0.2

The maximum adhesion of 11.9±0.3 N/cm was achieved when *AP-Monoamine M* was used. Contrary to the results from epoxy polymer adhesion evaluation (Section 5.3.4), the adhesion strength of copper on *AP-Monoamine S* modified polyimide film is much lower (2.4±0.2 N/cm) than the adhesion of copper on *AP-*

Monoamine M (11.9±0.3 N/cm) and *AP-Monoamine L* (11±0.2 N/cm) modified polyimide film. Since the number of nanoparticles in a unit of weight increases with decreasing diameter of particles, the dispersion with smaller particles diameter should contain a higher number of nanoparticles. By considering a perfect sphere and using 2.2 g/ml as the density of silica, the number of particles in 4 g/L of AP-Monoamine S is 4x1017 (AP-Monoamine M = 1 x1017). As described briefly before, the particles coverage on polyimide film surface is strongly dependent on the concentration of particles dispersion because of the number of particles. As demonstrated for *AP-Monoamine M*, when the amount of *AP-Monoamine* in dispersion is above the optimum concentration (1.6 g/L for *AP-Monoamine M*) multilayer of particles coverage due to the internanoparticles force between particles occurs. The aggregated nanoparticles act as weak boundary layer between two materials (polyimide and copper). As a result, adhesion strength of only 2.4±0.2 N/cm was obtained. This result is even lower than the adhesion strength of copper on polyimide film treated only with permanganate.

Although the particles coverage by *AP-Monoamine L* on polyimide film surface is not as high as that obtained for *AP-Monoamine S* and *AP-Monoamine M* particles, the adhesion strength is relatively high (11 ±0.2 N/cm). The low particles coverage is mainly due to the high density of amine functional groups on nanoparticles surface (Chapter 4). The repulsive force between charged nanoparticles keeps them away from each other. Unlike the *AP-Monoamine S*, the formation of multilayer of particles on the film surface is not observed by AFM for *AP-Monoamine L*. Consequently, adhesion failure due to weak internanoparticles interaction at the interface can be avoided. Moreover, the higher roughness on the surface of polyimide film treated with *AP-Monoamine L* (Table 6.9) might also give a distinct contribution to the adhesion enhancement, by providing higher mechanical interlocking side between copper and polyimide film.

In Cu/*AP-Monoamine*/polyimide assembly, the adhesion enhancement is not only contributed from introducing chemical bonds across the interface, but also from the surface morphology of polyimide film after treated with different particle sizes of *AP-Monoamine* (mechanical interlocking between copper and polyimide film).

6.3.5 Failure mode of deposited copper layers on *AP-Monoamine M* modified polyimide film surface

The adhesion failure of metal/polymer assemblies from electroless copper deposition on the *AP-Monoamine M* modified polyimide surface was briefly investigated. Figure 6.30 shows the surface morphology images of peeled polyimide film (a) and copper (b) from sample involving *AP-Monoamine M* treatment process that resulted in peel strength of 11.9±0.3 N/cm. The FESEM images give strong evidence for the existence of polyimide traces (bright traces) on the peeled copper surface. A large portion of polyimide film was ripped off from the surface and adhered strongly on the copper surface after peeling. This is likely a result of adhesion strength which is high enough to cause cohesive strength of the polyimide to fail. The results suggest that the adhesion failure mode involved the cohesive failure inside the polyimide substrate. The strong interaction between *AP-Monoamine M* and the polyimide surface contributed to the enhanced adhesion strength between copper and the polyimide surface treated with *AP-Monoamine M*. Furthermore, interaction between amine groups of *AP-Monoamine M* fixed on polyimide surface and palladium and copper also contributed to the adhesion strength enhancement.

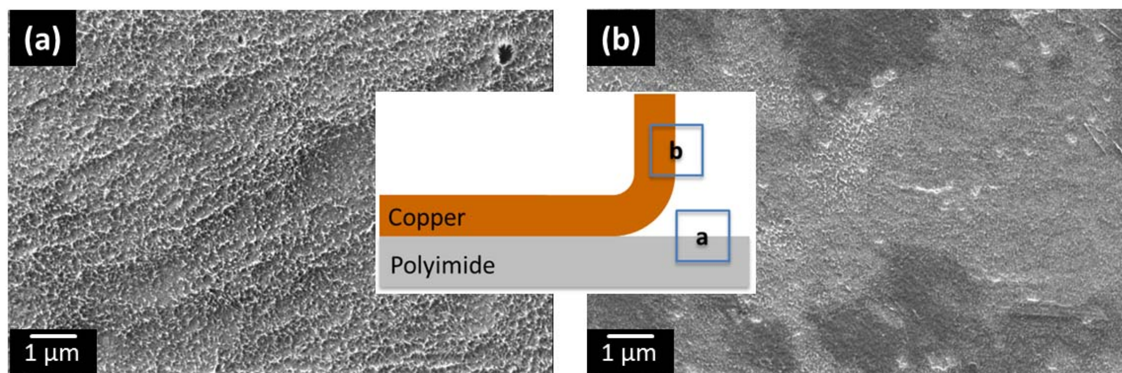

Figure 6.30 FE-SEM image of the surface morphology of peeled-off polyimide films which have been treated with 50 nm AP-Monoamine (a) and (b) a copper surface after adhesion evaluation

8. Conclusions

In this chapter, aminopropyl-functionalized silica nanoparticles (*AP-Monoamine M*) were used to modify the surface of polyimide film (Kapton® 200 H). The films were treated into alkaline permanganate solution prior to *AP-Monoamine M* treatment. In alkaline permanganate treatment, the film undergoes etch reaction rather than a simple reaction of hydrolysis of imide. The interaction force between *AP-Monoamine M* particles and polyimide film is the electrostatic attraction. The chemical reaction between imide groups of polyimide and amine groups of *AP-Monoamine M* to form amide was also considered as a possible chemical mechanism. The surface coverage of *AP-Monoamine M* particle is strongly influenced by the concentration of *AP-Monoamine M*, and the immersion time of polyimide film in *AP-Monoamine M* dispersion. The adsorbed *AP-Monoamine M* particles introduced amine groups, which can coordinate to the palladium catalyst used for electroless copper deposition, as well as to the copper. Hence, the adhesion between copper and polyimide film treated with *AP-Monoamine M* was enhanced. The strong adhesion between copper and polyimide film treated with *AP-Monoamine* M results in destruction of polyimide film after peeling.

The adhesion strength of copper on polyimide film modified with 0.8 g/L AP-Monoamine M increases with immersion time during dip coating, up to 9.8±0.4 N/cm. As the surface coverage of AP-Monoamine M particles increases. Weak boundary layer which result from aggregated particles of AP-Monoamine M at the polyimide/copper interface was observed, when the concentration of AP-Monoamine M is higher than 4 g/L. Hence, the adhesion strength decreases with increasing concentration of AP-Monoamine M, from 15±0.1 N/cm (1.6 g/L) to 3±0.3 N/cm (8 g/L). Contrary to the epoxy substrate discussed in Chapter 5, the adhesion strength decreased noticeably when the polyimide film was treated with AP-Monoamine S. The effect of the secondary force (mechanical adhesion) is more apparent for copper on polyimide film assembly than for copper on epoxy substrate.

Chapter 7 - Summary and Outlook

7.1 Summary

The poor adhesion between electrolessly deposited copper and dielectric materials is one of the major challenges in printed circuit board manufacturing. For this reason, numerous methods of modifying dielectric substrates have been developed and applied. Increasing the roughness of the dielectric surface is the most used approach to improve interfacial adhesion of copper plating on dielectric substrate. The future requirements of microelectronics industry (high density interconnections with smaller features and high frequency of transmission signal), require electroless deposition of copper on smooth dielectric surface. At the same time, good adhesion must be maintained.

In this work, a novel surface treatment method using functionalized silica nanoparticles is describe, to promote the adhesion of electrolessly deposited copper on the surface of dielectric substrate without additional roughening. The adhesion behavior of copper on the surface of dielectric substrate treated with functionalized silica nanoparticles, including various functional groups and sizes was investigated. Two commercially available dielectric materials were used as substrate: ABF-GX 92 (epoxy resin) from Ajinomoto Film Technology Company, Inc. Japan, and Kapton®200 H (Poly [*N, N′*-(oxydiphenylene)pyromellitimide]) from DuPont.

In the first part of this work, a surface modification method based on a silylation process has been used to prepare silica nanoparticles of desired size and surface functionality. Six types of functionalized silica nanoparticles were prepared: 3-aminopropyl (*AP-Monoamine*), N-(2-Aminoethyl)-3-Aminopropyl (*AP-Diamine*), 3-[2-(2-aminoethylamino)ethylamino]propyl (*AP-Triamine*), ureidopropyl (*AP-Ureido*), glycidoxypropyl (*AP-Glycidoxy*), and mercaptopropyl (*AP-Mercapto*). In the case of *AP-Monoamine*, three different sizes of nanoparticles were prepared, *AP-Monoamine S* (TEM diameter = 14±3 nm), *M* (TEM diameter = 18±3 nm) and *L* (TEM diameter = 44±6 nm). The modified particles have shown distinctive changes in the surface properties, especially the isoelectric point (IEP). The chemical derivatization method was used to determine the amount of amino groups on *AP-Monoamine*, *AP-Diamine* and *AP-Triamine* nanoparticles surface quantitatively. The characterization of the

sample using TEM, DLS, zeta potential, FTIR-ATR and UV-Vis indicates that multilayers of amino silane are formed at the silica surface.

The adhesion of copper on epoxy substrate modified with functionalized silica nanoparticles was investigated. The adhesion strength between copper and epoxy substrate has strong dependence on the functional groups at silica nanoparticles surface. No adhesion improvement was found when *AP-Mercapto* was used to modify the substrate, and only slight improvement of adhesion strength was obtained when *AP-Ureido* and *AP-Glycidoxy* were introduced at the interface. The introduction of the aminopropyl functionalized silica nanoparticles (*AP-Monoamine*) on epoxy substrate surface exhibit the highest adhesion strength improvement, from 0.6±0.1 N/cm to 9.2±0.3 N/cm with good thermal stability. Besides, the *AP-Monoamine* treatment on epoxy substrate can be effective for increasing the palladium adsorption, which is used as catalyst for electroless copper deposition.

In particular, it was demonstrated that the adhesion strength of copper on epoxy substrate modified with *AP-Monoamine M* particles increased with the nanoparticles concentration, immersion temperature and time. The adhesion strength of copper on epoxy substrate treated with *AP-Monoamine L* (4.7±1.1 N/cm) is significantly lower than *AP-Monoamine S* (8.8±0.2 N/cm) or *AP-Monoamine M* (9.2±0.3 N/cm), because of the poor surface coverage by larger particles. It was also found that the adhesion strength has strong dependence on the chain length of the amine, following the order: monoamine (-NH_2) > diamine (-NH-NH_2) > triamine (-NH-NH- NH_2). From the peeled samples, it was confirmed that the failure resulted in the cohesive of epoxy resin. The strong adhesion was attributed to the strong interaction between aminopropyl groups of the *AP-Monoamine* with palladium and copper, and the fact that the *AP-Monoamine* was covalently bonded to the epoxy substrate surface. A significant different in the thermal expansion coefficient between copper and epoxy substrate layer results in tensile stress across the interface, leading to extensive delamination between the two materials at elevated temperature.

A similar experiment has been conducted in order to obtained information about the influence of the aminopropyl functionalized silica nanoparticles (*AP-Monoamine*) on the adhesion behavior between copper and polyimide films, Kapton® 200 H. The adhesion strength increased significantly, up to 15±0.1 N/cm, when *AP-Monoamine M* applied on the polyimide film surface prior to copper plating. It was

noticed that for low concentration (0.8 g/l) of *AP-Monoamine M*, the adhesion strength increases with immersion time. When the concentration of *AP-Monoamine M* is higher than 1.6 g/l, the aggregation between particles is easily formed at polyimide surface. It serves as weak boundary layer at copper/polyimide interface after copper deposition, the driving force to the adhesion degradation. Therefore, the adhesion strength decreased noticeably from 15±0.1 N/cm (1.6 g/l) to 3.2±0.2 N/cm (8 g/l). The strong adhesion of copper on polyimide film treated with aminopropyl functionalized silica nanoparticles contributed from: 1. the chemical reaction of imide species N(C=O) of polyimide with aminopropyl functionalized silica nanoparticles to form amide groups –NH-(C=O)– , 2. good affinity of aminopropyl groups to palladium or copper atoms and ions, to form amino-, aquo- complex, 3. additional secondary force (mechanical adhesion) from the anchoring of copper by filling the nano-roughening structure of film surface treated with aminopropyl functionalized silica nanoparticles.

7.2 Outlook

The work described in this thesis contributes to the new application of silica nanoparticles, as adhesion enhancer of two different materials, which may induce further studies for understanding the chemical reaction between nanoparticles and polymers, as well as between particles and metals. In the future the work of this project may proceed in a number of directions, including the synthesis of silica nanoparticles carrying two different types of functional group on the same particle (Janus nanoparticles). By using this approach, adhesion enhancement on broad range of different polymers and metals would be expected. Controlling the functionalization of nanoparticles surface as attractive route to tune nanoparticles properties, and control the function of the modified substrates. Furthermore, the stability of the nanoparticles depending on the surface functional group needs to be investigated, especially in aqueous media.

The second area of focus should be a continued investigation of adhesion in two materials system, especially when the nanoparticles were introduced at the interface. Utilizing better understand of the adhesion mechanism between two distinct materials. Model experiment by using identical molecules could help in simplifying the investigation process.

In addition, selective adsorption of the palladium catalyst and the copper atoms on aminopropyl functionalized silica could be used as attractive route to manufacture fine line conductive patterning of dielectrics.

Finally, since application is the ultimate driving force in this work, incorporating the system discovered in the laboratory into bigger scale is one of the challenges in the future.

Zusammenfassung

Die schlechte Adhäsion zwischen stromlos abgeschiedenem Kupfer und Dielektrikum ist eine der größten Herausforderungen bei der Produktion von Leiterplatten. Aus diesem Grund wurden zahlreiche Methoden zur Modifizierung von dielektrischen Substraten entwickelt und angewendet. Am häufigsten wurde die Rauheit der Oberfläche des Dielektrikums erhöht, um die Grenzflächenhaftung bei der Verkupferung auf dielektrischen Materialien zu verbessern. Die zukünftigen Anforderungen der Mikroelektronik-Industrie verlangen eine stromlose Kupferabscheidung auf glatten dielektrischen Oberflächen, wobei gleichzeitig die gute Adhäsion beibehalten werden muss.

In dieser Arbeit wurde eine neue Methode zur Oberflächenbehandlung mittels funktionalisierter Silica-Nanopartikel verwendet. Dadurch konnte die Adhäsion von stromlos abgeschiedenem Kupfer auf der dielektrischen Oberfläche ohne zusätzliches Aufrauen gefördert werden. Es wurde das Adhäsionsverhalten von Kupfer auf der Oberfläche von dielektrischen Materialien untersucht, die mit unterschiedlich funktionalisierten und unterschiedlich großen Silica-Nanopartikel behandelt wurden. Zwei handelsübliche dielektrische Materialien wurden als Basismaterial verwendet: ABF-GX 92 (Epoxidharz) von Ajinomoto Film Technology Company, Inc. Japan und Kapton®200 H (Poly[N,N-(oxydiphenylen)pyromellitimid]) von DuPont.

Im ersten Teil dieser Arbeit wurde mittels einer Oberflächenmodifikationsmethode beim Silylierungsprozess Silica-Nanopartikel mit unterschiedlichen Größen und Funktionalitäten dargestellt. Sechs unterschiedlich funktionalisierte Silica-Nanopartikel 3-aminopropyl (AP-Monoamine), N-(2-Aminoethyl)-3-Aminopropyl(AP-Diamine), 3-[2-(2-aminoethylamino)ethylamino]propyl (AP-Triamine), Ureidopropyl (AP-Ureido), Glycidoxypropyl (AP-Glycidoxy), und Mercaptopropyl (AP-Mercapto) wurden synthetisiert. Im Fall von *AP-Monoamine* wurden drei unterschiedliche Größen synthetisiert: *AP-Monoamine S* (TEM Durchmesser = 14±3 nm), *M* (TEM Durchmesser = 18±3 nm) und *L* (TEM Durchmesser = 44±6 nm). Die modifizierten Partikel zeigen unverwechselbare Veränderungen ihrer Oberflächeneigenschaften und unterscheiden sich insbesondere im Wert des isoelektrischen Punkts (IEP). Mittels chemischer

Derivatisierung wurden die Aminogruppen auf der Nanopartikeloberfläche der *AP-Monoamine*, *AP-Diamine* und *AP-Triamine* quantitativ im Photometer nachgewiesen. Die Charakterisierung der Proben mit DLS, Zeta-Potential, FTIR-ATR und UV-Vis Spektroskopie weisen darauf hin, dass sich Mehrfachschichten von Aminosilanen auf der Silica-Oberfläche gebildet haben.

Die Adhäsion von Kupfer auf Epoxidmaterial wurde untersucht, das zuvor mit Silica-Nanopartikeln modifiziert worden war. Die Adhäsionsstärke zwischen Kupfer und Epoxidmaterial hängt sehr stark von den funktionellen Gruppen auf der Silica-Nanopartikeloberfläche ab. Bei der Verwendung von *AP-Mercapto* zur Modifizierung des Substrates wurde keinerlei Haftungsverbesserung festgestellt. Die Adhäsionskraft wurde durch die Einführung von *AP-Ureido-* und *AP-Glycidoxy-*Gruppen an den Grenzflächen ein wenig erhöht. Die Einführung von aminofunktionalisierten Silica-Nanopartikeln (*AP-Monoamine*) auf der Epoxidsubstratoberfläche erhöhte die Adhäsionskraft von 0,6±0,1 N/cm auf 9,2±0,3 N/cm mit einer guten thermischen Stabilität. Zusätzlich kann man mit der AP-*Monoamine*-Behandlung auf dem Epoxidmaterial die Adsorption von Palladium erhöhen, das als Katalysator bei der stromlosen Kupferabscheidung dient.

Im Besonderen wurde gezeigt, wie die Adhäsionskraft von Kupfer auf dem Epoxidmaterial, das mit *AP-Monoamine M* Partikeln modifiziert wurde, mittels Nanopartikelkonzentration, Eintauchtemperatur und Behandlungsdauer verbessert wurde. Die Adhäsionskraft von Kupfer auf Epoxidmaterial, das mit *AP-Monoamine L* (4,7±1,1 N/cm) behandelt wurde, ist aufgrund der niedrigen Oberflächenbedeckung der größeren Partikel deutlich niedriger als bei Modifikation mit *AP-Monoamine S* (8,8±0,2 N/cm) oder *AP-Monoamine M* (9,2±0,3 N/cm). Die Untersuchungen haben zusätzlich ergeben, dass die Kettenlänge der verwendeten Amine ebenfalls einen starken Einfluss auf die Adhäsionskraft hat; dabei gilt der Reihenfolge nach: Monoamin ($-NH_2$) > Diamin ($NH-NH_2$) > Triamin ($NH-NH-NH_2$). Von den in Abzugstests abgeschälten Proben konnte bestätigt werden, dass das Haftungsversagen nun durch Kohäsionsbruch im Basismaterial verursacht wird. Die große Adhäsion zwischen Kupfer und Epoxidmaterial entsteht einerseits durch die starke Interaktion zwischen den Aminopropylgruppen der *AP-Monoamine* mit Palladium und Kupfer und andererseits durch eine kovalente Bindung der *AP-Monoamine* an die Oberfläche des Epoxidmaterials. Der signifikante Unterschied im

thermischen Expansionskoeffizienten zwischen Kupfer und den Schichten des Epoxidmaterials führt zu einer Zugspannung quer über die gesamte Grenzfläche. Dies sorgt für eine umfangreiche Delaminierung zwischen den beiden Materialien bei erhöhter Temperatur.

Weitere Untersuchungen wurden durchgeführt, um Informationen über den Einfluss von aminopropyl-funktionalisierten Silica-Nanopartikeln (*AP-Monoamine*) auf die Adhäsion zwischen Kupfer und Polyimidfilm Kapton® 200 H zu erhalten. Die Adhäsionskraft wurde erheblich erhöht, auf bis zu 15±0,1 N/cm, als *AP-Monoamine M* vor der Kupfermetallisierung auf die Polyimidfilmoberfläche aufgebracht wurde. Es wurde festgestellt, dass bei geringer Konzentration (0,8 g/L) des *AP-Monoamine M* die Adhäsionskraft mit der Eintauchzeit steigt. Wenn die Konzentration des *AP-Monoamine M* mehr als 1,6 g/L beträgt, kommt es zur Ausfällung der Partikel auf der Polyimidoberfläche. Dies erzeugt eine schwache Grenzschicht zwischen Kupfer und Polyimid nach der Kupferabscheidung, was zu einer starken Abnahme der Adhäsion führt. Die Adhäsionskraft des Kupfers sinkt beträchtlich von 15±0,1 N/cm (1,6 g/L) auf 3,2±0,2 N/cm (8 g/L). Die starke Adhäsion von Kupfer auf dem Polyimidfilm, der mit aminopropyl-funktionalisierten Silica-Nanopartikeln behandelt wurde, ist auf folgende Gründe zurückzuführen:

1. Die Imid-Spezies N(C=O) des Polyimids formt mit den aminopropyl-funktionalisierten Silica-Nanopartikeln Amidgruppen –NH-(C=O)-.

2. Aminopropylgruppen haben eine gute Affinität zu Palladium- oder Kupferatomen und -Ionen und können Amino- oder Aquakomplexe formen.

3. Eine zusätzliche sekundäre Kraft (mechanische Adhäsion) wird von der Verankerung von Kupfer in den Füllstellen der durch die aufgetragenen aminopropyl-funktionalisierten Silica-Nanopartikel gebildeten nanogerauten Oberfläche (additive Rauigkeit) des Polyimidfilms erzeugt.

References

[1] A. Beganskienė, V. Sirutkaitis, M. Kurtinaitienė, R. Juškėnas, A. Kareiva, *Mater Sci (Medžiagotyra)* **2004**, *10*, 287-290.

[2] G. Socrates, G. Socrates, *Infrared and Raman characteristic group frequencies: tables and charts*, Wiley Chichester, **2001**.

[3] N. Hiyoshi, K. Yogo, T. Yashima, *Microporous and Mesoporous Materials* **2005**, *84*, 357-365.

[4] C. A. R. Costa, C. A. P. Leite, F. Galembeck, *The Journal of Physical Chemistry B* **2003**, *107*, 4747-4755.

[5] J. Miao, H. Wan, G. Guan, *Catalysis Communications* **2011**, *12*, 353-356.

[6] S. R. Culler, H. Ishida, J. L. Koenig, *Journal of Colloid and Interface Science* **1985**, *106*, 334-346.

[7] Y. J. Gong, Z. Hong Li, D. Wu, Y. H. Sun, F. Deng, Q. Luo, Y. Yue, *Microporous and Mesoporous Materials* **2001**, *49*, 95-102.

[8] R. Peña-Alonso, F. Rubio, J. Rubio, J. L. Oteo, *J Mater Sci* **2007**, *42*, 595-603.

[9] N. Nagai, H. Hashimoto, *Applied Surface Science* **2001**, *172*, 307-311.

[10] P. Eisler, *My life with the printed circuit*, Lehigh University Press, **1989**.

[11] C. F. Coombs, *Printed circuits handbook*, McGraw-Hill New York, **2008**.

[12] *Semiconductor Insustry Association, International Technology Roadmap for Semiconductors* **2008**.

[13] Prismark, *The Semiconductor and Packaging Report* **2013**.

[14] J.-H. Lee, S. Byun, S. Kang, S. Kim, *Meeting Abstracts* **2006**, *MA2005-02*, 686.

[15] J. E. Cross, US Patent, US4217182 A, **1980**.

[16] H. Azimi, *Microelectronic Packaging Substrates* **2013**.

[17] D. Schröer, R. J. Nichols, H. Meyer, *Electrochimica Acta* **1995**, *40*, 1487-1494.

[18] J. Ge, M. P. K. Turunen, J. K. Kivilahti, *Thin Solid Films* **2003**, *440*, 198-207.

[19] J. Ge, M. P. K. Turunen, J. K. Kivilahti, *Journal of Polymer Science Part B: Polymer Physics* **2003**, *41*, 623-636.

[20] S. Siau, A. Vervaet, E. Schacht, A. Van Calster, *Journal of The Electrochemical Society* **2004**, *151*, C133-C141.

[21] S. Siau, A. Vervaet, L. Van Vaeck, E. Schacht, U. Demeter, A. Van Calster, *Journal of The Electrochemical Society* **2005**, *152*, C442-C455.

[22] H. Lee, S. M. Dellatore, W. M. Miller, P. B. Messersmith, *Science* **2007**, *318*, 426-430.

[23] Y. Liao, B. Cao, W.-C. Wang, L. Zhang, D. Wu, R. Jin, *Applied Surface Science* **2009**, *255*, 8207-8212.

[24] D. Schaubroeck, E. Van Den Eeckhout, J. De Baets, P. Dubruel, L. Van Vaeck, A. Van Calster, *Journal of Adhesion Science and Technology* **2012**, *26*, 2301-2314.

[25] J. R. Lancaster, J. Jehani, G. T. Carroll, Y. Chen, N. J. Turro, J. T. Koberstein, *Chemistry of Materials* **2008**, *20*, 6583-6585.

[26] S. Siau, A. Vervaet, E. Schacht, U. Demeter, A. Van Calster, *Thin Solid Films* **2006**, *495*, 348-356.

[27] G. H. Yang, E. T. Kang, K. G. Neoh, Y. Zhang, K. L. Tan, *Langmuir* **2000**, *17*, 211-218.

[28] G. H. Yang, E. T. Kang, K. G. Neoh, *Applied Surface Science* **2001**, *178*, 165-177.
[29] Z. J. Yu, E. T. Kang, K. G. Neoh, *Polymer* **2002**, *43*, 4137-4146.
[30] Z. J. Yu, E. T. Kang, K. G. Neoh *Journal of The Electrochemical Society* **2002**, *149*, C10-C17.
[31] W. C. Wang, E. T. Kang, K. G. Neoh, *Applied Surface Science* **2002**, *199*, 52-66.
[32] A. Garcia, N. Hanifi, B. Jousselme, P. Jégou, S. Palacin, P. Viel, T. Berthelot, *Advanced Functional Materials* **2013**, n/a-n/a.
[33] M. Charbonnier, M. Alami, M. Romand, *Journal of The Electrochemical Society* **1996**, *143*, 472-480.
[34] M. Charbonnier, M. Romand, *International Journal of Adhesion and Adhesives* **2003**, *23*, 277-285.
[35] N. Inagaki, T. Sakaguchi, *Polymer surface modification: Relefance to adhesion* **2009**, *5*.
[36] P. C. Hidber, W. Helbig, E. Kim, G. M. Whitesides, *Langmuir* **1996**, *12*, 1375-1380.
[37] S. Brandow, M.-S. Chen, R. Aggarwal, C. Dulcey, J. Calvert, W. Dressick, *Langmuir* **1999**, *15*, 5429-5432.
[38] M. S. Chen, C. S. Dulcey, L. A. Chrisey, W. J. Dressick, *Advanced Functional Materials* **2006**, *16*, 774-783.
[39] D. D. Gandhi, M. Lane, Y. Zhou, A. P. Singh, S. Nayak, U. Tisch, M. Eizenberg, G. Ramanath, *Nature* **2007**, *447*, 299-302.
[40] K. Mori, IWATE UNIV, **2008**.
[41] D.-l. Liu, Z.-g. Yang, C. Zhang, *Materials Science and Engineering: B* **2010**, *166*, 67-75.
[42] G. Brist, S. Hall, S. Clouser, T. Liang, in *ECWC 10 Conf., IPC Printed Circuits Expo*, **2005**, pp. S19-12.
[43] A. J. Kinloch, *Adhesion and adhesives: science and technology*, Springer, **1987**.
[44] J. Schultz, M. Nardin, *Handbook of adhesive technology* **1994**, 19-33.
[45] T. Young, *Philosophical Transactions of the Royal Society of London* **1805**, *95*, 65-87.
[46] J. W. McBain, D. G. Hopkins, *The Journal of Physical Chemistry* **1924**, *29*, 188-204.
[47] I. Skeist, *Journal of Polymer Science: Polymer Letters Edition* **1983**, *21*, 301-302.
[48] L. Pauling, *The Natune of the Chemical Bond and the Structure of Molecules and Crystals: An Introduction to Modern Structural Chemistry, Vol. 18*, Cornell University Press, **1960**.
[49] R. Good, R. Patrick, *Marcel Dekker, New York* **1967**, *1*, 21.
[50] F. M. Fowkes, *Physicochemical Aspects of Polymer Surfaces* **1983**, *2*, 583.
[51] J. J. Bikerman, *Industrial & Engineering Chemistry* **1967**, *59*, 40-44.
[52] S. Siau, A. Vervaet, S. Nalines, E. Schacht, A. Van Calster, *Journal of The Electrochemical Society* **2004**, *151*, C816-C830.
[53] S. Siau, A. Vervaet, S. Nalines, E. Schacht, A. Van Calster, *Journal of The Electrochemical Society* **2004**, *151*, C831-C849.
[54] A. Bhattacharya, J. W. Rawlins, P. Ray, *Polymer grafting and crosslinking*, Wiley, **2008**.
[55] X. Sui, S. Zapotoczny, E. M. Benetti, P. Schon, G. J. Vancso, *Journal of Materials Chemistry* **2010**, *20*, 4981-4993.

[56] M. Charbonnier, F. Gaillard, F. Bessueille, M. Romand, *Polymer Surface Modification: Relevance to Adhesion* **2009**, *5*, 217.
[57] J. M. Burkstrand, *Journal of Vacuum Science and Technology* **1978**, *15*, 223-226.
[58] L. J. Gerenser, *Journal of Vacuum Science & Technology A: Vacuum, Surfaces, and Films* **1988**, *6*, 2897-2903.
[59] M. Charbonnier, M. Romand, Y. Goepfert, D. Léonard, F. Bessueille, M. Bouadi, *Thin Solid Films* **2006**, *515*, 1623-1633.
[60] M. Charbonnier, M. Romand, Y. Goepfert, *Surface and Coatings Technology* **2006**, *200*, 5028-5036.
[61] E. P. Plueddemann, *The Journal of Adhesion* **1970**, *2*, 184-201.
[62] A. Ulman, *Chemical Reviews* **1996**, *96*, 1533-1554.
[63] G. L. Witucki, *Journal of coatings technology* **1993**, *65*, 57-57.
[64] T. G. Vargo, J. A. Gardella, J. M. Calvert, M.-S. Chen, *Science* **1993**, *262*, 1711-1712.
[65] K. L. Mittal, *Metallized Plastics, Vol. 2*, Springer, **1991**.
[66] E. Budke, J. Krempel-Hesse, H. Maidhof, H. Schüssler, *Surface and Coatings Technology* **1999**, *112*, 108-113.
[67] D. P. Long, J. M. Blackburn, J. J. Watkins, *Advanced Materials* **2000**, *12*, 913-915.
[68] E. Sacher, *Metallization of polymers 2*, Springer, **2002**.
[69] D. Zabetakis, W. J. Dressick, *ACS Applied Materials & Interfaces* **2009**, *1*, 4-25.
[70] A. Garcia, *Thèse de doctorat de l'École Polytechnique* **2011**.
[71] G. O. Mallory, J. B. Hajdu, *Electroless plating: fundamentals and applications*, **1990**.
[72] M. Wojnicki, K. Pacławski, E. Rudnik, K. Fitzner, *Hydrometallurgy* **2011**, *110*, 56-61.
[73] M. Paunovic, *Plating* **1968**, *55*, 1161.
[74] H. Narahashi, *The 63rd Electronic Components and Technology Conference (ECTC)* **2013**.
[75] *Ajinomoto Fine Techno Co., Inc, ABF Recent Development* **2010**.
[76] V. Ratta, *PhD Dissertation* **1999**, *Chapter 1*.
[77] DuPont, *DuPont™, Kapton® HN Technical Data Sheet* **2011**.
[78] M. L. McConnell, *Analytical Chemistry* **1981**, *53*, 1007A-1018A.
[79] *Zetasizer Nano Series Technical Note. MRK654-01* **2011**.
[80] *Malvern Instruments Ltd., Zetasizer Nanoseries User Manual* **2009**.
[81] B. Chu, *Laser light scattering*, Elsevier, **1974**.
[82] S. H. Behrens, D. G. Grier, *The Journal of Chemical Physics* **2001**, *115*, 6716-6721.
[83] W. B. Russel, D. A. Saville, W. R. Schowalter, *Colloidal dispersions*, Cambridge University Press, **1992**.
[84] *Elementar Analysensysteme GmbH, CHNOS Elementaranalysator Vario EL Cube Bedienungsanleitung* **2010**.
[85] D. A. Skoog, F. J. Holler, T. A. Nieman, **1998**.
[86] T. G. Waddell, D. E. Leyden, M. T. DeBello, *Journal of the American Chemical Society* **1981**, *103*, 5303-5307.
[87] P. K. Dutta, W. Turbeville, *The Journal of Physical Chemistry* **1991**, *95*, 4087-4092.
[88] V. Semiconductor, *accessed Last Accessed: March* **2012**, *10*, 2012.

[89] B. Stuart, in *Kirk-Othmer Encyclopedia of Chemical Technology*, John Wiley & Sons, Inc., **2000**.
[90] C.-P. S. Hsu, *Handbook of instrumental techniques for analytical chemistry* **1997**, *249*.
[91] *Pike Technology Application Note., ATR – Theory and Applications* **2011**.
[92] J. F. Watts, J. Wolstenholme, *Wiley-VCH* **2003**, *1*, 224.
[93] J. C. Vickerman, I. S. Gilmore, *Surface analysis: the principal techniques, Vol. 2*, Wiley Online Library, **2009**.
[94] G. Binnig, C. F. Quate, C. Gerber, *Physical Review Letters* **1986**, *56*, 930-933.
[95] Q. Zhong, D. Inniss, K. Kjoller, V. B. Elings, *Surface Science Letters* **1993**, *290*, L688-L692.
[96] J. M. Mermet, *Journal of Analytical Atomic Spectrometry* **2005**, *20*, 11-16.
[97] X. Hou, B. T. Jones, in *Encyclopedia of Analytical Chemistry*, John Wiley & Sons, Ltd, **2006**.
[98] G. H. Bogush, M. A. Tracy, C. F. Zukoski Iv, *Journal of Non-Crystalline Solids* **1988**, *104*, 95-106.
[99] W. Stöber, A. Fink, E. Bohn, *Journal of Colloid and Interface Science* **1968**, *26*, 62-69.
[100] B. Radhakrishnan, R. Ranjan, W. J. Brittain, *Soft Matter* **2006**, *2*, 386-396.
[101] R. D. Badley, W. T. Ford, F. J. McEnroe, R. A. Assink, *Langmuir* **1990**, *6*, 792-801.
[102] R. Brown, *The Philosophical Magazine, or Annals of Chemistry, Mathematics, Astronomy, Natural History and General Science* **1828**, *4*, 161-173.
[103] R. K. Iler, *John Wiley & Sons, Inc.* **1979**.
[104] G. Ghosh, *Optics Communications* **1999**, *163*, 95-102.
[105] B. J. Berne, R. Pecora, *Dynamic light scattering: with applications to chemistry, biology, and physics*, Courier Dover Publications, **1976**.
[106] F. Krumeick, *Laboratory of Inorganic Chemistry, disponível em http://www. microscopy. ethz. ch/downloads/Interactions. pdf, consultado em* **2011**, 3-08.
[107] E. Meyer, *Progress in Surface Science* **1992**, *41*, 3-49.
[108] H. Choi, I. W. Chen, *Journal of Colloid and Interface Science* **2003**, *258*, 435-437.
[109] E. P. Plueddemann, *Silane coupling agents*, Springer, **1982**.
[110] E. T. Vandenberg, L. Bertilsson, B. Liedberg, K. Uvdal, R. Erlandsson, H. Elwing, I. Lundström, *Journal of Colloid and Interface Science* **1991**, *147*, 103-118.
[111] G. V. Franks, *Journal of Colloid and Interface Science* **2002**, *249*, 44-51.
[112] H. K. Hall, *Journal of the American Chemical Society* **1957**, *79*, 5441-5444.
[113] M. Pálmai, L. N. Nagy, J. Mihály, Z. Varga, G. Tárkányi, R. Mizsei, I. C. Szigyártó, T. Kiss, T. Kremmer, A. Bóta, *Journal of Colloid and Interface Science* **2013**, *390*, 34-40.
[114] G. P. Knowles, J. V. Graham, S. W. Delaney, A. L. Chaffee, *Fuel Processing Technology* **2005**, *86*, 1435-1448.
[115] K. M. R. Kallury, P. M. Macdonald, M. Thompson, *Langmuir* **1994**, *10*, 492-499.
[116] J. H. Moon, J. W. Shin, S. Y. Kim, J. W. Park, *Langmuir* **1996**, *12*, 4621-4624.
[117] S. Ek, E. I. Iiskola, L. Niinistö, J. Vaittinen, T. T. Pakkanen, A. Root, *The Journal of Physical Chemistry B* **2004**, *108*, 11454-11463.
[118] E. Soto-Cantu, R. Cueto, J. Koch, P. S. Russo, *Langmuir* **2012**, *28*, 5562-5569.
[119] L. T. Zhuravlev, *Langmuir* **1987**, *3*, 316-318.

[120] M.-C. Brochier Salon, M. Abdelmouleh, S. Boufi, M. N. Belgacem, A. Gandini, *Journal of Colloid and Interface Science* **2005**, *289*, 249-261.
[121] B. Kannan, D. A. Higgins, M. M. Collinson, *Langmuir* **2012**, *28*, 16091-16098.
[122] C. C. P. Chan, N. R. Choudhury, P. Majewski, *Colloids and Surfaces A: Physicochemical and Engineering Aspects* **2011**, *377*, 20-27.
[123] C.-H. Kuo, H.-Y. Chang, C.-P. Liu, S.-H. Lee, Y.-W. You, J.-J. Shyue, *Physical Chemistry Chemical Physics* **2011**, *13*, 3649-3653.
[124] R. C. Weast, *The American Journal of the Medical Sciences* **1969**, *257*, 423.
[125] M. Tokunaga, J. F. Larrow, F. Kakiuchi, E. N. Jacobsen, *Science* **1997**, *277*, 936-938.
[126] E. N. Jacobsen, *Accounts of Chemical Research* **2000**, *33*, 421-431.
[127] L. Favretto, W. A. Nugent, G. Licini, *Tetrahedron Letters* **2002**, *43*, 2581-2584.
[128] Y. Yu, J. Addai-Mensah, D. Losic, *Science and Technology of Advanced Materials* **2012**, *13*, 015008.
[129] E. N. Jacobsen, F. Kakiuchi, R. G. Konsler, J. F. Larrow, M. Tokunaga, *Tetrahedron Letters* **1997**, *38*, 773-776.
[130] N. B. Colthup, L. H. Daly, S. E. Wiberley, in *Introduction to Infrared and Raman Spectroscopy (Third Edition)* (Eds.: N. B. Colthup, L. H. Daly, S. E. Wiberley), Academic Press, San Diego, **1990**, pp. 355-385.
[131] H. Kind, A. M. Bittner, O. Cavalleri, K. Kern, T. Greber, *The Journal of Physical Chemistry B* **1998**, *102*, 7582-7589.
[132] A. M. Bittner, *Surface Science Reports* **2006**, *61*, 383-428.
[133] P. K. Jal, S. Patel, B. K. Mishra, *Talanta* **2004**, *62*, 1005-1028.
[134] M. V. Lombardo, M. Videla, A. Calvo, F. G. Requejo, G. J. A. A. Soler-Illia, *Journal of Hazardous Materials* **2012**, *223–224*, 53-62.
[135] *ASTM International, ASTM D6862 – 11* **2011**.
[136] *JEDEC Solid State Technology Association, JESD22-A110-B* **1999**.
[137] *JEDEC Solid State Technology Association, IPC/JEDEC J-STD-020D* **2007**.
[138] G. E. P. Box, D. W. Behnken, *Technometrics* **1960**, *2*, 455-475.
[139] R. H. Myers, A. I. Khuri, W. H. Carter, *Technometrics* **1989**, *31*, 137-157.
[140] J. Sall, L. Creighton, A. Lehman, *JMP start statistics: a guide to statistics and data analysis using JMP and JMP IN software*, SAS Institute, **2005**.
[141] M. G. González, J. C. Cabanelas, J. Baselga, *Infrared Spectroscopy–Materials Science, Engineering and Technology* **2012**.
[142] H. R. Beyer, W. Walter, *Beyer/Walter Organic Chemistry: A Comprehensive Degree Text and Source Book*, Horwood Pub Limited, **1997**.
[143] G. K. White, *Cryogenics* **1964**, *4*, 2-7.
[144] B. G. Jung, S.-H. Min, C.-W. Kwon, S.-H. Park, K.-B. Kim, T.-S. Yoon, *Journal of The Electrochemical Society* **2009**, *156*, K86-K90.
[145] J. Klein, Y. Almog, P. Luckham, in *Polymer Adsorption and Dispersion Stability, Vol. 240*, American Chemical Society, **1984**, pp. 227-244.
[146] R. P. Hanzlik, A. Hamburg, *Journal of the American Chemical Society* **1978**, *100*, 1745-1749.
[147] K. Prasad, A. K. Rao, M. S. Mohan, *Journal of Coordination Chemistry* **1987**, *16*, 251-262.
[148] A. M. Crouch, L. E. Khotseng, M. Polhuis, D. R. Williams, *Analytica Chimica Acta* **2001**, *448*, 231-237.
[149] E. H. Wong, R. Rajoo, T. B. Lim, M. Yui-Wing, *Components and Packaging Technologies, IEEE Transactions on* **2005**, *28*, 862-868.
[150] I. Linossier, F. Gaillard, M. Romand, T. Nguyen, *The Journal of Adhesion* **1999**, *70*, 221-239.

[151] T. Nguyen, E. Byrd, D. Bentz, C. Lint, *Progress in Organic Coatings* **1996**, *27*, 181-193.
[152] P. A. Thiel, T. E. Madey, *Surface Science Reports* **1987**, *7*, 211-385.
[153] Q. H. Fan, A. Fernandes, E. Pereira, J. Grácio, *Diamond and Related Materials* **1999**, *8*, 1549-1554.
[154] J. J. Cruywagen, R. J. Kriek†, *Journal of Coordination Chemistry* **2007**, *60*, 439-447.
[155] K. F. Lam, X. Chen, G. McKay, K. L. Yeung, *Industrial & Engineering Chemistry Research* **2008**, *47*, 9376-9383.
[156] I. Gallardo, J. Pinson, N. Vilà, *The Journal of Physical Chemistry B* **2006**, *110*, 19521-19529.
[157] N. Inagaki, S. Tasaka, K. Hibi, *Journal of Polymer Science Part A: Polymer Chemistry* **1992**, *30*, 1425-1431.
[158] Z. Wang, A. Furuya, K. Yasuda, H. Ikeda, T. Baba, M. Hagiwara, S. Toki, S. Shingubara, H. Kubota, T. Ohmi, *Journal of Adhesion Science and Technology* **2002**, *16*, 1027-1040.
[159] X. D. Huang, S. M. Bhangale, P. M. Moran, N. L. Yakovlev, J. Pan, *Polymer International* **2003**, *52*, 1064-1069.
[160] S. Lee, S. S. Park, H. K. Lee, *Macromolecular Symposia* **2007**, *249-250*, 586-590.
[161] F. D. Egitto, L. J. Matienzo, *IBM Journal of Research and Development* **1994**, *38*, 423-439.
[162] Y. Nakamura, Y. Suzuki, Y. Watanabe, *Thin Solid Films* **1996**, *290–291*, 367-369.
[163] K. W. Lee, S. P. Kowalczyk, J. M. Shaw, *Langmuir* **1991**, *7*, 2450-2453.
[164] H. Okumura, T. Takahagi, N. Nagai, S. Shingubara, *Journal of Polymer Science Part B: Polymer Physics* **2003**, *41*, 2071-2078.
[165] D. Wolany, T. Fladung, L. Duda, J. W. Lee, T. Gantenfort, L. Wiedmann, A. Benninghoven, *Surface and Interface Analysis* **1999**, *27*, 609-617.
[166] C. E. Baumgartner, L. R. Scott, *Journal of Adhesion Science and Technology* **1995**, *9*, 789-799.
[167] F. Garbassi, E. Occhiello, in *Polyimides: Fundamentals and Applications* (Eds.: M. Gosh, K. L. Mittal), **1996**, pp. 367-388.
[168] H. Ishida, S. T. Wellinghoff, E. Baer, J. L. Koenig, *Macromolecules* **1980**, *13*, 826-834.
[169] M. Kauer, *Masterarbeit, Technische Universität Berlin Fakultät II für Chemie, Physik und Mathematik* **2013**.
[170] G. Beamson, D. Briggs, *High resolution XPS of organic polymers: the Scienta ESCA300 database, Vol. 4*, Wiley Chichester, **1992**.
[171] W. Yu, T.-M. Ko, *European Polymer Journal* **2001**, *37*, 1791-1799.
[172] B. D. Silverman, J. W. Bartha, J. G. Clabes, P. S. Ho, A. R. Rossi, *Journal of Polymer Science Part A: Polymer Chemistry* **1986**, *24*, 3325-3333.
[173] L. P. B. a. A. I. Braise, in *Polyimide: Synthesis, characterization and applications Vol. 1* (Ed.: K. L. Mittal), Penum Press, New York, **1984**, pp. 537-545.
[174] D. C. P. S. Bagus, S. P. Kowalczyk, G. Pacchioni, and F. Parmigiani, *Journal of Electron Sperctroscopy Related Phenomena* **1990**, 69.
[175] R. Flitsch, D.-Y. Shih, *Journal of Adhesion Science and Technology* **1996**, *10*, 1241-1253.
[176] A. M. Ektessabi, S. Hakamata, *Thin Solid Films* **2000**, *377–378*, 621-625.
[177] Z. Kolská, A. Řezníčková, V. Švorčík, *e-Polymers* **2012**, *12*, 960-972.

[178] Y. Min, M. Akbulut, K. Kristiansen, Y. Golan, J. Israelachvili, *Nat Mater* **2008**, *7*, 527-538.
[179] A. S. Dimitrov, K. Nagayama, *Langmuir* **1996**, *12*, 1303-1311.
[180] T. S. Yoon, J. Oh, S. H. Park, V. Kim, B. G. Jung, S. H. Min, J. Park, T. Hyeon, K. B. Kim, *Advanced Functional Materials* **2004**, *14*, 1062-1068.
[181] M. H. Kim, S. H. Im, O. O. Park, *Advanced Functional Materials* **2005**, *15*, 1329-1335.
[182] B. G. Prevo, O. D. Velev, *Langmuir* **2004**, *20*, 2099-2107.
[183] Y. Xiao, T.-S. Chung, M. L. Chng, *Langmuir* **2004**, *20*, 8230-8238.
[184] H. K. Yun, K. Cho, J. K. Kim, C. E. Park, S. M. Sim, S. Y. Oh, J. M. Park, *Polymer* **1997**, *38*, 827-834.
[185] D. Briggs, *Handbook of X-ray Photoelectron Spectroscopy Vol. 3*, Heyden & Son Ltd., **1981**.
[186] A. J. Pertsin, Y. M. Pashunin, *Applied Surface Science* **1991**, *47*, 115-125.

Appendix

Appendix 1 Amine Functional Group Concentration on Silica by a Chemical Derivitization Method

A chemical derivatization method was used to determine the number of amino functional groups covalently bonded on the silica nanoparticle surface.

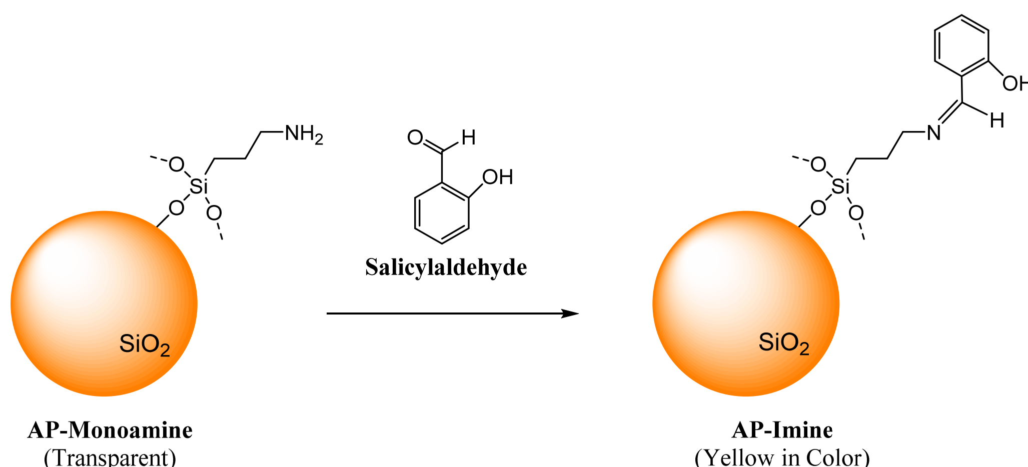

Scheme A1.1 Reaction scheme for the derivitization method.

In this method, **AP-Monoamine** was purified before use to remove all precursors, especially those containing amine which can also react with the indicator molecule. Salicylaldehyde was used as the indicator molecule as it easily reacts with the primary amine on the functionalized silica nanoparticles.[86] The resulting adduct **AP-Monoamine** suspension turns bright yellow and has a strong maximum absorbance at around 404 nm.

UV/Visible spectrum was obtained using a Perkin Elmer Lambda 25 double beam operation in conjunction with the software Perkin Elmer UV WinLab. A calibration curve was created by using a 3-aminopropyltriethoxysilane (APTES) as the model molecule (See Appendix). The absorbance at 404 nm was measured as a function of APTES concentration.

Measurement Parameters (for UV-vis spectrometer)

Parameters	Values
Scan range	300-500 nm
Scan speed	120 nm/min
Data Interval	0.1 nm

Measurement Procedure

1. Place 10 µL of the silica nanoparticle suspension (***AP-Monoamine***) and 100 µL of 1M salicylaldehyde (MW = 122.12) in absolute ethanol in a 10 mL volumetric flask and fill the flask with ethanol.
2. Shake vigorously and let stand for half an hour.
3. Fill up the solution into a disposable polystyrene cuvette.
4. Prepare another cuvette with ethanol only as background for absorption measurement.
5. Place cuvettes in UV-vis spectrometer and start the measurement.

Measurement Results and Relevant Calculations

Below is an example calculation for a sample of ***AP-Monoamine*** with the following characteristics:

A_{404} = **0,359 (from UV-vis absorption measurement)**
Particle size/diameter = **52 nm (from DLS measurement)**

In the calculations below, the amine functional group will be referred to as APTES.

Part 1: Calculation the number of APTES molecules

Using the calibration curve (Appendix A), the concentration of APTES in our solution is:

$$[APTES] = \frac{Abs(404nm) - 0,0117}{1180.2}$$

$$[APTES] = \frac{0.0359 - 0,0117}{1180.2} = 2.943 * 10^{-4} M$$

Dilution factors: the solution diluted by 1000 times the original concentration.
Thus, the original APTES concentration should be:

$$[APTES]_{original} = 2.943 * 10^{-4} M * 1/10^{-3} = 0.2943 M$$

Considering 1 L of solution, using Avogadro's number, there number of APTES molecules is:

$$number_of_APTES_molecules = 0.2943 * N_A$$

$$number_of_APTES_molecules = 0.2943 * (6.022 * 10^{23}) = 1.7721 * 10^{23}$$

Part 2: Calculation of total surface area of silica nanoparticles

Consider ONE nanoparticle as a perfect sphere with a diameter of 52 nm and silica density (ρ = 2.2 g/cm^3). The mass of this ONE nanoparticle can be approximated to be:

$$m_{sphere} = \frac{4}{3}\pi * \rho * r^3 \text{ (r in cm)}$$

$$m_{sphere} = \frac{4}{3}\pi * 2.2 * (26*10^{-7})^3 = 1.62*10^{-16} g$$

To get the number of nanoparticles, considering 1 L of nanoparticle suspension solution, the total mass (75 g) is divided by the mass of a single nanoparticle:

$$number_of_NP = \frac{m_T}{m_{sphere}}$$

$$number_of_NP = \frac{75g}{1.62*10^{-16}} = 4.63*10^{17}$$

The surface area of ONE nanoparticle considering again the nanoparticle as a perfect sphere is:

$$A_{sphere} = 4\pi r^2$$

$$A_{sphere} = 4\pi (26)^2 = 8494\ nm^2$$

Thus, the total surface area of the nanoparticles is:

$$A_{Total} = number_of_NP * A_{sphere} = 4.63*10^{17} * 8494 = 3.9327*10^{21}\ nm^2$$

Part 3: Calculation of amine functional group concentration

Thus, the total number of APTES molecules per nm^2 is:

$$\frac{number_of_APTES_molecules}{A_{Total}(nm^2)} = \frac{1.7721*10^{23}}{3.9327*10^{21}} = 45$$

Calibration Curve

- The reaction of salicylaldehyde with APTES molecules creating a yellow adduct with maximum absorption at 404 nm.
- 6 x 10 mL stock solutions containing 0, 20 μL, 40 μL, 60 μL, 80 μL and 100 μL of APTES in ethanol were prepared.
- To avoid the absorbance from going out of range, the stock solutions were further diluted. 100 μL of the stock solution was placed in a 10 mL volumetric flask and filled with ethanol. Final concentrations are shown in the table below.

Stock Solution	APTES conc [M]	$A_{404\ nm}$
1	0	0,011784
2	0,0000854	0,108598
3	0,000171	0,217511
4	0,000256	0,314762
5	0,000342	0,415910
6	0,000427	0,513645

The characteristic absorbance of the adduct at 404 nm was plotted against the APTES concentration and a linear fit trendline was approximated by Microsoft Excel to give the calibration curve equation. Thus, we obtain the resulting equation:

$$[APTES] = \frac{Abs(404nm) - 0{,}0117}{1180.2}$$

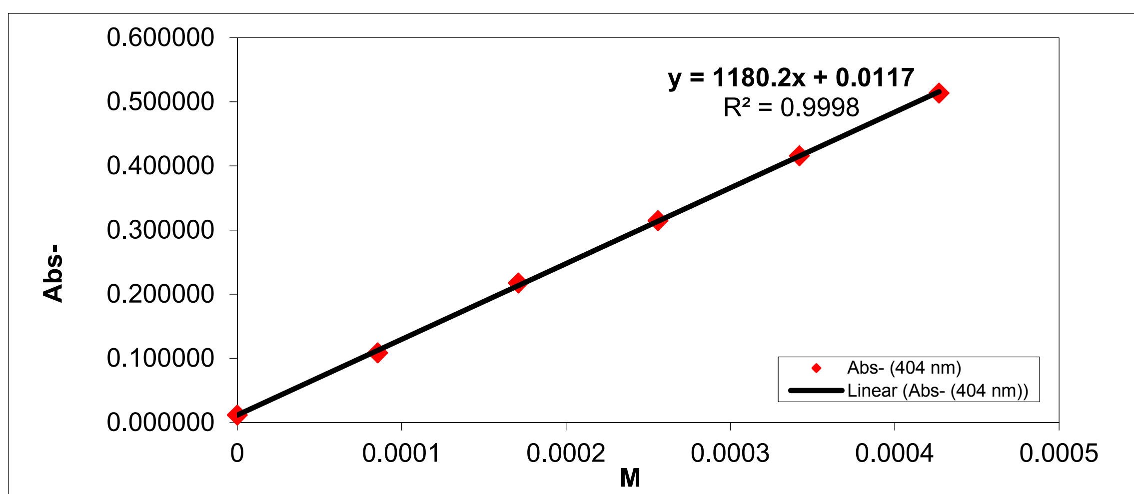

Figure A1.1 A Calibration curve was created by measuring the absorbance intensity at 404 nm. (Correlation coefficient = 0.99)

Appendix 2

Elemental analysis Calculation

With the assumption 1 g as the total mass, the mass and moles of C, H, N, and S can be calculated by using the following equation

$$Mass\ of\ (C/H/N/S) = (C/H/N/S) mass\ \% * \frac{1\ g}{100\ \%}$$

$$Moles\ of\ C = mass\ of\ C * \frac{1\ mole\ C}{12\ g\ C}$$

$$Moles\ of\ H = mass\ of\ H * \frac{1\ mole\ H}{1\ g\ H}$$

$$Moles\ of\ N = mass\ of\ N * \frac{1\ mole\ N}{14\ g\ N}$$

$$Moles\ of\ S = mass\ of\ S * \frac{1\ mole\ S}{32\ g\ S}$$

The number of APTES molecules is

$$number\ of\ APTES\ molecules = moles\ of\ N * (6 * 10^{23})$$

$$number\ of\ DPTES\ molecules = moles\ of\ N * (6 * 10^{23})/2$$

$$number\ of\ TPTMS\ molecules = moles\ of\ N * (6 * 10^{23})/3$$

$$number\ of\ MPTS\ molecules = moles\ of\ S * (6 * 10^{23})$$

By using the radius of the particle and the density of the particle the total surface area (nm^2) of silica nanoparticles can be calculated. Please refer to the Appendix 1 part 2 for the calculation of the surface area of the particles.

Thus, the total number of molecules per nm^2 is:

$$molecules/nm^2 = \frac{number_of_molecules}{A_{Total}(nm^2)}$$

Table A2. 1 The CHNS elemental composition of various functionalized silica nanoparticle measured by elemental analysis

AP name	C [%]	H [%]	N [%]	S [%]	C [mmol]	H [mmol]	N [mmol]	S [mmol]	Coverage [molecules/nm2]
AP-Monoamine M	20.7	6.0	5.0	0	17.25	60.0	3.57	0	14
AP-Diamine	32.2	7.5	9.0	0	26.83	75.00	6.43	0	13
AP-Triamine	32.4	7.4	9.7	0	27	74.00	6.93	0	9
AP-Mercapto	15.4	2.9	0	7	12.83	29.00	0	2.19	9

Appendix 3

TEM Images

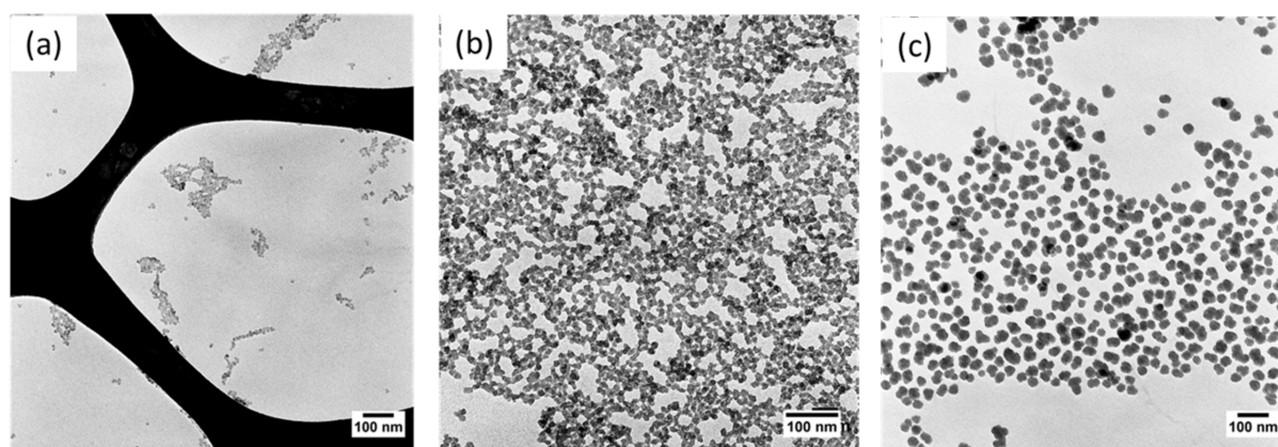

Figure A3. 1 The TEM images of (a) AP-Hydroxyl S, (b) AP-Hydroxyl M, and (c) AP-Hydroxyl L

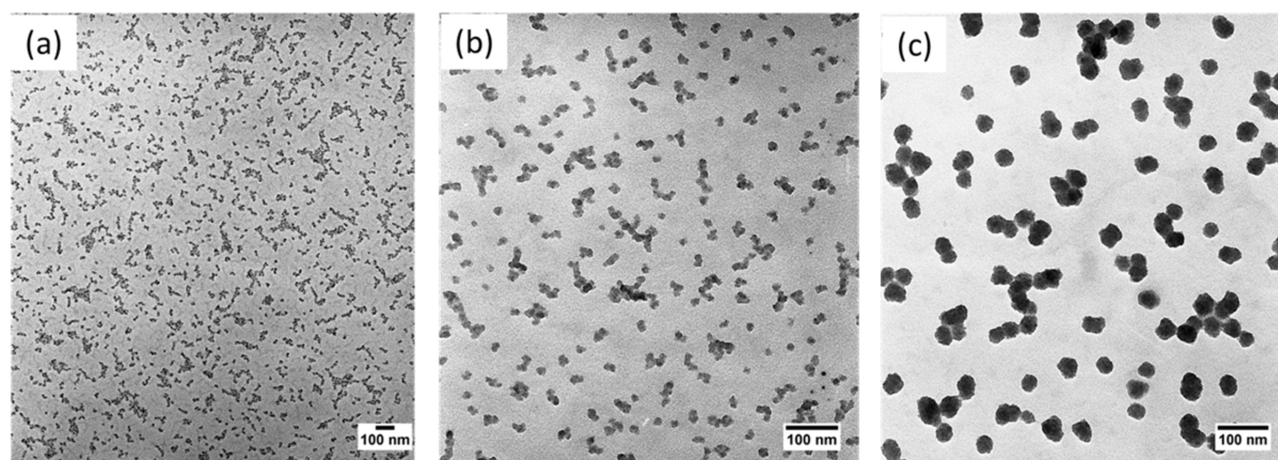

Figure A3. 2 The TEM images of (a) AP-Monoamine S, (b) AP-Monoamine M, and (c) AP-Monoamine L

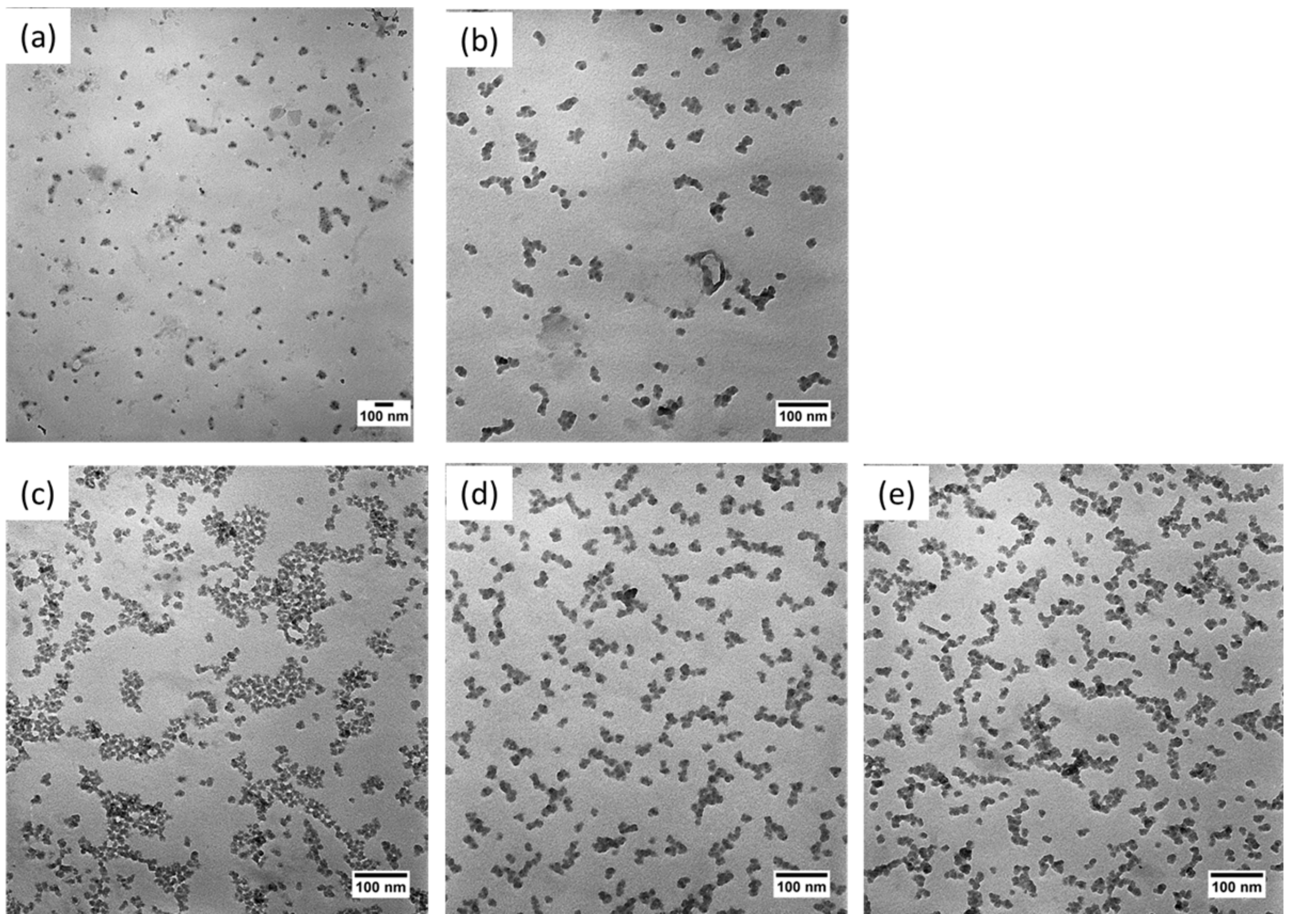

Figure A3. 3 The TEM images of (a) AP-Gylcidoxy, (b) AP-Mercapto, (c) AP-Ureido, (d) AP-Diamine, and (e) AP-Triamine

Appendix 4

(a)

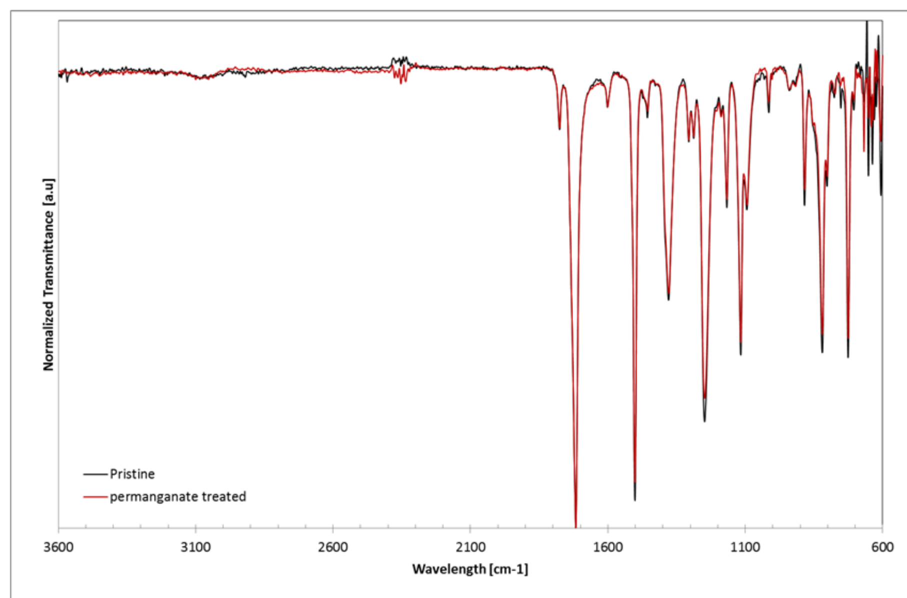

(b)

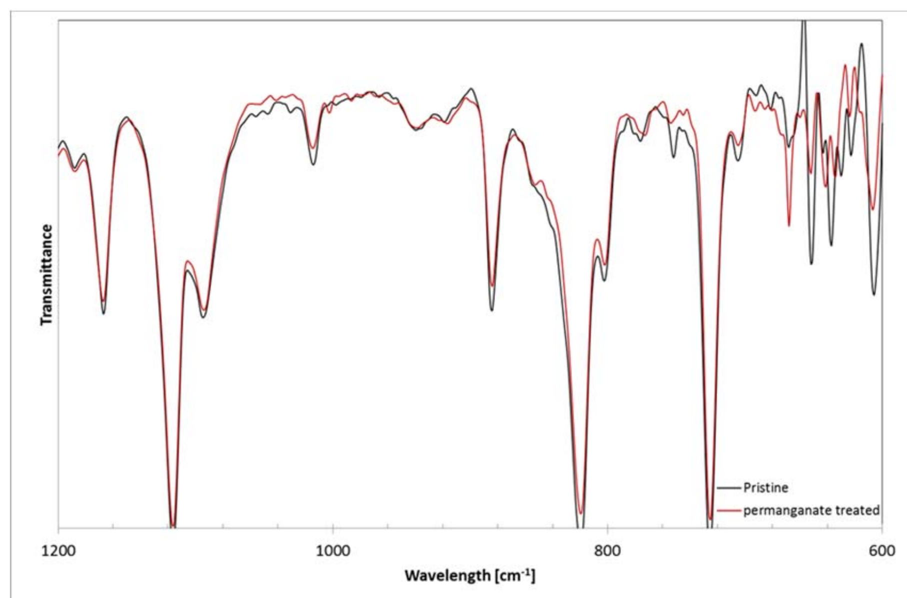

Figure A4. 1 FTIR-ATR spectra of pristine (black) and 1 min permanganate treated (red) polyimide film. The spectra were collected from (a) 600-3600 cm^{-1} and (b) 600-1200 cm^{-1}

Appendix 5

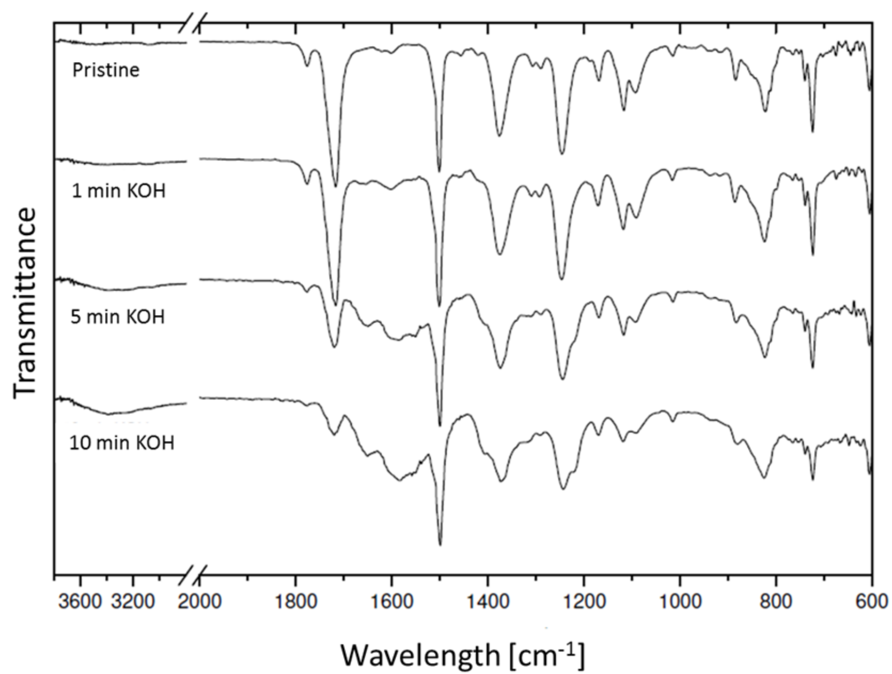

Figure A5. 1 FTIR-ATR spectra of KOH treated polyimide film.[169] The polyimide film was immersed into 1 M KOH solution at 80 °C for different immersion time

Appendix 6

(a)

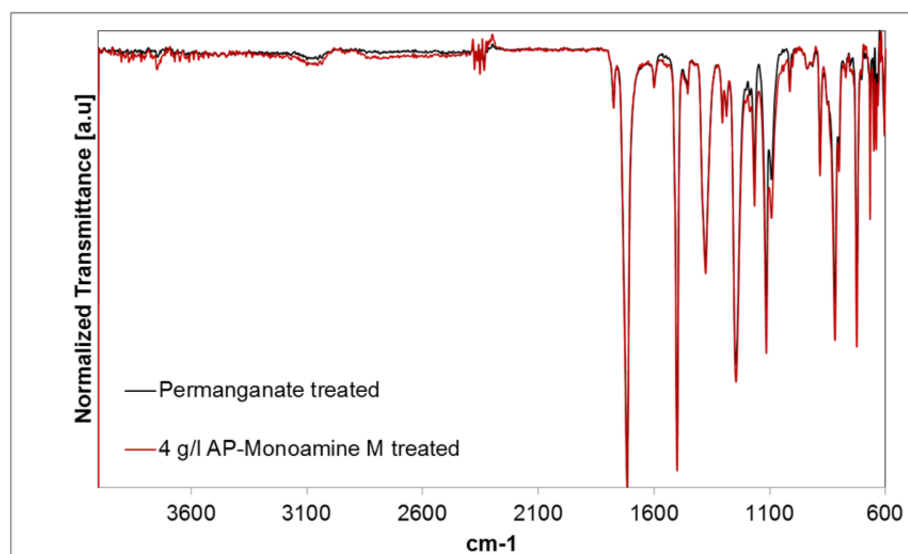

(b)

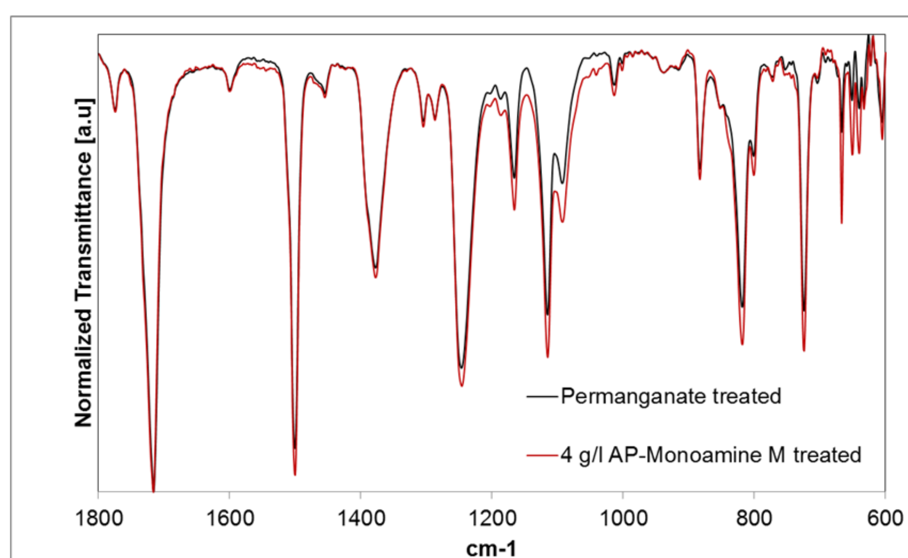

Figure A6. 1 The FTIR spectra of polyimide film treated with permanganate (black) and 4 g/L of *AP-Monoamine M* (red). The spectra were collected from (a) 600-3600 cm^{-1} and (b) 600-1800 cm^{-1}

List of publications

Patents

2013 European Patent (Submitted)

Dirk Tews, Fabian Michalik, Belén Gil-Ibanéz, Thomas Thomas, Martin Thoms

Novel adhesion promoting agents for bonding dielectrics material to metal layers

Application No. 13170640.0-1362

2013 European Patent (Published)

Thomas Thomas, Lutz Brandt, Lutz Stamp, Hans-Jürgen Schreier

Novel adhesion promoting agents for metallization of substrate surfaces

Patent No. EP 2 602357 A1

2013 Worldwide Patent (Published)

Thomas Thomas, Lutz Brandt, Lutz Stamp, Hans-Jürgen Schreier

Novel adhesion promoting agents for metallization of substrate surfaces

Patent No. WO2013083600 A2

Abbreviations and symbols

A	Baseline of the correlation function in DLS; Absorbance in UV-Vis
AFM	Atomic Force Microscope
AP-Diamine	Diamine functionalized silica nanoparticles
AP-Glycidoxy	Glycidoxy functionalized silica nanoparticles
AP-Mercapto	Mercapto functionalized silica nanoparticles
AP-Monoamine	Monoamine functionalized silica nanoparticles
AP-Triamine	Triamine functionalized silica nanoparticles
AP-Ureido	Ureido functionalized silica nanoparticles
B	Intercept of the correlation function
b	Path length in UV-Vis
BSE	Back-scattered Electron
c	Concentration of absorbing species
CTE	Constant of Thermal Expansion
d_h	Hydrodynamic diameter
DLS	Dynamic Light Scattering
DMAc	*N,N*-dimethylacetamide
d_p	Evanescent wave penetration depth in FTIR-ATR
D_T	Translation diffusion coefficient
E_B^{Vac}	Binding energy in vacuum of insulated sample
ECD	Electrolytic Copper Deposition
E_k	Kinetic energy
e-less	Electroless deposition
FESEM	Field Emission Scanning Electron Microscope

FTIR	Fourier Transform Infra-red
FTIR-ATR	Fourier Transform Infra-red-Attenuated Total Reflectance
G(τ)	Autocorrelation function
h	Hours
hv	X-ray photon energy
IC	Integrated Circuit
ICP-OES	Inductively Coupled Plasma-Optical Emission Spectroscopy
ITRS	International Technology Roadmap for Semiconductors
Kapton®200 H	Poly [N, N'-(oxydiphenylene)pyromellitimide]
LDV	Laser Doppler Velocimetry
min	Minutes
n	Refractive index of the suspension
n(t)	Scattering intensity at time *t*
n_1	Sample refractive index in FTIR-ATR
n_2	Crystal refractive index in FTIR-ATR
NMP	*N*-methylpyrrolidone
ODA	4,4'-oxydianiline
OFG	Oberflächen - Festkörper - Grenzflächen
P	Intensity of light transmitted through the sample in UV-Vis
P_0	Intensity of the incident light in UV-Vis
PAMAM	Polyamidoamine
PCB	Printed Circuit Board
PCS	Photon Correlation Spectroscopy
PE	Primary Electron
PMDA	pyromellitic dianhydride
PWB	Printed Wiring Board
q	Modulus of scattering vector

QELS	Quasi-elastic Light Scattering
RSAI (%)	Relative Surface Area Increase
S_A(nm)	Average Roughness
SAP	Semi Additive Process
SE	Secondary Electron
S_Q(nm)	Root Mean Square Roughness
S_T (nm)	Maximum Height Difference
t	Time
TEOS	TetraEthylOrthoSilicate
Tg	Glass Transition Temperature
TLC	Through holes Low Current density
Tr	Easymax reactor temperature
UV-Vis	Ultraviolet-Visible Spectroscopy
XPS	X-ray Photoelectron Spectroscopy
ε	Molar absorbtivity
Θ	Scattering angle in DLS; Angle of incident beam in FTIR-ATR
λ	Laser wavelength
π	Circle mathematical constant, 3.14
τ	Delay time
ϕ_e	Energy of the flooding electron
ϕ_s	Insulated sample work function